Max Schmallegger, BSc MSc

Radicals in Photochemical Transformations: Models for Biological Pathways and Intermediates in Chemical Synthesis

DISSERTATION

zur Erlangung des akademischen Grades

Doktor der Naturwissenschaften

eingereicht an der

Technischen Universität Graz

Betreuer

Univ.-Prof. Mag.rer.nat. Dr.phil, Georg Gescheidt-Demner

Institut für Physikalische und Theoretische Chemie

Fakultät für Technische Chemie, Verfahrenstechnik und Biotechnologie

Graz, Mai 2019

EIDESSTATTLICHE ERKLÄRUNG

Ich erkläre an Eides statt, dass ich die vorliegende Arbeit selbstständig verfasst, andere als die angegebenen Quellen/Hilfsmittel nicht benutzt, und die den benutzten Quellen wörtlich und inhaltlich entnommenen Stellen als solche kenntlich gemacht habe. Das in TUGRAZonline hochgeladene Textdokument ist mit der vorliegenden Dissertation identisch.

Datum

Unterschrift

Acknowledgments

I am very lucky and thankful to all the people who helped and supported me during my doctoral thesis.

First of all, I want to thank my supervisor Prof. Georg Gescheidt for his guidance, countless important discussions and moral support throughout the years and for the pleasant working environment he provided. But most importantly, I thank Georg for the fun I had working on my projects, all the opportunities he provided me and for the freedom he gave me in my research.

I also wholeheartedly thank the great colleagues in our group: Anna, Edi, Philipp, Dimi and Anne-Marie, thank you for inspirational discussions, great input to my work, for help with my experiments and a fantastic working atmosphere.

I thank Hilde, Marion and Christian, for their help with experiments, lab equipment, organizational questions and computer issues as well as moral support. I additionally want to thank my Bachelor students Lisbeth, Philipp, Andrea, Sandro and Stefan for their help in performing measurements.

Moreover, I want to thank all scientific collaborators I was lucky to work with during my doctoral thesis: I want to especially thank Antonio Barbon, Lev Weiner and everybody who was involved in the work on electron transfer, Prof. Grützmacher for our collaboration in the projects related to BAPO photoinitiators, Angela Chemelli for SAXS and DLS measurements, which were invaluable in many studies, and everybody else who contributed to this doctoral thesis.

Finally, I want to thank my friends and family who are always there for me. I especially thank my parents, my brother and Leni for their support and patience with me. All of this would not have been possible without you.

Abstract

This doctoral thesis addresses the light-induced formation of radical species and other reactive intermediates. It elucidates their follow-up reactions with special focus on addition, hydrogen-atom transfer, proton-transfer, and electron-transfer reactions. The aim of this thesis is an in-depth study of different aspects of light-induced radical chemistry providing a deeper understanding of biomimetic systems, applications in photo-polymerization and light-induced nanomaterial fabrication. To this end, two different projects are particularly discussed:

The first project addresses photo-induced electron- and proton-transfer reactions in biomimetic systems. The research shown here is crucial for understanding fundamental aspects of biological electron- and proton-transfer reactions and is highly useful for models describing complex biological systems. In addition, the results presented here provide a starting point to construct intricate systems for solar energy conversion.

The second project is targeted toward the reactivity of photo-initiators for radical polymerization. It aims at extending their use to the reduction of Cu^{2+} salts. The new pathways of simultaneous photo-polymerization and photo-reduction opens the door for the synthesis of metal-polymer nanocomposites for the fabrication of heterogeneous catalysts, conducting polymers and sensor systems.

The main experimental techniques employed in these projects are optical spectroscopy, transient absorption spectroscopy, continuous-wave electron paramagnetic resonance (EPR), chemically induced dynamic nuclear polarization (CIDNP) and chemically induced dynamic electron polarization (CIDEP). These spectroscopic methods address different kinetic time-scales and properties of chemical species, complementing each other to give a more complete picture of these highly relevant, light-induced transformations.

In summary, the results presented in this thesis provide novel insights into light-induced transformations for modelling and understanding complex biological reactions and photo-induced synthesis.

Kurzfassung

Gegenstand dieser Doktorarbeit ist die licht-induzierte Bildung von radikalischen Spezies und anderer reaktiver Intermediate, sowie die Aufklärung derer Folgechemie mit besonderem Fokus auf Additions-, Wasserstoff-Atom Transfer, Protonen-Transfer und Elektronen-Transfer Reaktionen. Das Ziel ist eine eingehende Untersuchung unterschiedlicher Aspekte licht-induzierter Radikalchemie um ein tieferes Verständnis für diese Reaktionen zu erlangen. Sie sind hochrelevant in bio-mimetischen Untersuchungen, Photo-Polymerisationen und der licht-induzierten Nanomaterial-Herstellung. Hierzu werden zwei Projekte diskutiert:

Das erste Projekt beschäftigt sich mit licht-induzierten Elektronen- und Protonen-Transfer Reaktionen in Modellsystemen für komplexe biologische Prozesse und in bio-mimetischen Membranen. Die darin enthaltenen Ergebnisse sind von Bedeutung für das Verständnis von grundlegenden Aspekten in biologischen Elektronen- und Protonen-Tranfer Reaktionen. Darüber hinaus können diese Untersuchungen als Ausgangspunkt zur Herstellung komplexer Systeme für die Energieumwandlung von Sonnenlicht dienen.

Das zweite Projekt beleuchtet die Reaktivität von Photoinitiatoren für radikalische Polymerisationen und zeigt, dass diese auch zur Reduktion von Cu^{2+} dienen können. Des weiteren wurden Untersuchungen zu simultanen Polymerisationen und Reduktionen mit Photoinitiator Systemen durchgeführt. Die entsprechenden Ergebnisse ermöglichen die Herstellung von Metal-Polymer Nano-Verbundstoffen, die in Zukunft das Potential haben als leitende Polymere, heterogene Katalysatoren oder Sensorsysteme eingesetzt zu werden.

Die in dieser Doktorarbeit beschriebenen Untersuchung wurden mithilfe statischer und zeitaufgelöster optischer Spektroskopie, sowie diverser Magnetresonanzspektroskopie-Techniken durchgeführt. Diese spektroskopischen Methoden erlauben die Untersuchung von chemischen Spezies auf unterschiedlichen Zeitskalen und ergeben ein vollständigeres Bild dieser hochrelaventen, licht-induzierten Reaktionen

Diese Doktorarbeit gibt neue Einblicke in licht-induzierte Umwandlungen. Sie sind sowohl für das Verständnis von komplexen biologischen Reaktionen, als auch für die Anwendungen in photochemischen Synthesen von höchster Bedeutung.

Table of Contents

1. Introduction

The interaction between light and matter, the particular subject of *Photochemistry*, is one of the fundamental processes in nature. It is the basis of photosynthesis, vision and the biosynthesis of vitamin D. Without photochemical transformations, life on earth would not be possible. In its simplest form, photochemistry involves the following overall process:

$$R + h\nu \rightarrow R^* \rightarrow P$$

R is a molecule absorbing a photon ($h\nu$) reaching an electronically excited state R*, which further reacts to yield a stable product P. This product formation can proceed via three fundamentally distinct pathways, called primary photochemical processes, as summarized in Scheme 1[1]:

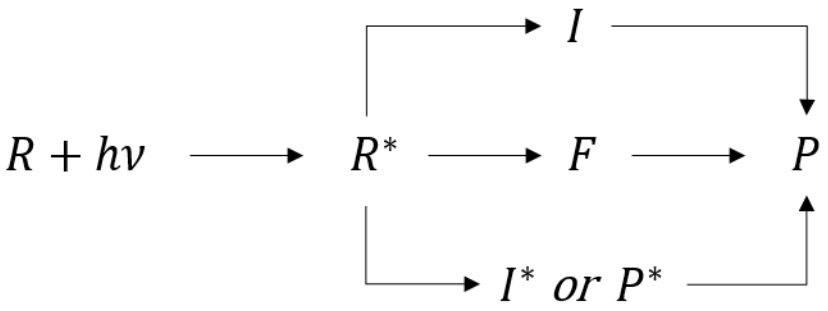

Scheme 1. Primary photochemical processes yielding a product P from the reaction between R and light

1 The first pathway (R* → I → P) proceeds via the formation of a discrete reactive intermediate I. Here, I is a radical pair, a biradical or a zwitterion.

2 The second pathway (R* → F → P) does not proceed via a discrete intermediate, but through a “funnel” F, taking R* to P. In terms of potential energy surfaces, this funnel can be described as a conical surface intersection.

3 The third pathway (R* → I* → P or R* → P* → P) involves the formation of an excited-state intermediate (I*) or and excited-state product (P*).

In a first step, a molecule R is irradiated and reaches its electronically excited state R*. Here, the additional energy causes an altered electronic structure and therefore, the reactivity of R* is drastically different from R. Excited states may participate in different reactions due to their higher energy and their altered electronic arrangement.[2] Scheme 2 summarizes the most important reaction pathways for an excited molecule R*. These character of the follow-up conversions is either physical, where the excess energy relaxes without chemical conversion (Scheme 2, marked blue) or chemical, where the excess energy leads to new chemical species (Scheme 2, marked yellow).

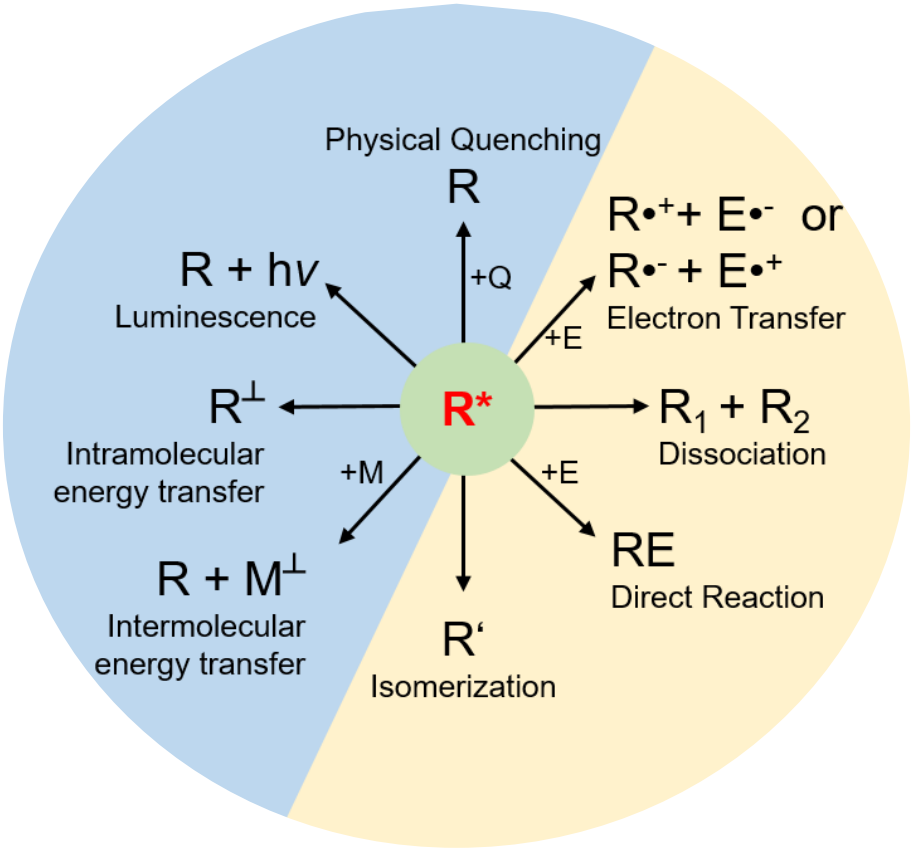

Scheme 2. Summary of important chemical (yellow) and physical pathways (blue) to convert excess energy from an excited molecule R*.

The most important physical reaction pathways are inter- and intramolecular energy transfer, luminescence and physical quenching (blue zone in Scheme 2):

- Intermolecular and intramolecular energy transfer lead to the generation of excited electronic states different to R* formed in the initial absorption step. In intermolecular energy transfer, the excess energy is transferred to a different chemical species M, forming $M^{\perp}$ and R. In intramolecular energy transfer, a new electronic state $R^{\perp}$ of the initial molecule R* is populated.
- The emission of radiation by R* to convert electronic excitation - fluorescence and phosphorescence - are summarized under the general term luminescence. Fluorescence describes radiation from an excited singlet state of R*, while in phosphorescence, radiation occurs from a triplet state of R*.
- The last physical route to lose excess energy is physical quenching, where the electronic energy of R* is converted to translational or vibrational energy by collision with a quencher atom or molecule Q.

A simple way to summarize the electronic states of a chemical species and the physical pathways to convert excess energy from R* is the Jablonski diagram (Scheme 3).[3]

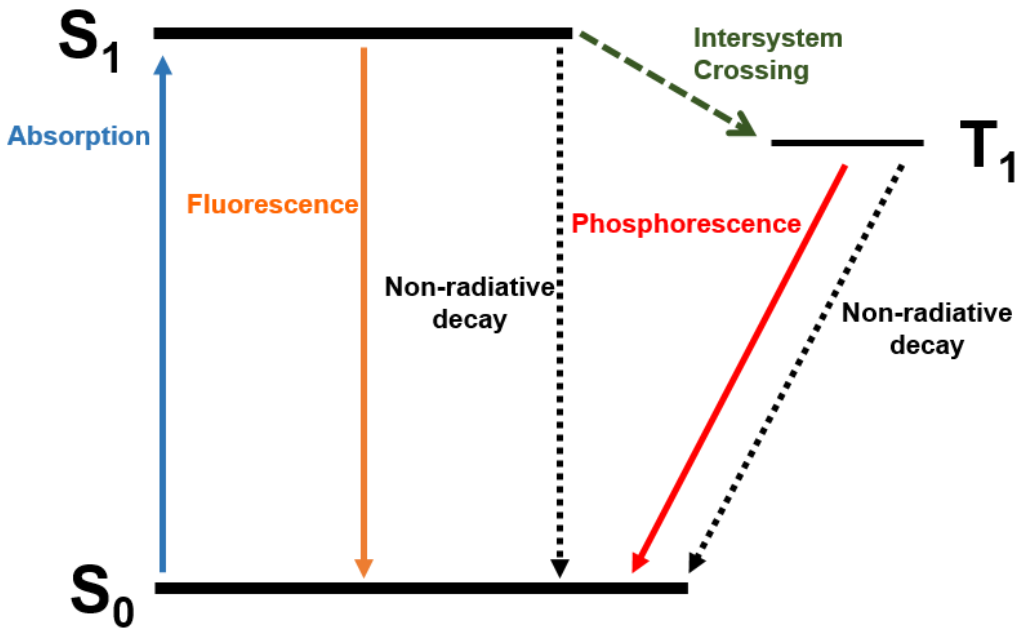

Scheme 3. Simplified Jablonski diagram, summarizing the most important transitions between electronic states of a molecule; the vibrational levels are omitted for clearness

The Jablonski diagram summarizes the ground state, first excited states and their multiplicity and possible transitions between the states: The ground state S_0 (singlet state) is excited to the first excited singlet state S_1 by absorption of electromagnetic radiation. This S_1 state can undergo radiative (fluorescence) or non-radiative decay (inter- or intramolecular energy transfer and physical quenching) back to the ground state or intersystem crossing (ISC) to a triplet state T_1. This T_1 state again can undergo radiative (phosphorescence) or non-radiative decay back to the ground state.

The yellow zone in Scheme 2 represents the chemical pathways, where the excess energy of R* leads to the formation of new chemical species. The most important chemical reaction pathways are electron transfer, dissociation, direct reactions and isomerization:

- In electron transfer, the excitation energy of R* is used to promote a reaction, either by overcoming an activation barrier or as a consequence of the new electronic arrangement in the excited state. Electron transfer reactions are usually intermolecular processes between R* and E, forming a radical-ion pair. (either $R^{\bullet+}$ and $E^{\bullet-}$ or $R^{\bullet-}$ and $E^{\bullet+}$). However, also intramolecular reactions, where one part of an excited molecule R* attacks another part, are well-established.
- Dissociation leads to the fragmentation of R* into two (or more) chemical species R_1 and R_2. In dissociation reactions, the energy of the absorbed photon has to be high enough to rupture a chemical bond.
- Direct reactions are similar to electron transfer reactions: In both pathways, the excitation energy of R* is used to promote a reaction. In direct reactions, R* reacts with a different molecule E, yielding a new chemical product RE.
- Another chemical pathway to convert excess energy is the isomerization of R*. A typical example for this pathway is the *E-Z* isomerization of a double bond in the excited state, forming the new species R'.

Scheme 2 reveals that free radicals are prominent primary reaction products in photochemistry. They can be formed via the above-mentioned chemical pathways: Dissociation of a bond via homolytic bond cleavage produces two neutral radicals[4], while electron-transfer reactions yield a radical anion and a radical cation. Whether R* donates an electron to E and forms a radical cation $R^{\bullet+}$ or accepts an electron, forming a radical anion $R^{\bullet-}$ depends on the redox properties of the two reaction partners.[5]

Most free radicals are highly reactive and can undergo a number of different follow-up reactions. Due to their reactivity and versatility, free radicals are important not only in biology and fundamental chemistry, but also in areas of industrial and applied chemistry, including autoxidation reactions and polymerizations. Among the most important reactions of free radicals are recombination, addition reactions, rearrangements, decomposition and hydrogen-atom transfer (HAT) and electron-transfer (ET) reactions.[6]

In this doctoral thesis, the photo-induced formation of short-lived intermediates, especially radicals, is investigated in depth. I will elucidate the follow-up reactions of these radical species with a special focus on addition, hydrogen-atom transfer and electron-transfer reactions.

This thesis comprises two main sections: The first section addresses photo-induced electron and proton-transfer reactions in model systems for complex biological processes and in biomimetic membranes. The second section focusses on the reactivity of photo-initiators for radical polymerization. It also aims to extend this reactivity to the reduction of Cu^{2+} salts. In addition, this doctoral thesis comprises two studies focussing on electron paramagnetic resonance spectroscopy and its application in detecting stable organic radicals and other paramagnetic species. Particularly, these studies address the use of EPR in teaching and in detecting paramagnetic Ti^{3+} centres in metal-organic frameworks.

1.1. Electron Transfer and Proton Transfer Processes in Biological Systems

Redox reactions are at the core of many important energy conversion processes in chemistry and biology. In these important conversion reactions, electrons are transferred. This electron transfer can be accompanied by a simultaneous proton-transfer (PT). Alternatively, PT can also precede or follow the electron transfer in consecutive processes. One of the most fundamental processes on earth – photosynthesis in green plants, where carbon dioxide and water are converted to oxygen and hydrocarbons – involves the transfer of electrons and protons. When talking about these fundamental reactions, four main pathways, summarized in the "Square Scheme" (Scheme 4), can be distinguished. An insight into these different processes and pathways is crucial for the understanding of important biological reactions like photosynthesis, and also for the development and optimization of chemical reactions and processes.[7,8]

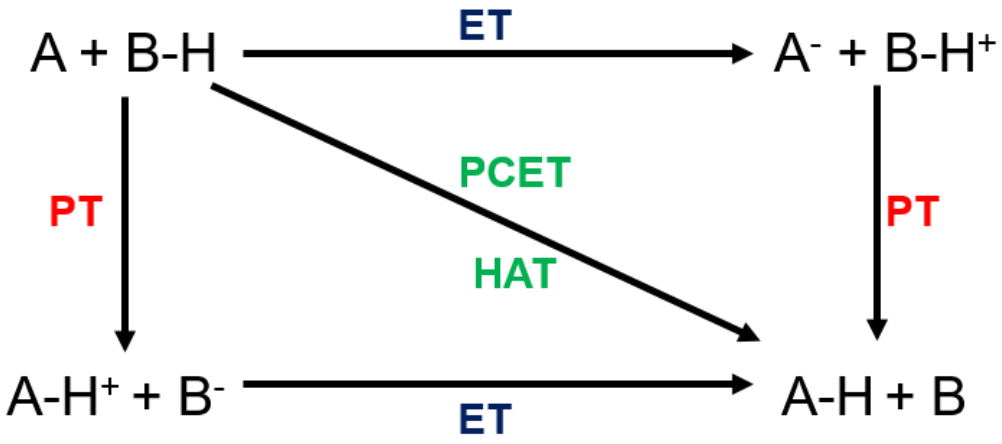

Scheme 4. Square scheme summarizing PCET and HAT reactions (diagonal), discrete ET reactions (horizontal) and discrete PT reactions (vertical).

1. Electron transfer (ET): In this reaction, an electron is transferred from one chemical species to another, changing the redox state of both reaction partners (see Scheme 4, horizontal reactions). ET is a key step in countless chemical reactions and is also an essential step in many biological processes, including oxygen binding, photosynthesis, and respiration.[9,10] Many of these biological electron transfer reactions involve transition

metal complexes, but there are also numerous examples for ET by organic molecules and reactive intermediates such as radicals.[11–13]

2. Proton Transfer (PT): Proton transfer reactions are comparable to ET reactions in that they lead to the formation of two ions (Scheme 4, vertical reactions). The most prominent form of these reactions are PT by Lewis acids.[14]

3. Proton-Coupled Electron Transfer (PCET): This reaction pathway involves the transfer of both an electron and a proton (Scheme 4, diagonal). Strictly speaking, in PCET a single electron and a single proton are transferred in a concerted way. The proton and electron are transferred from different orbitals in the donor to different orbitals in the acceptor in a single, concerted step. PCET reactions play an important role in photosynthesis, nitrogen fixation and oxygen reduction.[7,15]

4. Hydrogen Atom Transfer (HAT): Hydrogen atom transfer reactions resemble PCET in that an electron and a proton are transferred (Scheme 4, diagonal). In contrast to PCET however, both are transferred from the same orbital in the donor to the same orbital in the acceptor. Because of this definition, HAT is viewed as a radical pathway. This reaction pathway is especially important in the autoxidation of lipids and in radical polymerizations.[16–18]

As mentioned above, ET processes are fundamental in all living organisms. In cases where the electron donor and acceptor have considerable mobility (*e.g.* in solution), they will collide, forming an interaction complex. The electron transfer will occur in this complex, yielding an ion pair. In those cases, the rate of electron transfer is governed by the diffusion rate (k_{Diff}) of the donor and the acceptor.[19,20] Equation 1 represents a general electron transfer reaction from a donor *D* and an acceptor *A* via the formation of an interaction complex and an ion pair in solution.

$$A + D \xrightarrow{k_{Diff}} A\|D \xrightarrow{k_{ET}} A^-\|D^+ \xrightarrow{k_{Diff}} A^- + D^+ \qquad (\mathbf{1})$$

However, the electron transfer mechanism in biological systems often differs from the mechanism in solution, since the two partners are separated at a long distance. This separation can occur by

fixation of the donor- and acceptor-systems in DNA and RNA[21,22] or in proteins.[23–27] Additionally, the donor and the acceptor might be separated by dendrimers[28] or phospholipid bilayers.[29]

For such long-distance electron transfer reactions, different mechanisms are involved: Tunnelling (also called superexchange) of electrons between sites[30,31], electron hopping in organized media,[32] and adiabatic ET with the medium playing a prominent role[32,33]:

1. For tunnelling, the interaction between donor and acceptor is determined by an electronic coupling matrix element, with theory predicting that the reaction rate depends exponentially on the donor/acceptor distance.[32] This mechanism is especially important for ET in proteins. The distance-dependence of the ET in tunnelling is described by Marcus theory (see Equation 2).[9] In this equation, H_{DA} describes the electronic coupling between donor and acceptor, ΔG^0 is the reaction free energy and λ is the reorganization energy, accounting for changes in solvation and molecular rearrangement following ET.

$$k_{ET} = \sqrt{\frac{4\pi}{h^2 \lambda k_B T}}\, {H_{DA}}^2 \exp\left[-\frac{(\lambda + \Delta G^0)^2}{4\lambda k_B T}\right] \quad (\mathbf{2})$$

2. For distances exceeding the upper limit, electron tunnelling can be overcome by multistep electron hopping reactions. According to this mechanism, the overall distance between the primary donor and the final acceptor is split into a series of short ET steps.[34] The hopping model of ET was first developed for biopolymers, especially DNA and RNA.[35]

3. Long-range ET in biological systems can also proceed via adiabatic ET. This pathway is characterized by a sensitivity of the electron transfer rate process to solvent properties like reorganization, both in an isotropic environment[36] or in a heterogeneous medium.[37]

Long-range electron transfer is a crucial step in a number of biological processes. Among the systems which are used by nature to separate donor- and acceptor-pairs, lipid bilayer membranes are among the most common ones. As an example, the charge separation of electron-donor and –acceptor is one of the foundations of photosynthetic systems and an understanding of ET across lipid bilayers is crucial for the rational design of artificial photosynthetic devices. However, the complexity of “real” biological membranes often necessitates the use of simple model systems to

help developing and testing concepts about photosynthesis and the role of the lipid bilayer in long-range electron transfer.[38] To this end, a number of studies investigating electron transfer reactions across lipid bilayers have been performed, using biomimetic model membranes.[39–42]

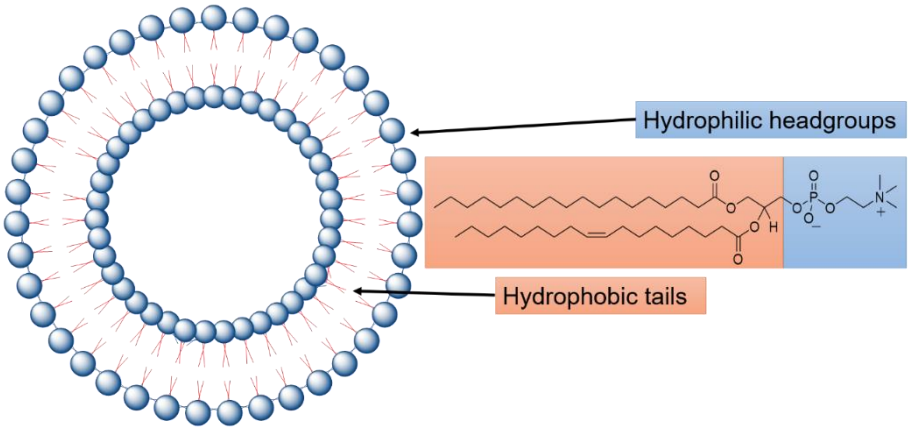

Scheme 5. Simplified representation of a unilamellar liposome comprised of the phosphatidylcholine *1-Palmitoyl-2-oleoylphosphatidylcholine* (POPC)

Unilamellar liposomes composed of phospholipids serve as suitable models for biological membranes.[43–46] They are constituted by phospholipids like phosphatidylcholine (PC) with long alkyl “tails” and a polar headgroup and are, therefore, amphiphilic (Scheme 5). Unilamellar phospholipids have a typical membrane thickness of 3 – 5 nm and particle diameter ranging from 20 – 100 nm for small unilamellar vesicles (SUV) and 100 – 1000 nm for large unilamellar vesicles (LUV).

1.2. Reactivity of Radical Photoinitiators

Photo-induced radical polymerization is a widely used method in a broad range of industrial applications, including coatings, semiconductors, 3-D printing, stereo-lithography and medicine.[47,48] The major advantages of this technique are the high curing speed, spatial resolution, applicability at low temperature and the possibility to produce solvent-free formulations.

A key component in photo-induced radical polymerization is the photoinitiator (PI). Its excitation by light is the initial process in the polymerization. Therefore, testing the PI efficiency and improving its performance together with the development of novel initiator systems is an ongoing process. A PI must fulfil several criteria: Firstly, it has to absorb light of a desired wavelength with high efficiency (quantum yield). Secondly, the reactive species formed upon irradiation should show high reactivity toward monomers.[48,49]

Photo-induced radical polymerization involves three main steps, which are depicted in Scheme 6. The initiation features the radical generation upon irradiation of the PI, followed by the addition of the primary radicals to a monomer. This first addition step then starts the chain growth reaction (propagation). The chain growth is terminated either by radical recombination or by disproportionation reactions.[18]

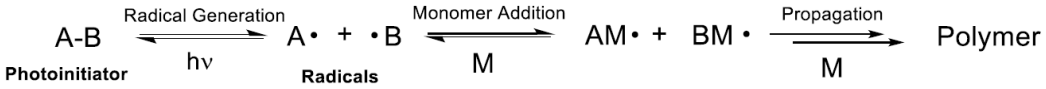

Scheme 6. General reaction scheme for photo-induced radical polymerization by a Norrish type I initiator.

Photoinitiator systems can be divided into two categories: Norrish type I initiators undergo bond cleavage, directly forming radical species. Upon irradiation, the photo-initiator is excited to an excited singlet state. Then, in most cases, the PI undergoes intersystem crossing (ISC) to a triplet state. In this triplet state the initiator subsequently undergoes bond cleavage (see Scheme 7). The prototype of this photo-reaction is the cleavage of a σ-bond adjacent to a carbonyl group. Depending on the substitution pattern on the carbonyl group, either α- or β-cleavage of the parent PI is preferred.[50] Typical examples of Norrish type I PIs are aryl ketones (*e.g.* benzoin derivatives, α-hydroxy ketones and α-amino ketones) and acylphosphane oxides.

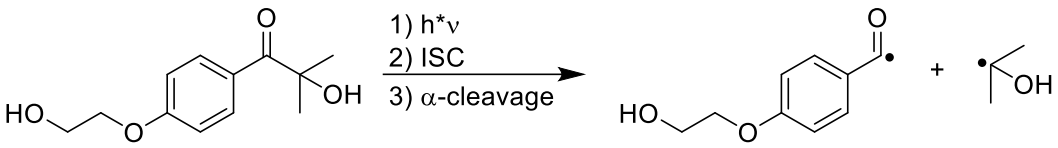

Scheme 7. Bond-cleavage of the commercial α-hydroxy ketone photoinitiator *Irgacure 2959* upon irradiation and subsequent intersystem crossing

In a Norrish type II reaction, the radical species are formed in a bimolecular reaction between the photo-excited PI molecule and a donor system. This donor can undergo either a hydrogen-atom transfer or an electron-transfer to the PI, forming a neutral initiator radical (Scheme 8a) or an initiator radical anion (Scheme 8b), respectively. These Norrish type II initiators are usually ketones such as benzophenone[51], acetophenone[52] or camphroquinone.[53] Typical donor systems are alcohols (hydrogen atom donors) or secondary and tertiary amines (electron donors).[54–56] Due to their higher efficiency and rate of decomposition, Norrish type I PIs are more widely applied then type II PIs.[57]

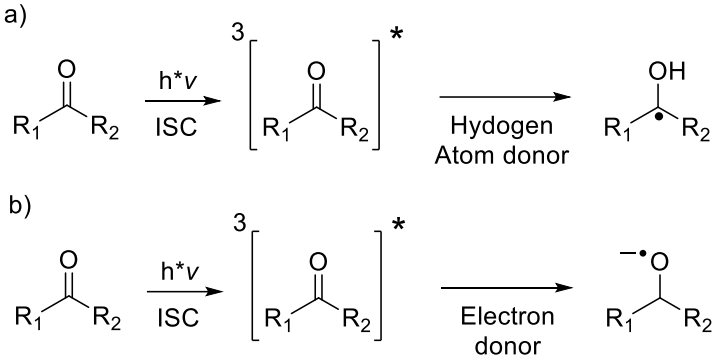

Scheme 8. Photo-sensitization mechanism for a ketone/hydrogen-donor system (a) and a ketone/electron donor system (b) upon irradiation and intersystem crossing to the triplet state.

An additional application to polymerization reactions for both Norrish type I and type II is their usage for the photo-induced fabrication of metal nanomaterials. These metal nanomaterials, especially nanoparticles (NPs), have experienced a vast growth in interest over the last years: Metallic NPs often exhibit remarkable chemical properties differing from the bulk material[58,59], leading to applications *e.g.* for molecular imaging[60] or catalysis,[61] and in fields like nonlinear optics and electric conduction.[62–64]

A variety of methods for the synthesis of metallic nanoparticles has been reported. They include chemical, thermal, radiation-chemical, sono-chemical, and photo-chemical methods.[65–68] However, many of these approaches require expensive reagents, hazardous reaction conditions, and long reaction times combined with difficult isolation procedures[66,69]. Photochemical methods offer a valuable access to producing metal nanoparticles in a controlled way.[58,70–76] They allow a simple and fast one-pot synthesis under mild conditions employing readily available precursors. Additionally, photochemical methods offer size control of the particles by altering irradiation times.[74,77]

For the photo-chemical reduction of metal nanoparticles, different approaches exist. The simplest approach is the direct photo-reduction, where the elemental nanoparticles form by direct excitation of a metal source.[58] In the direct photo-reduction, the excited metal source either undergoes a reaction with solvent molecules or a disproportionation reaction, yielding the elemental metal. This method is widely employed for silver[78], gold[79] and platinum salts.[80]

An alternative approach for the photo-chemical metal reduction is photosensitization.[81,82] Here, a photo-active reagent which generates reactive intermediates upon irradiation is employed. An example of this approach is the above-mentioned use of photoinitiators, producing free radicals as reactive intermediates upon irradiation. In turn, these intermediates reduce the metal salts to elemental metal nanoparticles. Compared to direct photo-reduction, this approach is fast and efficient. Furthermore, this method provides more flexibility of the excitation wavelength, as it depends on the absorption properties of the sensitizer and not the nature of the metal precursor.[58]

Free radicals are type of redox-active compounds widely employed in the photo-induced metal reduction. As mentioned above, the PI precursors for these radicals can be classified Norrish type I or type II PIs, according to the formation mechanism: hydrogen abstraction (or electron transfer) and bond cleavage. The former group produces radical intermediates by electron or hydrogen transfer from a donor to the radical precursor (see Scheme 9). Prominent examples of compounds in this group are ketones such as acetophenone[58], acetone[51] and benzophenone[83]. In these reactions, highly reactive ketyl radicals or ketyl radical anions are formed.[55,84]

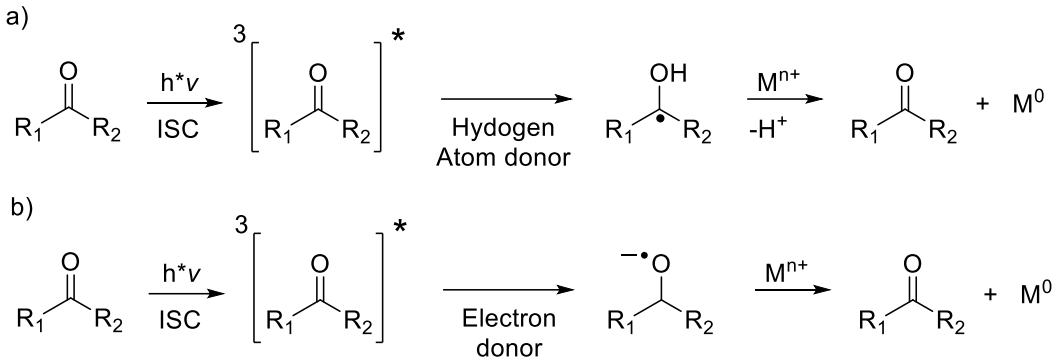

Scheme 9. Photo-sensitization mechanism for a ketone/hydrogen-donor system (a) and a ketone/electron donor system (b) with subsequent metal reduction by the radical species formed.

The second approach for formation of reducing radicals in metal nanoparticle synthesis is bond cleavage. A number of different photo-induced bond cleavage processes are applied for the synthesis of metal nanoparticles. One compound class employed in this approach are α-hydroxyketones.[85,86] Upon irradiation, these α-hydroxyketones produce highly reactive ketyl radicals capable of reducing metal salts to their elemental forms (see Scheme 10). An additional class of compounds which have gained increasing popularity in photo-induced metal reduction are bis(acyl)phosphane oxide photo-initiators.[87,88]

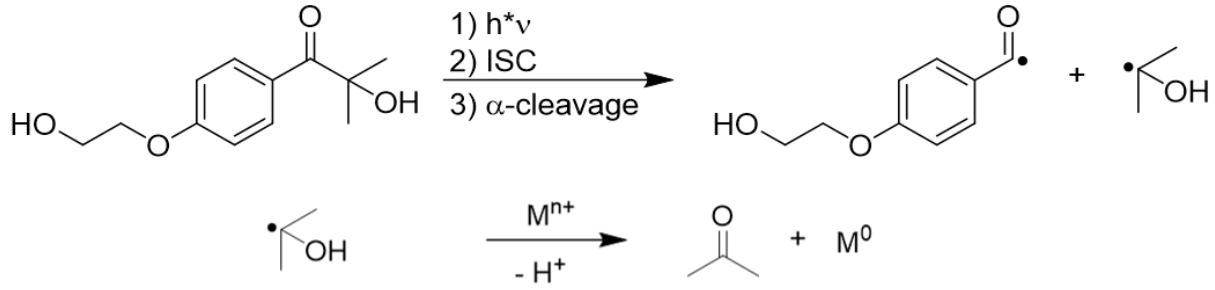

Scheme 10. Bond-cleavage of the commercial α-hydroxyketones *Irgacure 2959* upon irradiation and subsequent metal reduction by the ketyl radical produced

One class of metallic nanomaterials which are particularly interesting are copper nanoparticles (CuNPs). This interest is explained by the high natural abundance of copper and its low cost, combined with practical and straightforward ways for producing CuNPs.[59] The use of earth abundant and inexpensive metals for nanoparticle synthesis is attractive as a viable alternative to the rare and expensive noble-metal catalysts used in a wide range of commercially employed chemical processes.[89]

Copper nanoparticles and materials based on those have remarkable chemical properties. They have been applied for catalysis[59,61,90–94], molecular imaging, as chemical and biological sensors[60,95], and in the fields of optics, optoelectronics, photonics and electric conduction.[62–64,96,97] In addition, copper-polymer nanocomposites display additional characteristics such as antibacterial properties.[98]

A particular challenge in copper reduction for nanoparticle is the unfavourable redox potential of Cu^{2+} salts compared to other metal ions such as Pd^{2+} or Ag^{+}. Still, different photo-induced processes for the copper nanoparticles synthesis are described in literature. As an example, aromatic ketones and α-hydroxyketones serve as photo-reducing agents for copper salts.[10,52,86,99–101]

In addition to challenging reduction, overcoming the limited stability of CuNPs is particularly important.[59] Here, the design and development of novel and cost-effective approaches for the formation of stable CuNPs is required. A possible approach to overcome these stability issues is the use of photoinitiators to simultaneously reduced Cu^{2+} to the elemental copper nanoparticles and embed them in a tailor-made polymer matrix by radical polymerization in a simple one-pot approach. This approach could allow the construction of stable copper-polymer nanocomposites with well-defined chemical properties for the fabrication of conducting polymers, novel systems for heterogeneous catalysis and chemiresistive sensor systems

1.3. Methodology

In this doctoral thesis, a wide range of experimental techniques have been employed to monitor different aspects of free radical reactivity and photo-induced processes. The main techniques employed are optical (UV-VIS) spectroscopy, transient absorption spectroscopy, continuous-wave electron paramagnetic resonance spectroscopy (cw-EPR), chemically induced dynamic electron polarization (CIDEP) spectroscopy and chemically induced dynamic nuclear polarization (CIDNP) spectroscopy.

Optical spectroscopy is employed to observe chemical reactions on a millisecond - minute timescale, accompanied by a change in absorption, e.g. the formation of elemental copper and the photo-bleaching of photo-initiator systems. Transient absorption spectroscopy is used to gain insight into the kinetics of short-lived intermediates such as radicals and triplet-states. The characterization of these short-lived radical intermediates is preformed using cw-EPR, CIDEP and CIDNP spectroscopy. In addition, cw-EPR is also used for kinetic studies on stable paramagnetic species. In the following chapter, an overview and introduction to these experimental techniques is presented.

1.3.1. UV-VIS Spectroscopy

In this work, an UV-Vis spectrometer equipped with optical fibres was used. This allows static steady-state measurements of absorption spectra and time-resolved measurements with simultaneous light irradiation. This setup can be employed for monitoring photochemical or photo-induced reactions on a millisecond – minute time scale. Irradiation of the samples – if necessary - was performed either with a HgXe lamp (λ_{max} = 365 nm) or a bluphase lamp (λ_{max} = 470 nm) placed perpendicular to the light path of the spectrometer. In addition, magnetic stirring of the sample was employed during the measurements to ensure sufficient mixing and homogenous illumination. This experimental setup was employed for observing the reduction of Cu^{2+} to Cu^{0} by monitoring the characteristic copper plasmon absorption band centred around 580 nm and also electron transfer from nitroxyl radicals to $[Ru(bpy)_3]^{3+}$ by monitoring a characteristic absorption band at 452 nm.

1.3.2. Transient Absorption Spectroscopy

Transient absorption spectroscopy, also called laser flash photolysis (LFP) spectroscopy, is an extension to conventional (UV-VIS) absorption spectroscopy. It is used for the detection of reactive intermediates in chemical reactions on a nanosecond-millisecond timescale.

The first development of transient absorption spectroscopy was the flash photolysis setup created by Norrish and Porter. In their setup, the light pulse of a flash lamp was used to generate reactive intermediates.[102] In modern transient absorption spectroscopy, a short pulse from a laser is employed for creating reactive intermediates. Together with modern computer controls and electronic tools for data acquisition, this has led to time resolutions of up to 10^{-15} seconds. Still, nanosecond transient absorption techniques are an important tool in physical chemistry as many radical reactions occur on a nanosecond – microsecond timescale.

Scheme 11 displays the typical setup of a transient absorption spectrometer. The lasers used as irradiation sources are positioned perpendicular to the path of the monitoring beam. In this work, the third harmonic (λ = 355 nm) of a Nd:YAG laser was used. The source of the monitoring beam is usually a xenon lamp, operated in pulsed fashion, thereby drastically increasing the signal-to-noise ratio.[103] The detection system comprises a monochromator and a photomultiplier tube (PMT), allowing for a fast response and supporting high output currents.

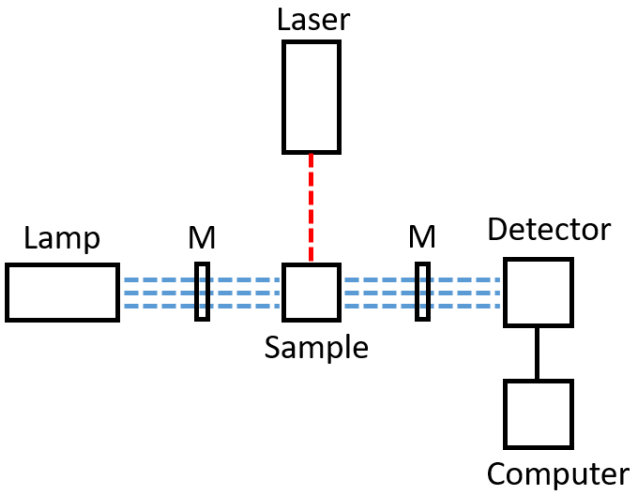

Scheme 11. Typical configuration of nanosecond transient absorption system with a laser as irradiation source (M = monochromator).

In transient absorption spectroscopy, the observed parameter is the change in absorbance (ΔOD). This change can be positive, if a newly formed species (*e.g.* triplet states or radicals as reactive intermediates) absorbs in the monitored wavelength range. Negative signals for ΔOD can occur either by bleaching of the parent compound from the laser beam or by emission (fluorescence or phosphorescence) from a newly formed intermediate. All this information can be extracted from the transient absorption spectra. However, one has to be aware that the intensity of the signals depends on many different parameters.[102] The most substantial ones are summarized below:

- The signal intensity depends on the energy-per-pulse delivered from the laser. Usually, energies ranging from 5 – 25 mJ/pulse are employed.
- The signal intensity is proportional to quantum yield of transient formation and the difference in excitation coefficients between the transient species and its precursor.
- The signal intensity depends on the concentration of the transient species. Many reactive intermediates can decay via self-reactions. If these self-reaction (e.g. dimer formation of disproportionation) are not of interest, the transient concentration should be kept low enough to minimize the effect of these side reactions.
- ΔOD itself is independent of the monitoring light intensity I_0. However, high I_0 can negatively affect the signal-to-noise ratio, leading to distorted signal and a non-linear response.

Transient absorption spectroscopy can be employed systematically for the identification and kinetic studies of reactive intermediates. Within this doctoral thesis, transient absorption spectroscopy was used for the identification of reactive intermediates from photo-initiator systems for polymerization and in the reduction of Cu^{2+}. An example is given below in Figure 1, showing a transient absorption spectrum of the benzil/triethylamine (TEA) system in acetonitrile and a reference measurement without TEA. Photolysis of benzil yields two distinct peaks at 350 nm and at 480 nm, which are both attributable to the excited state of benzil.[10,56,104,105] Upon addition of TEA, the absorptions centred at 480 and 350 nm disappear, while two new, broad bands centred at 360 and 580 nm appear; they are assigned to the benzil radical anion.[106,107] In this study, using transient absorption spectroscopy, we confirmed that upon photolysis of the benzil/TEA system a fast electron transfer occurs, leading to the formations the benzil radical anion and the TEA radical cation.[10]

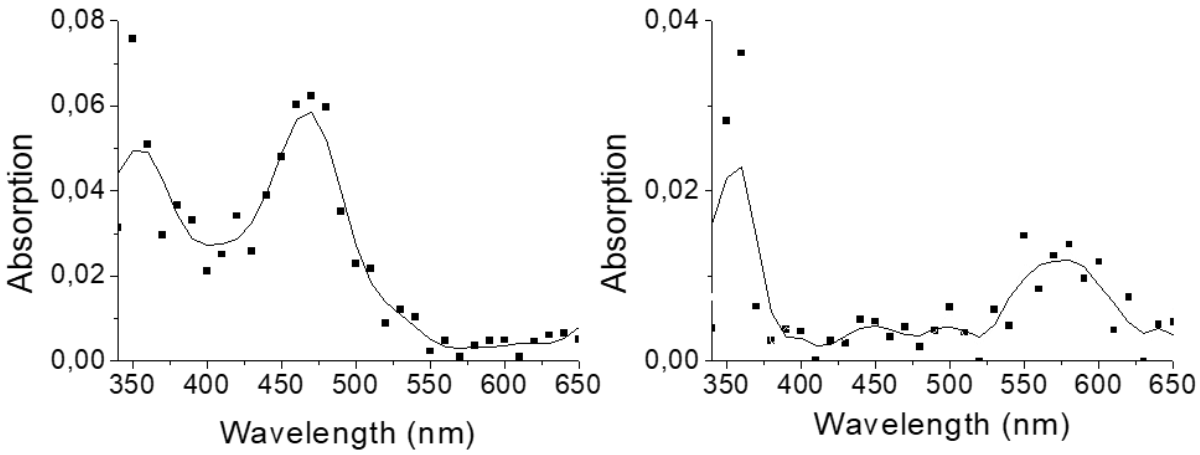

Figure 1. Transient absorption spectra of radicals produced by photolysis of benzil in CH_3CN (left) and CH_3CN/triethylamine (right) 0.2 µs after the laser pulse.

As mentioned above, transient absorption spectroscopy is also a powerful tool for kinetic studies of reactive intermediates. In simple cases, where the reactive intermediate of interest can be monitored directly and follows clean first-order kinetics (e.g. decay of triplet states), rate constants can be extracted by fitting the decay signal. More often, species observable by transient absorption spectroscopy follow a second-order rate law, making a straight-forward extraction of kinetic rate constants more challenging. This problem can be overcome using a pseudo-first order approach. Under typical transient absorption conditions, the reactive intermediates are present in concentrations several order of magnitude smaller than the compounds they react with. As a result, the concentration of the latter can be regarded as constant during the decay of the transient species. An example for this pseudo-first order behaviour is the decay of a BAPO-derived phosphanoyl radical **P•** in the presence of a monomer.[108] The reaction between **P•** and monomers follows a second-order rate law. The rate constants for this reaction are easily obtained by performing a pseudo-first order experiment in transient absorption spectroscopy (see Figure 2, Equation 3).

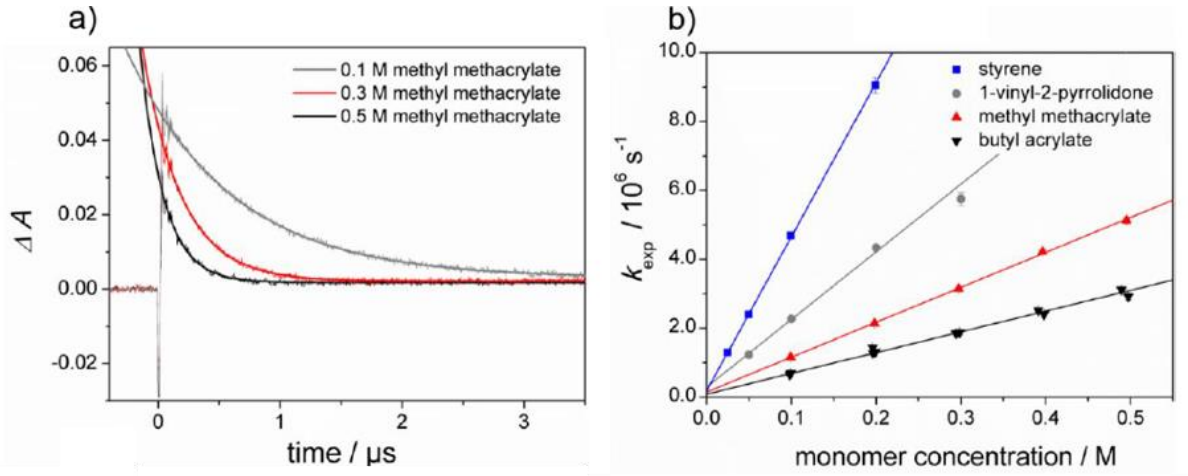

Figure 2. (a) Decay traces for a phosphanoyl radical **P•** in the presence of methyl methacrylate at three different concentrations (0.1 M, 0.3 M and 0.5 M) recorded following excitation by a laser flash (excitation wavelength: 355 nm, monitoring wavelength: 465 nm (b) Plots of the experimental rate constants k_{exp} of **P•** versus monomer concentrations.

The decay of the phosphanoyl radical **P•** follows pseudo-first order behaviour and the experimental rate constant (k_{exp}) is related to the second-order rate constant according to Equation 3,

$$k_{exp} = k_0 + k_x [X] \quad (\mathbf{3})$$

where k_0 is the rate of decay for **P•** in the absence of monomer, [X] is the monomer concentration and k_X is the second-order constant for the reaction between **P•** and monomer. By plotting of k_{exp} versus monomer concentration, the second-order rate constant are obtained as the slope of the resulting line (see Figure 2b).

1.3.3. Electron Paramagnetic Resonance Spectroscopy

Electron Paramagnetic Resonance (EPR) spectroscopy is an absorption technique based on the interaction between electromagnetic radiation and magnetic moments of a sample. Atoms and molecules have discrete energy levels. EPR spectroscopy probes energy differences *ΔE* of magnetic states of unpaired electrons in an atom or molecule in the presence of a magnetic field. In X-band EPR, microwaves are used to induce transitions between these states at an appropriate magnetic field B_0 according to the following relationship called resonance condition:

$$\Delta E = \mathrm{h} * \nu = g_e * \mu_B * B_0 \quad (\mathbf{4})$$

Every electron has an intrinsic angular moment called “spin” *s*. Due to the negative charge of the electron, this angular momentum induces a magnetic field, that in turn induces a magnetic moment *μ.* The electron is a ½ particle and therefore has two distinct magnetic configurations, which are characterized by the magnetic quantum numbers m_s = + ½ and m_s = - ½. The configuration with m_s = + ½ is called α-spin, the configuration characterized by m_s = - ½ is called β-spin. In the absence of an external magnetic field B_0 both magnetic configurations are energetically degenerate. As soon as the unpaired electron interacts with an external magnetic field, this degeneracy is removed, generating two states with different energies. Here, the energy is the lowest if the magnetic moment *μ* is oriented parallel to the external magnetic field (m_s = - ½) and highest if *μ* is anti-parallel to B_0 (m_s = + ½). This splitting of energetically degenerated states in the presence of an external magnetic field is called Zeeman effect (Scheme 12) and the states are populated according to the Boltzmann distribution. The energies of the two states are given by:

$$E_{+1/2} = +1/2 * g_e * \mu_B * B_0 \quad (\mathbf{5})$$

$$E_{-1/2} = -1/2 * g_e * \mu_B * B_0 \quad (\mathbf{6})$$

Here, g_e is the so-called g-factor of the electron (g_e = 2.0023192 for a free, isolated electron)[109], B_0 is the strength of the external magnetic field and μ_B is a constant called the Bohr magneton (μ_B = 9.2740099 * 10^{-24} J/T). The energy difference between α-spin und β-spin is given by:

$$\Delta E = g_e * \mu_B * B_0 \quad (\mathbf{7})$$

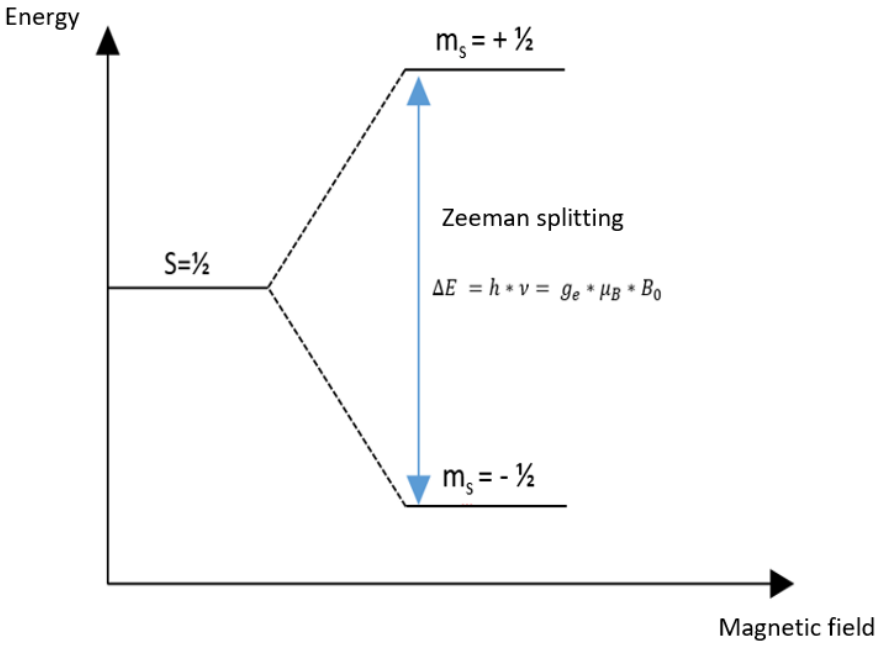

Scheme 12. Zeeman splitting of an electron in an external magnetic field.

From the resonance condition (Equation 4), we can see that the g-factor g_e is a crucial parameter in EPR spectroscopy. The Bohr magneton μ_B is constant and the strength of the external magnetic field B_0 can be measured. Therefore, the g-factor g_e is the only parameter that has to be obtained to determine the energy difference ΔE between two spin states. For organic radicals and other paramagnetic substances, this value differs from the value for the free electron. It is possible to determine the g-factor directly:

$$g_e = \frac{h * \nu}{\mu_B * B_0} \quad (\mathbf{8})$$

However, this requires both the frequency ν and the magnetic field B_0 to be measured precisely, which can be difficult in practice. Therefore, it is more common to determine the g-factor of an unknown sample relative to a substance with known g-factor *e.g.* DPPH (2,2-diphenyl-1-picrylhydrazyl; g_e = 2.0036),

$$g_{unknown\ radical} = \frac{g_{reference} * B_{reference}}{B_{unknown\ radical}} \quad (\mathbf{9})$$

In theory, the determination of the g-factor allows the identification of an unknown radical. However, the identification is often not possible since – especially for organic radicals – the values of g_e are within a very narrow range, rendering the identification of a radical using only the g-factor practically impossible.

Analogous to the electron Zeeman splitting, which is caused by the interaction of the magnetic moment of the electron with the external magnetic field, there also is a nuclear Zeeman effect. Atomic nuclei comprising a nuclear spin quantum number $I \neq 0$ also have a magnetic moment μ. This magnetic moment leads to a splitting of nuclear-spin energy levels in the presence of an external magnetic field. A nuclear spin with the corresponding quantum number I can have

$$2 * I + 1$$

different orientations. Accordingly, the energy levels of nuclei with I = ½ (e.g. ^{1}H, ^{13}C, ^{19}F) show an additional splitting of the two electron Zeeman levels into two nuclear Zeeman levels, respectively (Scheme 13, left). Nuclei with I = 1 (z. B. ^{2}H, ^{14}N) show an additional splitting of the electron Zeeman levels into three nuclear Zeeman levels (Scheme 13, right). Due to this additional splitting, more transitions are possible in the molecule and it is possible to gain information on the chemical environment of the paramagnetic substance.[109,110] In combination with the selection rules $\Delta m_s = \pm 1$ and $\Delta m_I = 0$, this leads to complex but highly informative spectral patterns.

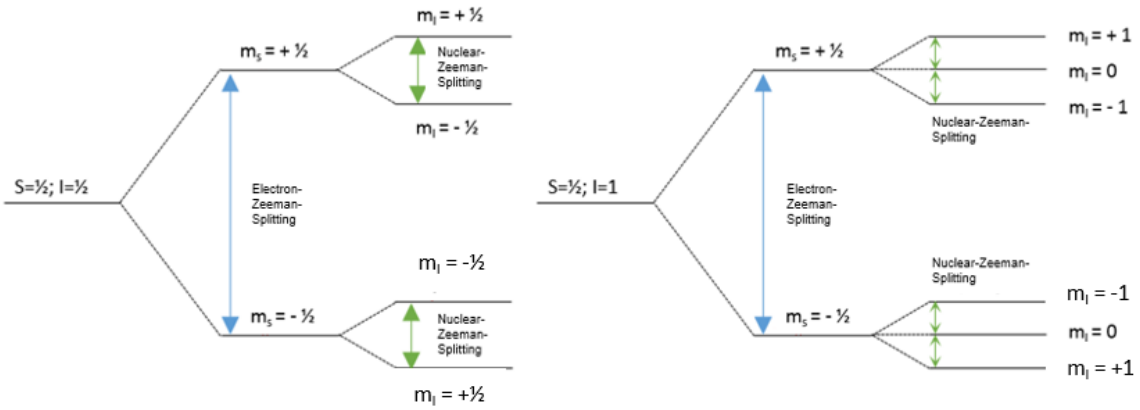

Scheme 13. Electron Zeeman splitting and nuclear Zeeman splitting of an electron and a I = ½ nucleus (left) or a I = 1 nucleus (right) in an external magnetic field.

In addition to the interaction of the magnetic moments of electrons and nuclei with an external magnetic field, there is also an interaction of the magnetic moments with each other. This hyperfine interaction causes a shift of the nuclear Zeeman levels either to higher or lower energy and is reflected by the isotropic hyperfine coupling constant ***a***, as is depicted in Scheme 14.

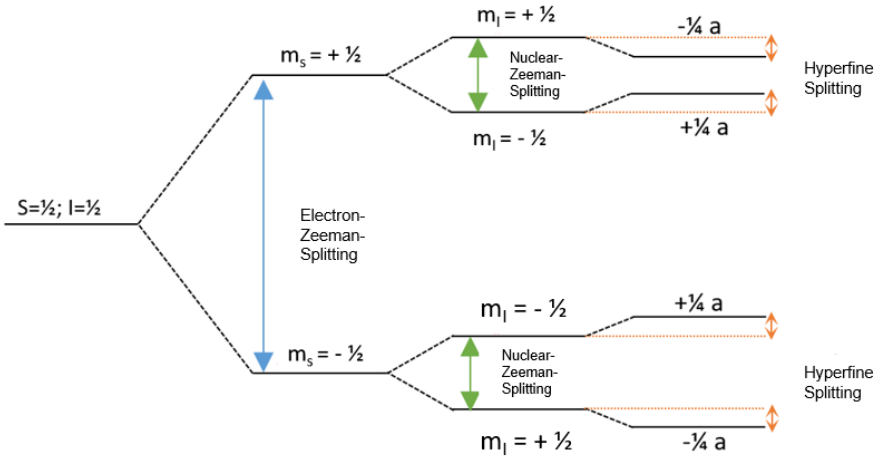

Scheme 14. Electron Zeeman splitting, nuclear Zeeman splitting and hyperfine interaction of an electron and a I = ½ nucleus in an external magnetic field.

1.3.4. Chemically Induced Dynamic Electron Polarization Spectroscopy

Chemically Induced Dynamic Electron Polarization (CIDEP) spectroscopy (sometimes also called time resolved electron paramagnetic resonance spectroscopy TR-EPR), an experimental technique based on EPR spectroscopy, allows the detection of radicals on a short timescale (ns-ms).[111] On these short time scales, the population of the energy levels deviates from the Boltzmann distribution, giving rise to polarized signals of enhanced absorption or emission. Two different mechanisms – the radical pair mechanism (RPM) and the triplet mechanism (TM) – can cause these polarized signals. From CIDEP spectra it is possible to obtain information on the structure of the primarily formed radicals and the spin multiplicity of the precursor. Employing line-width methods, it is also possible to carry out kinetic studies.[112]

Radical pairs can be created either by homolytic bond-cleavage, electron transfer or hydrogen atom transfer. These processes are induced thermally or photo-chemically in CIDEP spectroscopy. In both cases, the spin multiplicity of the parent molecule is conserved: Thermally generated radical pairs are usually born in the singlet state, whereas photochemical generation can lead to radical pairs formed in the triplet state. A third possible pathway for the generation of a radical pair is by encounter of two different free radicals. Radical pairs formed by encounter of two radicals can, in theory, be in the singlet and the triplet state. However, singlet pairs will usually recombine rapidly, and therefore the triplet character dominates for this reactions pathway.[113]

In a radical pair, the distance between the two radical species is small and thus they have to be handled as a spin-coupled radical pair. The two radicals interact with each other and therefore an overall spin state has to be regarded. This spin correlation arises from a purely quantum mechanical effect called exchange interaction *J*.[114] The exchange interaction is large at small distances. At these small distances, the triplet and the singlet state have a large energy difference and therefore, there is little mixing between the spin states (Scheme 15a). In addition, at high magnetic field, the triplet energy levels are split into three sublevels T_{+1}, T_0 and T_{-1} by Zeeman interaction. The exchange interaction decreases exponentially with distance. Therefore, at larger distances, the energy difference between the singlet state and the T_0 triplet state becomes small, allowing singlet-triplet mixing (S-T mixing, Scheme 15a).[115] A representation of the S-T mixing process is given by the vector model shown in Scheme 15b. Here, the electron spin state of the initial radical pair oscillates between triplet (T_0) and singlet (S) multiplicity via a mixed state ($c_sS+C_TT_0$) due to the different Larmor frequencies of the two radicals S_1 and S_2.

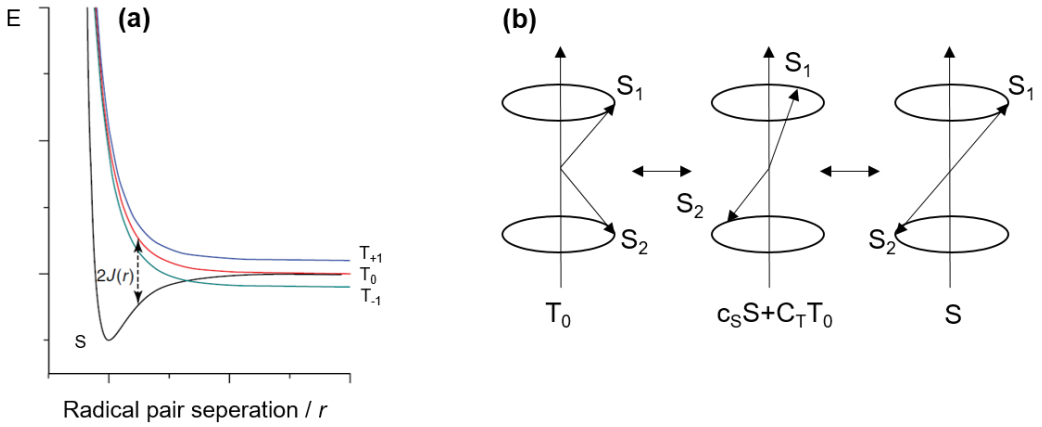

Scheme 15. (a) Energy level diagram of a radical pair in the presence of an external magnetic field as function of the radical pair separation r. (b) Vector representation of the Singlet-Triplet Mixing

In addition to the radical-pair mechanism, the triplet mechanism leads to the polarization of signals. It can only be detected in cases when the radical pair is generated photo-chemically, as a triplet precursor is required. The polarization is built up during the intersystem crossing to the triplet state from the excited singlet state. At high magnetic fields, the three levels of the triplet state are not energetically degenerated, resulting in different populations (see Scheme 15a). This difference in population of the three levels leads to polarization (Scheme 16). The size of the polarization depends on the following parameters:[116]

1. the rotational correlation time of the precursor molecule
2. the zero-field splitting constant of the excited triplet states
3. the lifetime of the triplet state
4. the applied magnetic field

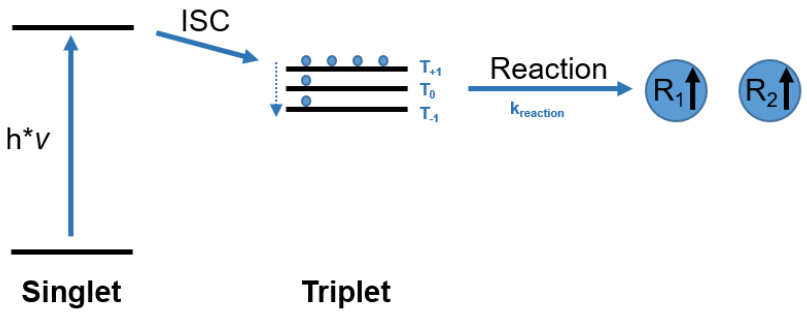

Scheme 16. Mechanistic representation of the selective population of the T_{+1} state due to the triplet mechanism in CIDEP experiments.

As can be seen in Scheme 16, the preferred population of the T_{+1} state leads to emission signals. Accordingly, polarization originating from the triplet mechanism leads to signals of identical phase and enhancement.

CIDEP spectra can be recorded two ways: either using continuous-wave EPR (cw-EPR) or the more recent Fourier-transformation EPR (FT-EPR). In this work, cw-EPR was employed. The experimental setup for these experiments usually consists of a laser serving as a nanosecond light source and direct detection by a X-Band EPR spectrometer. The signal acquisition is synchronized with the laser trigger and recorded using a digital oscilloscope.

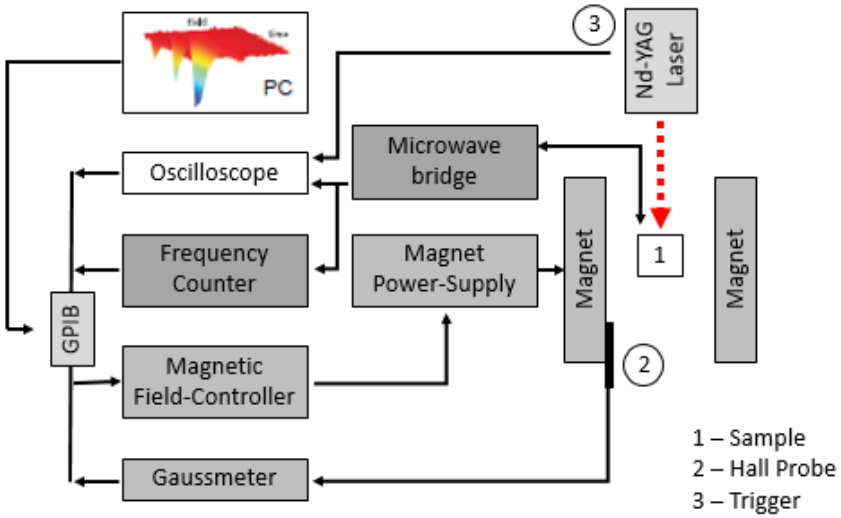

Scheme 17. Experimental setup of a CIDEP spectrometer.

1.3.5. Chemically Induced Dynamic Nuclear Polarization Spectroscopy

Chemically Induced Dynamic Nuclear Polarization (CIDNP) spectroscopy, an experimental technique based on NMR, allows observing radical reactions occurring on a short timescale (ns-ms) by detecting polarizations in follow-up products bearing information about the radical reaction pathway.

The effect leading to the non-Boltzmann intensities (polarizations) observed in CIDNP spectroscopy is the radical pair mechanism, analogous to the effect observed in CIDEP (see chapter 1.3.4.). Diamagnetic products are formed in a magnetically polarized state deviating from the Boltzmann distribution as a result from interactions between unpaired electrons and nuclear spins in the preceding radical reaction. Thus, signals in CIDNP experiments show enhanced absorption and emission, as is depicted in Figure 3.

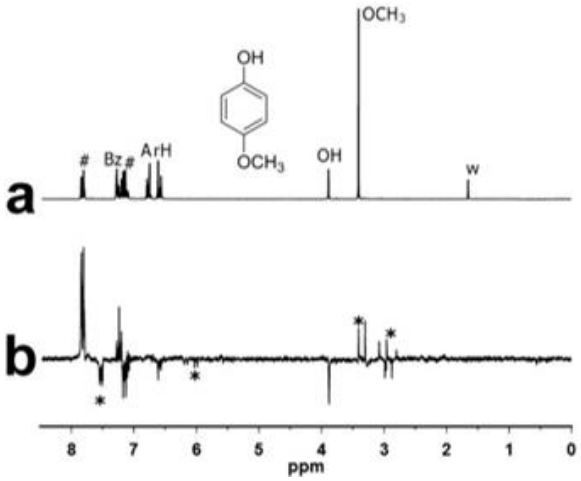

Figure 3. ^{1}H NMR spectrum (a) and of ^{1}H CIDNP spectrum (b) of 4-methoxyphenol and benzophenone (BP) in benzene-d_6 at 293 K. Abbreviations: water (w); solvent residual signal (Bz), BP signals (#), hydroxyl hydrogens (OH), aromatic hydrogens (ArH), benzylamino hydrogens (CH_2), newly formed products of radical reaction (*).

A representation of the radical pair mechanism resulting in the formation of polarized signals in CIDNP experiments is shown in Scheme 18. The radical pair is formed either from a singlet or triplet precursor, which can undergo nuclear-spin selective singlet-triplet mixing. This singlet-triplet mixing process is analogous to CIDEP (see Scheme 15b). Subsequently, singlet and triplet radical pairs undergo different reactions, leading to the polarized signal in the diamagnetic

product. Cage products are formed by recombination of the initial radical pair, whereas escape products are formed by a radical pair which has diffused outside the solvent cage.

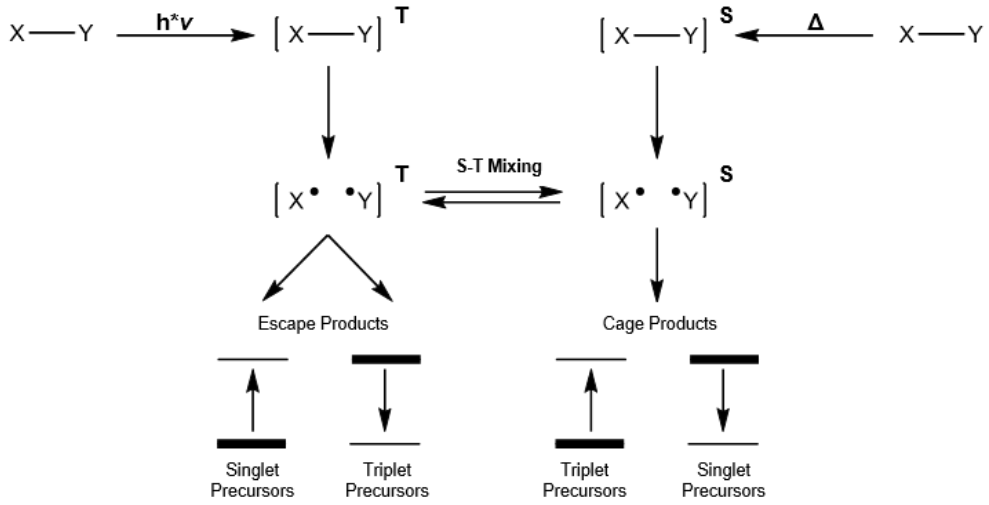

Scheme 18. Reaction scheme of the radical pair mechanism in CIDNP spectroscopy.

The rate of S-T mixing is proportional to the difference of the Larmor frequencies $\Delta\omega$ of the electron spins in the two radicals, according to Equation 10.[117] Immediately after the radical pair formation, the spin state of the system is the same as in the precursor. Within a certain time, the two radicals will diffuse apart and the exchange interaction becomes negligible (see Scheme 15a). The two radicals are no longer constrained to preserve their relative orientation and start to precess independently in the magnetic field. The spins in two non-identical radicals will precess with different Larmor frequencies resulting in singlet-triplet mixing. The difference between the Larmor frequencies is given by:

$$\Delta\omega = \omega_2 - \omega_1 = \frac{1}{2}\left[H_o \Delta g\, \beta_e h^{-1} + \sum_{i=1}^{n} a_{1i} m_{1i} - \sum_{j=1}^{k} a_{2j} m_{2j}\right] \quad (\mathbf{10})$$

The first term of the equation describes the spin-orbit interaction, while the other two terms account for electron coupling, which is the same as hyperfine splitting in EPR spectroscopy. As an example, we look at a radical pair formed in the T_0 state with only one radical carrying magnetically active nuclei ($|m_{1i}| = ½$, $\Delta g > 0$, $a_{1i} > 0$). For such a radical pair, there are two possible values for $\Delta\omega$ depending on the spin orientation, meaning that the rate of Singlet-Triplet Mixing depends on the nuclear spin orientation:

$$\alpha;\ m_{1i} = +\frac{1}{2}, \qquad \Delta\omega_{+} = \frac{1}{2}\left[H_o \Delta g\ \beta_e h^{-1} + \frac{1}{2}\ a_{1i}\right] \quad (\mathbf{11})$$

$$\beta;\ m_{1i} = -\frac{1}{2}, \qquad \Delta\omega_{-} = \frac{1}{2}\left[H_o \Delta g\ \beta_e h^{-1} - \frac{1}{2}\ a_{1i}\right] \quad (\mathbf{12})$$

A radical pair can be generated either thermally or photo-chemically inside the NMR spectrometer. In this work, photo-chemical methods were employed. The setup consists of a Bruker 200 MHz NMR spectrometer and either a Nd:YAG laser operating at 355 nm or a high pressure HgXe lamp. The setup for CIDNP experiments is essentially the same as in NMR, only with the addition of a quartz rod guiding the light of the laser into the spectrometer to the NMR tube (Scheme 19).

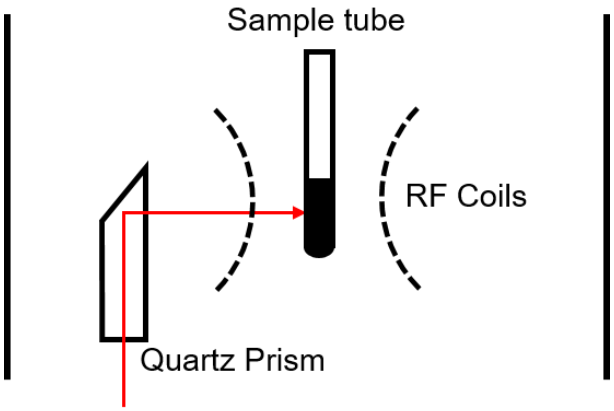

Scheme 19. Setup of the NMR probe-head in CIDNP experiments with a laser as an external light source.

1.4. Publications

The publications and manuscripts contributing to this doctoral thesis are reproduced in Chapter 2 – 4. Chapter 2 addresses different aspects of electron transfer and proton transfer in model systems for complex biological processes.

The first publication reports on the solvent dependence of electron and proton transfer from novel phenolic compounds with intramolecularly connected basic moieties to photo-excited benzophenone. The synthesis of these novel compounds was performed by C. Viglianisi at the University of Florence. Their solvent-dependent photo-oxidation was studied in cooperation with R. Amorati and L. Valgimigli (University of Bologna), using CIDNP spectroscopy and Density Functional Theory (DFT) calculations.[118]

The second manuscript addresses the photo-induced oxidation of nitroxyl radicals embedded into liposomes to photo-excited $[Ru(bpy)_3]Cl_2$ residing in the aqueous phase outside the lipid bilayer. The aim of this study was to assess the contribution of lipid bilayers for electron transfer processes in biological systems. This was achieved in cooperation with A. Barbon (University of Padova), I. Bilkis (Hebrew University, Rehovot) and L. Weiner (Weizmann Institute, Rehovot), employing optical, cw-EPR and TR-EPR spectroscopy.

Chapter 3 comprises studies discussing various aspects of the reactivity of photoinitiators for radical polymerization and studies aimed to extend the reactivity of photoinitiators to copper reduction for the synthesis of nanomaterials.

The first publication reports on novel bis(acyl)phosphane oxide (BAPO) derivatives, featuring functional groups allowing to adjust their hydrophilicity or lipophilicity. The synthesis was performed in the group of H. Grützmacher (ETH Zurich), while we contributed studies of their efficacy as radical initiators using transient absorption, CIDEP and CIDNP spectroscopy.[108] The experimental results show that these modifications do not alter the polymerization-initiating properties of the phosphanoyl radicals formed upon bond cleavage.

The following publications address photo-induced radical polymerizations at water-oil interfaces in microemulsions using BAPO photo-initiators. In collaboration with M. Zalibera and co-workers (Slovak University of Technology, Bratislava), we have investigated the initiation reactions using optical spectroscopy and CIDEP experiments.[119]

The third publication in this chapter describes the bifunctional reactivity of BAPO photo-initiators in the presence of water and alcohols, performed in collaboration with H. Grützmacher (ETH Zurich) and C. Barner-Kowollik (Queensland University of Technology, Brisbane). This extensive mechanistic study was performed employing cw-EPR and CIDEP spectroscopy, transient absorption spectroscopy and mass spectrometry (MS) experiments in combination with kinetic simulations.[120]

Another publication, extending on the conventional use of photoinitiators, is a mechanistic study of the photo-induced copper reduction by the benzil/triethylamine photoinitiator system. Both the formation of elemental copper and the reaction pathway involving transient radical species are confirmed employing steady-state and transient absorption spectroscopy and EPR spectroscopy.[10]

We also expend on the above mentioned bifunctional reactivity of BAPO photo-initiators in aqueous and alcoholic media in an additional manuscript. We describe how this reactivity can be employed for the synthesis of copper nanoparticles, as confirmed by optical spectroscopy, Scanning Electron Microscopy (SEM) and Dynamic Light Scattering (DLS). Furthermore, this system allows simultaneous reduction/polymerisation reactions yielding copper-polymer nanocomposites.

This doctoral thesis concludes with two additional publications addressing various aspects of EPR spectroscopy and its application. These publications are summarized in Chapter 4.

The first publication in this chapter describes a laboratory experiment designed to teach the basics of EPR spectroscopy to undergraduate chemistry students. This laboratory course was realized at Graz University of Technology and incorporated into an already existing laboratory course on Molecular Analysis and Spectroscopy.[121]

The final publication in this thesis addresses the synthesis and characterisation of Titanium-based metal organic frameworks for electro-catalytic NH_3 synthesis from N_2. The synthesis and parts of the characterisation was performed in the group of M. Oschatz (MPI Potsdam). We contributed EPR measurements, verifying the presence of catalytically active Ti^{3+} centres in the materials.

1.5. References

[1] N. J. Turro, V. Ramamurthy, J. C. Scaiano, *Principles of Molecular Photochemistry: An Introduction*, University Science Books, **2009**.

[2] C. E. Wayne, R. P. Wayne, *Photochemistry (Oxford Chemistry Primer)*, Oxford University Press, **2005**.

[3] A. Jabłoński, *Nature* **1933**, *131*, 839–840.

[4] M. J. Perkins, *Radical Chemistry: The Fundamentals (Oxford Chemsitry Primers)*, Oxford University Press, **2005**.

[5] J. Mattay, *Angew. Chemie Int. Ed. English* **1987**, *26*, 825–845.

[6] J. K. Kochi, Ed. , *Free Radicals: Volume I, Dynamics of Elementary Processes*, John Wiley {&} Sons, Inc., **1973**.

[7] M. H. V Huynh, T. J. Meyer, *Chem. Rev.* **2007**, *107*, 5004–5064.

[8] S. Y. Reece, D. G. Nocera, *Annu. Rev. Biochem.* **2009**, *78*, 673–699.

[9] R. A. Marcus, N. Sutin, *BBA Rev. Bioenerg.* **1985**, *811*, 265–322.

[10] M. Schmallegger, G. Gescheidt, *Monatshefte für Chemie - Chem. Mon.* **2018**, *149*, 499–504.

[11] L. Eberson, *Adv. Phys. Org. Chem.* **1982**, *18*, 79–185.

[12] D. G. Whitten, *Acc. Chem. Res.* **1980**, *13*, 83–90.

[13] S. Dadashi-Silab, S. Doran, Y. Yagci, *Chem. Rev.* **2016**, *116*, 10212–10275.

[14] E. E. Caldin, V. Gold, *Proton-Transfer Reactions*, Springer, **1975**.

[15] D. R. Weinberg, C. J. Gagliardi, J. F. Hull, C. F. Murphy, C. A. Kent, B. C. Westlake, A. Paul, D. H. Ess, D. G. McCafferty, T. J. Meyer, *Chem. Rev.* **2012**, *112*, 4016–4093.

[16] J.-F. Poon, D. A. Pratt, *Acc. Chem. Res.* **2018**, acs.accounts.8b00251.

[17] M. Griesser, D. Neshchadin, K. Dietliker, N. Moszner, R. Liska, G. Gescheidt, *Angew. Chemie - Int. Ed.* **2009**, *48*, 9359–9361.

[18] G. Moad, D. H. Solomon, *The Chemistry of Radical Polymerization*, Elsevier, **2006**.

[19] R. A. Scott, A. G. Mauk, H. B. Gray, *J. Chem. Educ.* **2009**, *62*, 932.

[20] R. A. Marcus, *J. Phys. Chem. B* **2002**, *102*, 10071–10077.

[21] B. Giese, *Acc. Chem. Res.* **2000**, *33*, 631–636.

[22] A. Manetto, S. Breeger, C. Chatgilialoglu, T. Carell, *Angew. Chemie - Int. Ed.* **2005**, *45*, 318–321.

[23] H. B. Gray, J. R. Winkler, *Annu. Rev. Biochem.* **1996**, *65*, 537–561.

[24] H. B. Gray, J. R. Winkler, *Q. Rev. Biophys.* **2003**, *36*, 341–372.

[25] C. Chatgilialoglu, C. Ferreri, K. Matyjaszewski, *Chempluschem* **2016**, *81*, 11–29.

[26] D. Astruc, *Nat. Chem.* **2012**, *4*, 255–267.

[27] M. Grätzel, in *Heterog. Photochem. Electron Transf.*, CRC Press, **1989**, pp. 43–86.

[28] D. Gust, T. A. Moore, A. L. Moore, *Acc. Chem. Res.* **2001**, *34*, 40–48.

[29] S. Fukuzumi, K. Ohkubo, T. Suenobu, *Acc. Chem. Res.* **2014**, *47*, 1455–1464.

[30] A. Ponce, H. B. Gray, J. R. Winkler, *J. Am. Chem. Soc.* **2000**, *122*, 8187–8191.

[31] O. S. Wenger, B. S. Leigh, R. M. Villahermosa, H. B. Gray, J. R. Winkler, *Science (80-.).* **2005**, *307*, 99–102.

[32] H. B. Gray, J. R. Winkler, *Proc. Natl. Acad. Sci. U. S. A.* **2005**, *102*, 3534–9.

[33] A. Polimeno, A. Barbon, P. L. Nordio, W. Rettig, *J. Phys. Chem.* **1994**, *98*, 12158–12168.

[34] M. Cordes, B. Giese, *Chem. Soc. Rev.* **2009**, *38*, 892.

[35] E. Meggers, M. E. Michel-Beyerle, B. Giese, *J. Am. Chem. Soc.* **1998**, *120*, 12950–12955.

[36] S. Antonello, F. Formaggio, A. Moretto, C. Toniolo, F. Maran, *J. Am. Chem. Soc.* **2003**, *125*, 2874–2875.

[37] A. B. Ricks, K. E. Brown, M. Wenninger, S. D. Karlen, Y. A. Berlin, D. T. Co, M. R. Wasielewski, *J. Am. Chem. Soc.* **2012**, *134*, 4581–4588.

[38] J. N. Robinson, D. J. Cole-Hamilton, *Chem. Soc. Rev.* **1991**, *20*, 49.

[39] W. E. Ford, G. Tollin, *Photochem. Photobiol.* **1982**, *36*, 647–655.

[40] A. Warshel, D. W. Schlosser, *Proc. Natl. Acad. Sci. U. S. A.* **1981**, *78*, 5564–5568.

[41] K. C. Hwang, D. Mauzerall, *Nature* **1993**, *361*, 138–140.

[42] P. Nicholls, J. West, A. D. Bangham, *Biochim. Biophys. Acta* **1974**, *363*, 190–201.

[43] G. M. El Maghraby, B. W. Barry, A. C. Williams, *Eur. J. Pharm. Sci.* **2008**, *34*, 203–222.

[44] G. Sessa, G. Weissmann, *J. Lipid Res.* **1968**, *9*, 310–318.

[45] C. Ferreri, C. Chatgilialoglu, in *Membr. Lipidomics Pers. Heal.*, **2015**, pp. 3–20.

[46] E. Rideau, R. Dimova, P. Schwille, F. R. Wurm, K. Landfester, *Chem. Soc. Rev.* **2018**, *47*, 8572–8610.

[47] C. Chatgilialoglu, A. Studer, *Encyclopedia of Radicals in Chemistry Biology and Materials*, John Wiley {&} Sons, Inc., **2012**.

[48] J. P. Fouassier, X. Allonas, J. Lalevée, C. Dietlin, *Photochemistry and Photophysics of Polymer Materials*, John Wiley {&} Sons, Inc., **2010**.

[49] K. Dietliker, *A Compilation of Photoinitiators Commercially Available for UV Today*, SITA Technology Limited, **2002**.

[50] M. D. Person, P. W. Kash, L. J. Butler, *J. Chem. Phys.* **1992**, *97*, 355–373.

[51] Y. Yonezawa, T. Sato, S. Kuroda, K. Kuge, *J. Chem. Soc. Faraday Trans.* **1991**, *87*, 1905.

[52] M. Sakamoto, M. Fujistuka, T. Majima, *J. Photochem. Photobiol. C Photochem. Rev.* **2009**, *10*, 33–56.

[53] K. Ikemura, T. Endo, *Dent. Mater. J.* **2010**, *29*, 481–501.

[54] N. Filipescu, F. L. Minn, *J. Am. Chem. Soc.* **1968**, *90*, 1544–1547.

[55] C. Devadoss, R. W. Fessenden, *J. Phys. Chem.* **1991**, *95*, 7253–7260.

[56] J. C. Scaiano, *J. Phys. Chem.* **1981**, *85*, 2851–2855.

[57] S. C. Ligon, B. Husár, H. Wutzel, R. Holman, R. Liska, *Chem. Rev.* **2014**, *114*, 557–589.

[58] M. Sakamoto, M. Fujistuka, T. Majima, *J. Photochem. Photobiol. C Photochem. Rev.* **2009**, *10*, 33–56.

[59] M. B. Gawande, A. Goswami, F. X. Felpin, T. Asefa, X. Huang, R. Silva, X. Zou, R. Zboril, R. S. Varma, *Chem. Rev.* **2016**, *116*, 3722–3811.

[60] R. F. Minchin, D. J. Martin, *Endocrinology* **2010**, *151*, 474–481.

[61] J. Spivey, F. Tao, *Metal Nanoparticles for Catalysis: Advances and Applications*, The Royal Society Of Chemistry, **2014**.

[62] G. Schmid, *Clusters and Colloids: From Theory to Applications*, Wiley, **1994**.

[63] B. C. Gates, *Chem. Rev.* **1995**, *95*, 511–522.

[64] N. A. Dhas, C. P. Raj, A. Gedanken, *Chem. Mater.* **1998**, 1446–1452.

[65] B. L. Cushing, V. L. Kolesnichenko, C. J. O'Connor, *Chem. Rev.* **2004**, *104*, 3893–3946.

[66] J. A. Dahl, B. L. S. Maddux, J. E. Hutchison, *Chem. Rev.* **2007**, *107*, 2228–2269.

[67] A. Roucoux, J. Schulz, H. Patin, *Chem. Rev.* **2002**, *102*, 3757–3778.

[68] N. A. Dhas, C. P. Raj, A. Gedanken, *Chem. Mater.* **2006**, *9*, 1446.

[69] R. Mittu, *Int. Adv. Res. J. Sci. Eng. Technol.* **2016**, *3*, 37–40.

[70] Y. Yang, L. Liu, H. Yin, D. Xu, G. Liu, X. Song, J. Liu, *J. Phys. Chem. C* **2013**, *117*, 11858–11865.

[71] J. C. Scaiano, C. Aliaga, S. Maguire, D. Wang, *J. Phys. Chem. B* **2006**, *110*, 12856–12859.

[72] T.-L. Wee, B. D. Sherman, D. Gust, A. L. Moore, T. A. Moore, Y. Liu, J. C. Scaiano, *J. Am. Chem. Soc* **2011**, *133*, 16742–16745.

[73] T. Itakura, K. Torigoe, K. Esumi, *Langmuir* **1995**, *11*, 4129–4134.

[74] K. L. Mcgilvray, M. R. Decan, D. Wang, J. C. Scaiano, *J. Am. Chem. Soc.* **2006**, *128*, 15980–15981.

[75] M. L. Marin, K. L. Mcgilvray, J. C. Scaiano, *J. Am. Chem. Soc.* **2008**, 16572–16584.

[76] L. Maretti, P. S. Billone, Y. Liu, J. C. Scaiano, *J. Am. Chem. Soc.* **2009**, *131*, 13972–13980.

[77] O. R. Miranda, T. S. Ahmadi, *J. Phys. Chem. B* **2005**, *109*, 15724–34.

[78] H. Hada, Y. Yonezawa, A. Yoshida, A. Kurakake, *J. Phys. Chem.* **1976**, *80*, 2728–2731.

[79] S. Eustis, M. A. El-Sayed, *Chem. Soc. Rev.* **2006**, *35*, 209–217.

[80] M. Harada, H. Einaga, *Langmuir* **2006**, *22*, 2371–2377.

[81] A. Henglein, *Chem. Rev.* **1989**, *89*, 1861–1873.

[82] J. Belloni, *Catal. Today* **2006**, *113*, 141–156.

[83] N. Kometani, H. Doi, K. Asami, Y. Yonezawa, *Phys. Chem. Chem. Phys.* **2002**, *4*, 5142–5147.

[84] N. Filipescu, F. L. Minn, *J. Am. Chem. Soc.* **1968**, *90*, 1544–1547.

[85] J. C. Scaiano, K. G. Stamplecoskie, G. L. Hallett-Tapley, *Chem. Commun.* **2012**, *48*, 4798.

[86] N. L. Pacioni, A. Pardoe, K. L. McGilvray, M. N. Chrétien, J. C. Scaiano, *Photochem. Photobiol. Sci.* **2010**, *9*, 766–774.

[87] Y. Yagci, M. A. Tasdelen, S. Jockusch, *Polymer (Guildf).* **2014**, *55*, 3468–3474.

[88] R. Nazar, S. Ronchetti, I. Roppolo, M. Sangermano, R. M. Bongiovanni, *Macromol. Mater. Eng.* **2015**, *300*, 226–233.

[89] F. Zaera, *Chem. Soc. Rev.* **2013**, *42*, 2746–2762.

[90] A. G. Nasibulin, P. P. Ahonen, O. Richard, E. I. Kauppinen, I. S. Altman, *J. Nan* **2001**, 385–400.

[91] S. Bhadra, A. Saha, B. C. Ranu, *Green Chem.* **2008**, *10*, 1224–1230.

[92] P. Singh, A. Katyal, R. Kalra, R. Chandra, *Catal. Commun.* **2008**, *9*, 1618–1623.

[93] C.-S. Chen, C.-C. Chen, C.-T. Chen, H.-M. Kao, *Chem. Commun.* **2011**, *47*, 2288–2290.

[94] K. Larmier, W. C. Liao, S. Tada, E. Lam, R. Verel, A. Bansode, A. Urakawa, A. Comas-Vives, C. Copéret, *Angew. Chemie - Int. Ed.* **2017**, *56*, 2318–2323.

[95] Y. Zhang, L. Su, D. Manuzzi, H. V. E. de los Monteros, W. Jia, D. Huo, C. Hou, Y. Lei, *Biosens. Bioelectron.* **2012**, *31*, 426–432.

[96] F. E. Kruis, H. Fissan, A. Peled, *J. Aerosol Sci.* **1998**, *29*, 511–535.

[97] H. S. Kim, S. R. Dhage, D. E. Shim, H. T. Hahn, *Appl. Phys. A Mater. Sci. Process.* **2009**, *97*, 791–798.

[98] L. Tamayo, M. Azócar, M. Kogan, A. Riveros, M. Páez, *Mater. Sci. Eng. C* **2016**, *69*, 1391–1409.

[99] S. Kapoor, T. Mukherjee, *Chem. Phys. Lett.* **2003**, *370*, 83–87.

[100] S. Giuffrida, L. L. Costanzo, G. Ventimiglia, C. Bongiorno, *J. Nanoparticle Res.* **2008**, *10*, 1183–1192.

[101] N. Nishida, A. Miyashita, N. Hashimoto, H. Murayama, H. Tanaka, *Eur. Phys. J. D* **2011**, *63*, 307–310.

[102] J. C. Scaiano, *React. Intermed. Chem.* **2005**, 847–871.

[103] J. C. Scaiano, *J. Am. Chem. Soc.* **1980**, *102*, 7747–7753.

[104] J. Gersdorf, J. Mattay, H. Goerner, *Sect. Title Phys. Org. Chem.* **1987**, *109*, 1203–1209.

[105] M. Mukai, S. Yamauchi, N. Hirota, *J. Phys. Chem* **1992**, *6*, 3305–3311.

[106] T. Okutsu, M. Ooyama, H. Hiratsuka, *J. Phys. Chem. A* **2000**, *104*, 288–292.

[107] M. Hayon, E.; Ibata, T.; Lichtin, N. N.; Simica, *J. Phys. Chem.* **1972**, *76*, 2072–2078.

[108] A. Eibel, M. Schmallegger, M. Zalibera, A. Huber, Y. Bürkl, H. Grützmacher, G. Gescheidt, *Eur. J. Inorg. Chem.* **2017**, 2469–2478.

[109] M. Brustolon, E. Giamello, *Electron Paramagnetic Resonance: A Practitioner's Toolkit*, Wiley, **2009**.

[110] V. Chechik, E. Carter, D. Murphy, *Electron Paramagnetic Resonance (Oxford Chemistry Primer)*, Oxford University Press, **2016**.

[111] A. Yurkovskaya, O. Morozova, G. Gescheidt, *Encyclopedia of Radicals in Chemistry, Biology and Materials*, Wiley, **2012**.

[112] I. Gatlik, P. Rzadek, G. Gescheidt, *J. Am. Chem. Soc.* **1999**, 8332–8336.

[113] M. Goez, *Concepts Magn. Reson.* **1995**, *7*, 69–86.

[114] S. H. Pine, *J. Chem. Educ.* **1972**, *49*, 664.

[115] H. Hayashi, *Introduction to Dynamic Spin Chemistry: Magnetic Field Effects on Chemical and Biochemical Reactions*, World Scientific Publishing Co. Pte. Ltd., **2004**.

[116] C. M. R. Clancy, V. F. Tarasov, M. D. E. Forbes, *Electron Paramagnetic Resonance*, Royal Society Of Chemistry, Cambridge, UK, **1998**.

[117] C. P. Slichter, *Principles of Magnetic Resonance*, Springer, **1978**.

[118] R. Amorati, L. Valgimigli, C. Viglianisi, M. Schmallegger, D. Neshchadin, G. Gescheidt, *Chem. - A Eur. J.* **2017**, *23*, 1–9.

[119] D. Darvasiová, Z. Barberiková, A. Eibel, M. Schmallegger, G. Gescheidt, M. Zalibera, D. Neshchadin, *Polym. Chem.* **2017**, *8*, 6943–6947.

[120] M. Schmallegger, A. Eibel, J. P. Menzel, A. Kelterer, M. Zalibera, C. Barner-Kowollik, H. Grützmacher, G. Gescheidt, *Chem. - A Eur. J.* **2019**, DOI 10.1002/chem.201900935.

[121] M. Schmallegger, G. Gescheidt, *J. Chem. Educ.* **2018**, *95*, 2013–2016.

2. Publications on Electron Transfer and Proton Transfer Processes in Biological Systems

2.1. Proton-Coupled Electron Transfer from Hydrogen-Bonded Phenols to Benzophenone Triplets

Riccardo Amorati,*[a] Luca Valgimigli,[a] Caterina Viglianisi,[b] Max Schmallegger,[c] Dmytro Neshchadin,*[c] and Georg Gescheidt[c]

[a] Department of Chemistry “G. Ciamician”, University of Bologna

[b] Department of Chemistry “Ugo Schiff”, University of Florence

[c] Institute of Physical and Theoretical Chemistry, Graz University of Technology,

Published in: *Chemistry – A European Journal* **2017**, 23, 5299–5306.

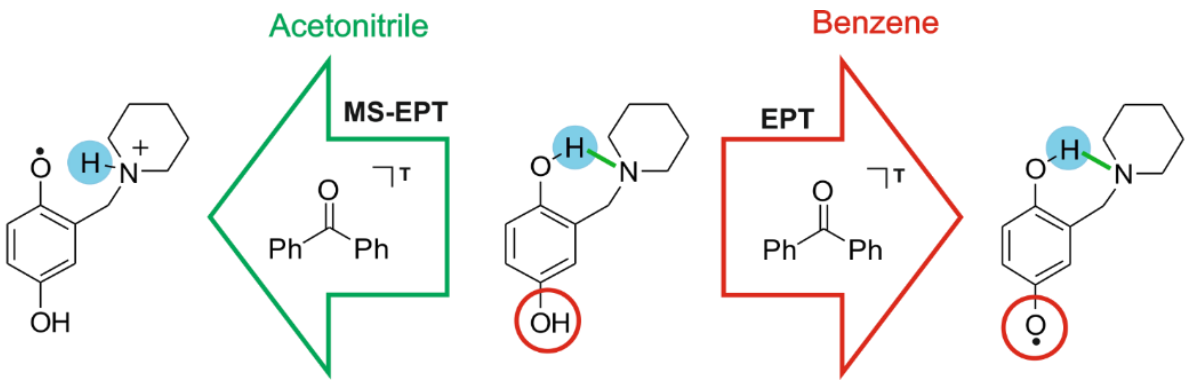

2.1.1. Abstract

Phenols with intramolecular hydrogen bond between a pendant base and the phenolic OH group react differently in polar and non-polar environments with electron/proton acceptors. This was demonstrated by using time resolved chemically induced dynamic nuclear polarization (TR CIDNP) and theoretical calculations. In benzene, those phenols undergo a concerted electron–proton transfer (EPT) that yields neutral ketyl and phenoxyl radicals. In polar acetonitrile, the reaction mechanism turns into an electron transfer from the phenol to the triplet ketone, accompanied by the shift of a proton from the phenolic OH group to the nitrogen atom of the pendant base to form a distonic radical cation. This behavior is similar to that of tyrosine H-bonded to basic residues in some radical enzymes. This solvent-induced mechanism switch in proton-coupled electron transfers is important in different biological systems, in which the same metabolites and intermediates can react differently depending on the specific local environments.

2.1.2. Introduction

Key redox elements for energy harvesting in cells (e.g., the tyrosine–histidine dyad in Photosystem II)[1] are often constituted by a base and a phenolic group being able to establish hydrogen bonds. Such molecular systems have also been utilized as models to understand proton-coupled electron transfers (PCET).[2] In such systems, electron transfer (ET) and proton transfer (PT) from a phenol to an acceptor can proceed by sequential (ET/PT or PT/ET) or a concerted electron–proton transfer (EPT) process, [1b] also called coupled proton–electron transfer (CPET).[3] In a multi-site EPT (MS-EPT or separated CPET) [1b,3], the electron and the proton are transferred in a concerted fashion to spatially distinct electron and proton acceptors. Phenols H-bonded to a base are much better electron donors than “free” phenols because the incipient phenoxyl radical cations are deprotonated “instantly” by the base during the ET, by the MS-EPT mechanism.[2] Understanding the factors that determine the choice of a system between a stepwise or a (multi-site) concerted mechanism is the basis for harnessing and exploiting the potentials of PCET reactions in many fields, such as energy transduction,[4] organic synthesis,[5] antioxidant chemistry,[6] and nanochemistry.[7]

The aim of this work is to distinguish between the above pathways by utilizing time-resolved CIDNP (chemically induced dynamic nuclear polarization) spectroscopy, a method which provides a molecular fingerprint of reactive intermediates at a nanosecond timescale.[8] Thus, it is possible to distinguish between decisive intermediate radicals, for example, $\mathbf{1}^{-H}$. or $\mathbf{1}^{\cdot+}$ (Scheme 1).

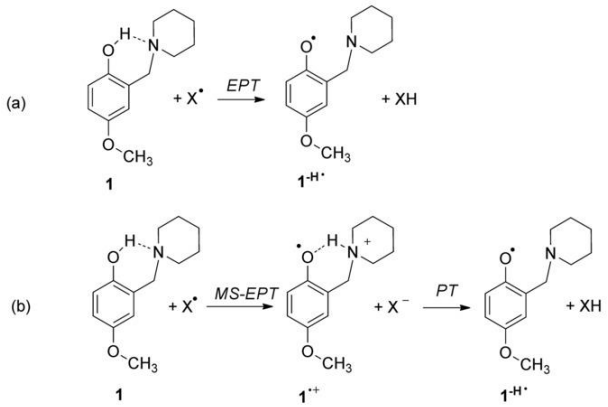

Scheme 1 Reaction pathways for the reaction of a phenol H-bonded to a pendant base with X. radicals in solvents with contrasting polarities: (a) benzene, (b) acetonitrile.

We have shown that phenol **1**, with the OH group H-bonded to an alkylamine, reacts with peroxyl radicals through an EPT mechanism (Scheme 1a; X.=ROO.) and its rate constant does not depend significantly on the solvent.[9] In contrast, when the phenol reacts with 2,2′-diphenylpicrylhydrazyl radical (dpph.), the reaction becomes much faster in acetonitrile than in benzene. This suggests that the mechanism of the reaction of **1** with dpph. proceeds by solvent-dependent pathways: an EPT mechanism is active in benzene, whereas stepwise MS-EPT/PT dominates in acetonitrile (see Scheme 1a, b X.=dpph.).[9] Accordingly, systematically applying solvents leading to the preference of one of the possible paths of PCET and the careful choice of the reacting radical provide a strategy for establishing specific intermediates. The mechanism shown in Scheme 1 b was deduced only from kinetic studies (based on optical spectroscopy), and from the detection of dpph− anion as an intermediate. A clear-cut identification of intermediates like $\mathbf{1}^{\cdot+}$ could not be achieved.[9] Indeed, the difficulty of identifying transient species often restricts studies of PCET reactions to indirect observations.[2,10]

Here, we show how previously elusive intermediates that appear in the mechanism shown in Scheme 1 can be established by time-resolved CIDNP.[8] We report the photo-induced reactions between benzophenone (BP) triplet and phenols **1–3** covalently linked to an amine base. Whereas in 4-methoxy-2-(1-piperidinylmethyl)phenol (**1**) and 4-hydroxy-2-(1-

piperidinylmethyl)phenol (**2**), the lone pair at the piperidine N-atom can accept a hydrogen bond from the phenolic H atom, in 4-methoxy-3-(1-piperidinylmethyl)phenol (**3**), such an H-bond cannot be formed. Phenols **4** and **5** (4-methoxyphenol and hydroquinone, respectively), were also investigated as reference compounds. Accordingly, the application of CIDNP to appropriately designed reaction mixtures is well suited to provide new insights into the interplay of factors shifting PCET mechanistic pathways.

2.1.3. Results

Photo-CIDNP experiments

Design of the experiments: CIDNP is an NMR-based spectroscopic technique that allows detection of short-lived free radical intermediates through their long-lived diamagnetic products.[8] In CIDNP experiments, spin-correlated free radical pairs are generated thermo- or photochemically in a high magnetic field. Free radicals (radical ions) in those radical pairs can follow two distinct routes: recombination or disproportionation, immediately in cage, or diffusion and reaction with free radicals present in the bulk. We generate these radical pairs by exciting benzophenone (BP) to its triplet state. This reactive state (lifetime ca. 35 µs) undergoes solvent-dependent reactions. In nonpolar solvents, the reaction of benzophenone triplets with phenols is known to proceed through the formation of an H-bonded exciplex. The follow-up EPT yields a ketyl and a phenoxyl radical (Scheme 2 a).[11] Electron-donating substituents on phenol increase the rate of the reaction. With the increasing polarity of the solvent, hydrogen bonding to the solvent competes with the formation of the exciplex, thus slowing down the reaction.[12] Under these conditions, the reaction may proceed by a stepwise ET/PT mechanism (see Scheme 2 b).[13] In water, the reaction between benzophenone triplets and phenols occurs exclusively through an ET/PT mechanism, which is facilitated by stabilization of the charged intermediates by water.[14] Those reactions find applications in the antioxidant treatment of UV light-mediated skin damage[15] and in the degradation of phenolic pollutants in wastewater treatment facilities.[16]

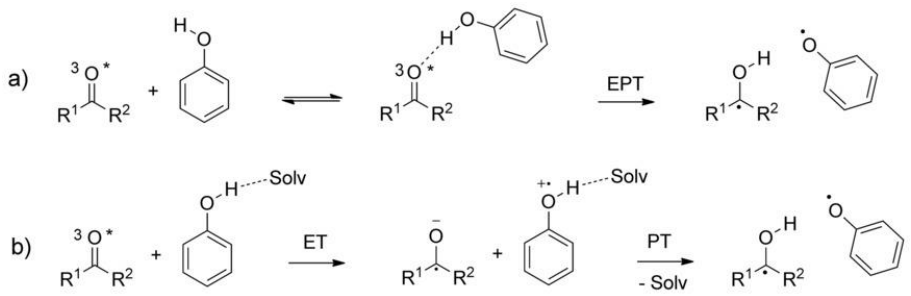

Scheme 2. Solvent-dependent reaction pathways for the reaction of phenol with ketone triplets.

In our experiments, the triplet of benzophenone (^{3}BP*) was generated by using a 355 nm laser flash. A rather short observing radio frequency pulse (4 µs) allowed detection of polarization mostly from geminate (cage) products. All experiments were performed in deuterated benzene and acetonitrile under nitrogen atmosphere. *tert*-Octylamine (TOA) was chosen as the reference base because it reacts slowly with ketone triplets due to the lack of cleavable C−H bonds in the α-position to the N-atom (see Figure S1 in the Supporting Information).[17,18]

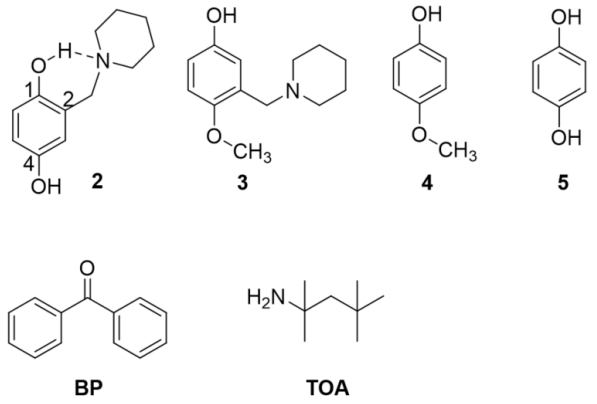

Experiments in benzene: ^{1}H NMR and CIDNP spectra in C_6D_6 of **1**, **2**, **4**, **5** and benzophenone together with signal assignments are presented in Figure 1. In C_6D_6, spectra obtained with **1** and **2** show that most of the CIDNP polarizations stem from the signals attributed to the parent phenol and benzophenone. This clearly indicates that reactions of **1** and **2** with benzophenone triplets are reversible on the timescale of our experiment.[19] In contrast to **1** and **2**, CIDNP spectra obtained with **4** and **5** (lacking the pendant base) contain polarizations of newly formed substances marked by the asterisks in Figure 1. In the spectrum of **4**, the corresponding signals can be tentatively assigned to coupling products of ketyl and phenoxyl radicals. Reaction of **5** with

^{3}BP* leads to the formation of benzoquinone as confirmed by the NMR of the reference sample. The size and the sign of CIDNP polarizations describe the spin distribution in free radicals that are formed during the reaction. In phenol **1**, the strongest polarizations are attributed to the aromatic hydrogens and protons of the OCH_3 and $ArCH_2N$ moieties. No polarization is shown by the piperidinic H-atoms of **1**. This coherently shows that ^{3}BP* does not react with the piperidinic methylene groups but exclusively with the phenolic OH forming phenoxyl and ketyl radicals. This reactivity pattern markedly differs from that of cumyloxyl radicals ($CumO^{\cdot}$), which were previously reported to react with **1** (in MeCN) mainly through H-atom abstraction from the piperidinic or benzylic CH_2.[20] With phenol **2**, no polarization arises from methylene groups of the piperidinic moiety. In principle, two distinct phenoxyl radicals can be formed. However, the CIDNP polarization pattern, in which benzylic hydrogens (ArC**H_2**N) are not polarized at all, points toward the hydrogen abstraction from the OH group at position 4. Phenol **3** was not soluble enough in benzene; therefore, it was not investigated in this solvent. Phenols **4** and **5** both form phenoxyl radicals and they both undergo recombination reactions to form coupling products. This is indicated by the polarization of aromatic H atoms and new signals in the CIDNP spectrum. In the case of **5**, the transfer of the second OH hydrogen leads to the formation of benzoquinone, which is clearly visible in the spectrum, as previously noted.

Experiments in acetonitrile: Upon changing the solvent to deuterated acetonitrile, all phenols **1**–**5** show polarization signals attributable to a phenoxyl radical, partly similar to the behavior in C_6D_6 solution (Figure 2). In CD_3CN, almost all polarizations belong to the NMR spectra of the parent phenols, so the reaction is nearly completely reversible on the timescale of our CIDNP experiment. In the case of **5**, this means that the primary phenoxyl (semiquinone) radical is not converted to benzoquinone by the loss of the second hydrogen atom, reasonably because H-bond formation between the 4-OH group and solvent molecules slows down its abstraction.[21]

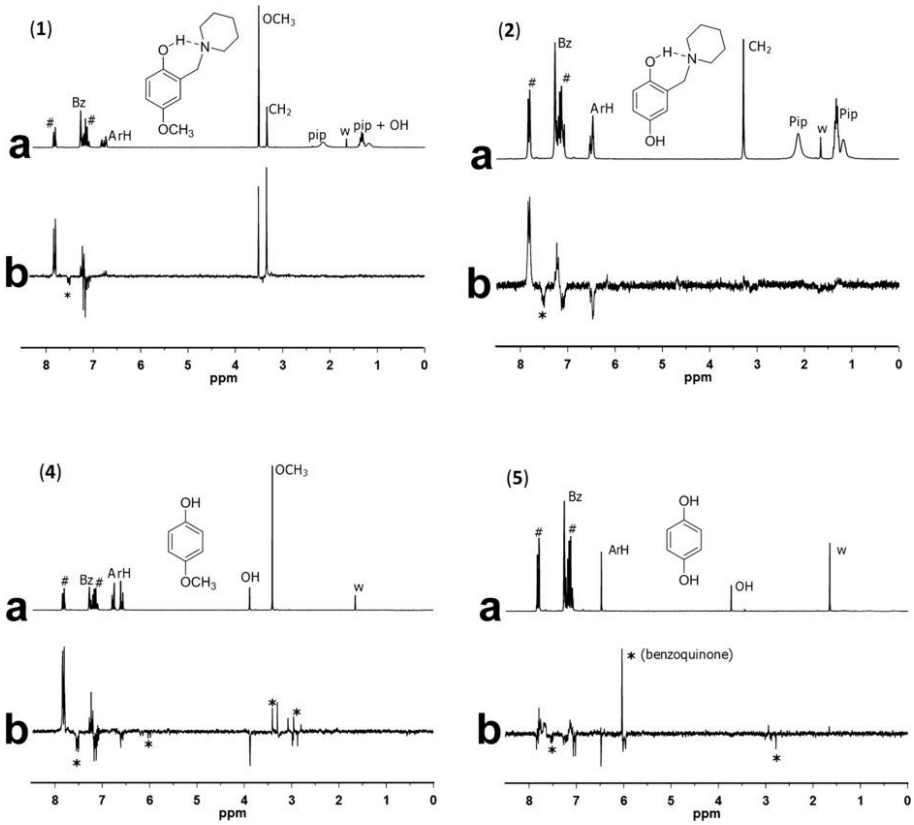

Figure 1. (a) ^{1}H NMR spectra of **1**, **2**, **4**, and **5** with BP in C_6D_6 at 293 K. b)^{1}H CIDNP spectra. Abbreviations: water (w); solvent residual signal (Bz), BP signals (#), piperidine hydrogens (Pip), hydroxyl hydrogens (OH), aromatic hydrogens (ArH), benzylamino hydrogens (CH_2), newly formed products of radical reaction (*).

The CIDNP spectrum of **2** in CD_3CN displays polarization on the Ar**CH_2**N group different from observed in C_6D_6, meaning that the phenoxyl radical on the OH group at position 1 is formed. In phenol **3**, the polarization is located on the aromatic H atoms and on the OCH_3 group, and, to a smaller extent, on the Ar**CH_2**N group, again indicating the formation of a phenoxyl radical. To assess the importance of the covalent link between the phenolic moiety and the alkylamino base, we performed experiments by mixing **4** and **5**, both lacking the pendant base, with *tert*-octylamine. The CIDNP spectra recorded in deuterated benzene and acetonitrile are reported in Figure 3. The peak shift in NMR spectra caused by TOA indicates that in C_6D_6, formation of H-bonds between the amine and the phenols occurs, whereas no significant interaction can be evidenced in CD_3CN (see also Figure S2 in the Supporting Information). As expected, no polarization signals arising from the amine are present. Upon comparing the spectra of **4** with and without TOA, we can assume that amine addition did not significantly change the CIDNP spectra and therefore the

reaction pathway. On the other hand, spectra of **5**, consisting of one line for all equivalent aromatic protons, do not provide any mechanistic insight. In the case of **4** in C_6D_6, however, the presence of TOA decelerates byproduct formation.

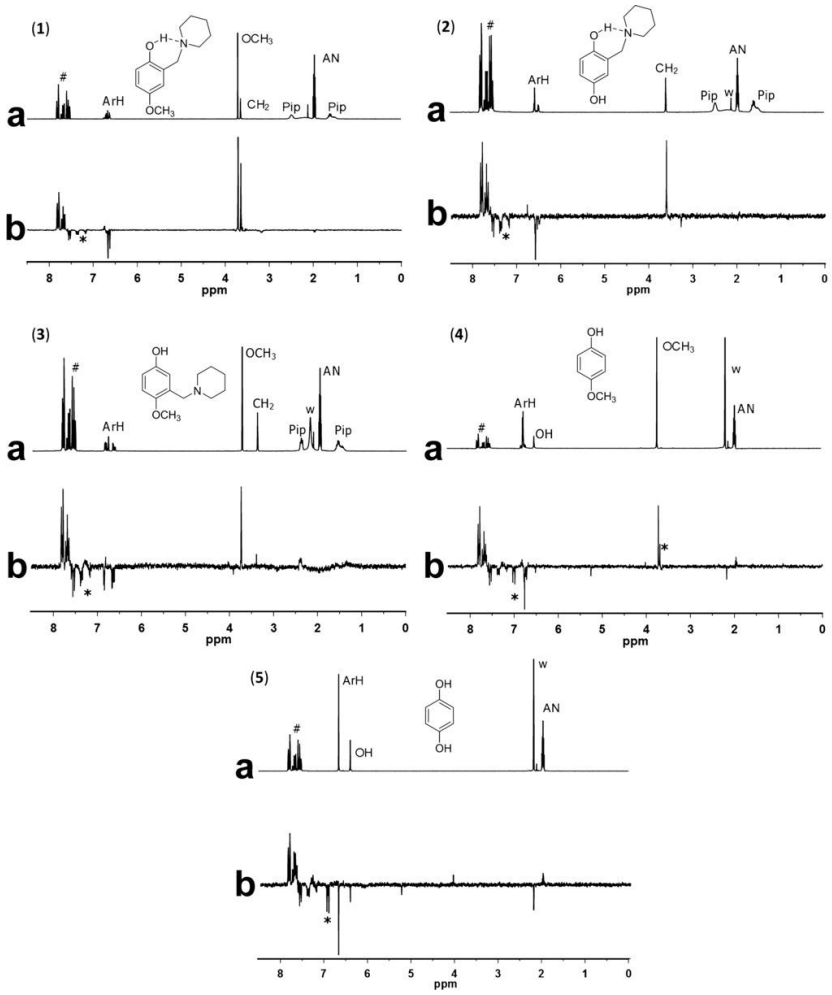

Figure 2. (a) ^{1}H NMR spectra of **1**, **2**, **4**, and **5** with BP in C_6D_6 at 293 K. b)^{1}H CIDNP spectra. Abbreviations: water (w); solvent residual signal (Bz), BP signals (#), piperidine hydrogens (Pip), hydroxyl hydrogens (OH), aromatic hydrogens (ArH), benzylamino hydrogens (CH_2), newly formed products of radical reaction (*).

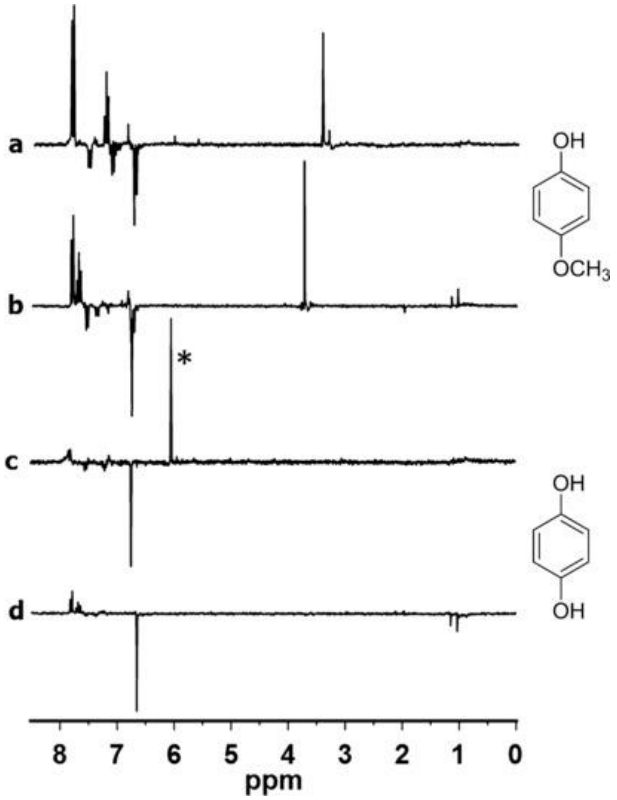

Figure 3. ^{1}H CIDNP spectra for the reaction of **4** (spectra a, b) and of **5** (spectra c, d) in the presence of *tert*-octylamine (15 mm) in C_6D_6 (a, c) and in CD_3CN (b, d). Benzoquinone signal is labeled by an asterisk.

Quantum mechanical calculations and semi-quantitative CIDNP analysis As we have mentioned above, CIDNP polarizations of nuclei in diamagnetic products are proportional to hyperfine coupling constants (*hfc*) of those nuclei in the precursor radicals. The *hfc*, in turn, reflect the structure of such radicals. To gain structural information on the radical species involved in the reactions of phenols **1**–**4**, we performed quantum mechanical calculations on the corresponding free radicals and radical cations.[22] To economize on calculation time, we replaced piperidine moieties with dimethylamino groups, whereas $MeNH_2$ was chosen as an analogue of TOA. Calculated hyperfine coupling constants in most stable conformations of neutral radicals and radical cations are reported in Schemes 3 and 4, respectively. According to calculations, the structure of radicals strongly depends on the presence of the charge (radical cations) and the position at which the pendant base is attached with respect to the phenoxyl oxygen. For neutral radicals $\mathbf{1}^{-H\cdot}$ and $\mathbf{2}^{-H\cdot}$, the pendant base tends to turn as far as possible from the radical center. For radical $\mathbf{2}^{-H}$, two distinct structures (Scheme 3) can be realized, however $\mathbf{2}^{-H\cdot}$(**A**) is found to be lower in energy by about 7 kcal mol^{-1}. This contrasts with the arrangement in $\mathbf{1}^{\cdot+}$ and $\mathbf{2}^{\cdot+}$, in which the ammonium ion (formed upon intramolecular proton transfer from the phenolic OH to the amine

base) is strongly bound to the phenoxyl oxygen by an intramolecular hydrogen bond. In radicals obtained from **3**, the pendant base is far enough from the radical center and the intramolecular bond is not established. For **3**, calculations predict two tautomers $\mathbf{3}^{\cdot+}$(**A**) and $\mathbf{3}^{\cdot+}$(**B**), which differ in proton location. The former, in which the proton is attached to the nitrogen, is slightly lower in energy (by 3.7 kcal mol^{-1}).

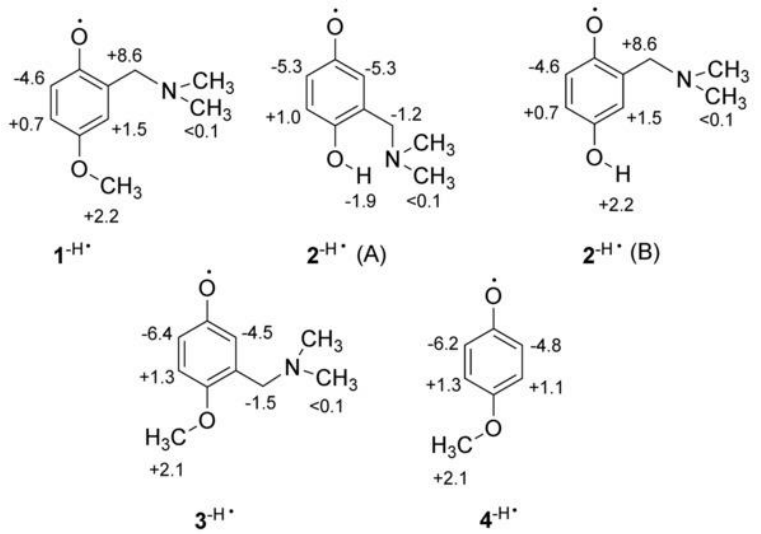

Scheme 3. Calculated (B3LYP/TZVP) hyperfine coupling constants (in Gauss) of hydrogen atoms in MeCN for neutral phenoxyl radicals.

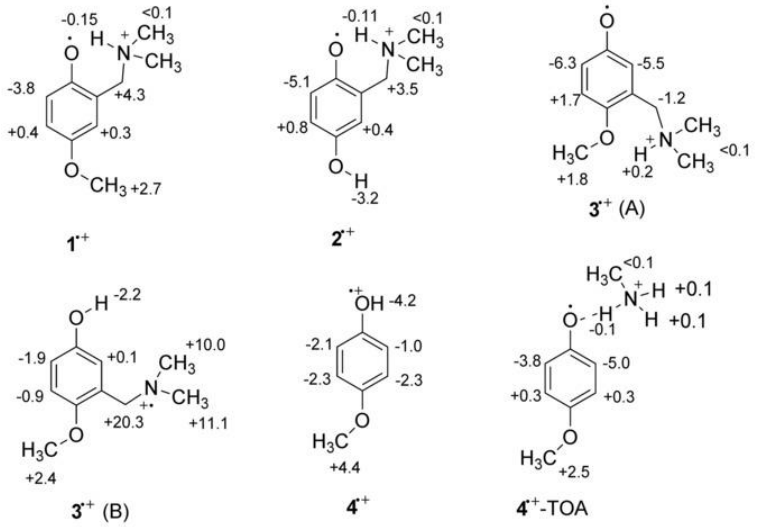

Scheme 4. Calculated (B3LYP/TZVP) hyperfine coupling constants (in Gauss) of hydrogen atoms in MeCN for phenoxyl radical cations.

These structural peculiarities must be reflected in the distribution of the unpaired spin, which allowed us to distinguish between radicals using CIDNP polarizations. The comparison between calculated hyperfine coupling constants (*hfc*) of selected nuclei and their polarizations in diamagnetic products is presented in Table 1. There, ratios of CIDNP polarizations normalized on the amount of the equivalent protons [(I^1/n^1)/ (I^2/n^2)] are set against the ratios of hyperfine coupling constants for the corresponding protons [hfc^1/hfc^2].[23] Comparison of experimental and calculated values lets us evaluate the specific contribution of the radical or radical cation species in the CIDNP spectrum. For **1** in benzene, the ratio of CIDNP signals for the Ar**CH$_2$**N/ArH and Ar**CH$_2$**N/OCH$_3$ groups (see Table 1) is in good agreement with that calculated for **1**$^{-H\cdot}$ in the gas phase (exp: 11.1 and 5.7, calc: 13.2 and 4.9, respectively). In acetonitrile, although the agreement is rather poor, the CIDNP polarizations can be attributed to **1**$^{\cdot+}$, because it has consistently lower hfc^1/hfc^2 values than **1**$^{-H\cdot}$. In the case of **2**, experimental CIDNP spectra in benzene can be attributed to **2**$^{-H\cdot}$(A) (exp: 0.13, calc: 0.5), and those in acetonitrile to **2**$^{\cdot+}$ (exp: 1.6, calc: 2.6 G). This assignment is consistent with the change of the reactive hydroxyl group from 4-OH to 1-OH passing from benzene to acetonitrile. In the case of phenol **3**, CIDNP spectra in MeCN could either be attributed to the neutral radical **3**$^{-H\cdot}$ or to the N-protonated radical cation (**3**$^{\cdot+}$, structure A). However, the latter assignment is unlikely because it would require that, after the electron transfer from **3** to ^{3}BP*, the proton is transferred over a relatively large distance from the phenolic OH to the pendant base, instead of being transferred to BP$^{\cdot-}$. As acetonitrile is an aprotic solvent, it does not assist such proton shifts.[24] Formation of an O-protonated radical cation **3**$^{\cdot+}$(B) can be excluded because it has a significant spin population on the piperidinic CH_2 groups (see Scheme 4). For phenol **4**, both in benzene and acetonitrile, the ratio of CIDNP signals better matches **4**$^{-H\cdot}$ rather than **4**$^{\cdot+}$. In the case of **4**+TOA, as the radical cation transfers the H^+ to the amine, calculated *hfc* values of **4**$^{\cdot+}$-TOA are mid-way between those of **4**$^{-H\cdot}$ and **4**$^{\cdot+}$. In both solvents, experimental data are better matched to the neutral radical **4**$^{-H\cdot}$, which has lower hfc^1/hfc^2 values than **4**$^{\cdot+}$-TOA. The CIDNP spectrum of **5** could not be analyzed in this way as all protons are equivalent. We also considered the possibility that ^{3}BP* abstracts an H-atom from the Ar**CH$_2$**N groups, forming C-centered radicals (see Supporting Information). However, the involvement of these radicals was excluded because calculations predicted significantly high *hfc* at the piperidinic CH_2 groups.

Table 1. Ratio of the integral of CIDNP polarizations, normalized to the number of equivalent H atoms [(I^1/n^1)/(I^2/n^2)], and ratio of the calculated coupling constants [hfc^1/hfc^2] for the neutral and the cation radicals, in the gas phase or in acetonitrile (in brackets). The groups of proton considered are indicated in the second column. [a] $ArCH_2N$=benzylic hydrogens; ArH=aromatic hydrogens (mean value); OCH_3=methoxy hydrogens; [b] structure $\mathbf{2}^{-H\cdot}$(A). [c] N-protonated tautomer, structure $\mathbf{3}^{\cdot+}$(A).

Phenol	Groups[a]	$[I^1/n^1]/[I^2/n^2]$ CIDNP		hfc^1/hfc^2 calc. [Gauss]	
		C_6D_6	CD_3CN	Neutral radical	Cation radical
1	$ArCH_2N/ArH$	11	0.5	13.2 (10.8)	3.9 (4.3)
	$ArCH_2N/OCH_3$	5.7	2.1	4.9 (3.9)	1.6 (1.6)
2	$ArCH_2N/ArH$	0.13	1.6	0.50 (0.38)[b]	2.3 (2.6)
3	$ArCH_2N/ArH$	–	0.17	0.50 (0.35)	0.39 (0.36)[c]
	$ArCH_2N/OCH_3$	–	0.36	1.1 (0.50)	0.99 (0.66)[c]
4	OCH_3/ArH	0.60	0.67	0.44 (0.62)	2.4 (2.3)
4+TOA	OCH_3/ArH	0.51	0.48		1.4 (1.3)

2.1.4. Discussion

In benzene, the reaction of ^{3}BP* with all investigated phenols yields neutral phenoxyl and ketyl radicals, suggesting the occurrence of EPT, as delineated in Scheme 1. Within the kinetic resolution of the CIDNP experiments, the contribution of stepwise electron and proton transfer cannot be excluded. The dichotomic behavior of ^{3}BP* as a concerted EPT or stepwise ET/PT oxidizer has been the object of many investigations, all of which essentially agree in recognizing that the EPT transition state has strong contributions from charge-transfer resonance structures [Eq. 1 [25a] and that in some conditions the reaction is better described as a stepwise ET/PT process.[11,12,17,25]

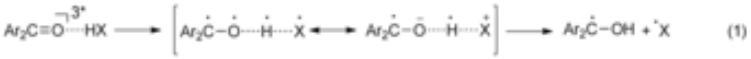

(1)

However, the fact that there is no evidence of alkyl radical formation in the CIDNP spectra of **1** and **2** is noteworthy and allows us to derive mechanistic considerations. Griller et al. reported that in benzene, ^{3}BP* abstracts H-atoms from the α-CHN of di- and tri-alkylamines with large rate constants (k≈3×10^9 m^{-1} s^{-1} in C_6H_6).[17] For comparison, the rate constant for a reaction with *para*-methoxyphenol (**4**) is only slightly higher, 4.5×10^9 m^{-1} s^{-1} in C_6H_6.[12] In the presence of photo-

generated ^{3}BP*, amines are reported to afford intense CIDNP spectra due to the formation of α-aminoalkyl radicals or amine radical cations, which can be distinguished thanks to their characteristic polarization pattern.[26] Their reaction relies on the stabilization of the transition state by charge transfer with the nitrogen lone pair,[17,25] so it is hampered by non-covalent interactions in which the N-atom is a donor of electron density. This is actually the case for compounds **1** and **2**, in which a reduction of the reactivity of the CH_2N groups toward ^{3}BP* is expected because of the presence of an intramolecular H-bond between the phenolic OH and the N-atom. However, the same structural feature also lowers the reactivity of the phenolic OH in **1**, as the intramolecularly H-bonded OH group is less available to form the H-bonded exciplex than "free" OH groups.[9] The balancing of these two effects is difficult to predict in advance and may vary with the abstracting radical. Recently, some of us have shown that the reaction of **1** with the cumyloxyl radical (CumO·) in MeCN affords only carbon-centered radicals, originating from the α-CHN groups, whereas in **3**, abstractions from OH and CH_2N groups by CumO· are occurring equally.[20] The CIDNP spectra in benzene indicate that in molecules containing both phenolic and amine groups, ^{3}BP* preferentially abstracts the phenolic H-atom by EPT (see Scheme 5 A). This is borne out by regarding a hypothetical ET/PT mechanism, in which deprotonation after the ET step would afford both phenoxyl and α-aminoalkyl radicals. We calculated that the α-amino benzylic radical (i.e., ArCH·N) of **1** is less stable than the phenoxyl radicals $\mathbf{1}^{-H\cdot}$ only by 1.0 kcal mol^{-1} (see Supporting Information).

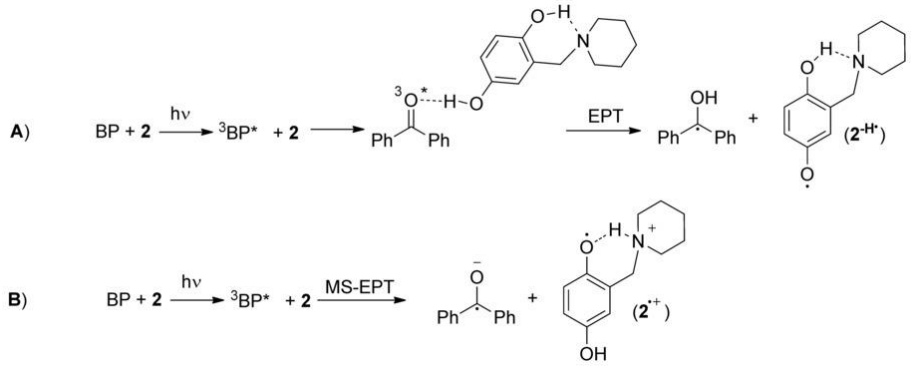

Scheme 5. Proposed mechanism for the reaction of **2** with ^{3}BP* in benzene (A) and acetonitrile (B).

In contrast to reactions performed in benzene, in acetonitrile, the results vary depending on the phenol used. Phenol **3**, bearing the pendant base in a position not suitable for intramolecular H-bonding to the OH group, and **4**, lacking the pendant base, afford neutral phenoxyl radicals. This occurs either through a concerted EPT from the fraction of phenol not H-bonded to the solvent

(see Scheme 1), or by a fast in-cage stepwise ET/PT process. However, the absence of polarization on the piperidinic protons in **3** suggests that the reaction is an EPT directed toward the phenolic OH by formation of an H-bonded exciplex. Instead, with phenols **1** and **2**, polarizations of CIDNP spectra indicate formation of the distonic radical cations $\mathbf{1}^{\cdot+}$ and $\mathbf{2}^{\cdot+}$, which are formed as a consequence of an MS-EPT from **1** or **2** to ^{3}BP* (Scheme 5 B). The different behavior of **1** and **2** compared to that of **3** and **4** agrees with free energies for electron transfer to ^{3}BP*, that can be calculated as −8.6, −10.5, +0.2, and +2.3 kcal mol^{-1} for **1**–**4**, respectively, by using the Rehm–Weller equation[27] (neglecting the Coulombic contribution),[11] the redox potentials of **1**–**4** (1.04, 0.96, 1.42, 1.51 V vs. NHE in MeCN, respectively),[9] and that of ^{3}BP*.[25d] Most interestingly, phenol **2** turned out to be a sensitive probe of the reaction mechanism, because the change from EPT to MS-EPT was easily detectable by the position of the OH group bearing the radical. This is also the first CIDNP spectroscopic evidence of the formation of distonic radical cations during the oxidation of H-bonded phenols, which integrates the few reports obtained by EPR[28] and UV/Vis spectroscopy.[2,28] In this regard, the sharp distinction of the different transients involved in the reaction, provided by CIDNP spectroscopy, allows for a clear-cut distinction among the different PCET mechanisms, providing full support for a mechanism switch as a function of the reaction medium. Finally, addition of TOA seems to have no major effect on the reaction products of **4**, as reaction with ^{3}PB* affords $\mathbf{4}^{-H\cdot}$ in both investigated solvents, showing that the MS-EPT occurs only when the phenolic OH and the amine function are pre-organized at the beginning of the reaction through the formation of an intramolecular H-bond. This result is in line with previous observations that MS-EPT requires H-bond contact between the H-atom donor and the base, which may also be mediated by a hydroxyl group acting as proton relay.[29] This also explains why adrenalin, which has a pendant amine group distant from the reactive *ortho*-di-phenolic group, reacts with ^{3}BP* by EPT without the intermediacy of phenolic radical cations.[30] It should be noted that, although our studies underline the importance of the proximity of the pendant base to the phenolic OH for the MS-EPT mechanism to take place, this is entirely related to the accessibility of suitable geometries for establishing the intramolecular H-bond. Therefore, phenols like tyrosine residues in peptides, having amine functions at an H-bond distance from the phenolic OH might react in a similar way.

2.1.5. Conclusion

In this work, we have presented the first clear-cut distinction between the various pathways of proton-coupled electron transfer to a triplet ketone by identifying the transient intermediates according to the reaction medium, utilizing time- resolved CIDNP spectroscopy. Reactions of all the four phenols with triplet ketones in non-polar solvents (benzene), proceed by a concerted electron–proton transfer (EPT) independently of the presence and location of pendant bases. These reactions lead to the formation of neutral ketyl and phenoxyl radicals. On the other hand, the reactivity of phenols toward excited ketones drastically differs in polar environment. The change in solvent polarity does not influence the reaction mechanism of **3** and **4** but switches the reactivity pattern of **1** and **2** towards multisite electron–proton transfer (MS-EPT, see Scheme 5), in which the electron transfer to the ketone and the proton migration from the phenol to the nitrogen atom of the pendant base becomes a concerted process. The relative position of the pendant base and the phenolic OH is the key structural feature controlling the “switch” of the reaction mechanism. This type of reaction control must be taken into account, particularly in biological systems such as radical enzymes featuring tyrosyl radicals,[1] in which virtually the same reactions can occur either in polar or non-polar environments, and in the applications of benzophenone in the photo-labeling and photo-grafting of peptides, proteins, and oligonucleotides.[31]

2.1.6. Experimental Section

Chemicals: Compounds **1**–**3** were synthesized as previously reported.[9] All other chemicals and solvents were of the highest purity commercially available.

^{1}H CIDNP experiments: ^{1}H CIDNP spectra were collected on Bruker AVANCE DPX 200 MHz NMR spectrometer equipped with the wide bore ^{1}H CIDNP probe head and synchronized with Quantel Brilliant B Nd/YAG laser. Composite pulse presaturation followed by a short (ca. 8 ns, 355 nm) laser flash and 4 μs (ca. 90 deg. flip angle) radiofrequency observing pulse provided the observation of the background-free CIDNP polarizations. Phenols and benzophenone concentrations were 10–25 mm. All samples were bubbled with dry argon for 5 min prior to CIDNP experiments to remove oxygen.

Theoretical calculations: Geometries and frequencies were calculated at the B3LYP/6–31+g(d,p) level of theory in the gas phase, by using the Gaussian 09 software package. Coupling constants (*hfs*) were computed by performing single point calculations at the B3LYP/TZVP level of theory[14b] in the gas phase and in MeCN by using the default SCRF continuum solvent mode[22] on the most stable conformations (see the Supporting Information for the optimized geometries and energies). For the sake of clarity, as the introduction of solvent marginally affected the values of the calculated coupling constants, only those obtained with implicit MeCN solvent are shown in Schemes 3 and 4. For magnetically equivalent H-atoms, the average hyperfine coupling constant is indicated. Regarding the ketyl radical, its (protonated) neutral and anion radicals have very similar *hfc* values (see Supporting Information), thus their CIDNP spectra could not provide any mechanistic insight.

2.1.7. References

[1] a) M. Wikstrom, V. Sharma, V. R. I. Kaila, J. P. Hosler, G. Hummer, *Chem. Rev.* **2015**, *115*, 2196−2221; b) D. R. Weinberg, C. J. Gagliardi, J. F. Hull, C. F. Murphy, C. A. Kent, B. C. Westlake, A. Paul, D. H. Ess, D. G. McCafferty, T. J. Meyer, *Chem. Rev.* **2012**, *112*, 4016−4093; c) J. J. Warren, J. M. Mayer *Biochemistry*, **2015**, 54, 1863–1878; d) S. Hammes-Schiffer, *J. Am. Chem. Soc*. **2015**, *137*, 8860−8871.

[2] a) I. J. Rhile, T. F. Markle, H. Nagao, A. G. DiPasquale, O. P. Lam, M. A. Lockwood, K. Rotter, J. M. Mayer, *J. Am. Chem. Soc.* **2006**, *128*, 6075-6088; b) T. F. Markle, J. M. Mayer, *Angew. Chem. Int. Ed.* **2008**, 47, 738-740. c) M.-T. Zhang, T. Irebo, O. Johansson, L. Hammarstrom, *J. Am. Chem. Soc*. **2011**, *133*, 13224–13227; d) T. F. Markle, I. J. Rhile, J. M. Mayer, *J. Am. Chem. Soc*. **2011**, *133*, 17341–17352; e) T. F. Markle, M.-T. Zhang, M.-P. Santoni, L. O. Johannissen, L. Hammarstrom, *J. Phys. Chem. B*, **2016**, 120, 9308–9321.

[3] J. J. Warren, T. A. Tronic, J. M. Mayer, *Chem. Rev.* **2010**, *110*, 6961–7001.

[4] M. N. Jackson, Y. Surendranath, *J. Am. Chem. Soc.,* **2016**, *138*, 3228–3234; J. Chen, Y.-F- Li, P. Sit, A. Selloni, *J. Am. Chem. Soc*., **2013**, *135*, 18774–18777; X. Xie, E. Bakker *J. Am. Chem. Soc*., **2014**, *136*, 7857–7860.

[5] E.C. Gentry, R. R. Knowles, *Acc. Chem. Res*. **2016**, *49*, 1546–1556

[6] R. Amorati, A. Baschieri, G. Morroni, R. Gambino, L. Valgimigli, *Chem. Eur. J.* **2016**, *22*, 7924 – 7934; J. J. Hanthorn, R. Amorati, L. Valgimigli, D. A. Pratt, *J. Org. Chem*. **2012**,

77, 6895−6907; R. Amorati, G. F. Pedulli, D. A. Pratt, L. Valgimigli, *Chem. Commun*., **2010**, *46*, 5139–5141; T. Nakayama, B. Uno *Electrochimica Acta* **2016**, *208*, 304–309; Z. Zielinski, N. Presseau, R. Amorati, L. Valgimigli, D. A. Pratt, *J. Am. Chem. Soc.* **2014**, 136, 1570-1578; M. C. Foti, A. Slavova-Kazakova, C. Rocco, V. D. Kancheva, *Org. Biomol. Chem.*, **2016**, *14*, 8331-8337.

[7] J. N. Schrauben, R. Hayoun, C. N. Valdez, M. Braten, L. Fridley, J. M. Mayer, *Science*, **2012**, *336*, 1298-1301; G. A. Sotiriou, C. O. Blattmanna, Y. Deligiannakis, *Nanoscale*, **2016**, 8, 796-803; C. Viglianisi, V. Di Pilla, S. Menichetti, V. M. Rotello, G. Candiani, C. Malloggi, R. Amorati, *Chem. Eur. J*. **2014**, *20*, 6857 – 6860; M. Massaro, S. Riela, S. Guernelli, F. Parisi, G. Lazzara, A. Baschieri, L. Valgimigli, R. Amorati, *J. Mater. Chem. B*, **2016**, 4, 2229-2241.

[8] a) G. L. Closs, R. J. Miller, *J. Am. Chem. Soc*. **1979**, *101*, 1639–1641; b) J.-K. Vollenweider, H. Fischer, J. Hennig, R. Leuschner, *Chem. Phys*. **1985**, *97*, 217–234; c) K. M. Salikhov, I. N. Molin, A. L. Buchachenko. Spin polarization and magnetic effects in radical reactions. Amsterdam New York Budapest, Hungary: Elsevier Akadémiai Kiado, 1984

[9] R. Amorati, S. Menichetti, C. Viglianisi, M. C. Foti, *Chem. Commun*., **2012**, *48*, 11904–11906

[10] T. T. Eisenhart, W. C. Howland, J. L. Dempsey *J. Phys. Chem. B,* **2016**, 120, 7896–7905

[11] W. J. Leigh, E. C. Lathioor, M. J. St. Pierre, *J. Am. Chem. Soc.* **1996**, *118*, 12339-12348.

[12] P. K. Das, M. V. Encinas, J. C. Scaiano, *J. Am. Chem. Soc.* **1981**, *103*, 4154-4162; b) W.

[13] R. E. Galian, G. Litwinienko, J. Perez-Prieto, K. U. Ingold, *J. Am. Chem. Soc*. **2007**, *129*, 9280-9281.

[14] a) S. Canonica, B. Hellrung, J. Wirz, *J. Phys. Chem. A* **2000**, *104*, 1226-1232; b) D. Neshchadin, S. N. Batchelor, I. Bilkis, G. Gescheidt, *Angew. Chem. Int. Ed.* **2014**, *53*, 13288 –13292.

[15] M. C. Cuquerella, V. Lhiaubet-Vallet, J. Cadet, M. A. Miranda, *Acc. Chem. Res.* **2012**, *45*, 1558-1570.

[16] S. Canonica, B. Hellrung, P. Müller, J. Wirz, *Environ. Sci. Technol*. **2006**, *40*, 6636-6641.

[17] D. Griller, J. A. Howard, P. R. Marriott, J. C. Scaiano *J. Am. Chem. Soc*. **1981**, *103*, 619-623;

[18] M Salamone, G. A. DiLabio, M. Bietti, *J. Am. Chem. Soc*. **2011**, *133*, 16625–16634

[19] M. L. M. Schilling, *J. Am. Chem. Soc.* **1981**, *103*, 3077-3081; Z., Lucia, V. Bohmer, R. Kaptein. *J. Magn. Reson*. **1988**, *76*, 587-591.

[20] M. Salamone, R. Amorati, S. Menichetti, C. Viglianisi, M. Bietti *J. Org. Chem*. **2014**, *79*, 6196−6205

[21] R. Amorati, G. F. Pedulli *Org. Biomol. Chem*., **2012**, *10*, 814-818

[22] Gaussian 09, Revision D.01, M. J. Frisch, G. W. Trucks, H. B. Schlegel, G. E. Scuseria, M. A. Robb, J. R. Cheeseman, G. Scalmani, V. Barone, B. Mennucci, G. A. Petersson, H. Nakatsuji, M. Caricato, X. Li, H. P. Hratchian, A. F. Izmaylov, J. Bloino, G. Zheng, J. L. Sonnenberg, M. Hada, M. Ehara, K. Toyota, R. Fukuda, J. Hasegawa, M. Ishida, T. Nakajima, Y. Honda, O. Kitao, H. Nakai, T. Vreven, J. A. Montgomery, Jr., J. E. Peralta, F. Ogliaro, M. Bearpark, J. J. Heyd, E. Brothers, K. N. Kudin, V. N. Staroverov, R. Kobayashi, J. Normand, K. Raghavachari, A. Rendell, J. C. Burant, S. S. Iyengar, J. Tomasi, M. Cossi, N. Rega, J. M. Millam, M. Klene, J. E. Knox, J. B. Cross, V. Bakken, C. Adamo, J. Jaramillo, R. Gomperts, R. E. Stratmann, O. Yazyev, A. J. Austin, R. Cammi, C. Pomelli, J. W. Ochterski, R. L. Martin, K. Morokuma, V. G. Zakrzewski, G. A. Voth, P. Salvador, J. J. Dannenberg, S. Dapprich, A. D. Daniels, Ö. Farkas, J. B. Foresman, J. V. Ortiz, J. Cioslowski, and D. J. Fox, Gaussian, Inc., Wallingford CT, 2009.

[23] a) A. S. Kiryutin, O. B. Morozova, L. T. Kuh, A. V. Yurkovskaya, P. J. Hore, *J. Phys. Chem. B* **2007**, *111*, 11221–11227; b) D. Neshchadin, R. Levinn, G. Gescheidt, S. N. Batchelor, *Chem. Eur. J.* **2010**, *16*, 7008–16.

[24] M. S. Mehata *Chem. Phys. Lett*. **2007**, *436*, 357–361

[25] a) S. Inbar, H. Linschitz, S. G. Cohen, *J. Am. Chem. Soc.* **1981**, *103*, 1048-1054; b) L. R. Heeb, K. S. Peters, *J. Phys. Chem. B* **2008**, 112, 219-226; c) C. G. Shaefer, K. S. Peters, *J. Am. Chem. Soc*. **1980**, *102*, 7566-1567; d) P. J. Wagner, R. J. Truman, A. E. Puchalski, R. Wake, J. Am. Chem. Soc. **1986**, *108*, 1127-7138.

[26] a) M. Goez, I. Frisch, I. Sartorius, *Beilstein J. Org. Chem.* **2013**, *9*, 437–446; b) H. D. Roth, *Helv. Chim. Acta* **2006**, *89*, 2847-2860.

[27] D. Rehm, A. H. Weller, *Isr. J. Chem.* **1970**, *8*, 259-271.

[28] T. Maki, Y. Araki, Y. Ishida, O. Onomura, Y. Matsumura, *J. Am. Chem. Soc*. **2001**, *123*, 3371-3372.

[29] C. Costentin, M. Robert, J.-M. Savéant, C. Tard, *Angew. Chem. Int. Ed.* **2010**, *49*, 3803–3806.

[30] G. Cosa, J. C. Scaiano, *Org. Biomol. Chem.* **2008**, *6*, 4609–4614.

[31] G. Dormán, H. Nakamura, A. Pulsipher, G. D. Prestwich, *Chem. Rev*. **2016**, *116*, 15284–15398.

2.1.8. Supporting Information

Supporting information for this article is available on the WWW under *https://doi.org/10.1002/chem.201605931*

2.2. Kinetics of Electron Transfer Through a Phospholipid Bilayer

Max Schmallegger[a], Antonio Barbon[b], Marco Bortolus[b], Angela Chemelli[c], Itzhak Bilkis[d], Georg Gescheidt[a] and Lev Weiner[e]

[a] Institute of Physical and Theoretical Chemistry, Graz University of Technology
[b] Dipartimento di Scienze, Università degli Studi di Padova,
[c] Institute of Inorganic Chemistry, Graz University of Technology
[d] Faculty of Agricultural, Food and Environmental Sciences, Hebrew University
[e] Department of Chemical Research Support, Weizmann Institute of Science

Publication in Preparation

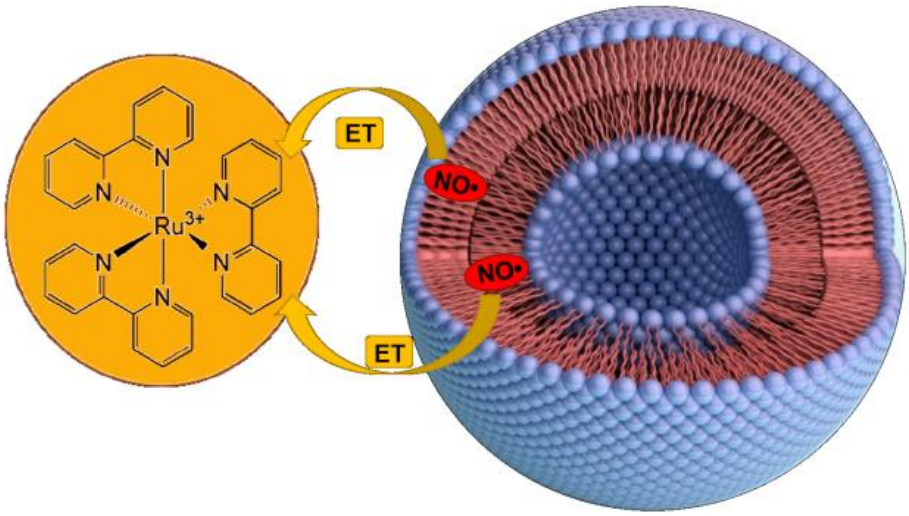

2.2.1. Abstract

Electron transfer is a fundamental process in energy conversion. In particular, it is an important element of energy production in biological systems such as mitochondria and chloroplasts. In these organelles, the conversion process occurs within biological membranes that contain both proteins and phospholipids, and the contribution of the phospholipids to electron transfer has not been well studied. In the present work, we incorporated 5-doxyl stearic acid and 16-doxyl stearic acid into unilamellar phospholipid vesi-cles composed of 1,2-dimyristoyl-sn-glycero-3-phosphocholine. Thus we generated two classes of vesi-cles in which the doxyl EPR probes were located at different depths within the bilayer. Photo-triggered generation of ([Ru(bpy)3]3+) residing outside the bilayer results in oxidation of the probes to the EPR-silent oxoammonium cation. The process was monitored by three independent methods, two of which followed disappearance of the EPR signal, while the third one monitored disappearance of the trivalent ruthenium species spectroscopically. All three methods yielded similar data. As anticipated, electron transfer for the 5-doxyl derivative was significantly faster than for the 16-doxyl derivative. Temperature-dependence measurements showed that the activation barriers for electron transfer were remarkably low (ΔG‡ ~ 40 kJ/mol). The rates determined below and above the liquid crystal to gel phase transition showed only a modest variation. Tunneling is the most plausible mechanism to account for our findings, which clearly demonstrate that elector transfer can occur through naked lipid bilayers, in the absence of proteins or other bridging species

2.2.2. Introduction

Electron transfer (ET) across organized molecular assemblies is a fundamental process in a broad repertoire of biological processes.[1–3] Extensive ET studies have been performed on various macromolecules and macromolecular assemblies, including proteins[1,4,5], DNA[6,7], dendrimers[8], lipid membranes[9], and artificial photosynthetic centers.[10,11] The latter are relevant to the process of, solar energy conversion.[12–18] Unilamellar liposomes composed of phospholipids serve as suitable models for biological membranes.[19–22] Many studies have been performed on electron transport across the bilayers of such vesicles.[16,23–27] However, they often rely on incorporating bulky donor or acceptor molecules into the lipid bilayer, thus distorting its structure. Other studies use asymmetric bilayers with two non-equivalent faces, exposed to (or incorporating) either the electron donor or the acceptor.[12,13,18,28,29] In this study we provide a novel paradigm for studying ET in biomimetic model membranes that involves virtually no distortion of

the phospholipid bilayer. Stable nitroxyl radicals (SNRs), which we employ as probes are small.[30] This allows us to obtain a realistic estimate of the contribution of the phospholipid bilayer to the rate of ET. Moreover, the temperature-dependence of the rate constants thus obtained can provide insight into the relative contributions of activated or tunneling mechanisms to ET. We use both optical and EPR spectroscopy to determine the positioning of the SNRs and the rate constants for their photo-stimulated oxidation. To this end, two probes, 5-doxyl stearic acid (**5DSA**) and 16-doxyl stearic acid (**16DSA**), were introduced into unilamellar liposomes composed of 1,2 dimyristoyl-sn-glycero-3-phosphocholine (DMPC).[31–33] Experimental data and molecular dynamics simulations in parent molecules[30,34] showed that the distance of the nitroxyl moiety from the membrane surface is ~0.75 nm for **5DSA**, and ~1.8 nm for **16DSA**. These differences allowed us to obtain distance-depend rate constants for ET. We chose DMPC as the phospholipid since its transition from a gel-like to a liquid crystalline phase at 296.6 K[35] makes it possible to study the effect of the rigidity of the lipid bilayer on the ET rate.[36] In the liquid crystalline state, lateral diffusion of lipids within the vesicle bilayer is rapid, whereas the transverse “flip-flop” motion is extremely slow.[37] Below 296.6 K, the transition to the gel-like phase causes all modes of mobility to decrease by orders of magnitude.[38,39]

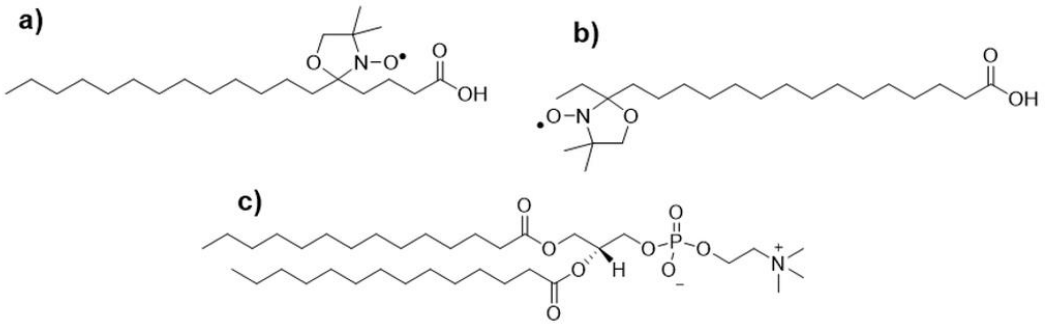

Scheme 1. Structures of the stable nitroxyl radicals **5DSA** (a) and **16DSA** (b), and of 1,2-dimyristoyl-sn-glycero-3-phosphocholine (DMPC) (c)

2.2.3. Experimental Section

Liposome preparation Liposomes were prepared by the ultra-sonication method.[40] Briefly, the phospholipid and the corresponding SNR (weight-ratio 50:1) were dissolved in 0.5 ml dichloromethane and dried to a thin film under a nitrogen stream in a test tube at room temperature. After further drying for 1 h under vacuum, the film was hydrated with 1 ml of buffer at neutral pH and then sonicated in an ultra-sonication bath for 15 minutes. Residual free SNRs were removed by dialysis.

Continuous-wave electron paramagnetic resonance Cw-EPR spectra were recorded on a Bruker X-band spectrometer (EMX, 100 kHz field modulation) at 275 K, 283 K, 303 K and 310 K with 1.5 G field modulation amplitude. Photolysis was conducted using a Hamamatsu Lightingcure LC4 Xe/Hg lamp. The concentration of the SNR was 2 x 10^{-5} M in all measurements, while those of [Ru(bpy)3]Cl2 and $(NH_4)_2S_2O_8$ were 1 x 10^{-5} M and 5 x 10^{-4} M, respectively.

Time-resolved electron paramagnetic resonance TR-EPR experiments were performed on an E580 ELEXSYS Bruker X-band spectrometer. The modulation frequency was 100 kHz and the modulation amplitude 2 G. The time resolved signal was recorded by using for detection the instrument lock-in amplifier connected to a fast digitizer. The modulation of the magnetic field was set to a frequency of 100 kHz, so that the time resolution was regulated by the time constant value (TC) to a maximum value of about 10 µs. The experimental procedure involved a single laser pulse to photo-excite $[Ru(bpy)_3Cl_2]$ in the sample and initiate the electron transfer depicted in Scheme 2, followed by observing the decay of the EPR signal. Photoexcitation was performed using a Quantel Rainbow Nd:YAG laser mounted with a second (532 nm), a third (355 nm) harmonic module, and an optical parameter oscillator set to 436 nm. The samples were prepared as described above.

Time-resolved UV-visible spectroscopy TR-UV-VIS spectra were recorded on a UV-Vis spectrometer equipped with optical fibres and a 1024-pixel diode-array detector (J&M Analytik AG, Essingen, Germany). Standard fluorescence quartz cuvettes were used for all measurements. Excitation of the samples was carried out using a Hamamatsu Lightingcure LC4 Xe/Hg lamp. The concentration of the SNR was 1 x 10^{-5} M in all measurements. The concentrations of $[Ru(bpy)_3]Cl_2$ and $(NH_4)_2S_2O_8$ were 1.41 x 10^{-5} M and 5 x 10^{-4} M for all measurements, respectively. The cuvette was irradiated for 30 s before each measurement to

convert all of the $[Ru(bpy)_3]^{2+}$ to its oxidized form. After injection of the liposomes containing the SNRs, the absorbance at 452 nm was monitored with readings acquired every 1 s.

Small angle X-ray scattering The SAXS equipment consisted of a SAXSpoint 2.0 (Anton-Paar, Graz, Austria) containing a Primux 100 micro microfocus X-ray source operating at λ=0.154 nm (Cu-K_α). Two-dimensional scattering patterns were recorded by a 2D EIGER R Series Hybrid Photon Counting (HPC) detector (Dectris Ltd, Baden-Daettwil, Switzerland). The samples were filled into a capillary (1 mm diameter) and measured for 300s nine times. The scattering patterns were averaged, edited by correcting the cosmic X-ray impacts. All measurements were performed at 20 °C. The absolute scale calibration was achieved by using water as a secondary standard.[41] All SAXS data have been evaluated by a generalized indirect Fourier transform (GIFT) method to determine the pair distance distribution functions.[42–44]

Dynamic light scattering The DLS equipment consisted of a diode laser (Coherent Verdi V5, λ= 532 nm) and a goniometer with single-mode fiber detection optics (OZ from GMP, Zürich, Switzerland). The data was acquired by a ALV/SO-SIPD/DUAL photomultiplier with pseudo-cross correlation and an ALV 7004 Digital Multiple Tau Real Time Correlator (ALV, Langen, Germany). The ALV software package was used to record and store the correlation functions. The light scattering was measured five times 30 s at a scattering angle of 90° and a Temperature of 25°C and the resulting correlation functions were averaged. The hydrodynamic radius was calculated by the optimized regulation technique software.[45]

2.2.4. Results

The SNRs react with $[Ru(bpy)_3]^{3+}$, generated in situ by photo-excitation of $[Ru(bpy)_3]^{2+}$ (residing in the aqueous phase) followed by oxidation of the excited $[Ru(bpy)_3]^{2+*}$ with ammonium persulfate. The photo-generated $[Ru(bpy)_3]^{3+}$ oxidizes the paramagnetic nitroxyl moiety (SNR) to the EPR-silent oxoammonium cation (Scheme 2). The kinetics of ET can be monitored both by following the decay of the EPR signal of the SNR ,[46–48] or of the reduction of optical absorption of the Ru^{3+} complex [49–51]

First we demonstrate that incorporation of the probe does not appreciably affect the bilayer structure of the liposomes. Dynamic light scattering (DLS) reveals that the liposomes containing

either **5DSA** or **16DSA** have a narrow size distribution with an average hydrodynamic radius of 53 nm (see Supporting Information). Small angle X-ray scattering (SAXS) reveals that the both control liposomes and those containing either of the probes have similar double-layer thicknesses of ca. 5.1 nm (see Supporting Information).[34]

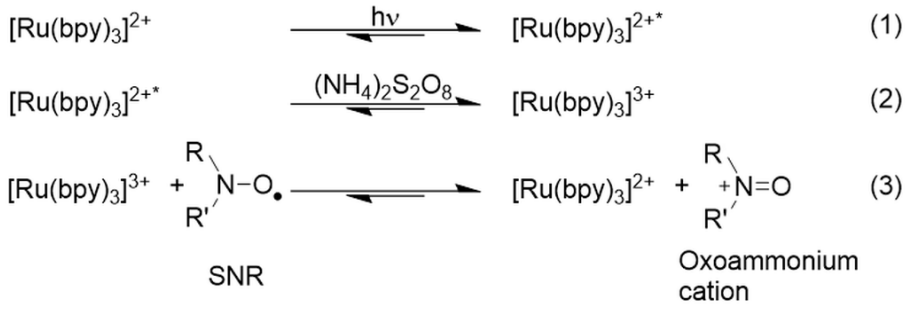

Scheme 2. Oxidation of an SNR by $[Ru(bpy)_3]^{3+}$ (3) via photo-induced ET between $[Ru(bpy)_3]^{2+}$ and ammonium persulfate (1) and (2).

The next step was to characterize the environment of the SNRs[52] using line-shape analysis via cw-EPR spectroscopy. The cw-EPR spectrum of **16DSA** embedded in the DMPC liposomes displays a clear reversible temperature dependence: below the phase-transition temperature of the phospholipid bilayer, the spectrum is that expected for a probe in a rigid, anisotropic environment (Figure 1) due to the restricted mobility of the SNR in the gel-like phospholipid phase. Above the transition temperature, in the liquid-crystal phase, **16DSA** exhibits narrow lines in the three-line EPR spectrum that are typical of an SNR located in an isotropic environment showing short rotational correlation times.[53,54] The cw-EPR spectrum of **5DSA** embedded in the DMPC liposomes displays a much smaller difference in anisotropy above and below the transition temperature of the DMPC. In contrast to **16DSA**, **5DSA** shows an EPR spectrum reflecting a rigid environment in the head group region of the lipid bilayer both below and above the transition temperature (Figure 1).[54] This corresponds well with the short distance between the >N–O• moiety and the rather rigid water/lipid interface and is in line with the long rotational correlation times that have been determined (see Supporting Information).[55]

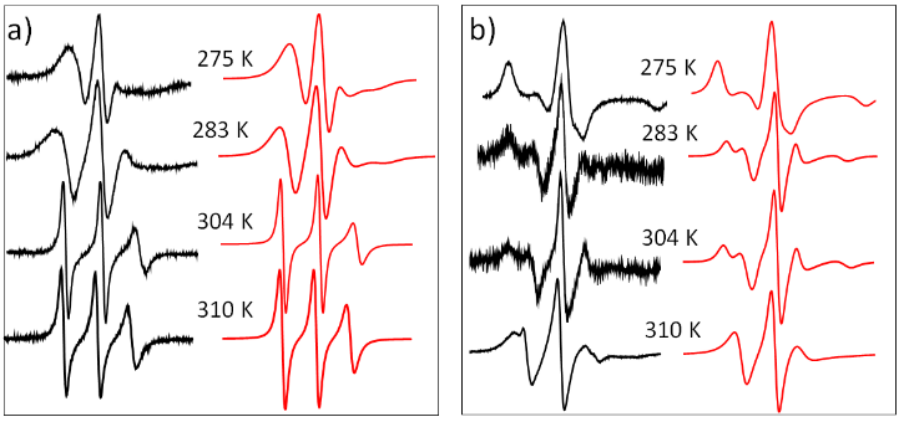

Figure 1. Temperature-dependence of the cw-EPR spectra of **16DSA** (a) and **5DSA** (b) embedded in DMPC liposomes in solution; experimental (black) and simulations (red). Simulations utilized the Easyspin[56]-based SimLabel[57] software.

The major part of this study involved determination of the kinetics of the ET process. We followed the decay of the EPR signals of the parent SNRs either by steady-state irradiation and EPR detection, or by pulsed-laser irradiation followed by rapid EPR detection (μs time regime). In addition, we followed the concentration of the oxidant, $[Ru(bpy)_3]^{3+}$, by optical spectroscopy so as to obtain the absolute rate constants. Upon steady-state irradiation, the decay curves for both spin labels (Figure 3a-d) display two components, corresponding to two distance regimes. This is most likely due to the probes bearing the SNRs being incorporated into both the inner and outer leaflets of the bilayer of the liposome (Scheme 3). Spin-labeled fatty acid alkyl chains, just like their unlabeled homologs, orient preferentially perpendicular to the membrane surface within the lipid bilayer.[31,58–60] The photo-generated oxidant $[Ru(bpy)3]^{3+}$, which resides exclusively in the outer aqueous phase, thus interacts with SNRs located at two distances (Scheme 3).

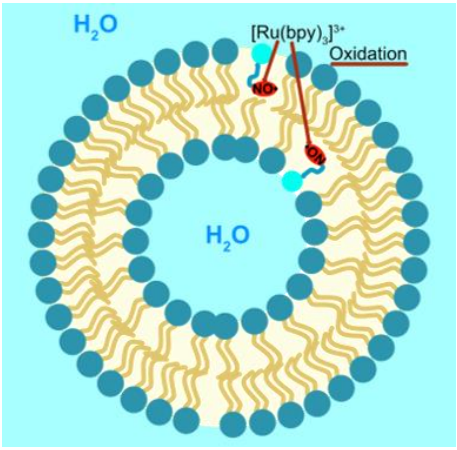

Scheme 3. Schematic representation of the two distance regimes (red lines) for interaction of $[Ru(bpy)_3]^{3+}$ with SNRs embedded in the lipid bilayer.

Our data resemble those describing two regimes for lipid bilayers containing chlorophyll-a, with methyl viologen serving as a water-soluble electron acceptor.[18] To establish the rate constants for ET,[61] the rate constant for the formation of $[Ru(bpy)_3]^{3+}$ and its steady-state concentration under our experimental conditions need to be known. Optical spectroscopy provides these parameters: upon irradiation of $[Ru(bpy)_3]Cl_2$ in the presence of $(NH_4)_2S_2O_8$, we observe a decrease in absorption at 452 nm, reflecting the conversion of $[Ru(bpy)_3]^{2+}$ to $[Ru(bpy)_3]^{3+}$ (Figure 2).[51,62,63] The reappearance of this absorption monitors the oxidation of the SNRs by $[Ru(bpy)_3]^{3+}$ (Eqn. 3, Scheme 2), which we assume to be a second-order reaction in our kinetic model (Supporting Information presents an analysis of the residuals, assuming various kinetic models, and find that a second-order reaction provides the best fit).

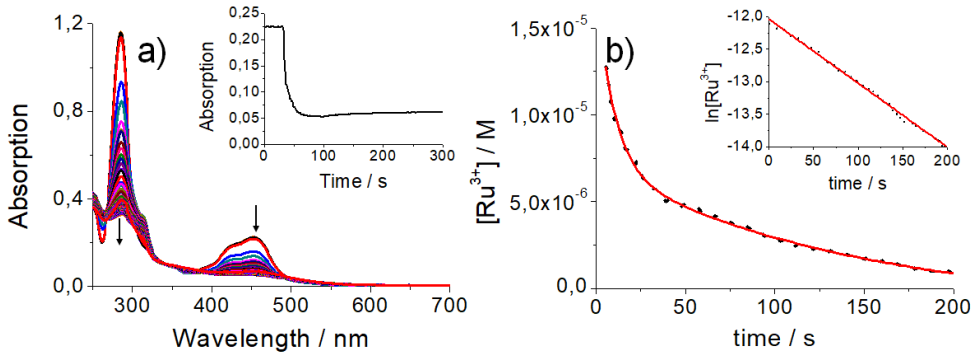

Figure 2. (a) Time-resolved absorption spectra of $[Ru(bpy)_3]Cl_2$ and $(NH_4)_2S_2O_8$ upon constant irradiation in aqueous solution. The inset shows the absorption change at 452 nm; (b) Time vs. concentration profile for the conversion of $[Ru(bpy)_3]^{3+}$ to $[Ru(bpy)_3]^{2+}$ monitored at 452 nm for a reaction mixture containing $[Ru(bpy)_3]Cl_2$, $(NH_4)_2S_2O_8$ and DMPC liposomes into which **16DSA** had been incorporated. Inset: plot of ln($[Ru(bpy)_3]^{3+}$) vs. time, justifying the second-order kinetic model

Using the data in Figure 3, the two-component kinetics for **5DSA** reveal one rate constant rising from 3.6 to 6.2 x 10^5 $M^{-1}s^{-1}$ on going from 275 to 310 K, and a second one increasing from 4.7 to 15 x 10^3 $M^{-1}s^{-1}$ in the same temperature range, thus being two orders of magnitude smaller. Analogously, for **16DSA**, the rate constants change from 1.6 to 3.8 x 10^5 $M^{-1}s^{-1}$, and from 6.8 to 33 x 10^3 $M^{-1}s^{-1}$, respectively (Table 1). These experimental data are in line with molecular dynamics simulations, which indicate that the SNR of **16DSA** penetrates 1 nm deeper into the membrane than **5DSA**.[32]

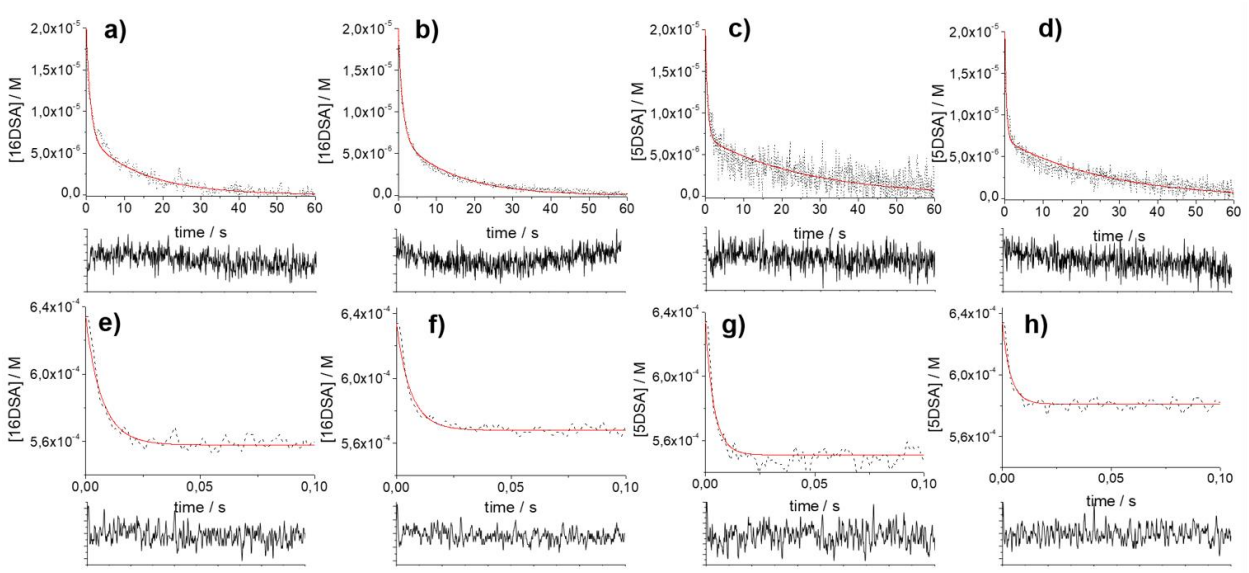

Figure 3. Experimental (black) and simulated (red) decay of the EPR intensity of **16DSA** at 283 K (a) and 304 K (b), and of **5DSA** at 283 K (c) and 304 K (d), embedded in the DMPC bilayer under continuous irradiation; and decay of the EPR intensity of **16DSA** at 283 K (e) and 304 K (f) and of **5DSA** at 283 K (g) and 304 K (h) upon pulse laser irradiation in the presence of $[Ru(bpy)_3]Cl_2$ and $(NH_4)_2S_2O_8$. The corresponding residuals of the fit (expanded view), assuming a second-order reaction, are shown below the decay curves. The different time scales for continuous and pulsed irradiation should be noted.

Table 1. Temperature dependence of the rate constants for the redox reaction between **5DSA** and **16DSA** embedded in the DMPC bilayer and $[Ru(bpy)_3]Cl_2$ and $(NH_4)_2S_2O_8$, using cw- and TR-EPR (exp. error 10% for all rate constants

SNR	T [K]	k_{ET} [$M^{-1}s^{-1}$] cw-EPR		k_{ET} [$M^{-1}s^{-1}$] TR-EPR
		Fast ET/10^5	Slow ET/10^3	Fast ET/10^5
5DSA	275 K	3.6	4.7	2.8
	283 K	4.0	6.0	3.2
	304 K	5.4	6.0	4.8
	310 K	6.2	15	5.6
16DSA	275 K	1.8	6.8	1.7
	283 K	2.0	9.7	2.3
	304 K	2.4	10	2.7
	310 K	3.8	33	4.0

We employed time-resolved EPR and pulsed-laser irradiation to extend our investigations to the microsecond range. In this case, we utilized liposome preparations that contained both external (Scheme 3) and internal $[Ru(bpy)_3]Cl_2$. Under these conditions, we expected to see exclusively one-component kinetics, displaying mainly the rapid reaction components, since the slow ET

component depicted in Scheme 3 is overruled by the faster processes. Indeed, the decay curves for the EPR signals of **16DSA** and **5DSA** (Figure 3e-h and Supporting Information) display only one component. The temperature-dependent rate constants obtained are summarized in Table 1, and are in agreement with those obtained for the fast component in the cw-EPR measurements (see also Supporting Information). We evaluated the temperature-dependent rate constants determined for the fast oxidation of the nitroxyl moieties of **5DSA** and **16DSA** using Eyring theory (see Supporting Information): The corresponding data are presented in and Table 2. The basically identical free activation energies, ΔG‡, of ca. 41 kJ/mol for both SNRs, **5DSA** and **16DSA**, indicate that there is almost no distance dependence in terms of activation barriers.

Table 2. Activation parameters for the fast ET calculated from the cw-EPR and TR-EPR data using the Eyring equation

SNR	$\Delta H^{\ddagger}$ [kJ/mol]		$\Delta S^{\ddagger}$ [J/mol K]		$\Delta G^{\ddagger}$ [kJ/mol]	
	cw-EPR	TR-EPR	cw-EPR	TR-EPR	cw-EPR	TR-EPR
5DSA	8±1	11±1	110±10	110±10	40±4	41±4
16DSA	12±1	11±1	111±9	102±8	42±5	42±5

2.2.5. Discussion

Several mechanisms can be involved in an ET process: tunneling or superexchange of electrons between sites [64,65], adiabatic ET[3,66], in which the medium may play a prominent role, and electron hopping in an organized medium.[3]

For tunneling to occur, the donor and acceptor pairs interact via an electronic coupling matrix element, and low energy barriers have been predicted, and experimentally established. [1–3] Theory predicts that the reaction rate will depend exponentially on the donor/acceptor distance, with characteristic distance coefficients (β) of the order of 10^{-1} nm^{-1}*.[3] Although various factors can lead to deviations from the exponential dependence, e.g. when anisotropic aspects are involved in rigid or semi-rigid systems[67], a general dependence on distance is retained.[68] If we assume that, in our specific case, $[Ru(bpy)_3]^{3+}$ is adsorbed at the interface and is linked to the nitroxide via a fatty acid “bridge”, the rate of ET, assuming a tunneling mechanism, should change by about three orders of magnitude (for β = 0.1 nm^{-1}) on going from **5DSA** to **16DSA**, whereas the change that we observed experimentally is significantly lower.

A second mechanism that may be considered for ET in liposomes is adiabatic ET. It is often characterized by a sensitivity of the ET process to solvent properties, i.e., to reorganization, whether in an isotropic environment[66] or in a micro-heterogeneous medium.[69] In our system, the alkyl chains of DMPC can be regarded as a solvent with very slow reorganization capabilities.[69] It is likely that the dynamics of the alkyl chains (equivalent to solvent relaxation) control the kinetics of ET and slow down the ET rates, which thus are expected to be much slower than in an aqueous solution.[47] However, our data do not display such a decrease in ET rates. Moreover, the temperature dependence does not support an adiabatic mechanism. Involvement of a hopping mechanism appears to be unlikely, because no electroactive component (e.g. an aromatic group) is located between the donor and the acceptor.[70]

None of the above models perfectly accounts for our experimental data. Altogether this suggests that more than one pathway may be responsible for the ET through the lipid bilayer with tunneling being a viable option[14] with a low activation barrier (Table 2). Complex mechanisms have been invoked already in other systems, such as proteins, where the ET process implies a coupling of more than one mechanism, including hopping steps. A general dependence on the distance is retained, but the ET rate is difficult to predict. It has been reported that almost identical ET rates can be found for distances between A/D pairs that differ by as much as 0.5 nm.[3]

Considering the contributions from tunneling, ET rates are governed by three parameters, according to Marcus theory (Equation 4)[2]; the electronic coupling between donor and acceptor H_{DA}, the reaction free energy ΔG^0 and the reorganization energy λ, accounting for changes in solvation and molecular rearrangement following ET.

$$k_{ET} = \sqrt{\frac{4\pi}{h^2 \lambda k_B T}}\, {H_{DA}}^2 \exp\left[-\frac{(\lambda + \Delta G^0)^2}{4\lambda k_B T}\right] \quad (4)$$

ΔG^0 can be predicted from the redox potential of the N-O•/N^+=O ‖ $[Ru(bpy)_3]^{2+}$/$[Ru(bpy)_3]^{2+}$ pair ($\Delta G^0 \approx 0.4$ eV, see Supporting Information), leading to a reorganization energy λ of ca. 2.3 ± 0.5 eV for both SNRs. This is compatible with reorganization energies reported for long-range ET in metalloproteins and donor-acceptor pairs covalently linked by aromatic linkers.[71,72] Using λ, the electronic coupling matrix element HDA amounts to $H_{AD} = 6 \times 10^{-3} \pm 2 \times 10^{-3}$ cm^{-1} for **5DSA** and **16DSA** (see Supporting Information).[73] This agrees with values obtained for electronic coupling matrix elements in long-range ET in proteins.[74,75]

2.2.6. Conclusion

Photo-induced oxidation of the SNRs in **5DSA** and **16DSA** by $[Ru(bpy)_3]^{3+}$ was employed to study ET in the phospholipid bilayers of DMPC liposomes by EPR and optical spectroscopy. Our results show that the rate constants for oxidation of the SNR moieties are mildly distance- and temperature-dependent. They also provide an exclusive insight into long-range ET within a basically undistorted lipid bilayer. The low activation barriers suggest that a tunneling channel is likely. A partial water penetration[70] of the bilayer could also accelerate the electron-transfer process.[29] Our methodology, implemented in this study (Ru/SNR combined with photo-oxidation), can be applied to systematically study biological and artificial membranes, for example to investigate the involvement of π-electrons or/and water bridges in long-range ET.

2.2.7. References

[1] H. B. Gray, J. R. Winkler, *Annu. Rev. Biochem.* **1996**, *65*, 537–561.

[2] R. A. Marcus, N. Sutin, *BBA Rev. Bioenerg.* **1985**, *811*, 265–322.

[3] H. B. Gray, J. R. Winkler, *Proc. Natl. Acad. Sci. U. S. A.* **2005**, *102*, 3534–9.

[4] H. B. Gray, J. R. Winkler, *Q. Rev. Biophys.* **2003**, *36*, 341–372.

[5] C. Chatgilialoglu, C. Ferreri, K. Matyjaszewski, *Chempluschem* **2016**, *81*, 11–29.

[6] B. Giese, *Acc. Chem. Res.* **2000**, *33*, 631–636.

[7] A. Manetto, S. Breeger, C. Chatgilialoglu, T. Carell, *Angew. Chemie - Int. Ed.* **2005**, *45*, 318–321.

[8] D. Astruc, *Nat. Chem.* **2012**, *4*, 255–267.

[9] M. Grätzel, in *Heterog. Photochem. Electron Transf.*, CRC Press, **1989**, pp. 43–86.

[10] D. Gust, T. A. Moore, A. L. Moore, *Acc. Chem. Res.* **2001**, *34*, 40–48.

[11] S. Fukuzumi, K. Ohkubo, T. Suenobu, *Acc. Chem. Res.* **2014**, *47*, 1455–1464.

[12] J. N. Robinson, D. J. Cole-Hamilton, *Chem. Soc. Rev.* **1991**, *20*, 49.

[13] P. Nicholls, J. West, A. D. Bangham, *Biochim. Biophys. Acta* **1974**, *363*, 190–201.

[14] M. Woodle, J. W. Zhang, D. Mauzerall, *Biophys. J.* **1987**, *52*, 577–586.

[15] K. I. Zamaraev, S. V Lymar, M. I. Khramov, *Pure Appl. Chem.* **1988**, *60*, 1039–1046.

[16] W. E. Ford, G. Tollin, *Photochem. Photobiol.* **1982**, *36*, 647–655.

[17] M. Tomkiewicz, G. A. Corker, *Chem. Phys. Lett.* **1976**, *37*, 537–542.

[18] W. E. Ford, G. Tollin, *Photochem. Photobiol.* **1982**, *35*, 809–819.

[19] G. M. El Maghraby, B. W. Barry, A. C. Williams, *Eur. J. Pharm. Sci.* **2008**, *34*, 203–222.

[20] G. Sessa, G. Weissmann, *J. Lipid Res.* **1968**, *9*, 310–318.

[21] C. Ferreri, C. Chatgilialoglu, in *Membr. Lipidomics Pers. Heal.*, **2015**, pp. 300–302.

[22] A. Dalzini, C. Bergamini, B. Biondi, M. De Zotti, G. Panighel, R. Fato, C. Peggion, M. Bortolus, A. L. Maniero, *Sci. Rep.* **2016**, *6*, 1–14.

[23] W. E. Ford, J. W. Otvos, M. Calvin, *Proc. Natl. Acad. Sci.* **1979**, *76*, 3590–3593.

[24] J. K. Hurley, F. Castelli, G. Tollin, *Photochem. Photobiol.* **1980**, *32*, 79–86.

[25] T. Matsuo, K. Takuma, Y. Tsutsui, T. Nishijima, *J. Coord. Chem.* **1980**, *10*, 187–193.

[26] A. Warshel, D. W. Schlosser, *Proc. Natl. Acad. Sci. U. S. A.* **1981**, *78*, 5564–5568.

[27] E. Tsuchida, M. Kaneko, H. Nishide, M. Hoshinof, *J. Phys. Chem.* **2002**, *90*, 2283–2284.

[28] K. C. Hwang, D. Mauzerall, *Nature* **1993**, *361*, 138–140.

[29] B. Limburg, E. Bouwman, S. Bonnet, *Chem. Commun.* **2015**, *51*, 17128–17131.

[30] A. Kyrychenko, A. S. Ladokhin, *J. Phys. Chem. B* **2013**, *117*, 5875–5885.

[31] W. L. Hubbell, H. M. McConnell, *Proc. Natl. Acad. Sci. U. S. A.* **1969**, *63*, 16–22.

[32] W. L. Hubbell, H. M. McConnell, *J. Am. Chem. Soc.* **1971**, *93*, 314–326.

[33] G. Mobbili, E. Crucianelli, A. Barbon, M. Marcaccio, M. Pisani, A. Dalzini, E. Ussano, M. Bortolus, P. Stipa, P. Astolfi, *RSC Adv.* **2015**, *5*, 98955–98966.

[34] E. Laudadio, R. Galeazzi, G. Mobbili, C. Minnelli, A. Barbon, M. Bortolus, P. Stipa, B. Bianche, *ACSOmega* **2019**, DOI 10.1021/acsomega.8b03395.

[35] A. Bedini, E. De Laurentiis, B. Sur, V. Maurino, C. Minero, M. Brigante, G. Mailhot, D. Vione, *Photochem. Photobiol. Sci.* **2012**, *11*, 1445–1453.

[36] J. F. Nagle, *Annu. Rev. Phys. Chem.* **1980**, *31*, 157–196.

[37] J. H. Fendler, *Chem. Rev.* **1987**, *87*, 877–899.

[38] E.-S. Wu, K. Jacobson, D. Papahadjopoulos, *Biochemistry* **1977**, *16*, 3936–3941.

[39] I. Tabushi, I. Hamachi, Y. Kobuke, *Tetrahedron Lett.* **1987**, 5899–5902.

[40] J. S. . Dua, A. C. . Rana, A. K. Bhandarim, *Int. J. Pharm. Stud. Res.* **2012**, *3*, 14–20.

[41] D. Orthaber, A. Bergmann, O. Glatter, *J. Appl. Crystallogr.* **2000**, *33*, 218–225.

[42] O. Glatter, *J. Appl. Crystallogr.* **1979**, *12*, 166–175.

[43] O. Glatter, *J. Appl. Crystallogr.* **1977**, *10*, 415–421.

[44] T. Frühwirth, G. Fritz, N. Freiberger, O. Glatter, *J. Appl. Crystallogr.* **2004**, *37*, 703–710.

[45] H. Schnablegger, O. Glatter, *Appl. Opt.* **1991**, *30*, 4889–96.

[46] L. M. Weiner, *Appl. Magn. Reson.* **2007**, *31*, 357–373.

[47] T. Eliash, A. Barbon, M. Brustolon, M. Sheves, I. Bilkis, L. Weiner, *Angew. Chemie - Int. Ed.* **2013**, *52*, 8689–8692.

[48] A. Barbon, M. Bortolus, A. A. Isse, V. A. Reznikov, L. Weiner, *Chem. Phys. Lett.* **2016**, *665*, 137–140.

[49] W. E. Ford, M. A. J. Rodgers, *J. Phys. Chem. B* **1997**, *101*, 930–936.

[50] K. Henbest, P. Douglas, M. S. Garley, A. Mills, *J. Photochem. Photobiol. A Chem.* **1994**, *80*, 299–305.

[51] N. D. Morris, M. Suzuki, T. E. Mallouk, *J. Phys. Chem. A* **2004**, *108*, 9115–9119.

[52] M. Brustolon, E. Giamello, *Electron Paramagnetic Resonance: A Practitioner's Toolkit*, Wiley, **2009**.

[53] D. Marsh, in *Membr. Spectrosc.* (Ed.: E. Grell), Springer, **1981**, pp. 51–142.

[54] E. Conte, F. Maria, H. Khandelia, G. Jeschke, E. Bordignon, *BBA - Biomembr.* **2013**, *1828*, 510–517.

[55] W. K. Subczynski, M. Raguz, J. Widomska, *Methods Mol. Biol.* **2010**, *606*, 247–269.

[56] S. Stoll, A. Schweiger, *J. Magn. Reson.* **2006**, *178*, 42–55.

[57] E. Etienne, N. Le Breton, M. Martinho, M. Mileo, V. Belle, *Magn. Reson. Chem.* **2017**.

[58] J. M. Boggs, J. C. Hsia, *Proc. Natl. Acad. Sci. U. S. A.* **1973**, *70*, 1406–9.

[59] P. Jost, L. J. Libertini, V. C. Hebert, O. H. Griffith, *J. Mol. Biol.* **1971**, *59*, 77–98.

[60] D. O. Nettleton, P. D. Morse, J. W. Dobrucki, H. M. Swartz, N. J. F. Dodd, *BBA - Biomembr.* **1988**, *944*, 315–320.

[61] S. Hoops, R. Gauges, C. Lee, J. Pahle, N. Simus, M. Singhal, L. Xu, P. Mendes, U. Kummer, *Bioinformatics* **2006**, *22*, 3067–3074.

[62] A. Juris, V. Balzani, F. Barigelletti, S. Campagna, P. Belser, A. von Zelewsky, *Coord. Chem. Rev.* **1988**, *84*, 85–277.

[63] K. Kalyanasundaram, M. Grätzel, M. K. Nazeeruddin, *J. Phys. Chem* **1992**, 5865–5872.

[64] A. Ponce, H. B. Gray, J. R. Winkler, *J. Am. Chem. Soc.* **2000**, *122*, 8187–8191.

[65] O. S. Wenger, B. S. Leigh, R. M. Villahermosa, H. B. Gray, J. R. Winkler, *Science (80-.).* **2005**, *307*, 99–102.

[66] A. Polimeno, A. Barbon, P. L. Nordio, W. Rettig, *J. Phys. Chem.* **1994**, *98*, 12158–12168.

[67] S. Antonello, F. Formaggio, A. Moretto, C. Toniolo, F. Maran, *J. Am. Chem. Soc.* **2003**, *125*, 2874–2875.

[68] M. D. Newton, *J. Electroanal. Chem.* **1997**, *438*, 3–10.

[69] R. B. Pansu, K. Yoshihara, *J. Phys. Chem.* **1991**, *95*, 10123–10133.

[70] A. B. Ricks, K. E. Brown, M. Wenninger, S. D. Karlen, Y. A. Berlin, D. T. Co, M. R. Wasielewski, *J. Am. Chem. Soc.* **2012**, *134*, 4581–4588.

[71] J. R. Winkler, H. B. Gray, *Chem. Rev.* **2014**, *114*, 3369.

[72] M. Kuss-Petermann, O. S. Wenger, *J. Am. Chem. Soc.* **2016**, *138*, 1349–1358.

[73] J. Sukegawa, C. Schubert, X. Zhu, H. Tsuji, D. M. Guldi, E. Nakamura, *Nat. Chem.* **2014**, *6*, 899–905.

[74] J. S. Kretchmer, N. Boekelheide, J. J. Warren, J. R. Winkler, H. B. Gray, T. F. Miller, *Proc. Natl. Acad. Sci.* **2018**, *115*, 6129–6134.

[75] P. Siddarth, R. A. Marcus, *J. Phys. Chem.* **1993**, *97*, 13078–13082.

3. Publications on the Reactivity of Radical Photoinitiators

3.1. Extending the Scope of Bis(acyl)phosphane Oxides: Additional Derivatives

Anna Eibel,[a] Max Schmallegger,[a] Michal Zalibera,[a], [b] Alex Huber,[c] Yasmin Bürkl,[a] Hansjörg Grützmacher,*[c] and Georg Gescheidt*[a]

[a] Institute of Physical and Theoretical Chemistry, Graz University of Technology
[b] Institute of Physical Chemistry and Chemical Physics, Slovak University of Technology in Bratislava
[c] Laboratory of Inorganic Chemistry, ETH Zurich

Published in: *European Journal of Inorganic Chemistry* **2017**, 18, 2469–2478.

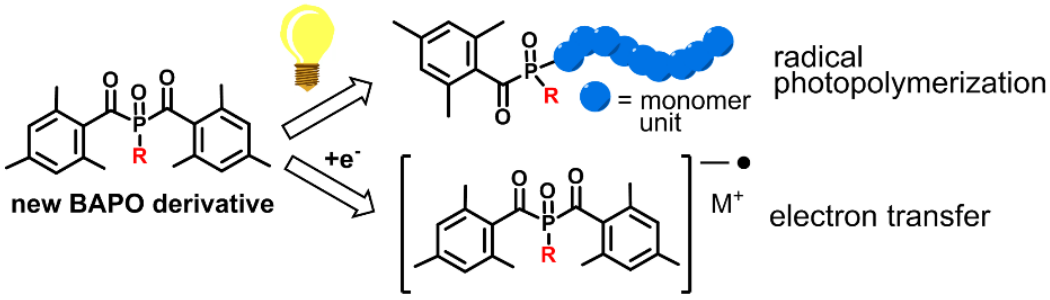

3.1.1. Abstract

A series of novel bis(acyl)phosphane oxide (BAPO) photoinitiators has been synthesized and tested with respect to their efficiency in the initiation step of radical photopolymerizations. The transient absorption spectra of the phosphanoyl radicals obtained upon laser-flash photolysis reveal maxima at ca. 450 – 460 nm. Rate constants for the addition of these radicals to the double bonds of butyl acrylate, methyl methacrylate, 1-vinyl-2-pyrrolidone and styrene have been determined. All phosphanoyl radicals have been found to react most rapidly with styrene and slowest with butyl acrylate. Low fluorescence quantum yields of 0.1–0.3% reveal, that the studied BAPOs undergo efficient intersystem crossing followed by α-cleavage. The heat profiles of selected photo-polymerizations have been observed using a high-resolution infrared camera. Thermal imaging experiments show substantial monomer-dependent exothermicity. All BAPO derivatives can additionally act as electron acceptors as indicated by cyclic voltammetry and EPR spectroscopy.

3.1.2. Introduction

Bis(acyl)phosphane oxides (BAPOs) have been among the most successful initiators for photo-induced radical polymerizations.[1–5] Photolysis of BAPOs leads to the formation of a phosphanoyl and a mesitoyl radical via triplet-state α-cleavage with high quantum yields (Scheme 1).[6,7] Both radicals are efficient in initiating radical polymerizations. Still, enhancing the scope of BAPOs in terms of specific excitation wavelengths and solubility remains a challenge. To this end, several modifications, particularly at the phenyl substituents of the benzoyl moieties have been introduced.[1] Advanced synthetic protocols however allow to attach various groups directly at the phosphorus atom of BAPOs.[5,8–11] Here, we introduce five novel BAPO derivatives and besides describing their synthesis, we report on their optical spectra, *α*-cleavage reactions, the kinetics of their addition to double bonds, reduction potentials, and the EPR spectra of selected one-electron reduced species.

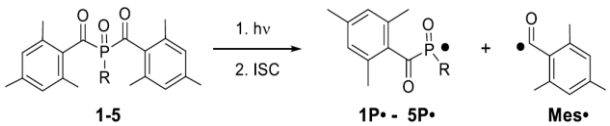

Scheme 1. Photolysis of BAPO derivatives **1**–**5** to give phosphanoyl radicals **1P•**–**5P•** and the mesitoyl radical **Mes•**. For the substituents R, see Scheme 2.

3.1.3. Results and Discussion

Synthesis and Characterization of BAPOs 1–5 The new BAPO derivatives **1**–**5** were synthesized as shown in Scheme 2 using a synthesis method which we reported briefly in a previous communication.[5] The readily available sodium bis(mesitoyl)phosphide, Na[P(COMes)$_2$] (Mes = 2,4,6-trimethylphenyl) is reacted with a hydrocarbon halide, R-X, in dimethoxyethane (DME) as solvent in a temperature range between 25 °C and 60 °C to give cleanly the corresponding bis(acyl)phosphanes, R-P(COMes)^2, which are characterized by their characteristic ^{31}P NMR chemical shifts in the range from 40 – 70 ppm [R = 1-phenylethyl: ^{31}P NMR δ = 71.1 ppm; R = 1-naphtylmethyl: ^{31}P NMR δ = 52.9 ppm; R = 2-(2-methoxyethoxy)ethyl: ^{31}P NMR δ = 44.9 ppm; R = 3-bromopropyl: ^{31}P NMR δ = 48.5 ppm; R = 3-(triethoxysilyl)propyl: ^{31}P NMR δ = 50.8 ppm]. In some cases, longer reaction times are needed in order to achieve complete conversion. These bis(acyl)phosphanes were subsequently oxidized without prior isolation to give the bis(acyl)phosphane oxides **1**–**5** in mostly excellent overall yields. The oxidation of (EtO)$_3$Si- (CH$_2$)$_3$-P(COMes)$_2$ with H_2O_2 requires a solvent change from DME to toluene and careful removal of sodium iodide by extraction of the organic with aqueous potassium carbonate in order to achieve a satisfactory yield (63%) of **5** as wax-like yellow solid. The BAPO derivatives **1** and **2** are yellow solids with melting points at 178 °C and 119 °C, respectively, while **3**–**4** are obtained as yellow viscous oils. All compounds are thermally stable at least up to 150 °C. The molecular structure of the 1-phenylethylderivative **1** was determined by X-ray diffraction with single crystals. A plot is shown in Figure 1. The unit cell of **1** contains both enantiomers of which only the R-enantiomer is shown. These two molecules interact via intermolecular π- stacking between the mesityl rings which are at about 3.7 Å distance from each other. As also observed for other BAPOs[5] and the commercially available Irgacure® 819[12] the distances between the carbon centers of the COMes groups and the phosphorus atom are unusually long [P1-C11

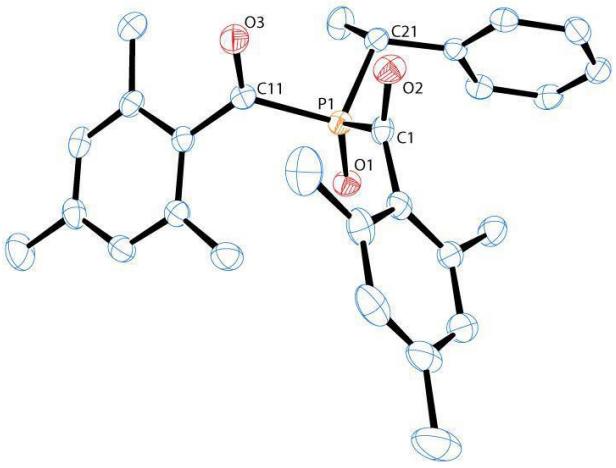

1.905(2) Å, P1-C1 1.895(1) Å] and even longer than the P-C21 bond [1.832(2) Å] although the latter contains a sp^3 valence electron hybridized carbon center while the acyl groups contain sp^2 carbons to which shorter bonds are expected. In contrast to other BAPO derivatives which show skewed arrangements between the P=O unit and the COMes groups, the COMes groups in **1** are in almost parallel arrangement and point to the opposite direction with respect to the central P=O unit.

Figure 1. Plot of the structure of **1**. Thermal ellipsoids are shown at a 50% probability level. For clarity, hydrogen atoms are omitted.

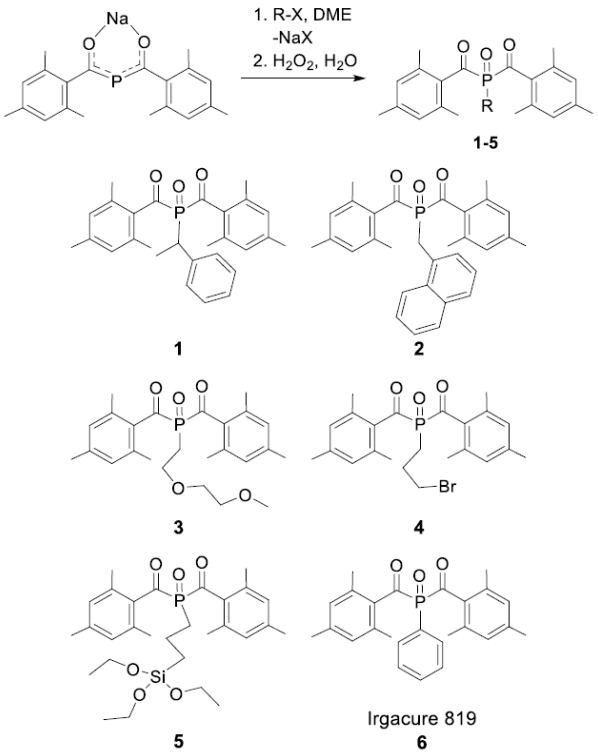

Scheme 2. Synthesis and skeletal diagrams of BAPOs **1–5** and of commercially available BAPO Irgacure® 819 (**6**).

Spectroscopic Investigations

Absorption and Emission Spectra. Figure 2 displays the UV-VIS absorption spectra of compounds **1**–**5** with intense π-π* absorptions around 315 -320 nm (**1-4**) and around 300 nm (**5**) and with distinct weak bands above 350 nm. The latter ones are attributable to *n*-π* transitions, responsible for an *α*-cleavage between the P(O)–C(O) bond leading to phosphanoyl (**1P•**–**5P•**) and mesitoyl (**Mes•**) radicals (Scheme 1). Derivative **1** exhibits a band at 375 nm and the highest-

wavelength *n*-π* transition at 435 nm, higher than that of the well-established commercially available BAPO **6** (*ca*. 420 nm).[2] Naphthalene derivative **2** shows a somehow similar spectral shape as **1** whereas **3**–**5** possess less structured broad bands reaching to 430 nm. This observation shows that the substitution with a π system, which is separated from the P atom by a non-conjugating methylene group has a slight but not extended influence on the long-wave absorption of BAPOs. The substituents connected to the phosphorus center in **3**–**5** *via* sp^3 carbon atoms behave essentially in an identical way (Figure 2, top). To test if the π substituents in **1** and **2** alter the photophysical reaction pathways in terms of allowing an extended reactivity in the singlet state, we have measured fluorescence spectra. Using an excitation wavelength of 373 nm, **1**–**4** show fluorescence with almost identical Stokes shifts at *ca*. 455 nm and very low quantum yields substantially below 0.4% (Figure 2, bottom and Table 1).

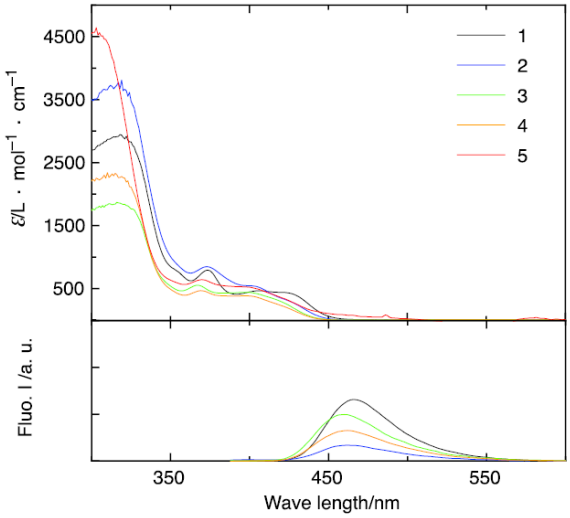

Figure 2. Top: UV-Vis absorption spectra of compounds **1**–**5** (two weak peaks in the spectrum of compound **5** at 486 nm and 582 nm are due to spectrometer artifacts); bottom: fluorescence emission spectra in acetonitrile normalized by absorbance at the excitation wavelength (373 nm). For fluorescence measurements, the absorbance of the solutions was kept at ca. 0.1 to avoid inner filter effects.

In contrast to **1**–**4**, BAPO **5** showed no detectable fluorescence, indicating that the excited singlet state of **5** preferentially reacts via intersystem crossing to the excited triplet state, or via internal conversion. Table 1 summarizes the fluorescence quantum yields (Φ_F) of **1**–**4** determined by comparison with the known quantum yield of 9,10-diphenylanthracene (Φ_{ST} = 0.95 in cyclohexane) according to standard procedure.[13] These results correspond to those obtained for related BAPOs and mono(acyl)phosphane oxides (MAPOs).[6] Accordingly, for **1**–**5** efficient intersystem crossing and subsequent *α*-cleavage can be expected.

Table 1. Fluorescence quantum yields (Φ_F) of **1–5** in acetonitrile solutions (A ≤ 0.1)

Compound[]	Fluorescence quantum yield Φ_F (%)
1	0.314 ± 0.026
2	0.105 ± 0.001
3	0.286 ± 0.003
4	0.199 ± 0.005
5[a]	–

[a] no detectable fluorescence

Phosporous-centered Radicals and their Reactivity. Figure 3 shows transient optical absorption spectra obtained upon irradiation of **1**–**5** with a Nd-YAG laser at 355 nm.

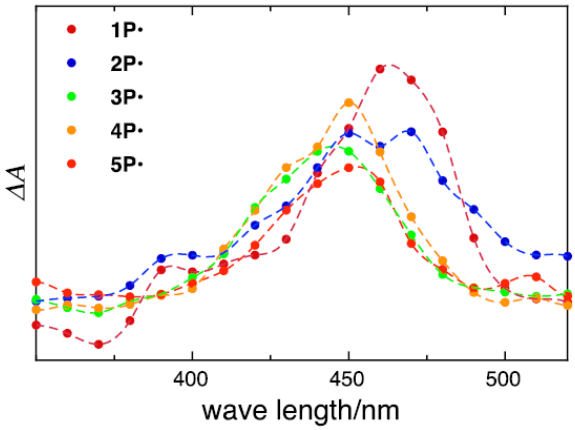

Figure 3. Transient optical absorption spectra (absorbance change *ΔA* versus wavelength) of phosphanoyl radicals **1P•–5P•** recorded 200 – 300 ns after laser excitation (355 nm, 8 ns) of **1–5** in argon-saturated acetonitrile solutions (absorbance at 355 nm ~ 0.3).

The bands centred at ca. 450 nm with lifetimes at a microsecond time scale are attributable to the phosphanoyl radicals **1P•–5P•**. Benzoyl-derived radicals like the mesitoyl radical **Mes•** do not reveal distinct absorptions in the VIS range and can only be observed by time-resolved IR and EPR spectroscopy.[14,15] The absorption peaks around 450 – 460 nm are in agreement with the spectra of related BAPO-based phosphanoyl radicals.[7,16]

The distinct absorptions of the phosphorus-centered radicals **1P•–5P•** allowed us to determine the rate constants for their addition to butyl acrylate, methyl methacrylate, 1-vinyl-2-pyrrolidone and styrene via pseudo-first-order kinetic analysis. Exponential fitting of the time decay traces obtained at various quencher concentrations, which were significantly higher than those of the

radicals, yielded the pseudo-first-order rate constants (k_{exp}).[7] The second order addition rate constants ($k_{monomer}$) are obtained from the slopes of their linear dependence on the monomer concentration. The corresponding curves are shown in Figure 4 for **1P•** (for **2P•–5P•** see the Supporting Information).

The addition rate constants for **1P•–5P•** are summarized in Table 2 and Figure 5. Generally, the reactivity toward the monomers increases in the following order: butyl acrylate < methyl methacrylate < 1-vinyl-2-pyrrolidone < styrene. The highest reactivity with the most electron-rich alkene (styrene) suggests that phosphanoyl radicals show electrophilic behavior and prefer to react with electron rich quenchers.

In Table 2, the data for the novel compounds **1P•–5P•** are compared with the rate constants previously determined for radicals **6P•** and **$Ph_2P(O)$•**, which are obtained by photolysis of commercially available Irgacure® 819 and Lucirin TPO®, respectively.

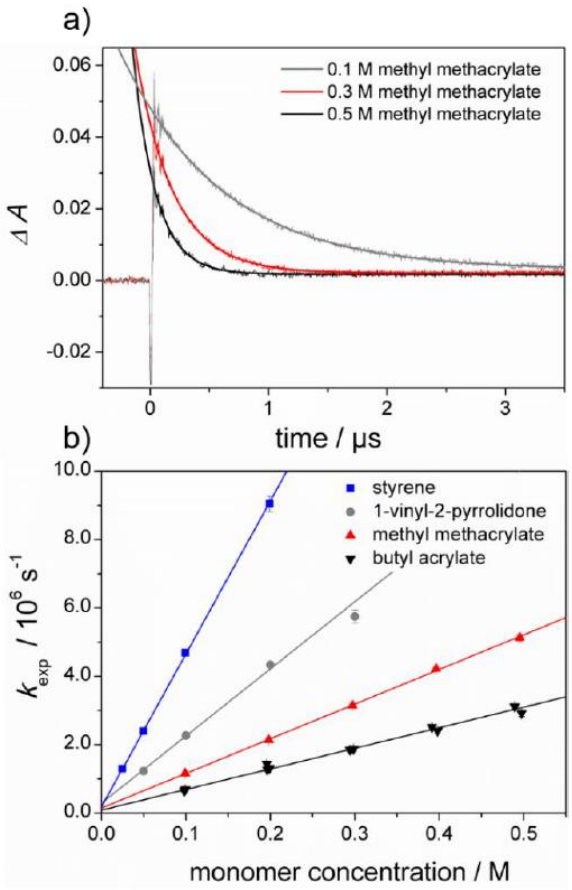

Figure 4. a) Decay traces for radical **1P•** in the presence of methyl methacrylate at three different concentrations (0.1 M, 0.3 M and 0.5 M) recorded following LFP of argon-saturated solutions of

1 in acetonitrile (excitation wavelength: 355 nm, monitoring wavelength: 465 nm; absorbance at 355 nm ~ 0.3). Experimental rate constants are obtained from exponential fitting of the time traces. b) Plots of the experimental rate constants k_{exp} of **1P•** versus monomer concentrations. Second order addition rate constants $k_{monomer}$ are obtained from the slopes.

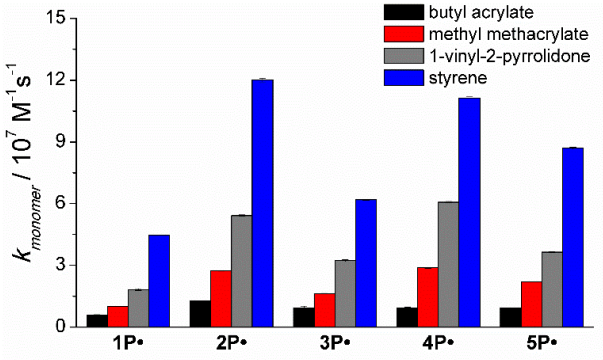

Figure 5. Second-order rate constants $k_{monomer}$ for the addition of the phosphanoyl radicals 1P•–5P• to butyl acrylate, methyl methacrylate, 1-vinyl-2-pyrrolidone, and styrene.

Table 2. Second-order rate constants for the addition of phosphanoyl radicals **1P•**–**5P•** to monomers and comparison with radicals **6P•** and Ph_2PO•. Errors are reported as twice the standard deviation from least squares analysis of the data.

	$k_{monomer}$ / 10^7 (M^{-1} s^{-1})			
	butyl acrylate	methyl methacrylate	1-vinyl-2-pyrrolidone	styrene
1P•	0.58 ± 0.02	1.01 ± 0.01	1.83 ± 0.04	4.45 ± 0.02
2P•	1.28 ± 0.02	2.73 ± 0.02	5.42 ± 0.04	12.0 ± 0.10
3P•	0.92 ± 0.10	1.63 ± 0.02	3.23 ± 0.06	6.19 ± 0.04
4P•	0.93 ± 0.05	2.88 ± 0.06	6.07 ± 0.08	11.1 ± 0.13
5P•	0.94 ± 0.01	2.19 ± 0.01	3,64± 0.07	8.69 ± 0.09
6P•	1.1[a] 0.87 ± 0.02[b] 2.8[a]	–	–	–
Ph_2PO•	1.98 ± 0.06[b]	–	–	–

[a] Reference [7]. [b] Reference [17]

TR-EPR and 31P CIDNP-NMR Spectroscopy. The structure-reactivity relationship of phosphanoyl radicals is influenced by the s-orbital character at the phosphorus center as well as by steric factors.[7,17–20] The ^{31}P hyperfine coupling constants (hfc), determined by (time-resolved) EPR, present insights into the s-orbital of the P center. Generally, the bigger the ^{31}P hfc gets, the higher the s-orbital character of the spin carrying orbital and the more efficient is the addition of

the P-centered radical to an acrylate double bond. This can be traced back to a correlation between the s-orbital character of the P-centered radical and the ^{31}P hfc.[17,21] BAPOs with alkyl substituents at the phosphorus atom generally reveal ^{31}P hfcs of *ca*. 25–27 mT.[17] Upon laser-flash photolysis (355 nm) of **1**, we have obtained the time-resolved EPR (TR-EPR, CIDEP) spectrum shown in Figure 6. It closely resembles the CIDEP spectra of related BAPOs recorded in the 50 ns time regime.[7,14,17,22] The phosphorus centred radical **1P•** gives rise to a doublet signal with a 31P hfc of 24.3 mT (g = 2.0042; calc. 31P hfc: 21.6 mT, see Supporting Information), whereas the mesitoyl radical **Mes•** appears as a rather narrow unresolved signal (g = 2.0005) in between the lines of the 31P doublet (Figure 6).

DFT calculations indicate that P-centered radicals **2P•–5P•** possess electronic structures rather closely resembling those of **1P•** (see Supporting Information). We therefore assume that the differences of the addition constants for **1P•–5P•** (Figure 5) can be traced back to steric factors. Radical **1P•** is very likely the sterically most congested radical, caused by the methyl and phenyl substituent at the sp^3 carbon center next to the phosphorus atom, contributing to the lower reactivity toward double bonds.

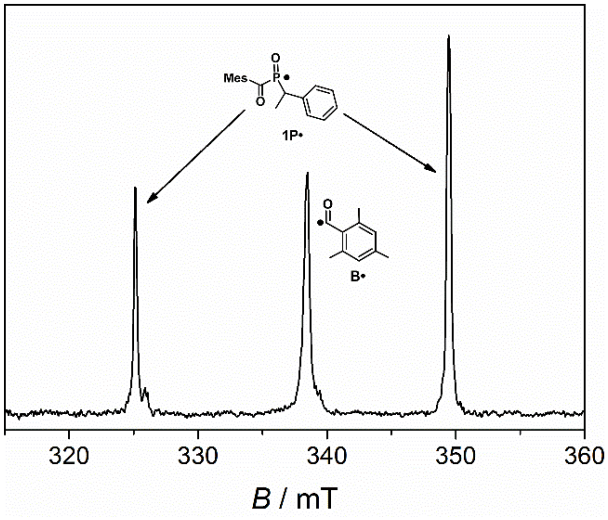

Figure 6. TR-EPR spectrum observed between 200-300 ns after laser flash photolysis (355 nm) of **1** (15 mM solution in toluene), ^{31}P hfc: 24.3 mT (microwave frequency: 9.474 GHz).

The α-cleavage of the photoinitiators **1–5** and the corresponding follow-up reactions can be conveniently followed using ^{31}P CIDNP spectroscopy. This NMR-based method provides information about reaction products formed via radical pairs.[22] Radical-pair-based phenomena lead to enhanced absorptive or emissive NMR signals of reaction products, caused by a non-Boltzmann population of magnetic energy levels. Figure 7 illustrates the products detected via ^{31}P CIDNP after photolysis of **2**.

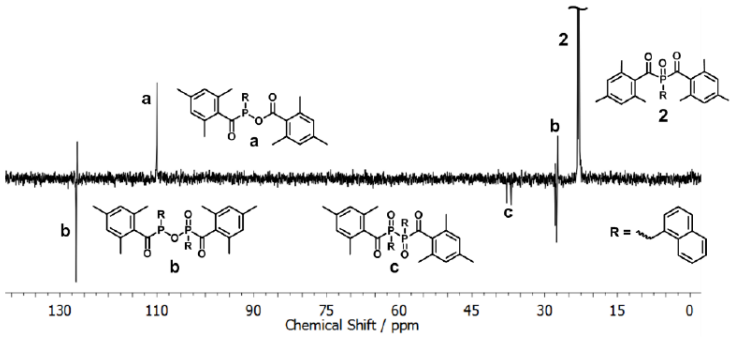

Figure 7. ^{31}P CIDNP-NMR spectrum of **2** in argon-saturated C_6D_6 (30° RF pulse; laser excitation at 355 nm, 60 mJ/pulse, 4 ms inter-pulse delay).

The radical pair **Mes•/P2•** can recombine regenerating the parent compound **2**. The benzoyl and the phosphanoyl radical may also form product **a** via P–O bond formation. Two phosphanoyl radicals **P2•** either yield **b** or **c** when reacting either via P,P or P,O recombination (Scheme 3). This reactivity pattern is general for all derivatives **1**–**5** (see Supporting Information for further spectra) and follows that reported for related photoinitiators.[4,23]

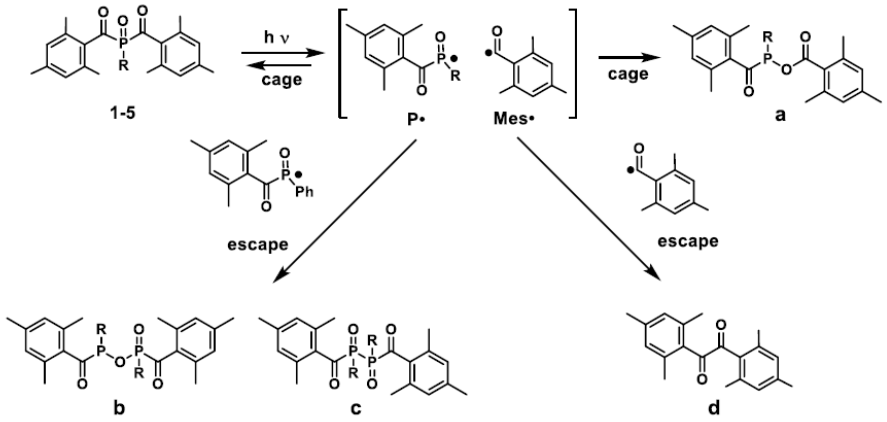

Scheme 3. Reaction pattern of the primary radicals **P•** and **Mes•**.

Following Polymerizations with a Thermal Camera. Another approach to explore the reactivity of BAPOs **1–5** was to follow the development of heat produced during polymerization reactions using a high-resolution infrared camera.[24] Argon-saturated samples were successively irradiated with UV light pulses (1s, 5s and 10s) while thermal videos were recorded. The lamp was positioned above the sample to avoid the heating of the glass vial along the path of the camera. Selected thermograms of the polymerization of butyl acrylate initiated by compound **3** are shown

in Figure 8a,b. For comparison, a reference sample containing only butyl acrylate in acetonitrile was prepared, showing a basically uniform low temperature upon irradiation (see the Supporting Information). However, when the sample contains the photoinitiator and butyl acrylate, substantial heating is detected (red, yellow color, Figure 8a,b). The corresponding heat profiles (temperature change vs. time, Figure 8c) show an increase in temperature with increasing irradiation periods (1s, 5s and 10s). Three positions in the solution volume (top, center and bottom) were chosen to monitor the temperature change. Figure 8c shows that the heat distribution within the sample is almost uniform. This might be due to the short light path of approximately 2 cm. The temperature changes are significantly more pronounced for the sample containing butyl acrylate than for methyl methacrylate, which is in line with the enthalpy for the addition of butyl acrylates to C-centered radicals being higher than for methyl methacrylate.[25] This indicates that the observed heat development is mainly caused by the exothermic polymerization chain growth rather than by the initiating process.

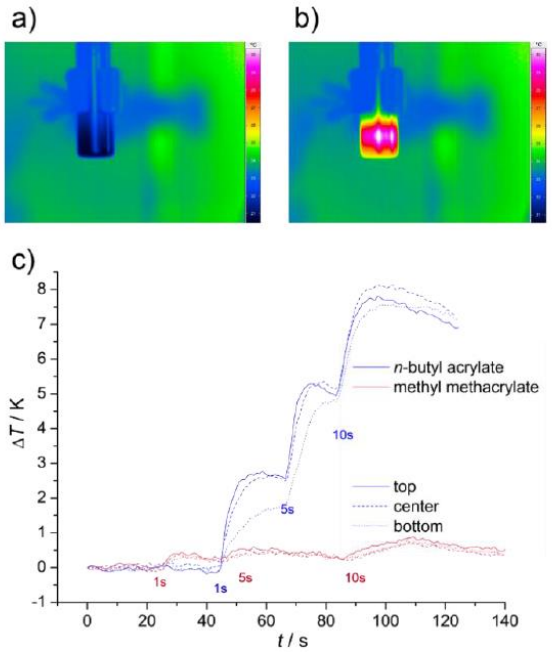

Figure 8. a,b) Glass vial containing a 1 mM solution of **3** in acetonitrile and butyl acrylate (1:1 v/v ratio) before (a) and after (b) 10 s irradiation with a Hg-Xe UV lamp. The line in the middle of the sample is caused by reflection. c) Plots of temperature change ΔT versus time t ($\Delta T = T_t - T_{initial}$). The three line styles represent the temperatures at the top, the center and the bottom of the sample volume, where the temperature was sampled. The irradiation times are indicated in the plot.

One-Electron Reduction Reactions of 1-5. Beside serving as photoinitiators, BAPO and MAPO derivatives have been shown to serve as electron-transfer-active agents, in particular revealing (quasi) reversible one-electron reductions.[26]. Accordingly, we have recorded cyclic voltammograms of **1–5** (see Figure 9 and the Supporting Information). For all derivatives, we were able to observe quasi-reversible reduction steps (except **5**, see Table 3), whereas no distinguishable signals occurred in the oxidative region. The one-electron reduction potentials of **1**–**4**, leading to the formation of the corresponding radical anions reveal a rather narrow range between -1.75 V and –1.81 V (vs. Fc+/Fc). Accordingly, the aromatic substituents, which are separated by sp^3 C-centers from the P atom hardly influence the electron donating/accepting properties of BAPOs. Reductions with a K-metal mirror in THF under high vacuum led to well distinguishable EPR spectra attributed to **1**$^{\bullet-}$–**5**$^{\bullet-}$ (Figure 10 and Supporting Information). The spectra are dominated by 31P hfc of *ca*. 2.2 mT for all radical anions (Table 4). These values closely resemble those obtained for **6** and related derivatives.[26] . This reveals that, as in the case of the P-centered radicals **1P•**–**5P•**, the delocalization of the charge and the spin in **1**$^{\bullet-}$–**5**$^{\bullet-}$ is basically confined to the acyl (mesitoyl) substituents and character of the additional substituents at the P(V) center does not have a marked effect on the electronic properties in **1**–**5** at the radical-anion stage.

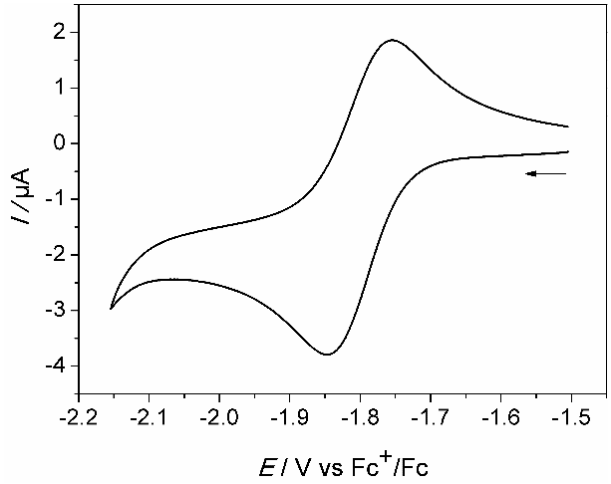

Figure 9. Cyclic voltammogram of **1** (1 mM in acetonitrile, supporting electrolyte: 0.1 M tetrabutylammonium tetrafluoroborate), recorded using a Pt working electrode, Pt counter electrode and Ag pseudo-reference electrode (100 mVs–1 scan rate). Potentials are given vs. Fc^+/Fc. The direction of the potential sweep is indicated by the arrow.

Table 3. Reduction potentials and CV peak separations for **1–5** and comparison with BAPO **6** (all values vs. Fc^+/Fc)

	1	**2**	**3**[c]	**4**	**5**[d]	**6**[c]
$E_{1/2}$ [V vs. Fc^+/Fc][a]	–1.80	–1.77	–1.81[b]	–1.80	–	–1.86
ΔE_p [V][b]	0.10	0.16	0.097[b]	0.14	–	0.089

[a] $E_{1/2} = (E_{pc} + E_{pa})/2$, E_{pc} and E_{pa} are cathodic and anodic peak potentials, respectively. [b] $\Delta E_p = (E_{pa} - E_{pc})$. [c] Data from ref.[26] [d] Reduction waves are not clearly distinguishable.

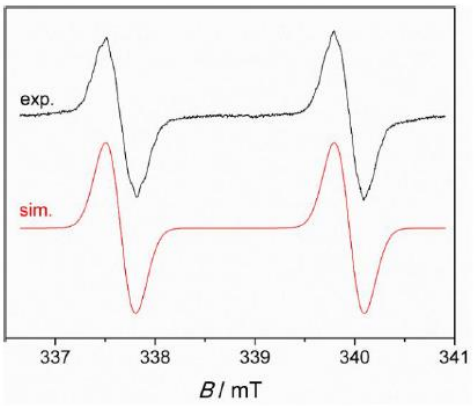

Figure 10. EPR spectrum of **2** obtained after K-metal reduction in THF (T = 200 K), together with its simulation (microwave frequency: 9.473 GHz).

Table 4. ^{31}P hfcs and g factors determined for $\mathbf{1}^{\bullet-}$–$\mathbf{5}^{\bullet-}$ compared to $\mathbf{6}^{\bullet-}$

	$\mathbf{1}^{\bullet-}$	$\mathbf{2}^{\bullet-}$	$\mathbf{3}^{\bullet-}$	$\mathbf{4}^{\bullet-}$	$\mathbf{5}^{\bullet-}$	**6**[a]
^{31}P hfc [mT]	2.24	2.29	2.19	2.18	2.22	2.20
g factor	2.004 ± 0.001	2.004 ± 0.001	2.004 ± 0.001	2.004 ± 0.001	2.004 ± 0.001	2.004

[a] Taken from ref.[26].

3.1.4. Conclusions

We have shown that the presented synthetic procedure allows a very convenient access to a variety of new P-substituents in bis(acyl)phosphane oxides. This approach can be used to adjust the hydrophilicity or lipophilicity of BAPO derivatives or allows introducing groups which can be utilized as anchors to specific environments (e.g. polyoxyethylene groups, Si-containing substituents, possibly intercallating π systems). These modifications do not deteriorate the excellent photoinitiating and electron-donating properties of this class of compounds, sustaining the character of **1P•**–**5P•** being decisive for their role as polymerization initiating P-centered radicals. The substitution patterns presented in this work have a slight effect on the positioning and the extinction coefficients of the *n*-π* bands, however a systematic behavior cannot be established. We plan now to utilize the (photo)chemistry of the conveniently accessible radical anions **1**$^{\bullet-}$–**5**$^{\bullet-}$.

3.1.5. Experimental Section

General Instrumentation. NMR spectra were recorded on Bruker Avance 500 MHz spectrometer with respect to ^{1}H. Chemical shifts are reported in ppm relative to TMS and residual chemical shifts of the solvent as the secondary standard (for ^{1}H and ^{13}C) and 85% H_3PO_4 (for ^{31}P). Coupling constants (*J*) are given in Hertz (Hz) as absolute values. The multiplicity of the signals is indicated as s, d, t, or m for singlets, doublets, triplets, or multiplets, respectively.

IR-spectra were measured on a Perkin-Elmer-Spectrum 2000 FT-IR-Raman spectrometer using the ATR technique. The relative intensities of the signals are indicated as s = strong, m = medium and w = weak. UV/VIS spectra were measured on a UV/VIS/NIR Lambda 19 spectrometer in 10 mm Quarz cuvettes (200 – 800 nm). Mass spectra were taken by the MS-service center of the Institute of Organic Chemistry (LOC) of the ETH Zürich on a ESI-Q-TOF system (maXis, Brucker Baltonics, Germany) coupled toan Agilent 1200 system (Agilent Ltd., Deutschland). The data were analyzed and evaluated using the Data Analysis 4.0 software package of Bruker Daltonics, Germany. Highly resolved mass spectra confirm the purity of **1**–**5**, since elemental analysis did not give satisfactory results for BAPO derivatives. The thermal properties of the compounds were investigated with simultaneous thermogravimetry (TG) and differential thermoanalysis (DTA) using a NETZSCH STA 409 apparatus. The measurements were performed under an atmosphere of argon in an Al2O3 crucibles. The heating rate was 2.0 or 10.0 °C/min within a temperature

range from 20 to 500 °C. Single crystals suitable for X-ray diffraction were protected with polyisobutylene oil in glovebox then transferred to the goniometer of an Oxford XCalibur, a Bruker SMART APEX or a Bruker APEX diffractometer; MoKα radiation (0.71073 Å). The structure was solved and refined using SHELXS.

Synthesis of 1-5. All manipulations with air or moisture sensitive compounds were performed in a Standard vacuum line using dried glass ware. All reactions were performed under an argon atmosphere in dried and argon saturated solvents. Sodium/benzophenone was used for drying toluene, diethylether and sodium, benzophenone, tetraglyme was used for drying DME. Air sensitive compounds were stored and weighed in a glove box from M Braun (Lab master 130 bzw. 150B-G). Chemicals were used as purchased from ABCR, Acros, Aldrich or Fluka.

1-phenylethyl-PO(COMes)2 (1). 5.016 g Na[P(COMes)2] x 0.5 DME (12.721 mmol) and 1.7 mL 1-phenylethylbromide (2.295 g, 12.401 mmol) were dissolved in 10 mL DME in a 50 mL Schlenk flask. After heating the reaction mixture to 60 °C for 24 h, a complete conversion to the corresponding phosphane is indicated by 31P NMR spectroscopy (δ = 71.1 ppm). 10 mL toluene were added and the suspension was cooled in an ice bath. Subsequently, 4.5 mL 30% H2O2 (approx. 4 equivalents) were added to achieve the quantitative oxidation to the bis(acyl)phosphane oxide 1. 30 mL Dichloromethane (DCM) were added and the resulting mixture was first extracted with 10 mL deionized water, then with 10 mL of a saturated aqueous Na2CO3 solution, then with 10 mL of a saturated aqueous NaCl solution, and finally again with 10 mL deionized water. The combined aqueous phases were extracted with 20 mL DCM. Afterwards the combined organic phases were dried over Na2SO4. After filtration and evaporation of all volatiles under vacuum at 60 °C (oil pump, 1 mbar) 4.927 g (11.035 mmol, 87 % yield) of BAPO 1 are obtained as yellow solid. **1H-NMR** (400.13 MHz, C6D6): δ = 7.56–7.55 (m, 4H, Ph), 7.29–7.27 (m, 2H, Ph), 7.08–7.05 (m, 4H, Ph), 6.68 (s, 4H, Mes), 6.53 (s, 4H, Mes), 4.38–4.31 (m, 2H, CH), 2.50 (s, 12H, o-Me), 2.09 (s, 3H, p-Me), 2.04 (s, 12H, o-Me), 1.98 (s, 3H, p-Me), 1.62 (dd, *3JHH* = 7.20 Hz, *3JPH* = 16.01 Hz, 3H, CH3). - **^{13}C{^{1}H}-NMR** (100.6 MHz, C6D6): δ = 215.8 (d, *J* = 50.0 Hz, CO), 215.3 (d, *J* = 54.6 Hz, CO), 141.5 (Mes-C4), 141.2 (Mes-C4), 138.5 (d, *J* = 4.4 Hz, Ph-C1), 137.8 (d, *J* = 41.7 Hz, Mes-C1), 136.5 (d, *J* = 40.0 Hz, Mes-C1), 137.6 (Mes-C2), 136.5 (Mes-C2), 130.1 (d, *J* = 6.3 Hz, Ph-C2), 129.8 (Mes-C3), 129.6 (Mes-C3), 129.1 (Ph-C4), 127.8 (d, *J* = 1.8 Hz, Ph-C3), 38.8 (d, *J* = 52.7 Hz, PCH), 21.3 (p-CH3), 21.2 (p-CH3),20.4 (o-CH3), 19.7 (o-CH3), 17.2 (d, *J* = 2.1 Hz, CCH3). - **^{31}P{^{1}H}-NMR** (162.0 MHz, C6D6): δ = 31.1. - **^{31}P-NMR** (162.0 MHz, C6D6): δ = 31.1 (dq, *3JPH* = 8.8 Hz, *2JPH* = 15.7 Hz). - **IR** (ATR [cm-1]): 2961.2 (w), 2928.3

(w), 2361.8 (w), 1662.3 (m), 1606.5 (m), 1493.5 (w), 1452.0 (m), 1420.3 (w), 1378.1 (w), 1261.7 (w), 1196.7 (s), 1146.3 (m), 1094.4 (m), 960.3 (w), 880.8 (m), 849.3 (s), 783.4 (s), 768.0 (s), 741.5 (m), 705.2 (s), 649.5 (m), 616.8 (m). - **UV/VIS** (ACN [nm], *ε* [l mol-1cm-1]): 416 (438, shoulder), 400 (469, max), 368 (790, max), 318 (2945, max), 245 (6845, shoulder), < 200 (42063, max). □ **MS** (ESI): *m/z* = 447.2076 (MH+). - **DTA/TG**: melting point 178°C, decomposition > 210°C □

X-Ray Diffraction: CCDC 1536239.

1-naphtylmethyl-PO(COMes)2 (2). 3.893 g Na[P(COMes)2] x 0.5 DME (9.896 mmol) and 1.726 g degassed chloromethylnaphthalin (9.771 mmol) were dissolved in 10 mL DME in a 50 mL Schlenk flask. After stirring the reaction mixture at room temperature for 4 hours, a complete conversion to the corresponding phosphane is indicated by 31P NMR spectroscopy (δ = 52.9 ppm). 10 mL toluene were added and the suspension was cooled in an ice bath. Subsequently, 5 mL 30% H2O2 (approx. 5 equivalents) were added. After 1 hour at 50 °C, the quantitative oxidation to the bis(acyl)phosphane oxide 2 was achieved. After addition of 50 mL DCM, the reaction mixture was first extracted with 20 mL deionized water, then with 20 mL of a saturated aqueous Na2CO3 solution, then with 20 mL of a saturated aqueous NaCl solution, and finally again with 20 mL deionized water. The combined aqueous phases were extracted with 20 mL DCM. Afterwards the combined organic phases were dried over Na2SO4. After filtration and evaporation of all volatiles under vacuum (oil pump, 1 mbar) 3.900 g (8.083 mmol, 82 % yield) of BAPO 2 are obtained as yellow solid. **1H-NMR** (300.13 MHz, C6D6): δ = 8.43 (d, *J* = 8.43 Hz, 1H, Naph), 7.69–7.60 (m, 3H, Naph), 7.44–7.18 (m, 3H, Naph), 6.55 (s, 4H, Mes), 4.23 (d, *J* = 12.31 Hz, 2H, PCH2), 2.20 (s, 12H, *o*-Me), 2.00 (s, 6H, *p*-Me). □ **13C{1H}-NMR** (75.5 MHz, C6D6): δ = 216.3 (d, *J* = 51.3 Hz, CO), 140.9 (Mes-C4), 136.4 (d, *J* = 40.8 Hz, Mes-C1), 136.2 (d, *J* = 0.6 Hz, Mes-C2), 134.1 (d, *J* = 2.1 Hz, Naph), 132.8 (d, *J* = 4.0 Hz, Naph), 129.8 (d, *J* = 6.3 Hz, Naph), 129.2 (Mes-C3), 128.4 (Naph), 128.2 (Naph), 127.1 (d, *J* = 8.5 Hz, Naph), 126.4 (Naph), 125.9 (Naph), 125.3 (d, *J* = 3.2 Hz, Naph), 125.2 (d, *J* = 1.2 Hz, Naph), 30.5 (d, *J* = 49.7 Hz, PCH2), 20.7 (*p*-CH3), 19.5 (*o*-CH3). □ 3**1P{1H}-NMR** (121.5 MHz, C6D6): δ = 22.9. □ **31P-NMR** (121.5 MHz, C6D6): δ = 22.9 (t, *J* = 12.2 Hz). □ **IR** (ATR [cm-1]): 2922.7 (w), 1663.6 (m), 1634.9 (w), 1605.3 (m), 1509.0 (w), 1419.4 (w), 1377.3 (w), 1295.2 (w), 1264.0 (w), 1214.4 (m), 1195.9 (s), 1148.4 (w), 1030.8 (w), 965.0 (w), 893.0 (w), 857.4 (m), 820.4 (m), 795.1 (m), 775.9 (s), 743.9 (m), 730.2 (w), 720.2 (m), 707.8 (w), 678.0 (w), 660.8 (w), 621.6 (w). □ **UV/VIS** (ACN [nm], ε [lmol-1cm-1]): 417 (269, shoulder), 396 (486, shoulder), 368 (757, max), 319 (3810, max), 292 (11676, shoulder), 282 (13081, max), 250 (9287, shoulder), 243 (11594, max), 239 (11588, max), 220 (60579, max), < 215 (< 60000, max). □**MS** (ESI): m/z = 483.2084 (MH+). □ **DTA/TG**:

melting point 119 °C, decomposition > 170 °C.

MeO(CH2CH2O)2-PO(COMes)2 (3). 4.048 g Na[P(COMes)2] x 0.5 DME (10.290 mmol) and 1.7 ml degassed bromodiethylene glycol (2.290 g, 11.885 mmol) were dissolved in 10 mL DME in a 50 mL Schlenk flask. After stirring the reaction mixture at 80 °C for 5 days, 31P NMR spectroscopy (δ = 44.9 ppm) indicates the complete conversion to the corresponding phosphane. The suspension was concentrated under vacuum (oil pump, 1 mbar), the residue suspended in 20 mL of ethanol, and the reaction mixture cooled to 0 °C in an ice bath before 1.2 mL 30% H2O2 (approx. 1 equivalent) were added to achieve quantitative oxidation. The reaction mixture was concentrated to dryness under vacuum and suspended in 20 mL of diethylether. Na2SO4 was added to remove residual water, the mixture filtered, and the clear filtrate concentrated under vacuum and 60 °C. The product 3 was obtained in 96 % yield (4.407 g, 9.915 mmol) as yellow oil. **1H-NMR** (300.13 MHz, C6D6): δ = 6.68 (s, 4H, Mes), 3.74 (dt, *J*PH = 15.31 Hz, *J*HH = 6.45 Hz, 2H, PCH2CH2), 3.34 (t, *J* = 4.95 Hz, 2H, CH2), 3.17 (t, *J* = 4.95 Hz, 2H, CH2), 3.11 (s, 3H, OMe), 2.59–2.51 (m, PCH2), 2.51 (s, 12H, *o*-Me), 2.09 (s, 6H, *p*-Me). **13C{1H}-NMR** (75.5 MHz, C6D6): δ = 215.9 (d, *J* = 55.8 Hz, CO), 140.7, (Mes-C4), 136.5 (d, *J* = 41.7 Hz, Mes-C1), 136.4 (Mes-C2), 129.2 (Mes-C3), 71.5 (CH2OMe), 70.11 (CH2CH2OMe), 63.6 (d, *J* = 4.8 Hz, PCH2CH2), 58.2 (OMe), 28.2 (d, *J* = 55.1 Hz, PCH2), 20.8 (*p*-Me), 19.9 (*o*-Me). **31P{1H}-NMR** (121.5 MHz, C6D6): δ = 25.0. **31P-NMR** (121.5 MHz, C6D6): δ = 25.2–24.8 (m). **IR** (ATR [cm-1]): 2921.3 (w), 2868.2 (w), 1721.0 (w), 1672.8 (m), 1607.3 (s), 1451.8 (m), 1421.4 (m), 1380.4 (w), 1295.8 (w), 1245.8 (w), 1196.2 (s), 1105.1 (s), 1034.0 (m), 957.6 (w), 886.5 (m), 849.9 (s), 770.6 (m), 741.4 (m), 699.8 (w), 619.2 (m). **UV/VIS** (ACN [nm], ε [lmol-1cm-1]): 394 (477, shoulder), 361 (603, max), 316 (18689, max), 291 (8021, max), 239 (6221, shoulder), < 200 (30299, max). **MS** (ESI): m/z = 445.2157 (MH+). **DTA/TG**: decomposition > 150 °C.

3-bromopropyl-PO(COMes)2 (4). 5.312 g Na[P(COMes)2] x 0.5 DME (13.502 mmol) and a tenfold excess of 15 ml degassed 1,3-dibromopropane (29.835 g, 147.786 mmol) were dissolved in 20 mL DME in a 50 mL Schlenk flask. After stirring the reaction mixture at 60 °C for 16 hours, 31P NMR spectroscopy (δ = 48.5 ppm) indicates the complete conversion to the corresponding phosphane. Oxygen (5.0, Pangas) was bubbled through the solution for 30 minutes at room temperature. Subsequently, 50 mL of diethylether were added and this mixture was extracted first with 15 mL distilled water, then two times with 15 mL of a saturated aqueous Na2CO3 solution, and finally with 15 mL distilled water. The combined aqueous phase was extracted once with 50 mL diethylether and the combined organic phases were dried over Na2SO4. After filtration, the

filtrate was concentrated to dryness on the vacuum at 60 °C. The residue was purified by flash-chromatography using hexane/ethylacetate 1:2 as eluent to give 5.2 g (83%) of product 5 as yellow oil. **1H-NMR** (300.13 MHz, C6D6): *δ* = 6.66 (s, 4H, Mes), 2.95 (t, *J* = 6.30 Hz, 2H, CH2Br), 2.46–2.30 (m, 2H, PCH2), 2.41 (s, 12H, *o*-Me), 2.15–1.98 (m, 2H, PCH2CH2), 2.08 (s, 6H, *p*-Me). **13C{1H}-NMR** (75.5 MHz, C6D6): *δ* = 216.4 (d, *J* = 54.0 Hz, CO), 141.0, (Mes-C4), 136.5 (d, *J* = 40.9 Hz, Mes-C1), 135.8 (Mes-C2), 129.3 (Mes-C3), 33.4 (d, *J* = 14.4 Hz, CH2Br), 25.1 (d, *J* = 54.1 Hz, PCH2), 25.0 (d, *J* = 3.4 Hz, PCH2CH2), 20.8 (*p*-Me), 19.6 (*o*-Me). **31P{1H}-NMR** (121.49 MHz, C6D6): *δ* = 26.1. **31P-NMR** (121.49 MHz, C6D6): *δ* = 26.4–25.9 (m). **IR** ATR [cm-1]): 2922.7 (w), 1735.7 (w), 1672.0 (m), 1607.3 (s), 1431.9 (m), 1378.6 (w), 1295.9 (w), 1241.6 (m), 1212.6 (s), 1193.9 (s), 1147.3 (m), 1035.5 (m), 958.6 (w), 888.0 (m), 849.7 (s), 757.1 (m), 736.9 (m), 619.0 (m). **UV/VIS** (ACN [nm], ε [lmol-1cm-1]): 394 (466, shoulder), 364 (552, max), 315 (2330, max), 294 (7283, max), 241 (5858, shoulder), < 200 (30959, max). **MS** (ESI): m/z = 463.1037 (MH+). **DTA/TG**: decomposition > 170 °C.

Synthesis of 3-(triethoxysilyl)propyl-PO(COMes)2 (5). 4.995 g Na[P(COMes)2] x 0.5 DME (12.697 mmol) and 4.228 g 1,3-iodopropyltriethoxysilane (4.228 g, 12.726 mmol) were dissolved in 20 mL DME in a 50 mL Schlenk flask. After stirring the reaction mixture at 60 °C for 2 hours, 31P NMR spectroscopy (*δ* = 50.8 ppm) indicates the complete conversion to the corresponding phosphane. The suspension was concentrated to dryness under vacuum and subsequently 10 mL toluene and 10 mL Diethylether were added. The resulting suspension was extracted two times with 10 mL of degassed aqueous K2CO3 (pH = 10). Then the mixture was cooled in an ice bath and a small amount of K2CO3 was added to assure saturation with K2CO3. Afterwards 1.8 mL H2O2 (30%, ca. 1.4 equiv.) were slowly added in order to oxygenate the phosphane to 5. 20 mL Diethylether were added before the suspension was extracted with two times 20 mL saturated aqueous Na2CO3, two times 10 mL saturated aqueous NaCl, and once with 10 mL of degassed aqueous K2CO3 (pH = 10). The combined aqueous phase were extracted once with 20 mL diethylether, the combined organic phases were dried over Na2CO3, all insoluble parts were filtered off, and the filtrate dried under vacuum at 60 °C. This treatment gave 4.367 g product 5 (7.988 mmol, 63%) in form of a yellow wax.**1H-NMR** (400.13 MHz, C6D6): *δ* = 6.66 (s, 4H, Mes), 3.82 (q, *J* = 6.94 Hz, 6H, OCH2CH3), 2.55–2.45 (m, 2H, PCH2), 2.48 (s, 12H, *o*-Me), 2.18–2.08 (m, 2H, PCH2CH2), 2.08 (s, 6H, *p*-Me), 1.23 (t, *J* = 7.00, 6H, OCH2CH3), 0.80 (t, *J* = 7.80 Hz, 2H, SiCH2). **13C{1H}-NMR** (100.6 MHz, C6D6): *δ* = 217.5 (d, *J* = 53.4 Hz, CO), 141.0 (Mes-C4), 137.3 (d, *J* = 40.2 Hz, Mes-C1), 136.2 (Mes-C2), 129.6 (Mes-C3), 58.7 (OCH2CH3), 29.8 (d, *J* = 52.3 Hz, PCH2), 21.2 (*p*-CH3), 20.2 (*o*-CH3), 18.7 (OCH2CH3), 16.2 (d, *J* = 4.3 Hz,

PCH2CH2), 12.9 (d, *J* = 12.4 Hz, SiCH2). □ **31P{1H}-NMR** (162.0 MHz, C6D6): *δ* = 29.0. □ **31P-NMR** (162.0 MHz, C6D6): *δ* = 29.1–28.9 (m). □ **IR** (ATR [cm-1]): 2974.5 (w), 2920.0 (w), 2878.6 (w), 2359.5 (w), 1669.6 (w), 1608.7 (m), 1441.2 (w), 138131 (w), 1293.9 (w), 1253.1 (w), 1211.2 (m), 1197.7 (m), 1164.7 (w), 1149.0 (m), 1075.8 (s), 1033.3 (m), 956.7 (m), 887.3 (m), 863.0 (w), 849.0 (m), 804.0 (m), 781.5 (m), 748.4 (m), 732.2 (m), 698.5 (w), 645.3 (w), 618.1 (m). □ **UV/VIS** (ACN [nm], ε [lmol-1cm-1]): 394 (359, shoulder), 365 (443, max), 303 (4643, max), 290 (5813, max), 243 (5486, shoulder), < 200 (33497 max). □ **MS** (ESI): m/z = 547.2632 (MH+). □ **DTA/TG**: melting point 37 °C, decomposition > 190 °C.

Materials and Solvents for Spectroscopic Investigations. The solvent acetonitrile was obtained from Roth (purity ≥ 99.9 %). Butyl acrylate (purity ≥ 99.0 %), methyl methacrylate (≥ 99.0 %), 1-vinyl-2-pyrrolidone (≥ 97.0 %) and styrene (≥ 99.5 %) were obtained from Fluka and used as received. The photoinitiator Irgacure® 819 (**6**) was obtained from BASF. All experiments were performed at ambient temperature.

Emission Spectroscopy. Solutions of the photoinitiators in acetonitrile were prepared so that the absorbance at and above the excitation wavelength was ≤ 0.1. The absorption spectra were recorded using a UV-3101 PC UV-VIS-NIR spectrometer (Shimadzu, Japan). Fluorescence emission spectra were recorded with a FluoroMax-2 spectral-fluorimeter (Horiba Scientific, Japan) at the excitation wavelength of 373 nm. Fluorescence quantum yields (*ΦF*) of **1**–**5** were determined by comparison with the known quantum yield of 9,10-diphenylanthracene (*ΦST* = 0.95 in cyclohexane).[13] Emission spectra were measured for each compound and for the standard at four different concentrations. The wavelength integrated intensities of these spectra were plotted versus the absorbance at the excitation wavelength (*A373*). From the slopes of these plots, the fluorescence quantum yields were calculated according to equation 1,[13]

$$\Phi_F = \Phi_{ST} \frac{I}{I_{ST}} \frac{A_{ST}}{A} \frac{\eta^2}{\eta_{ST}^2} \qquad (1)$$

where *I* is the integrated emission intensity, *A* the absorbance at 373 nm and *η* the refractive index of the solvent (acetonitrile for the BAPOs and cyclohexane for the standard ST).

Laser Flash Photolysis Experiments. The experiments were performed on a LKS80 Laser Flash Photolysis Spectrometer (Applied Photophysics, UK). Samples were excited with the frequency tripled light from the Spitlight Compact 100 (InnoLas, Germany) solid state Nd:YAG laser at 355 nm (pulse duration: 8 ns, energy: 10 mJ/pulse). The concentration of the BAPOs in the acetonitrile solutions was adjusted to achieve the absorbance of ~ 0.3 at 355 nm. The solutions were purged with argon for 10 minutes before the measurement. The transient absorption spectra were recorded in a quartz cuvette (1 cm x 1 cm) using a flow system driven by a peristaltic pump (0.012 L min^{-1}). Rate constants for the addition of the phosphanoyl radicals to the monomer double bonds were determined in pseudo-first-order experiments; solutions of the compounds in acetonitrile containing monomer-concentrations in the range of 0.5 M to 0.025 M and providing absorbance of ~ 0.3 at 355 nm were prepared. Static solutions were saturated with argon and then measured. The decay of the phosphanoyl radicals was recorded at the absorption maximum determined from the transient absorption spectra.

TR-EPR Spectroscopy. Continuous-wave time-resolved (TR) EPR experiments were performed on a Bruker ESP 300E X- band spectrometer (unmodulated static magnetic field) equipped with a 125 MHz dual channel digital oscilloscope (Le Croy 9400). As the light source, the frequency triplet light of a Nd:YAG laser was used (InnoLas Spitlight 400, 355 nm, operating at 20 Hz, ca. 7 mJ/pulse, 8 ns). The setup is controlled by the fsc2 software developed by Dr. J. T. Toerring (Berlin). Spectra were recorded by acquiring the accumulated (50 accumulations) time responses to the incident laser pulses at each magnetic field value of the chosen field range (field steps: 0.5 G). Argon-saturated solutions in toluene (~ 15 mM in photoinitiator concentration) were pumped through a quartz flat cell positioned in the cavity of the EPR spectrometer using a flow system (flow rate: 2-3 mL min^{-1}).

31P CIDNP-NMR Spectroscopy. The experiments were carried out with a 200 MHz Bruker AVANCE DPX spectrometer equipped by a custom-made CIDNP probe head. A Quantel Nd-YAG Brilliant B (355 nm, ~60 mJ/pulse, pulse length ~8−10 ns) operating at 20 Hz served as light source. mJ/pulse, pulse length ~ 8−10 ns) operating at 20 Hz was employed as the light source. The timing sequence of the experiment consists of a series of 180° radiofrequency (RF) pulses (applied to suppress the normally present NMR intensities), the laser flash, the 90° RF detection pulse and the acquisition of the FID. The spectra were recorded with ^{1}H decoupling and “dummy” CIDNP spectra employing the same pulse sequence but without the laser pulse were always

measured. Samples were prepared in deuterated benzene and deoxygenated by bubbling with argon before the experiment.

Thermal Imaging. Thermographic experiments were conducted with the VarioCAM high resolution infrared camera (InfraTec, Germany). Solutions of the photoinitiators in acetonitrile were mixed with the monomers in a 1:1 v/v ratio. The samples were purged with argon for 15 minutes. The polymerization was initiated by light pulses generated by a Hg-Xe-lamp (Hamamatsu, Japan) positioned above the vial containing the sample (see figure 5). Pulses of various durations (1s, 5s, 10s) were employed. Thermograms were recorded in order to monitor the heat profile of the reactions (recording frequency: 10 Hz). The data were evaluated using the IRBIS remote 3.0 software.

Cyclic Voltammetry. Cyclic voltammograms (CVs) were obtained with a PG580 potentiostat (Uniscan, UK) using a standard three-electrode electrochemical cell with platinum disk working (WE) and counter (CE) electrodes and a silver wire pseudoreference electrode (RE). Approximately 1mM sample solutions were prepared in acetonitrile with 0.1 M tetrabutylammonium tetrafluoroborate supporting electrolyte and purged with argon for 10 min before each experiment. CVs were recorded at 100 mV/s scan rate. All potentials are given vs. Fc^+/Fc, which was used as internal reference and are uncorrected from Ohmic drop.

EPR Spectroscopy. Radical anions of **1-4** were prepared in a special three-compartment EPR sample tube connected to the vacuum line. K-metal mirror was sublimated to the wall of the tube and THF (ca. 0.4 mL) was freshly condensed to dissolve the investigated compound. The sample was successively degassed by three freeze-pump-thaw cycles and sealed under high vacuum. Reductions were performed by contact of the THF solution of the parent molecule with the K-metal mirror in the evacuated sample tube. A Bruker X-band spectrometer, ESP 300 (equipped with an ENDOR unit, 12.5 kHz field modulation), both with an EUROTHERM temperature control unit, was used to record the cw-EPR spectra. Typical experimental conditions for the EPR spectra were 2mW microwave power and 0.03 mT field modulation. Spectra were analyzed with WinEPR and SimFonia software provided by the manufacturer of the spectrometer as well as with WinSim a public domain program. [27]

3.1.6. References

[1] W. Rutsch, K. Dietliker, D. Leppard, M. Köhler, L. Misev, U. Kolczak, G. Rist, *Prog. Org. Coatings* **1996**, *27*, 227–239.

[2] K. Dietliker, T. Jung, J. Benkhoff, H. Kura, A. Matsumoto, H. Oka, D. Hristova, G. Gescheidt, G. Rist, *Macromol. Symp.* **2004**, *217*, 77–98.

[3] K. K. Dietliker, *Chemistry and Technology of Uv and Eb Formulation for Coatings, Inks & Paints, Volume 3: Photoinitiators for Free Radical and Cationic Polymerisation*, SITA Technology, London, **1991**.

[4] U. Kolczak, G. Rist, K. Dietliker, J. Wirz, *J. Am. Chem. Soc.* **1996**, *118*, 6477–6489.

[5] A. Huber, A. Kuschel, T. Ott, G. Santiso-Quinones, D. Stein, J. Bräuer, R. Kissner, F. Krumeich, H. Schönberg, J. Levalois-Grützmacher, et al., *Angew. Chemie Int. Ed.* **2012**, *51*, 4648–4652.

[6] S. Jockusch, I. V. Koptyug, P. F. McGarry, G. W. Sluggett, N. J. Turro, D. M. Watkins, *J. Am. Chem. Soc.* **1997**, *119*, 11495–11501.

[7] S. Jockusch, N. J. Turro, *J. Am. Chem. Soc.* **1998**, *120*, 11773–11777.

[8] J. Wang, G. Siqueira, G. Müller, D. Rentsch, A. Huch, P. Tingaut, J. Levalois-Grützmacher, H. Grützmacher, Y. Habibi, L. A. Lucia, et al., *Chem. Commun.* **2016**, *52*, 2823–2826.

[9] S. Benedikt, J. Wang, M. Markovic, N. Moszner, K. Dietliker, A. Ovsianikov, H. Grützmacher, R. Liska, *J. Polym. Sci. Part A Polym. Chem.* **2016**, *54*, 473–479.

[10] D. E. Fast, M. Zalibera, A. Lauer, A. Eibel, C. Schweigert, A.-M. Kelterer, M. Spichty, D. Neshchadin, D. Voll, H. Ernst, et al., *Chem. Commun.* **2016**, 9917–9920.

[11] G. Müller, M. Zalibera, G. Gescheidt, A. Rosenthal, G. Santiso-Quinones, K. Dietliker, H. Grützmacher, *Macromol. Rapid Commun.* **2015**, *36*, 553–7.

[12] H. Gruetzmacher, J. Geier, D. Stein, T. Ott, H. Schoenberg, R. H. Sommerlade, S. Boulmaaz, J.-P. Wolf, P. Murer, T. Ulrich, *Chimia (Aarau).* **2008**, *62*, 18–22.

[13] M. Montalti, A. Credi, L. Prodi, M. T. Gandolfi, *Handbook of Photochemistry, 3rd Ed.*, CRC Press, Taylor & Francis Group, **2006**.

[14] G. W. Sluggett, C. Turro, M. W. George, I. V Koptyugjs, N. J. Turro, *J. Am. Chem. Soc.* **1995**, *117*, 5148–5153.

[15] C. S. Colley, D. C. Grills, N. a. Besley, S. Jockusch, P. Matousek, A. W. Parker, M. Towrie, N. J. Turro, P. M. W. Gill, M. W. George, *J. Am. Chem. Soc.* **2002**, *124*, 14952–14958.

[16] G. W. Sluggett, P. F. McGarry, I. V Koptyug, N. J. Turro, *J. Am. Chem. Soc.* **1996**, *118*, 7367–7372.

[17] I. Gatlik, P. Rzadek, G. Gescheidt, G. Rist, B. Hellrung, J. Wirz, K. Dietliker, G. Hug, M. Kunz, J.-P. Wolf, *J. Am. Chem. Soc.* **1999**, *121*, 8332–8336.

[18] C. Dursun, M. Degirmenci, Y. Yagci, S. Jockusch, N. J. Turro, *Polymer (Guildf).* **2003**, *44*, 7389–7396.

[19] G. W. Sluggett, P. F. Mcgarry, I. V Koptyug, N. J. Turro, *J. Am. Chem. Soc.* **1996**, *7863*, 7367–7372.

[20] M. Spichty, N. J. Turro, G. Rist, J.-L. Birbaum, K. Dietliker, J. P. Wolf, G. Gescheidt, *J. Photochem. Photobiol. A Chem.* **2001**, *142*, 209–213.

[21] G. W. Sluggett, P. F. McGarry, I. V Koptyug, N. J. Turro, *J. Am. Chem. Soc.* **1996**, *118*, 7367–7372.

[22] A. Yurkovskaya, O. Morozova, G. Gescheidt, in *Encycl. Radicals Chem. Biol. Mater.*, John Wiley & Sons, Ltd, **2012**.

[23] D. Neshchadin, A. Rosspeintner, M. Griesser, B. Lang, S. Mosquera-Vazquez, E. Vauthey, V. Gorelik, R. Liska, C. Hametner, B. Ganster, et al., *J. Am. Chem. Soc.* **2013**, *135*, 17314–17321.

[24] R. Geier, C. Wappl, H. Freiszmuth, C. Slugovc, G. Gescheidt, *Polym. Chem.* **2015**, *6*, 2488–2492.

[25] G. Moad, D. H. Solomon, *The Chemistry of Radical Polymerization*, Elsevier, **2006**.

[26] M. Zalibera, P.-N. Stébé, K. Dietliker, H. Grützmacher, M. Spichty, G. Gescheidt, *European J. Org. Chem.* **2014**, *2014*, 331–337.

[27] D. R. Duling, *J. Magn. Reson. Ser. B* **1994**, *104*, 105–110.

3.1.7. Supporting Information

Supporting information for this article is available on the WWW under *https://doi.org/10.1002/ejic.201700140.*

3.2. Probing the First Steps of Photoinduced Free Radical Polymerization at Water–Oil Interfaces

Denisa Darvasiová,[a] Zuzana Barberiková,[a] Anna Eibel,[b] Max Schmallegger,[b] Georg Gescheidt,[b] Michal Zalibera,*[a] and Dmytro Neshchadin*[b]

[a] Institute of Physical Chemistry and Chemical Physics, Slovak University of Technology in Bratislava

[b] Institute of Physical and Theoretical Chemistry, Graz University of Technology

Published in: *Polym. Chem.*, **2017**, *8*, 6943-6947.

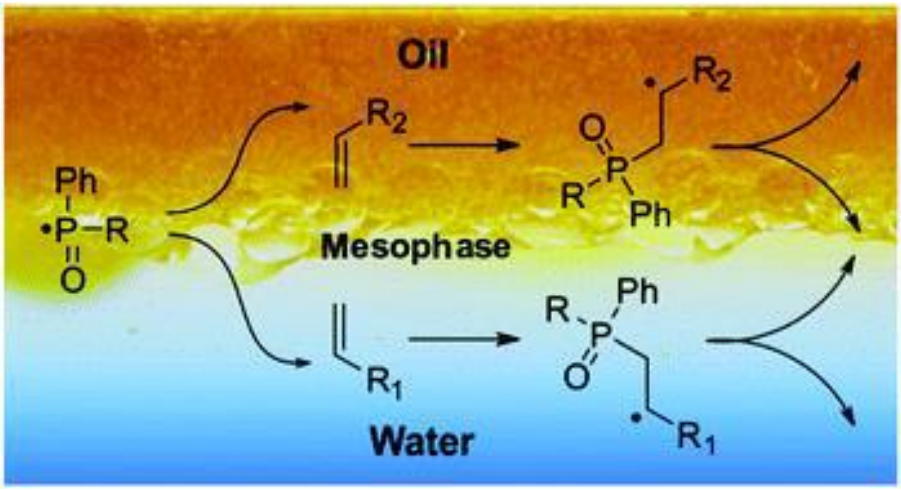

3.2.1. Abstract

Phosphanoyl radicals, produced by α-photocleavage of exclusively octane-soluble acylphosphane oxides, rapidly react with both water- and octane-soluble monomers in water-in-octane micro- emulsions. The presented mechanistic insights open the possibility for the tailored construction of photo-generated copolymers com- prising polar and non-polar blocks at the same time.

3.2.2. Main Text

Microemulsions are macroscopically isotropic liquid colloids that consist of water, oil (nonpolar organic solvent), surfactant and sometimes co-surfactant. Compared to conventional emul- sions, microemulsions are optically translucent and thermo- dynamically stable, making their preparation process-indepen- dent and not requiring mechanical energy.[1,2] The average size of microscopic domains in microemulsions typically varies from 10 to 50 nm. Depending on the amount of water, organic phase and surfactant, water-in-oil (w/o, direct), oil-in-water (o/w, reverse) and bicontinuous microemulsions with different microstructures and huge oil–water interfacial areas (up to 10^5 m2 L^{-1}) [2] can be prepared. [3] These unique properties of micro- emulsions determine the range of their applications: from template synthesis of nanoparticles (as nanoreactors/tem- plates) and thermal emulsion polymerization to drug delivery vehicles, cosmetics and heterogeneous catalysis. [4–6]

The optical translucency of microemulsions opens the door for their applications in photoinduced free radical polymerization reactions. Polymerizations initiated by (UV/visible) light allow spatially well-defined curing at high speed and low temperatures, resulting in reduced energy costs and improved bio- compatibility when compared to thermal polymerizations. [7–10]

A number of studies addressing photoinduced free radical polymerization in emulsions (*i.e.* surfactant-free emulsion polymerization) [11] and microemulsions[12–16] are known. However, to the best of our knowledge, there is no molecular-level mechanistic insight on the initiation mechanism of photopolymerizations in microemulsions yet. Moreover, we are not aware of any kinetic information on photoinduced free radical polymerization on the microsecond time-scale. In order to gain such mechanistic and kinetic evidence, we have investigated photopolymerization reactions in micro- emulsions, utilizing the well-studied and well-understood mono- and bisacylphosphane oxide (2,4,6-trimethylbenzoyl-diphenyl- phosphane oxide, **MAPO**) and bis(2,4,6-trimethylbenzoyl)-phenyl- phosphane oxide, **BAPO**) photoinitiators. [9,11,17–24] The photo- cleavage of these Norrish type I initiators leads to the formation of phosphanoyl and benzoyl radicals. Both radicals are able to add to the double bonds of monomers and thereby initiate the polymerization chain reactions (Scheme 1). These primary reactions can be conveniently monitored using time-resolved EPR (TR EPR) spectroscopy (exploiting the chemically induced dynamic electron polarization, CIDEP) [25–27] as well as laser-flash photolysis (LFP). [19,24]

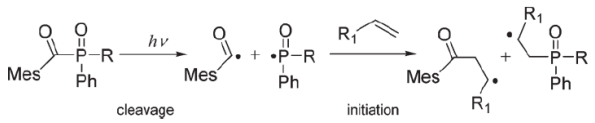

Scheme 1 Cleavage of phosphane oxides and initiation of the free radical polymerization.

Here, we describe the photoinduced cleavage of **MAPO** and **BAPO** in tertiary octane–water microemulsions with sodium dioctyl sulfosuccinate (**AOT**) as a surfactant. Moreover, we monitor the first addition of primary phosphanoyl free radicals to water- and oil-soluble monomers (Figure 1). We have chosen **AOT** from the set of different surfactants since it forms microemulsions without a co-surfactant, [28] which drastically reduces the number of the possible chemical reactions in the system and simplifies the understanding of the whole model.

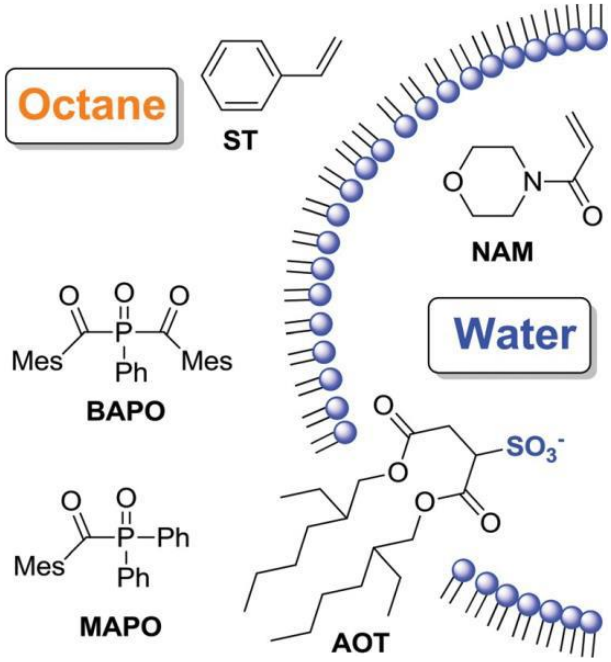

Figure 1 Chemical structures of photoinitiators, monomers and surfactant. The elements are placed according to the expected distribution between the oil and water phases.

The time-resolved EPR (TR EPR) spectra of **BAPO** and **MAPO** upon laser irradiation (λ = 355 nm) were recorded (Figure 2) in AOT microemulsions with the mass fraction of the surfactant γ = 0.2 and the volume fractions of water/octane Φ =0.33 and 0.67, respectively. The reference TR EPR spectra of **MAPO** and **BAPO** in neat octane in the presence of the surfactant were recorded in order to monitor the changes in chemical reactivity under different conditions. As shown in Figure 2, the reactivity pattern of **BAPO** in the microemulsion drastically differs from its behavior

in pure octane. Although in the shake-flask experiments, **BAPO** was found only in the organic octane phase (see the SUPPORTING INFORMATION), the TR EPR spectrum (Figure 2b) points to the reaction of the primary phosphanoyl radical **P1•** with water. [29] A comparison between Figure 2a and b reveals that the doublet assigned to **P1•** (hyperfine coupling constant, *hfc* = 25.7 mT) is weaker in the spectrum recorded in the micro- emulsion and a new doublet with a *hfc* of *ca.* 3 mT is present (Figure 2b).

Even though the exact mechanism of this reaction is not fully understood and the resulting free radical with a hyperfine coupling constant of *ca.* 3 mT is not unambiguously revealed,[29] we are going to use it for probing the surroundings of the photoinitiator. The TR EPR spectrum reveals that **P1•** reacts prodigiously with H2O. Since **BAPO** in a biphasic octane–water system was detected only in the organic phase, and the solubility of water in octane is very limited (*ca.* 99 mg dm−3), [30] the obtained result underpins that the phosphanoyl radical is generated in a water-rich mesophase, *i.e.* on the interface between oil (octane) and water. 31P NMR also indicates that the environment of the parent **BAPO** in the microemulsion is different from that of the neat octane.

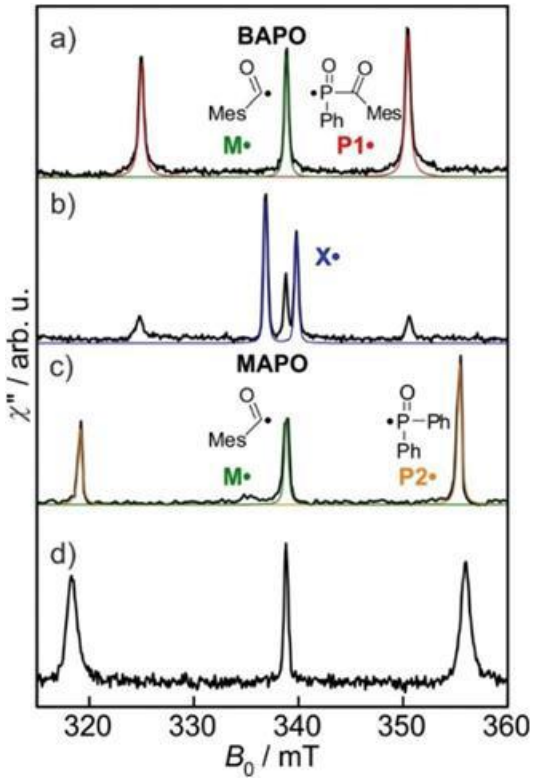

Figure 2 TR EPR spectra of **BAPO** (a) in an octane/**AOT** homogeneous solution and (b) in a water/octane/**AOT** microemulsion, and **MAPO** (c) in octane/**AOT** and (d) in a water/octane/**AOT** microemulsion observed between 150–250 ns after laser-flash photolysis (355 nm). Colored lines represent the simulation of the individual radical spectra.

An alternative and potentially complementary reaction path is the diffusion toward the water phase in quantities that are detectable by TR EPR immediately after the cleavage of **BAPO** (*ca.* 250 ns). The quenching rate constant of **P1•** by water in the microemulsion (2×10^6 M^{-1} s^{-1}, SUPPORTING INFORMATION) is only two times slower than that in a water-containing homogeneous solution (4.7×10^6 M^{-1} s^{-1}). This is the result of the high accessibility of the parent BAPO by water. It is critical to mention that the TR EPR of the conventional mixture of water and octane (1 : 1, v : v) in the presence of BAPO, as well as the emulsion of octane and water with sodium dodecyl sulfate (SDS) surfactant, did not show any reaction of **P1•** with water. This again proves the supremacy of microemulsions in terms of oil–water inter- phase surfaces. The reaction mechanism of **MAPO** has not changed in the microemulsion since phosphanoyl radical **P2•** does not react with water (see Figure 2c and d). [29] However we can expect that it is also well accessible by H2O molecules in the microemulsion. This inference is grounded on a similarity of chemical structures of both free radicals. The presence of **P2•** in a polar water-rich environment is additionally corroborated by the slightly higher value of the phosphorus *hfc* (37.6 mT) found in the microemulsion, as compared to the neat octane (36.3 mT), toluene (36.3 mT),[27] or benzene (36.5 mT)[31,32] (Table 1). The interaction of the polar solvent with the oxygen atom of the P–O• group leads to a larger bond polarization, and results in the partial localization of negative charge at the oxygen as well as higher unpaired spin density at the phos- phorus, similar to that established for the N–O• group of the nitroxide radicals. [33] The increase of the phosphorus *hfc* is then the consequence of the larger unpaired electron spin density at the P nucleus. Analogous arguments also hold for the changes of the P *hfc* in P1• (Table 1).

Table 1 Spin Hamiltonian parameters of the phosphanoyl and benzoyl radicals and their spin adducts with monomers in a water/octane/**AOT** microemulsion

	g-Factor	Hyperfine coupling constants/mT			
			a_H[c]		
Radical	g_{iso}[a]	a_P[b]	α[c] (2 H)	β[c] (1 H)	*o*,*p*-Ph[c] (3 H)
M•	2.0005				
P1•	2.0040	25.75 (25.48)[d]			
P2•	2.0041	37.57 (36.3)[d]			
X•	2.0031	2.95			
P1-NAM•	2.0028	6.70	1.75	1.71	
P2-NAM•	2.0028	6.70	1.75	1.71	
P1-ST•	2.0028	5.20	1.25	1.51	0.50
P2-ST•	2.0028	5.20	1.25	1.51	0.50

[a] ±0.0001. [b] ±0.08. [c] Due to the poor S/N ratio, the errors of the *hfc*s can be up to ±0.1. [d] In AOT/octane solution.

Considering that both **P1•** and **P2•** free radicals are present in a water-rich mesophase of the microemulsion, we assume that they will react with both oil- and water-soluble monomers in the microemulsion initiating free radical polymerization. This was examined by TR EPR and laser-flash photolysis (LFP). We chose styrene (**ST**) and 4-acryloylmorpholine (**NAM**) as exclusively oil- and water-soluble monomers, respectively. **NAM** is known to be a highly reactive non-toxic water-soluble monomer.[22] The NMR spectra confirm the presence of **ST** and **NAM** exclusively in the oil and water phases correspondingly (SUPPORTING INFORMATION). The TR EPR spectra recorded in the water/octane/**AOT** microemulsion containing the corresponding monomers (Figure 3) unequivocally show that both **P1•** and **P2•** react with the pair of monomers independent of their solubility/ miscibility with water and octane. The new radicals formed are the result of the addition of **P1•** and **P2•** to the double bonds of monomers, *i.e*. the primary initiation step in free radical polymerization (see also Scheme 1). The mesitoyl counterpart of **P1•** and **P2•** also clearly participates in the polymerization; however, the addition of benzoyl-type radicals to the double bonds is significantly slower. As a result, they are seen practically intact in the TR EPR spectra (Figure 3) even in the presence monomers.[34]

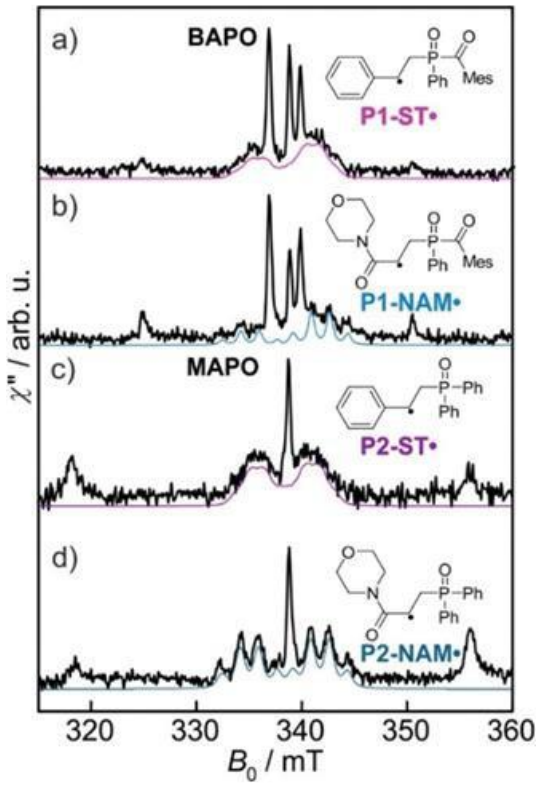

Figure 3 TR EPR spectra of **BAPO** (a, b) and **MAPO** (c, d) in a water/ octane/**AOT** microemulsion after the addition of **ST** (a, c) and **NAM** (b, d) monomers together with the simulated spectra of the radical adducts formed (colored lines).

We have determined the bimolecular rate constants for the first addition of phosphanoyl radicals to the double bonds of both monomers in the microemulsion using LFP. This was attained in pseudo-first-order experiments, *via* observing the quenching of the phosphanoyl radicals in the presence of increasing monomer concentration (SUPPORTING INFORMATION). The resulting bimolecular rate constants range from 0.89×10^8 to 2.95×10^8 M^{-1} s^{-1} (Table 2). Interestingly, they are almost one order of magnitude higher than typical rate constants obtained with similar photoinitiators/monomers in homogeneous and isotropic organic solvents and their mixtures.[19,24] A plausible explanation for these higher apparent reaction rate constants is an inhomogeneous distribution of components, *i.e.* a higher effective concentration of the monomer and photoinitiator in the mesophase between octane and water where they come into contact. The spatial prearrangement of reactants (photoinitiator and monomer) in an anisotropic environment can also contribute to the higher reaction rate constants.

Table 2 Bimolecular rate constants for the addition of phosphanoyl radicals to monomers, determined by LFP in a water/octane/**AOT** micro- emulsion at two detection wavelengths

Radical/monomer	$k_{(340\ nm)}/10^8$ M^{-1} s^{-1}	$k_{(460\ nm)}/10^8$ M^{-1} s^{-1}
P1˙/ST	2.14	2.34
P1˙/NAM	0.89	
P2˙/ST	1.13	
P2˙/NAM	2.95	

The ability of phosphanoyl radicals to initiate free radical polymerization with both water- and oil-soluble monomers can be utilized to create new functional polymers, which are not accessible through conventional photoinduced free radical polymerization because of the immiscibility of the components. After the initiation in the mesophase, there are two potential scenarios for the free radical polymerization process. First, a growing polymer chain can be continuously built in the mesophase producing a polymer that consists of hydro- phobic and hydrophilic moieties (Figure 4a and b). The oil and water phases play a role of reservoirs that supply fresh monomers to the growing chain. The composition of the polymer in this case can be controlled kinetically by the concentrations of monomers in water (**A**) and oil (**B**). The second scenario implies that after the initiation, the polymerization is transferred to the oil/water phase where the polymer is formed (Figure 4b and c).

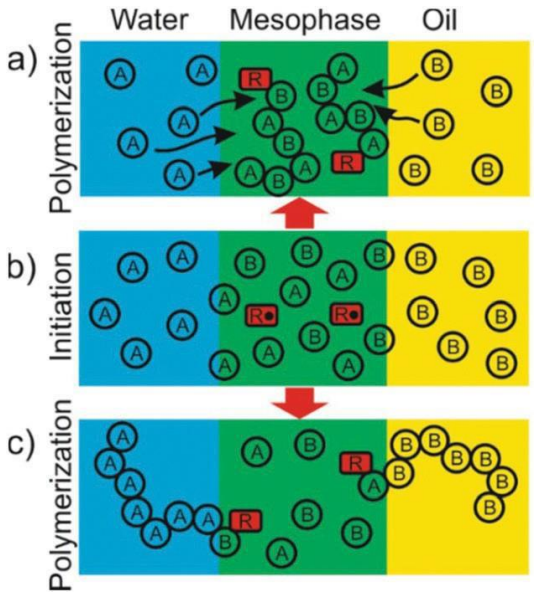

Figure 4 Possible scenarios of free radical polymerization in micro- emulsions after the initiation (b) in the mesophase between oil and water in the presence of water- (**A**) and oil- (**B**) soluble monomers. (a) Polymerization in the mesophase and (c) polymerization in the oil/water phases.

Here, the whole polymer consists of only one type of monomer as in a conventional free radical polymerization. However, it is possible, in our view, to control the head- group attached to the initiating radical (R•), by varying the concentrations of the monomers and their polarity. The switch from one scenario to another can be attained by either mechanical mixing of the reaction mixture or variation of the relative volumes of the oil and water phases.

In summary, we have shown that in water/octane/**AOT** micro- emulsions, phosphanoyl free radicals generated from **MAPO** and **BAPO** photoinitiators are produced in the water-rich meso-phase on the interface between water and octane. Phosphanoyl radical **P1•** reacts with water in that mesophase and therefore can be used as a convenient probe for the microemulsion microstructure. Moreover, we demonstrated that phosphanoyl radicals **P1•** and **P2•** are able to initiate free radical polymerization reacting with both water- and oil-soluble monomers with relatively high reaction rate constants. Together with the convenient methods for the modification of the **BAPO** scaffold reported recently,[11,21,24] the presented results open the possibility for a tailored design and construction of photo-generated copolymers containing polar and non-polar blocks at the same time. Fine-tuning of the monomer polarity and water/oil solubility can help create copolymers of different compositions and properties. The relative amount of different blocks with distinct polarities can potentially be attenuated by adjusting the concentration of monomers and relative volumes of the water and oil phases.

3.2.3. References

[1] D. J. McClements, *Soft Matter*, **2012**, *8*, 1719–1729.

[2] M. Schwuger, K. Stickdornt and R. Schomacker*, Chem. Rev.*, **1995**, *95*, 849–864.

[3] *Microemulsions: background, new concepts, applications, perspectives*, ed. C. Stubenrauch, Blackwell Publishing Ltd, Chichester, West Sussex, U.K. Ames, Iowa, **2009**.

[4] B. Richard, J. Lemyre and A. M. Ritcey, *Langmuir*, **2017**, *33*, 4748–4757.

[5] J. Bassi da Silva, S. B. de, S. Ferreira, O. de Freitas and M. L. Bruschi, *Drug Dev. Ind. Pharm*., **2017**, *43*, 1053–1070.

[6] M. Hejazifar, M. Earle, K. R. Seddon, S. Weber, R. Zirbs and K. Bica, *J. Org. Chem*., **2016**, *81*, 12332–12339.

[7] W. Rutsch, K. Dietliker, D. Leppard, M. Köhler, L. Misev, U. Kolczak and G. Rist, *Prog. Org. Coat.,* **1996**, *27*, 227–239.

[8] Y. Yagci, S. Jockusch and N. J. Turro, *Macromolecules*, **2010**, *43*, 6245–6260.

[9] K. Dietliker, T. Jung, J. Benkhoff, H. Kura, A. Matsumoto, H. Oka, D. Hristova, G. Gescheidt and G. Rist, *Macromol. Symp*., **2004**, *217*, 77–98.

[10] G. Moad and D. H. Solomon, The Chemistry of Radical Polymerization, Elsevier, 2006.

[11] G. Müller, M. Zalibera, G. Gescheidt, A. Rosenthal, G. Santiso-Quinones, K. Dietliker and H. Grützmacher, *Macromol. Rapid Commun*., **2015**, *36*, 553–557.

[12] A. Chemtob, B. Kunstler, C. Croutxé-Barghorn and S. Fouchard, *Colloid Polym. Sci*., **2010**, *288*, 579–587.

[13] L. Zhang, Z. Zeng, Y. Chen, C. Wu and J. Gao, *J. Appl. Polym. Sci.,* **1997**, *66*, 2543–2549.

[14] L. Wang, X. Liu and Y. Li, *Langmuir*, **1998**, *14*, 6879–6885.

[15] L. Wang, X. Liu and Y. Li, *Macromolecules*, **1998**, *31*, 3446– 3453.

[16] Y. Shang, G. Shan and P. Pan, *AIChE J.,* **2014**, *60*, 3276– 3285.

[17] G. W. Sluggett, P. F. McGarry, I. V. Koptyug and N. J. Turro, *J. Am. Chem. Soc.,* **1996**, *118*, 7367–7372.

[18] G. W. Sluggett, C. Turro, M. W. George, I. V. Koptyug and N. J. Turro, *J. Am. Chem. Soc*., **1995**, *117*, 5148–5153.

[19] S. Jockusch and N. J. Turro, *J. Am. Chem. Soc*., **1998**, *120*, 11773–11777.

[20] H. Gruetzmacher, J. Geier, D. Stein, T. Ott, H. Schoenberg, R. H. Sommerlade, S. Boulmaaz, J.-P. Wolf, P. Murer and T. Ulrich, *Chimia*, **2008**, *62*, 18–22.

[21] . Huber, A. Kuschel, T. Ott, G. Santiso-Quinones, D. Stein, J. Bräuer, R. Kissner, F. Krumeich, H. Schönberg, J. Levalois-Grützmacher and H. Grützmacher*, Angew. Chem.,*

Int. Ed., **2012**, *51*, 4648–4652.

[22] S. Benedikt, J. Wang, M. Markovic, N. Moszner, K. Dietliker, A. Ovsianikov, H. Grützmacher and R. Liska, *J. Polym. Sci., Part A: Polym. Chem*., **2016**, *54*, 473–479.

[23] D. E. Fast, M. Zalibera, A. Lauer, A. Eibel, C. Schweigert, A.-M. Kelterer, M. Spichty, D. Neshchadin, D. Voll, H. Ernst, Y. Liang, K. Dietliker, A.-N. Unterreiner, C. Barner-Kowollik, H. Grützmacher and G. Gescheidt, *Chem. Commun*., **2016**, *52*, 9917–9920.

[24] A. Eibel, M. Schmallegger, M. Zalibera, A. Huber, Y. Bürkl, H. Grützmacher and G. Gescheidt, *Eur. J. Inorg. Chem.,* **2017**, *2017*, 2469–2478.

[25] A. Yurkovskaya, O. Morozova and G. Gescheidt, in *Encyclopedia of Radicals in Chemistry, Biology, and Materials*, ed. C. Chatgilialoglu and A. Studer, John Wiley & Sons, Chichester, West Sussex, Hoboken, N.J., **2012**, p. 175.

[26] D. Hristova, I. Gatlik, G. Rist, K. Dietliker, J. P. Wolf, J. L. Birbaum, A. Savitsky, K. Möbius and G. Gescheidt, *Macromolecules*, **2005**, *38*, 7714–7720.

[27] I. Gatlik, P. Rzadek, G. Gescheidt, G. Rist, B. Hellrung, J. Wirz, K. Dietliker, G. Hug, M. Kunz and J. P. Wolf, *J. Am. Chem. Soc*., **1999**, *121*, 8332–8336.

[28] S. Nave, J. Eastoe, R. K. Heenan, D. Steytler and I. Grillo, *Langmuir*, **2000**, *16*, 8741–8748.

[29] R. Shergill, M. Haberler, C. B. Vink, H. V. Patten and J. R. Woodward, *Phys. Chem. Chem. Phys.*, **2009**, *11*, 7248.

[30] C. Black, G. G. Joris and H. S. Taylor, *J. Chem. Phys*., **1948**, *16*, 537–543.

[31] M. Kamachi, K. Kuwata, T. Sumiyoshi and W. Schnabel, *J. Chem. Soc.,* Perkin Trans. 2, **1988**, *961*.

[32] T. N. Makarov, A. N. Savitsky, K. Möbius, D. Beckert and H. Paul, *J. Phys. Chem. A*, **2005**, *109*, 2254–2263.

[33] I. R. Lantzke, D. E. Irish and T. E. Gough, in *Physical Chemistry of Organic Solvent Systems*, Springer US, Boston, MA, **1973**, pp. 405–523.

[34] C. S. Colley, D. C. Grills, N. A. Besley, S. Jockusch, P. Matousek, A. W. Parker, M. Towrie, N. J. Turro, P. M. W. Gill and M. W. George, *J. Am. Chem. Soc.,* **2002**, *124*, 14952–14958.

3.2.4. Supporting Information

Supporting information for this article is available on the WWW under *https://doi.org/10.1039/c7py01414g.*

3.3. The Unprecedented Bifunctional Chemistry of Bis(acyl)phosphane Oxides in Aqueous and Alcoholic Media

Max Schmallegger,[a]# Anna Eibel,[a]# Jan P. Menzel,[b] Anne-Marie Kelterer,[a] Michal Zalibera,[c] Christopher Barner-Kowollik,[b] Hansjörg Grützmacher,[d] and Georg Gescheidt*[a]

[a] Institute of Physical and Theoretical Chemistry, Graz University of Technology

[b] School of Chemistry, Physics and Mechanical Engineering, Queensland University of Technology (QUT)

[c] Institute of Physical Chemistry and Chemical Physics, Slovak University of Technology in Bratislava

[d] ETH Zurich, Swiss Federal Institute of Technology

# These authors contributed equally to this work.

Published in:

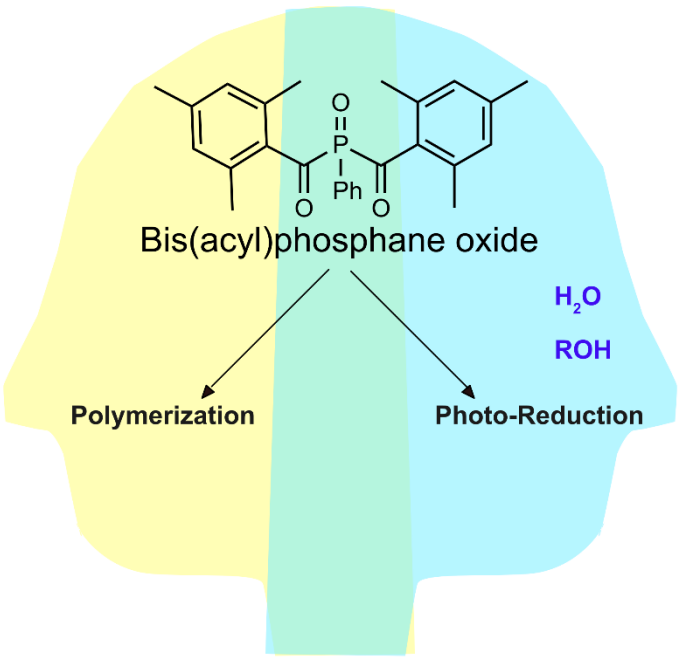

3.3.1. Abstract

Tailor-made photoinitiators will play an important role for efficient radical polymerisations in aqueous media, especially in hydrogel manufacturing. Bis(acyl)phosphane oxides (BAPOs) are among the most active initiators. Here we show that they display a remarkable photochemistry in aqueous and alcoholic media: Photolysis of BAPOs in the presence of water or alcohols provides a new delocalized π radical., which does not participate in the polymerization. It either converts into a monoacylphosphine oxide acting as a secondary photoactive species or, it acts as one-electron reducing agent. Upon the electron-transfer process it again produces a dormant photoinitiator. We have established the structure and the chemistry of this π radical using steady-state and time-resolved (CIDEP) EPR together with electrospray-ionization mass spectrometry, NMR and DFT calculations. Our results show that bis(acyl)phosphine oxides act as bifunctional reagents when applied in aqueous and alcoholic media.

3.3.2. Main Text

Bis(acyl)phosphane oxides (BAPOs) are widely employed and well investigated photoinitiators for radical polymerizations.[1–12] The generation of a phosphanoyl/benzoyl (**P•**/**B•**) radical pair upon photolysis of BAPOs (Scheme 1) and the initiation of radical polymerizations by these radicals is well established.[7–9]

An exceptional property of BAPOs is their wavelength dependent photochemistry, allowing diblock copolymer synthesis.[13–15] Recently, water soluble BAPO derivatives have been utilized to efficiently form functional polymers in aqueous media and at interfaces (*e.g.* in the fields of hydrogel production, inkjet printing, cell encapsulation and 3D printing).[14–23] Upon the photolysis of BAPOs in presence of time-resolved EPR spectra have been reported and phosphorus-containing radicals have been assigned to the EPR data (for details, see Chapter 10 in the Supporting Information).[24,25]

Here, we undertake an in-depth investigation of the reactivity of BAPO derivatives **1**-**3** (Scheme 1) in aqueous and alcoholic media.

Specifically, we utilize an array of complementary techniques, *i.e.* time-resolved and continuous-wave electron paramagnetic resonance (CIDEP and CW-EPR), ^{31}P-NMR, electrospray-ionization mass spectrometry (ESI-MS) and density functional theory (DFT) calculations.

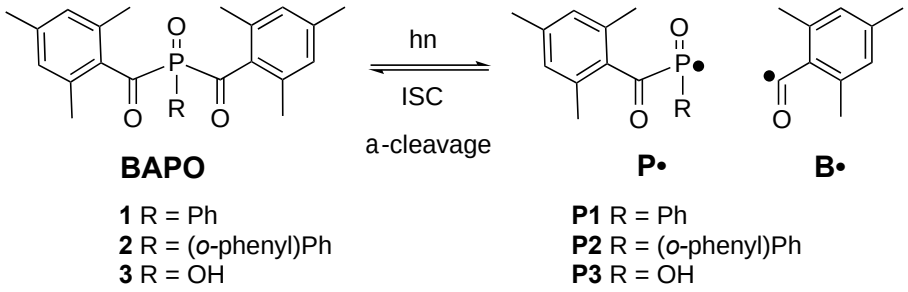

Scheme 1. a) Photolysis of BAPOs **1**–**3** in organic solvents, producing a primary phosphanoyl (**P•**) and benzoyl (**B•**) radical pair. Bond cleavage occurs from the excited triplet state after intersystem crossing (ISC).

It is well established that the photolysis of BAPOs yields the benzoyl radical **B•** and phosphanoyl radical **P•**, which have been characterized by time-resolved EPR (*e.g.* **1**, Figure 1a). These are the radicals initiating macromolecular chain growth. However, in the presence of H_2O or alcohols, two additional doublets (denoted as **C•** and **M•** in Figure 1) appear in the spectrum shortly after the primary **P•** and **B•** radicals are detected. One of these doublets persists substantially longer than the signals of **B•** and **P•** (**C•**, Figure 1, see also the Supporting Information, Figures S1 and S2)).

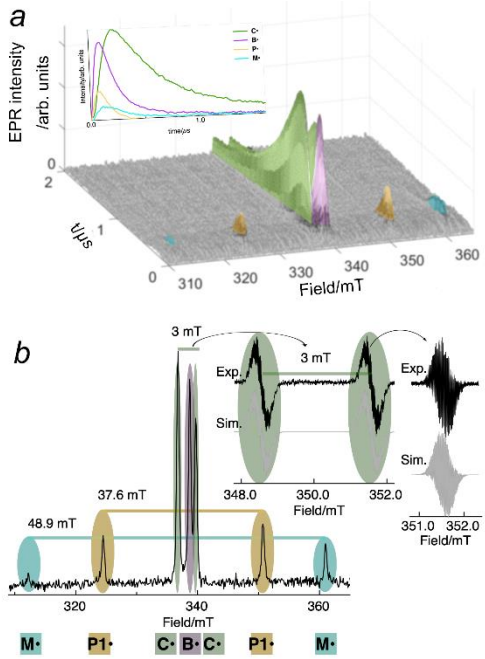

Figure 1. a) TR-EPR spectrum observed 50 ns – 2 μs after laser flash photolysis (355 nm) of **1** (15 mM) in acetonitrile/ethanol, b) cross section along the field axis 300 ns after the laser flash and CW-EPR spectra attributed to radical **C•** obtained upon photolyzing a solution of **1** in acetonitrile/ethanol (7:3) on an extended scale together with the highly resolved high-field line together with the corresponding simulations.

Whereas the peaks of the primary phosphanoyl radical **P1•** decrease with increasing water or alcohol content (see Figure S3 in the Supporting Information) those associated with **C•** become dominating. The signal of the benzoyl radical **B•** remains unaffected, underpining that the new radical is formed from **P1•** and contains a P atom. However, its ^{31}P hyperfine-coupling constant (hfc) of *ca*. 3 mT (Figure 1b) is one order of magnitude smaller than that of **P•**-type radicals (~35 mT).

To test if such a reaction is specific for BAPOs, we have performed analogous experiments with monoacylphosphine oxide (MAPO) **M1** (Figure S4), but the presence of water or alcohols did not affect its reactivity.

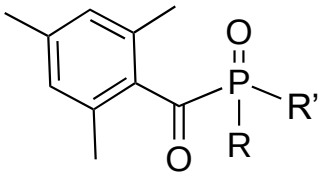

M (R = Ph)
1 R'= Ph
2 R'= H
3 R' = Et

To investigate if the presence of monomers has an influence on the formation and decay rates of radicals **P•**, **M•**, **B•**, and **C•**, we have photolyzed mixtures containing **1** and butyl acrylate (BA) in H_2O/acetonitrile, with H_2O/BA ratios of 0, 1:3, 1:1, and 15:2 (Figure 2). In the absence of H_2O, TR-EPR spectra reveal primary radicals **P1•**, **B•**, together with radicals indicating the growing polymer chain based on **P1** (**P1-BA•**) and **B•** (**B-BA•**) (Figure 2 and Scheme 3). In the same way as observed in the absence of the acrylate (Figure 1), increasing the H_2O content leads to marked growth of EPR signals attributed to a radical **C•** which becomes the dominating component. The signal representing the **P1•**-based polymer chain (**P1-BA•**) disappears (Figure 2b and 2c). In analogy to the experiments performed in the absence of BA, the signals based on the primary benzoyl radical (**B•**, and **B**–**BA•**) remain unaffected. The compositions of the TR-EPR spectral components from **P1•**, **B•**, **P1-BA•**, **B-BA•**, and **C•** depending on the H_2O content, are shown in Figure 3c (*cf*. Table S8).[1] It is evident that the higher the water content, the more the EPR signal attributed to **C•** grows whereas **P1•** and **P1-BA•** gradually disappear. Kinetic traces calculated based on the addition rate coefficients of the primary radicals to BA and that of **P1** to H_2O are shown in Figure 2d. This kinetic simulation underpins that at the initial stages of the polymerization, **P1•** predominately reacts with H_2O ($k_{H2O,}$ of 3.8 x 10^6 $M^{-1}s^{-1}$ is only slightly lower than the rate constant for the addition of **P1•** to BA, $k_{BA,P•}$ = 1.1 x 10^7 $M^{-1}s^{-1}$[8]). Together with its substantial persistence, this explains dominance of **C•** (Scheme 2, Figure 3).

[1] Owing to the EPR spectral pattern being dominated by the "triplet effect" (ref), it is justified translating TR-EPR intensities into relative radical concentrations

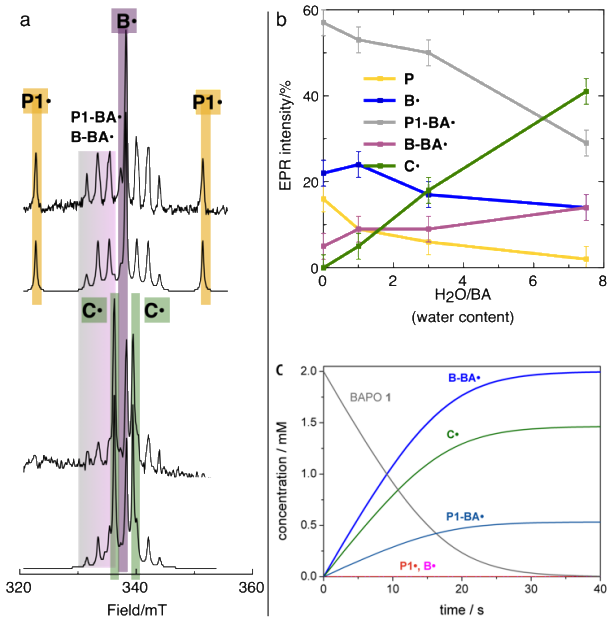

Figure 2. a) Inner part of TR-EPR spectra observed upon laser flash photolysis (355 nm) of **1** (15 mM) in the presence of BA (1.2 M) and H_2O; upper part, H_2O/BA ratio = 0 (water concentration: 0 M); lower part, H_2O/BA ratio = 7.5 (water concentration: 9 M)). The simulated spectra are below the exp. spectra. The spectra are taken between 400 and 600 ns after the laser pulse (boxcar averaging). b) Composition of the EPR signals (components **P1•**, **B•**, **P1-BA•**, **B-BA•** and **C•** in % (overall spectral contribution determined by simulation) depending on the water content of the reaction solutions. c) Kinetic simulation for the above components based on experimentally determined rate constants (for refs., see text and Table S7, Supporting Information for the data used for the EPR simulation)

These results demonstrate that in alcoholic and aqueous solutions, polymerizations are, in the first instance, initiated by the benzoyl radical **B•** whereas radicals of type **P•** will be efficiently converted to **C•**.

The substantially long lifetime of **C•** allows its observation via steady-state CW-EPR using a flow system. This provides highly resolved EPR spectra with significantly improved resolution (not attainable by the time-resolved method, see Figure 1). Advantageously, the primary radicals **B•** and **P•** do not negatively affect the highly resolved spectra, since they are too short-lived to be detected in this latter experiment. The EPR spectrum obtained upon photolysis of **1** in water/acetonitrile is dominated by a ^{31}P hfc of 3.03 mT (identical with the doublet indicated with **C•** in the TR-EPR spectra). Here, this markedly smaller ^{31}P hfc compared with **P**(**1**–**3**)**•** indicates that **C•** contains a phosphorus atom, yet without being a phosphorus-centred radical. Importantly, the EPR patterns inside the ^{31}P doublets depend on: *i*) The nature of the solvent; *i.e.* H_2O reveals a different pattern than D_2O, which again differs from MeOH and EtOH (Figures S6-S9 and Tables

S1-S3) and *ii*) on the substituents R of the parent **P•** radicals (Scheme 1, *cf*. Figure S5 in the Supporting Information). Consequently, the persistent radical **C•** contains the residue R attached to the phosphorus atom (Scheme 1) of the BAPO and the OR' group of the solvent (where R' is H, D or the alkyl group of the alcohol). DFT calculations suggest that water/alcohols preferentially add to the P=O group of the **P•** (rather than to the carbonyl C-atom) leading to phosphous-centered radical **P'•**. Figure 3 shows the calculated conversion of **P'•**, yielding the delocalized (benzoyl) radical **C•**, which is identified by its EPR data and their calculated counterparts (Figure S10 and resembles a protonated radical anion of a MAPO, Scheme S5). The tautomerization connecting **P'•** and **C•** is a downhill process (–62 kJ mol^{-1}) with a low activation barrier of 8.2 kJ mol^{-1}.

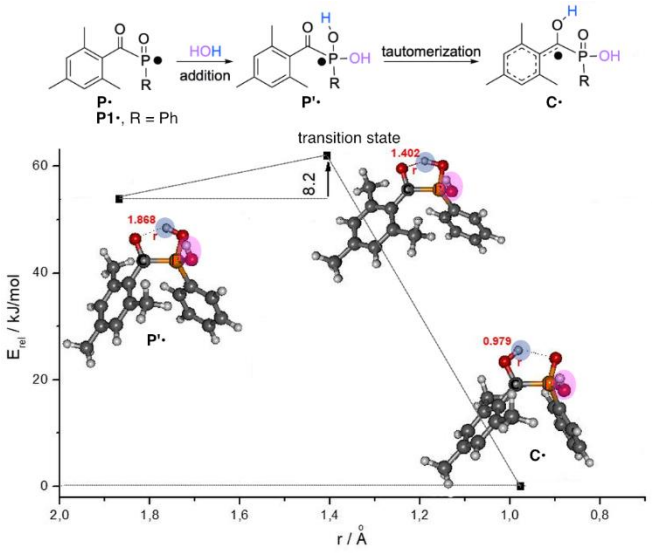

Figure 3. Calculated reaction pathway for the formation of **C•** via **P'**, which is formed by the addition of HOH to the P=O group. The distance between the carbonyl oxygen atom and the added proton from HOH serves as the reaction coordinate (for details, see the Supporting Information).

Further evidence for radical **C•** and insight into its fundamental reactivity arises from high-resolution electrospray ionization mass spectra (ESI-MS)[27,28] obtained upon photolysis of BAPO **1** in acetonitrile/water, acetonitrile/ethanol, or acetonitrile/D_2O. (see Figures S15-S17). Here, radical recombination, H-transfer, and fragmentation are the dominating reaction pathways (Scheme 2). Recombination of **C•** with **B•**, **P1•** or another **C•** yields CB, CP1 and CC (Scheme 2). Alternatively, the C–OH atom of C• is transferred to B• or P1•, yielding a mono(acyl)phosphane oxide (MAPO, **M1**–**M3**) and aldehydes **BH** or **P1H**.[8,29] In the presence of D2O the corresponding deuterated derivatives appear in the mass spectrum (Scheme S4, Table S9, Figure S16)

underpinning **C•** as the source of the transferred hydrogen (deuterium) atom. Cleavage of the C–P bond of C• (fragmentation) results in phosphinic and phosphonic acid derivatives P1A1 and P1A2. We have additionally investigated this fragmentation reaction via DFT. Upon elongation of the C-P bond of **C•**, the hydrogen atom of the C-O-H group is transferred to the P=O, producing a further benzoyl radical **B•** and species **P(III)**, which tautomerizes to the more stable phosphinic acid derivative **PA1**. Alternatively, **P(III)** can be oxidized to the phosphonic acid derivative **PA2** (see the Supporting Information, Scheme S2 and Figure S13).

The very efficient formation of a MAPO is substantiated by irradiating **1** in ethanol at wavelengths > 410 nm. ^{31}P NMR reveals a photoproduct with δ = 13.63 ppm, (Figure S18), which perfectly corresponds with the ^{31}P NMR signal of the commercially available MAPO photoinitiator Irgacure® TPO-L (**M1**, R' = OEt in Scheme 2, Figure S19). Additional proof arises from the TR EPR spectrum obtained upon photolysis of **1** in H_2O/acetonitrile at 355 nm. An additional doublet with an ^{31}P hfc of 48.9 mT (see Figure 1) occurs exactly matching the P-centered radical detected upon photolysis of MAPO Irgacure® TPO-L, **M1•,** R' = OEt, Figure S20). Accordingly, the formation of a MAPO via **P•**-type radicals in alcohol or H_2O is highly likely.

The preferred formation of a MAPO upon long-wavelength irradiation resembles the wavelength selective reactivity of BAPOs:[15,13] light of wavelengths > 410 nm does not cause the photocleavage of MAPOs, since they absorb below 410 nm (Figures S19 and S20).[15,13] This formation of a MAPO is decisive for the use of BAPOs in aqueous media, since this compound again is a photoinitiator and will remain in the polymer as a (dormant) photoactive species.[19]

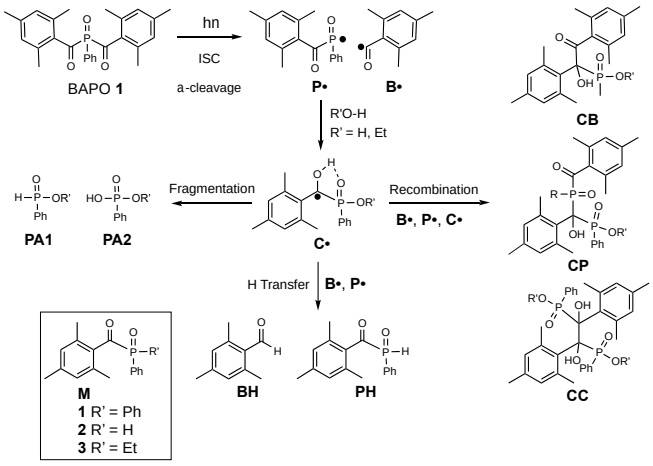

Scheme 2. Formation and follow-up reactions of **C•**. Recombination, H-transfer and fragmentation products identified via ESI-MS. For residues R of BAPOs **1**–**3** and the resulting MAPOs **M1**–**M3** refer to Scheme 1b. Residues R' correspond to H, D or the alkyl group of the alcohol.

This MAPO Radical **C•** is inert towards radical addition reactions. However, **C•** acts as an electron transfer agent. Tetracyanoethene (TCNE) was added to an aqueous acetonitrile solution of BAPO **1**, which was irradiated at 430 nm (LED). Immediately the TCNE radical anion $[TCNE]^{\bullet-}$ was detected (Scheme 3 and Supporting Information). This reactivity is observed in the presence and in the absence of BA.

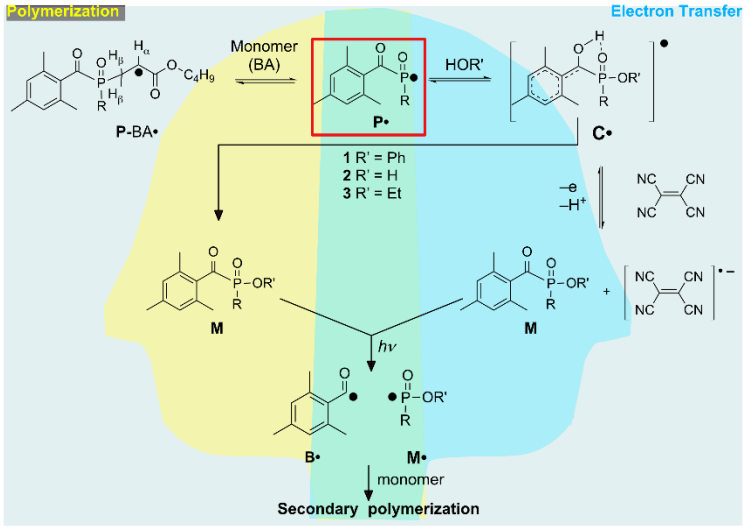

Scheme 3. Bifunctional reactivity of **P•** in non-aqueous and aqueous (R'OH solution: polymerization and electron transfer.

The photochemistry of bis(acyl)phosphane oxides in aqueous and alcoholic media indicates unexpected transformations of phosphanoyl radicals into the rather persistent radical **C•**, consistently characterized by EPR, TR-EPR, ESI-MS, and theoretical calculations. Radical **C•** resembles a protonated benzophenone radical with spin delocalization onto the adjacent phosphorus center. This radical is also closely related to the radical anion of monoacylphosphine oxides. The hyperfine data of these two radical types are closely related (refer the Supporting Information, section 7, Scheme S5).

In aqueous/acloholic media, the formation of **C•** competes with radical photopolymerizations initiated by radical **P•** . Although **C•** is unreactive towards monomers it is converted to a MAPO derivative. The latter serves as a secondary photoinitiator and may allow the synthesis of complex polymer architectures by performing simple polymerization steps with a single photoinitiator in aqueous media. The unprecedented reaction pathway involving radical **C•**, which serves as a reducing agent, opens the opportunity to initiate light-induced simultaneous radical and electron-transfer reactions.

3.3.3. References

[1] W. Rutsch, K. Dietliker, D. Leppard, M. Köhler, L. Misev, U. Kolczak, G. Rist, *Prog. Org. Coat.* **1996**, *27*, 227.

[2] K. Dietliker, T. Jung, J. Benkhoff, H. Kura, A. Matsumoto, H. Oka, D. Hristova, G. Gescheidt, G. Rist, *Macromol. Symp.* **2004**, *217*, 77.

[3] Y. Yagci, S. Jockusch, N. J. Turro, *Macromolecules* **2010**, *43*, 6245.

[4] U. Kolczak, G. Rist, K. Dietliker, J. Wirz, *J. Am. Chem. Soc.* **1996**, *118*, 6477.

[5] G. W. Sluggett, P. F. McGarry, I. V. Koptyug, N. J. Turro, *J. Am. Chem.Soc.* **1996**, *118*, 7367.

[6] G. W. Sluggett, C. Turro, M. W. George, I. V. Koptyug, N. J. Turro, *J. Am. Chem. Soc.* **1995**, *117*, 5148.

[7] S. Jockusch, I. V. Koptyug, P. F. McGarry, G. W. Sluggett, N. J. Turro, D. M. Watkins, *J. Am. Chem. Soc.* **1997**, *119*, 11495.

[8] S. Jockusch, N. J. Turro, *J. Am. Chem. Soc.* **1998**, *120*, 11773.

[9] I. Gatlik, P. Rzadek, G. Gescheidt, G. Rist, B. Hellrung, J. Wirz, K. Dietliker, G. Hug, M. Kunz, J.-P. Wolf, *J. Am. Chem. Soc.* **1999**, *121*, 8332.

[10] D. Hristova, I. Gatlik, G. Rist, K. Dietliker, J.-P. Wolf, J.-L. Birbaum, A. Savitsky, K. Möbius, G. Gescheidt, *Macromolecules* **2005**, *38*, 7714.

[11] D. Hristova-Neeley, D. Neshchadin, G. Gescheidt, *J. Phys. Chem. B* **2015**, *119*, 13883.

[12] M. Griesser, D. Neshchadin, K. Dietliker, N. Moszner, R. Liska, G. Gescheidt, *Angew. Chem. Int. Ed.* **2009**, *48*, 9359.

[13] E. D. Günersel, Y. Hepuzer, Y. Yağcı, *Angew. Makromol. Chem.* **1999**, *264*, 88.

[14] H. Grützmacher, J. Geier, D. Stein, T. Ott, H. Schönberg, R. H. Sommerlade, S. Boulmaaz, J.-P. Wolf, P. Murer, T. Ulrich, *CHIMIA***2008**, *62*, 18.

[15] A. Eibel, D. E. Fast, J. Sattelkow, M. Zalibera, J. Wang, A. Huber, G.Müller, D. Neshchadin, K. Dietliker, H. Plank et al., *Angew. Chem. Int. Ed.* **2017**, *56*, 14306.

[16] A. Eibel, M. Schmallegger, M. Zalibera, A. Huber, Y. Bürkl, H. Grützmacher, G. Gescheidt, *Eur. J. Inorg. Chem.* **2017**, 2469.

[17] A. Huber, A. Kuschel, T. Ott, G. Santiso-Quinones, D. Stein, J. Bräuer, R. Kissner, F. Krumeich, H. Schönberg, J. Levalois-Grützmacher et al., *Angew. Chem. Int. Ed.* **2012**, *51*, 4648.

[18] G. Müller, M. Zalibera, G. Gescheidt, A. Rosenthal, G. Santiso-Quinones, K. Dietliker, H. Grützmacher, *Macromol. Rapid Commun.* **2015**, *36*, 553.

[19] S. Benedikt, J. Wang, M. Markovic, N. Moszner, K. Dietliker, A. Ovsianikov, H. Grützmacher, R. Liska, *J. Polym. Sci. A Polym. Chem.* **2016**, *54*, 473.

[20] J. Wang, G. Siqueira, G. Müller, D. Rentsch, A. Huch, P. Tingaut, J. Levalois-Grützmacher, H. Grützmacher, *Chem. Commun.* **2016**, *52*,2823.

[21] J. Wang, S. Stanic, A. A. Altun, M. Schwentenwein, K. Dietliker, L. Jin, J. Stampfl, S. Baudis, R. Liska, H. Grützmacher, *Chem. Commun.* **2018**, *54*, 920.

[22] J. Wang, A. Chiappone, I. Roppolo, F. Shao, E. Fantino, M. Lorusso, D. Rentsch, K. Dietliker, C. F. Pirri, H. Grützmacher, *Angew. Chem. Int. Ed.* **2018**, *57*, 2353.

[23] D. E. Fast, M. Zalibera, A. Lauer, A. Eibel, C. Schweigert, A.-M. Kelterer, M. Spichty, D. Neshchadin, D. Voll, H. Ernst et al., *Chem. Commun.* **2016**, *52*, 9917.

[24] R. Shergill, M. Haberler, C. B. Vink, H. V. Patten, J. R. Woodward, *Phys. Chem. Chem. Phys.* **2009**, *11*, 7248.

[25] D. Darvasiová, Z. Barberiková, A. Eibel, M. Schmallegger, G.Gescheidt, M. Zalibera, D. Neshchadin, *Polym. Chem.* **2017**, *8*, 1719.

[26] A. Yurkovskaya, O. Morozova, G. Gescheidt in *Encyclopedia of Radicals in Chemistry, Biology and Materials* (Eds.: C. Chatgilialoglu, A. Studer), John Wiley & Sons, Chichester, West Sussex, Hoboken, N.J., **2012**.

[27] S. D. Hanton, *Chem. Rev.* **2001**, *101*, 527.

[28] S. Banerjee, S. Mazumdar, *Int. J. Anal. Chem.* **2012**, *2012*, 282574.

[29] C. S. Colley, D. C. Grills, N. A. Besley, S. Jockusch, P. Matousek, A. W. Parker, M. Towrie, N. J. Turro, P. M. W. Gill, M. W. George, *J. Am. Chem. Soc.* **2002**, *124*, 14952.

3.3.4. Supporting Information

Supporting information for this article is available on the WWW under *http://dx.doi.org/10.1002/chem.201900935*

3.4. Benzil/triethylamine: a photo-reducing system for Cu^{2+}

Max Schmallegger[a] and Georg Gescheidt[a]

[a] Institute of Physical and Theoretical Chemistry, Graz University of Technology

Published in: *Monatshefte für Chemie – Chemical Monthly* **2017**, 149, 499-504

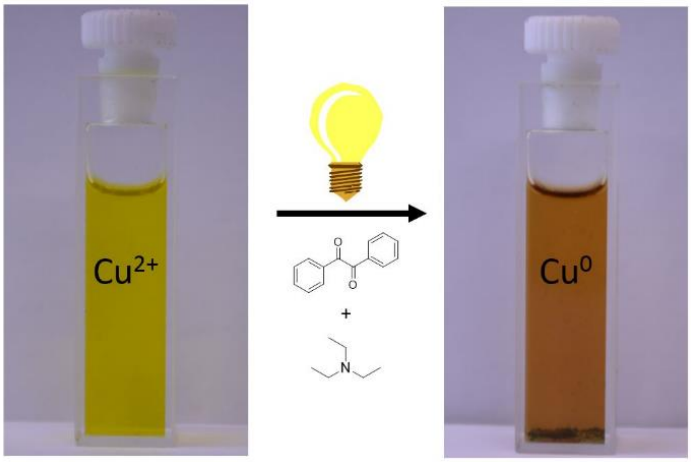

3.4.1. Abstract

We have investigated the photo-induced reduction of Cu^{2+} to Cu^0 using benzil/triethylamine mixtures. The formation of elemental Cu is indicated by the appearance of its characteristic plasmon absorption peaks at 515 nm and 620 nm. Importantly, the nature of the counter ion of the Cu^{2+} salt affects the reduction process. In the presence of Cl^- the reaction is faster than with SO_4^{2+}. Continuous-wave EPR provides insight into the mechanism: upon irradiation, triethylamine acts as electron donor leading to the formation of the benzil radical anion, which, in turn, reduces Cu^{2+} to Cu^0. Triethylamine is oxidized to its radical cation and undergoes rapid follow-up reactions.

3.4.2. Introduction

Nanomaterials have experienced a vast growth in interest over the last years. They have been utilized in fields like nonlinear optics and electric conduction. [1-3] Metallic nanoparticles have gained attention because of their remarkable chemical properties, leading to applications *e.g.* for molecular imaging[4] or catalysis.[5]

A key point for producing nanoparticles is the reduction of metal salts to elemental metals in a controlled way. Chemical, thermal, radiation-chemical, sonochemical, and photochemical methods have been followed in this context.[6-9] However, many of these approaches require expensive reagents, hazardous reaction conditions, and long reaction times combined with difficult isolation procedures.[7,10] Photochemical methods offer a valuable access to metal reductions allowing temporal and spatial control.[11-18] In such procedures, organic radical anions, produced by photochemical reduction, act as mediators, reducing metal cations to elementary metals.[16,19] A group of reagents often employed in photo-reductions of metal salts include ketones such as acetophenone[11], acetone[20], and benzophenone.[21] The use of ketones combined with hydrocarbons, alcohols, ethers, and amines has been reported.[22,23] In such reactions, highly reactive ketyl radicals or ketyl radical anions are formed as intermediates. A substantial requirement for the reducing species is their oxidation potential, since it has to match the potential for the reduction of the metal cation. In terms of metals, the generation of Cu nanoparticles from Cu^{2+} salts has been of prominent interest because of the favorable availability of Cu salts and the activity of Cu as catalyst, in photovoltaics, electronics, and optics.[24-27]

The aim of our investigation is to inspect if benzil (1,2-diphenylethane-1,2-dione,1) can be utilized for the photo-reduction of Cu^{2+} salts. Benzil is one of the most common (and low cost) diketones and its photochemistry has been well characterized[28,29]; nevertheless, benzil has yet only seen limited use in photo-induced redox reactions with metal salts. While the photo-reduction of ketones and diketones in the presence of donor systems, e.g., amines, and the intermediate formation of ketyl radicals are well understood, there are still remaining questions with regard to the mechanism of metal reduction. The mechanisms depicted in Scheme 1 have been suggested for the photo-reduction of metal salts. Here, either ketyl radicals[11,12,17,21] or the ketyl radical anions[30] act as electron donors.

In this publication, we report on the reaction of photo-excited benzil (**1**) and triethylamine (**2**) as a model donor with Cu^{2+} salts. We followed the reactions by steady-state photolysis (SSP), continuous-wave electron paramagnetic resonance (cw-EPR) spectroscopy, and laser-flash photolysis (LFP).

Scheme 1

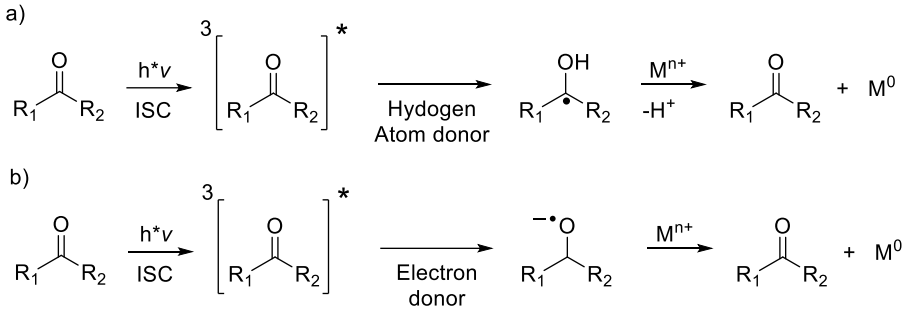

3.4.3. Results and Discussion

Steady-State Photolysis We have photolyzed (steady-state) a solution of **1** and **2** in CH_3CN containing either $CuCl_2$ or $CuSO_4$ leading to a new strong absorption band centered at 515 nm and a weaker band at 620 nm (Figure 1). They can be attributed to characteristic plasmon absorption bands of colloidal Cu.[31-35] It is well-established that the plasmon abosprtion of elemental copper depend on the size of the aggregates formed.[34-36] Therefore, the two absorption bands are in line with an initial formation of small copper aggregates resulting in the band centered at 515 nm, whereas that at 620 nm points to the slower growth of bigger colloids. Control experiments with solutions of the mixtures **1/2**, **1**/$CuCl_2$ ($CuSO_4$), **2**/$CuCl_2$ ($CuSO_4$), and singly $CuCl_2$ or $CuSO_4$ (see SI) substantiate these findings. None of these experiments yielded the bands at 515 and 620 nm upon photolysis. The solution **1/2** showed absorption spectra indicating the bleaching of the band attributed to parent benzil at 360 nm[37], whereas no spectral changes could be detected for the remaining controls. Accordingly, the copper salts are not decomposed in our irradiation experiments and are inert toward benzil in the absence of the amine and vice versa.

Remarkably, the rates for the reduction depend on the counterions of the copper salts (Figure2). For $CuCl_2$, the bands attributed to the plasmon absorption grow in at a faster rate than for $CuSO_4$. This is in line with the results of Pacioni et al. as well as Soares et al., who reported that chloride anions catalyze the disproportionation mediating the conversion of Cu^+ to Cu^0. [33,37] In addition, electrochemical studies have shown that catalytic amounts of Cl^- accelerate the reduction of Cu^{2+} to Cu^+ [38-10] (Scheme 2).

Scheme 2

$$Cu^{+} + Cu^{+} \rightleftharpoons Cu^{2+} + Cu^{0}$$

$$Cu^{+} + Cu^{+} + Cl^{-} \rightleftharpoons CuCl^{+} + Cu^{0}$$

$$Cu^{+} + Cu^{+} + Cl^{-} \rightleftharpoons CuCl^{-} + Cu^{2+}$$

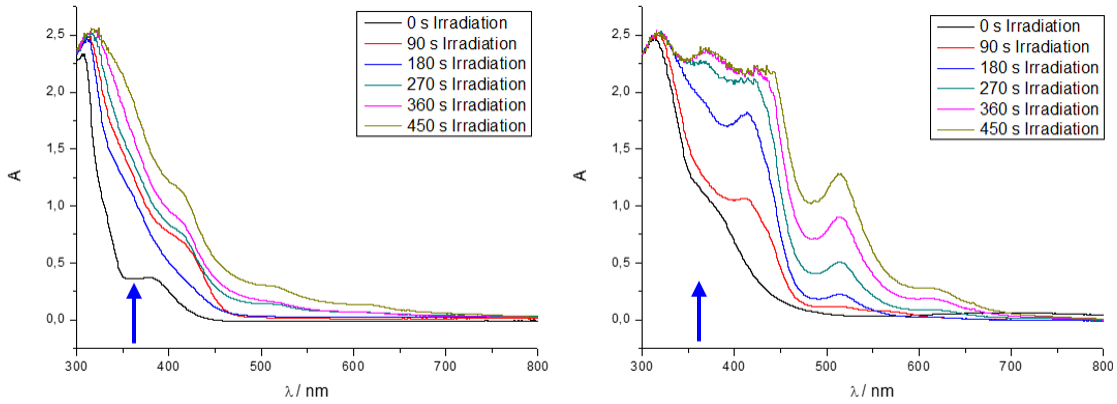

Figure 1 Absorbance spectra representing the generation of colloidal copper upon photolysis of the **1/2** system and $CuSO_4$ (left) or $CuCl_2$; the arrow represent the irradiation wavelength

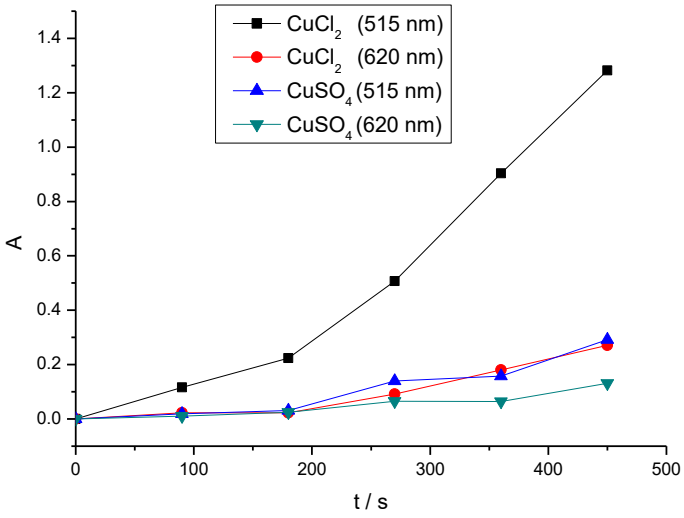

Figure 2 Time trace of the formation of colloidal copper monitored at 515 nm and 620 nm upon photolysis of the **1/2** system and $CuCl_2$ or $CuSO_4$

Continuous-wave Electron Paramagnetic Resonance When we observed the solutions of **1** in the presence of **2** in CH_3CN by cw-EPR under continuous irradiation, we have detected the characteristic EPR spectrum attributable to the radical anion of benzil (**1**$^{\bullet-}$). Simulations reveal (Figure 3, Table) an excellent agreement with previously published data.[42,43] The formation of **1**$^{\bullet-}$ indicates that upon irradiation **1** undergoes excitation and intersystem crossing to the triplet state **1*** [43] and is subsequently reduced by **2**, as indicated in Scheme 3. This is in line with previous studies showing that also for other aromatic ketones such as benzophenone, the corresponding radical anion was observed in photolysis experiments in the presence of alcohols[44] and amines.[45]

Scheme 3

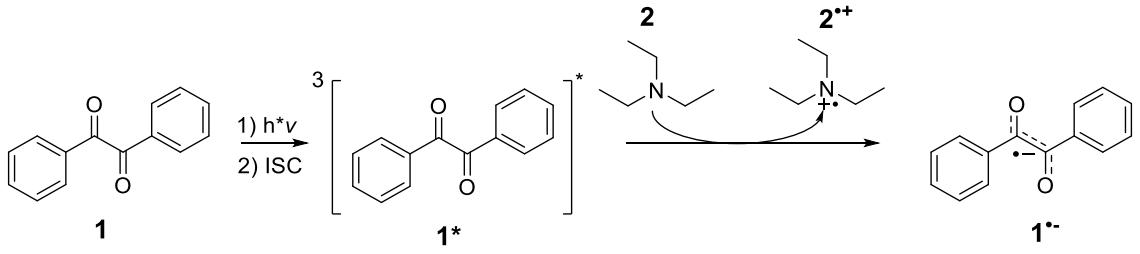

The radical cation of **2**$^{\bullet+}$, formed together with **1**$^{\bullet-}$, is not detected in the EPR spectrum. It is well established that radical cations of amines undergo follow-up reactions, leading to both diamagnetic and paramagnetic species[23,37,46,47] (Scheme 4). Beside parent **2**, the α-aminoalkyl radical **4** may serve as an electron-donating species.[17,37,48] Therefore, an additional reduction of Cu^{2+} by **4** should be considered when discussing the redox reactions in this system.[44] However, it was shown that **2**$^{\bullet+}$ can undergo rapid follow-up reactions leading to the formation of diamagnetic species.[33,45,46] Additionally, product analysis by 1H-NMR after irradiation (see Supporting Information) reveals formation of *N,N-diethylethenamine* (5), further rationalizing that the electron transfer from triethylamine - derived radicals only plays a minor role in this system.

Scheme 4

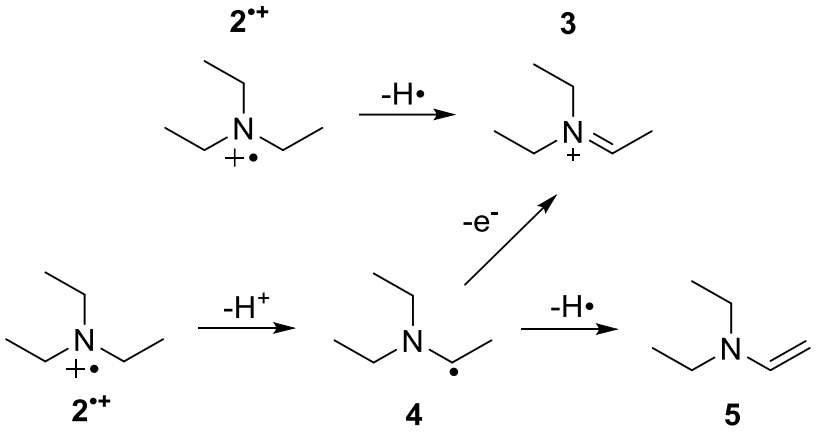

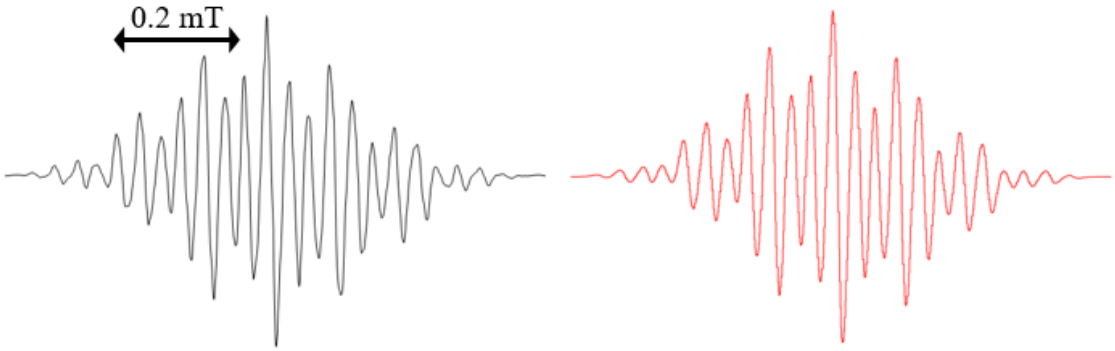

Figure 3. cw-EPR spectrum of **1**$^{\bullet-}$ obtained upon the reaction of **1**/**2** in CH_3CN under continuous irradiation; experimental (left) and simulation (right)

Table 1. Hyperfine coupling constants of **1**$^{\bullet-}$ in CH_3CN/**2**

Position	hfc / mT	
	CH_3CN	Literature[38]
a_{ortho} (4H)	0.103	0.099
a_{meta} (4H)	0.039	0.036
a_{para} (2H)	0.108	0.112

Laser Flash Photolysis To evaluate the role of **2** for the reduction of Cu^{2+} to Cu^0 at a short (ns) time scale, we have carried out laser-flash photolysis (LFP) experiments. Figure 4 shows transient absorption spectra of **1**/**2** in CH_3CN and corresponding reference measurements, in which **2** was omitted. Photolysis of **1** in CH_3CN yields two distinct peaks at 350 nm and at 480 nm, which are both attributable to **1***.[31,35,43] Upon addition of **2** to the solution, significant changes in the

spectrum occur: The absorptions centered at 480 and 350 nm disappear, while two new, broad bands centered at 360 and 580 nm appear; they are assigned to $\mathbf{1}^{\bullet-}$.[51-53] This indicates a fast electron transfer reaction of **1*** with **2**, leading to the formation of $\mathbf{1}^{\bullet-}$ and $\mathbf{2}^{\bullet+}$, respectively.[37,54]

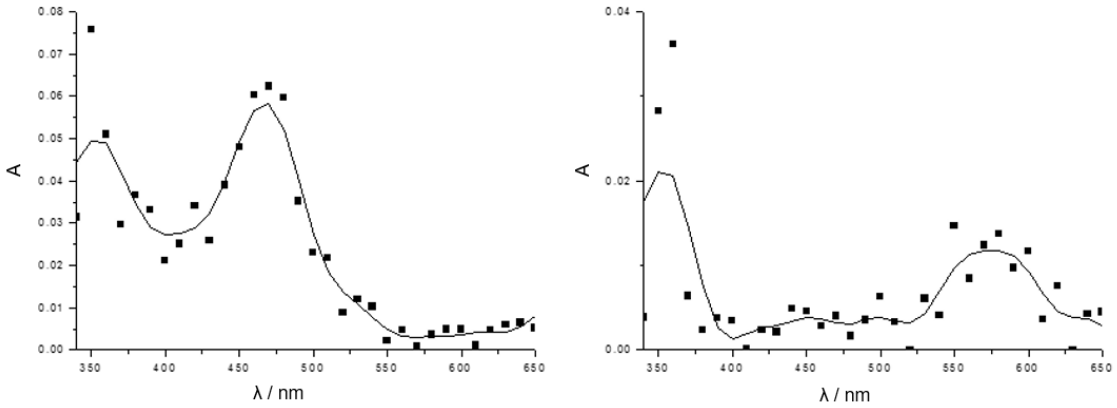

Figure 4 Transient absorption spectra of radicals produced by photolysis of **1** in CH_3CN (left) and CH_3CN/**2** 0.2 µs after the laser pulse. See text for the assignment of the absorption bands

3.4.4. Conclusions

Our spectroscopic investigation shows that benzil acts as an efficient photo-reducing agent for copper salts in the presence of an amine donor. The efficiency and the rate of the photo-reduction are markedly influenced by the counterions of the copper salts. We have demonstrated the intermediate formation of the benzil radical anion by cw-EPR and LFP. From our experiments, we conclude that $\mathbf{1}^{\bullet-}$, formed upon photolysis in the presence of **2**, is highly redox active and can reduce Cu^{2+} to Cu^0. In addition, no indication that the corresponding radical cation of **2** takes part in the reduction of Cu^{2+} to Cu^0could be found. This is presumably due to the fast follow-up reaction of $\mathbf{2}^{+}$, leading to the formation of diamagnetic products that are not redox active.

In future work, this cost-effective and simple approach for the photo-induced reduction of Cu^{2+} to elemental copper could be used for the production of copper nanoparticles by employing different irradiation times as well as characterization methods such as transmission electron microscopy (TEM) to form nanoparticles with defined shape and size.[16,55,56]

3.4.5. Experimental

Materials. Benzil (**1**) (Fluka), trimethylamine (**2**) (Sigma-Aldrich), copper(II)sulphate (Roth), copper(II)chloride (Riedel-de Haën) and acetonitrilie (Riedel-de Haën) were obtained at the highest purity available and employed as received.

Steady-State Photolysis. UV-Vis spectra were recorded on a fiber optics diode array spectrometer (J&M Analytik AG). Photolysis was conducted using a Hamamatsu Lightingcure LC4 (Hg-Xe lamp, 3500 mW/cm^2, λ_{max}=365 nm). The concentration of **1**, $CuSO_4$ and $CuCl_2$ were 5 mM for all measurements. The concentration of **2** was 100 mM in all measurements. 10 mg polyvinylpyrrolidone were added to all samples to help solubilize the copper salts and the formed Cu^0 precipitate.

EPR spectroscopy. Cw-EPR spectra were recorded on a Bruker X-band spectrometer (EMX, 100 kHz field modulation) at room temperature with 0.025 mT field modulation amplitude. The signals correspond to the steady-state concentration of radicals accumulated in flow system (0.4 mm quartz flat cell) under continuous irradiation The concentrations of **1** and **2** were 100 mM and 500 mM, respectively.

Laser flash photolysis. LFP experiments were carried out with a LKS80 spectrometer (Applied Photophysics). Excitation of the samples was carried out with the light of a frequency triplet Spitlight Compact 100 (Innolas) Nd:YAG laser at 355 nm (8 ns pulse duration; 10 mJ/pulse energy). The concentration of **1** in solution was adjusted to achieve absorbance of around 0.5 at the excitation wavelength. The concentration of **2** was 100 mM in all measurements.

^{1}H NMR experiments. ^{1}H NMR spectra (32 scans) were recorded on a 200 MHz Bruker Avance DPX spectrometer. Chemical shifts (δ) are reported in ppm relative to tetramethylsilane (TMS) using the residual undeuterated solvent as an internal reference (acetonitrile-d_3, δH = 1.94 ppm).

3.4.6. References

[1] G. Schmid, *Clusters and Colloids: From Theory to Applications*, Wiley, **1994**.

[2] B. C. Gates, *Chem. Rev.* **1995**, *95*, 511–522.

[3] N. A. Dhas, C. P. Raj, A. Gedanken, *Chem. Mater.* **1998**, 1446–1452.

[4] R. F. Minchin, D. J. Martin, *Endocrinology* **2010**, *151*, 474–481.

[5] J. Spivey, F. Tao, *Metal Nanoparticles for Catalysis: Advances and Applications*, The Royal Society Of Chemistry, **2014**.

[6] B. L. Cushing, V. L. Kolesnichenko, C. J. O'Connor, *Chem. Rev.* **2004**, *104*, 3893–3946.

[7] J. A. Dahl, B. L. S. Maddux, J. E. Hutchison, *Chem. Rev.* **2007**, *107*, 2228–2269.

[8] A. Roucoux, J. Schulz, H. Patin, *Chem. Rev.* **2002**, *102*, 3757–3778.

[9] N. A. Dhas, C. P. Raj, A. Gedanken, *Chem. Mater.* **2006**, *9*, 1446.

[10] R. Mittu, *Int. Adv. Res. J. Sci. Eng. Technol.* **2016**, *3*, 37–40.

[11] M. Sakamoto, M. Fujistuka, T. Majima, *J. Photochem. Photobiol. C Photochem. Rev.* **2009**, *10*, 33–56.

[12] Y. Yang, L. Liu, H. Yin, D. Xu, G. Liu, X. Song, J. Liu, *J. Phys. Chem. C* **2013**, *117*, 11858–11865.

[13] J. C. Scaiano, C. Aliaga, S. Maguire, D. Wang, *J. Phys. Chem. B* **2006**, *110*, 12856–12859.

[14] T.-L. Wee, B. D. Sherman, D. Gust, A. L. Moore, T. A. Moore, Y. Liu, J. C. Scaiano, *J. Am. Chem. Soc* **2011**, *133*, 16742–16745.

[15] T. Itakura, K. Torigoe, K. Esumi, *Langmuir* **1995**, *11*, 4129–4134.

[16] K. L. Mcgilvray, M. R. Decan, D. Wang, J. C. Scaiano, *J. Am. Chem. Soc.* **2006**, *128*, 15980–15981.

[17] M. L. Marin, K. L. Mcgilvray, J. C. Scaiano, *J. Am. Chem. Soc.* **2008**, 16572–16584.

[18] L. Maretti, P. S. Billone, Y. Liu, J. C. Scaiano, *J. Am. Chem. Soc.* **2009**, *131*, 13972–13980.

[19] O. R. Miranda, T. S. Ahmadi, *J. Phys. Chem. B* **2005**, *109*, 15724–34.

[20] Y. Yonezawa, T. Sato, S. Kuroda, K. Kuge, *J. Chem. Soc. Faraday Trans.* **1991**, *87*, 1905.

[21] N. Kometani, H. Doi, K. Asami, Y. Yonezawa, *Phys. Chem. Chem. Phys.* **2002**, *4*, 5142–5147.

[22] N. Filipescu, F. L. Minn, *J. Am. Chem. Soc.* **1968**, *90*, 1544–1547.

[23] C. Devadoss, R. W. Fessenden, *J. Phys. Chem.* **1991**, *95*, 7253–7260.

[24] L. Bunbury, *Can. J. Chem.* **1972**, 2499–2510.

[25] J. W. Park, E. K. Kim, K. K. Park, *Bull. Korean Chem. Soc.* **2002**, *23*, 1229–1234.

[26] A. Henglein, *Chem. Mater.* **1998**, *10*, 444–450.

[27] S. Kapoor, T. Mukherjee, *Chem. Phys. Lett.* **2003**, *370*, 83–87.

[28] S. Kapoor, D. K. Palit, T. Mukherjee, *Chem. Phys. Lett.* **2002**, *355*, 383–387.

[29] N. L. Pacioni, A. Pardoe, K. L. McGilvray, M. N. Chrétien, J. C. Scaiano, *Photochem. Photobiol. Sci.* **2010**, *9*, 766–774.

[30] J. Hambrock, R. Becker, A. Birkner, J. Wei, R. A. Fischer, *Chem. Commun.* **2002**, *1*, 68–69.

[31] G. H. Chan, J. Zhao, E. M. Hicks, G. C. Schatz, R. P. Van Duyne, *Nanoletters* **2007**, *7*, 1947–1952.

[32] P. Pootawang, N. Saito, S. Y. Lee, *Nanotechnology* **2013**, *24*, DOI 10.1088/0957-4484/24/5/055604.

[33] J. C. Scaiano, *J. Phys. Chem.* **1981**, *85*, 2851–2855.

[34] M. Soares, S. Wasle, K. G. Weil, K. Doblhofer, *J. Electroanal. Chem.* **2002**, *532*, 353–358.

[35] Z. Nagy, J. P. Blaudeau, N. C. Hung, L. A. Curtiss, D. J. Zurawski, *J. Electrochem. Soc.* **1995**, *142*, 10–13.

[36] B. K. Doblhofer, S. Wasle, D. M. Soares, K. G. Weil, G. Weinberg, G. Ertl, *Z. Phys. Chem.* **2003**, *217*, 479–491.

[37] A. Alberti, C. Seconi, G. F. Pedulli, A. Degl'Innocenti, *J. Organomet. Chem.* **1983**, *253*, 291–299.

[38] R. Dehl, G. K. Fraenkel, *J. Chem. Phys.* **1963**, *39*, 1793.

[39] J. Gersdorf, J. Mattay, H. Goerner, *Sect. Title Phys. Org. Chem.* **1987**, *109*, 1203–1209.

[40] G. Porter, F. Wilkinson, in *Prim. Photochem. Process. Aromat. Mol.*, **1996**, pp. 16794–16800.

[41] M. Hoshlno, S. Arai, S. Imamura, *J. Phys. Chem.* **1976**, *80*, 2724–2727.

[42] J. Hu, J. Wang, T. H. Nguyen, N. Zheng, *Beilstein J. Org. Chem.* **2013**, *9*, 1977–2001.

[43] S. Inbar, H. Linschitz, S. G. Cohen, *J. Am. Chem. SOC* **1981**, 1048–1054.

[44] N. Kim-Thuan, J. Scaiano, *Int J Chem Kinet* **1984**, *16*, 371–377.

[45] T. Kausche, J. Säuberlich, E. Trobitzsch, D. Beckert, K. P. Dinse, *Chem. Phys.* **1996**, *208*, 375–390.

[46] K. Bhattacharyya, P. K. Das, *J. Phys. Chem.* **1986**, *90*, 3987–3993.

[47] M. Mukai, S. Yamauchi, N. Hirota, *J. Phys. Chem* **1992**, *6*, 3305–3311.

[48] T. Okutsu, M. Ooyama, H. Hiratsuka, *J. Phys. Chem. A* **2000**, *104*, 288–292.

[49] M. Hayon, E.; Ibata, T.; Lichtin, N. N.; Simica, *J. Phys. Chem.* **1972**, *76*, 2072–2078.

[50] M. Mukai, S. Yamauchi, N. Hirota, *J. Am. Chem. Soc.* **1989**, 4411–4413.

3.4.7. Supporting Information

Supporting information for this article is available on the WWW under *https://doi.org/10.1007/s00706-017-2085-7*

3.5. Two in One Go: Wavelength- and Site-Selective Generation of Copper Nanoparticles and Polymer Matrices Using Bisacylphosphane Oxides

Max Schmallegger,[a] Anna Eibel,[a] Raffaele Ricco,[a] Angela Chemelli,[b] Sandro Kovac,[a] Franz Mautner,[a] Hansjörg Grützmacher,[c] and Georg Gescheidt*[a]

[a] Institute of Physical and Theoretical Chemistry, Graz University of Technology
[b] Institute of Inorganic Chemistry, Graz University of Technology
[c] ETH Zurich, Swiss Federal Institute of Technology

Publication in Preparation

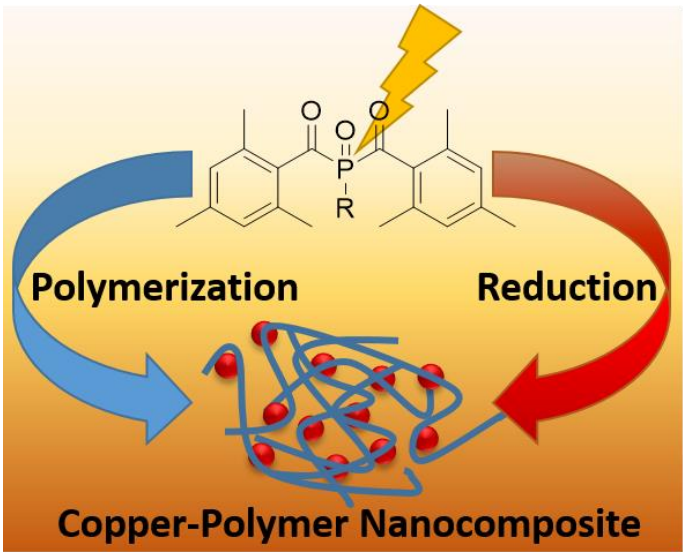

3.5.1. Abstract

Copper nanoparticles have been produced from Cu^{2+} salts by photo-induced reduction by bis(acyl)phosphane oxides (BAPOs) in the presence of H_2O and alcohols. Simultaneously, the nanoparticles can be selectively encapsulated in polymer matrices. The reductive power of the BAPOs particularly originates in a long-lived delocalized benzoyl-type carbon-centered radical formed via solvolysis of a primary phosphanoyl radical acting as an excellent electron-donor. Moreover, we show that carefully choosing the photo-reducing agent offers the possibility to control the size of the copper nanoparticles.

3.5.2. Main Text

Copper nanoparticles and materials based on those have remarkable chemical properties. They have been applied for catalysis[1–7], molecular imaging, as chemical and biological sensors[8,9], and in the fields of optics, optoelectronics, photonics and electric conduction.[10–14]

Metal nanoparticles are generally generated by the reduction of metal salts by chemical, electrochemical and thermal methods.[12,15–19]. However, these methods suffer from requiring expensive reagents, hazardous reaction conditions and long reaction times combined with difficult isolation procedures.[18,20] Photochemical reduction overcomes these limitations and additionally provides temporal and spatial control; *e.g.* aromatic ketones and α-hydroxyketones serve as photo-reducing agents for copper salts.[21–25][26]

Here we report on the preparation of Cu nanoparticles using phosphorus-based photoinitiators. Recently, bis(acyl)phosphane oxide photoinitiators[32,33,42,34–41] (BAPOs) gained attention as photo-reductants for the synthesis of copper nanoparticles[27] and for the photoreduction of copper(II) to copper(I) connected with photo-click chemistry, especially azide-alkyne cycloadditions.[28–31]

We have identified the delocalized ketyl-type radical (**C•**), rapidly formed upon solvolysis of the primary radical **P•** (Scheme 1). [Ref-C•] Here we show that it is this radical **C•** which acts as the primary agent reducing Cu^{2+} to $Cu^{0.}$ Moreover, we demonstrate that carefully choosing the photo-reducing agent and the reaction conditions allows controlling the size of the copper nanoparticles and site-selective polymerizations and metal depositions.

The current study has been accomplished utilizing an array of complementary techniques, *i.e.* continuous-wave electron paramagnetic resonance (CW-EPR), steady-state UV-VIS

spectroscopy, X-ray powder diffraction (XRD), dynamic light scattering (DLS) and scanning electron microscopy (SEM).

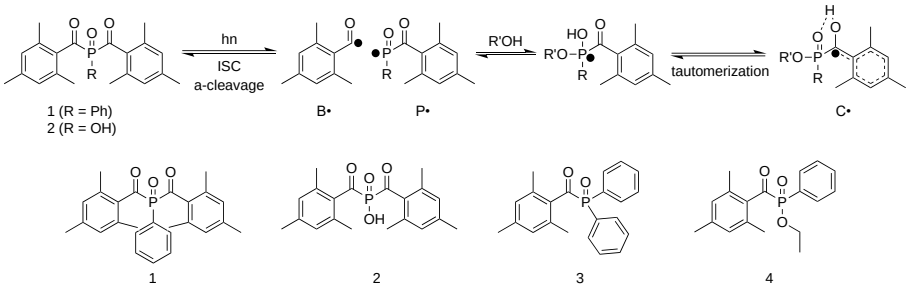

Scheme 1. Reaction pathway for the formation of C• upon photolysis of a **1** or **2** in aqueous or alcoholic media, b) Structures of **1, 2** and monoacylphosphine oxides (MAPOs) **3**, **4**

Irradiating a solution of **1** and $CuSO_4$ in methanol gives rise to a characteristic copper plasmon band of elemental copper centered at ca. 570 nm (Figure 1),[22,25,26,54–56] which reaches a maximum after *ca*. 5 minutes of irradiation. The formation of elemental copper is confirmed by X-ray powder diffraction (see Supporting Information, Figure S8).

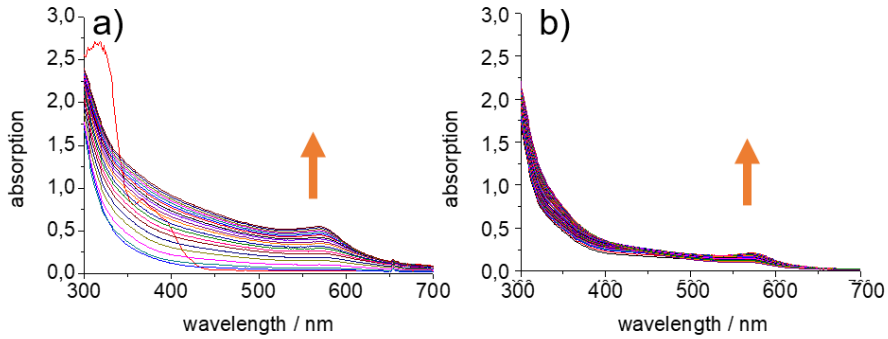

Figure 1. UV-VIS spectrum obtained upon photolysis (irradiation time 20 minutes; irradiation source high pressure Hg-Xe lamp) of (a) **1** and $CuSO_4$ or (b) **2** and $CuSO_4$ in methanol in the presence of the capping agent PVP; the arrow indicates the increase of the copper plasmon band upon irradiation

In the preceding publication, we established that photolysis BAPOs in aqueous or alcoholic environment yields the rather persistent benzoyl-type radical **C•**. [Ref-C•] In the presence of the electron acceptor tetracyanoethylene (TCNE), its radical anion was observed while **C•** was no longer detectable. [Ref-C•]. This points to radical **C•** (Scheme 2) rationalizing that the formation of **C•** being an efficient reducing agent.

To further substantiate the importance of **C•**-type radicals as crucial electron-transfer agents, we have carried out the following control experiments: *i*) We have photolysed monoacylphosphane oxides (MAPOs, **3** or **4**), but in these cases no Cu(SO_4) was converted to Cu(0) (see Supporting Information). *ii*) In aprotic solvents (*e.g.*, *N,N*-dimethylformamide, DMF*)* the formation of Cu nanoparticles could not be observed for both BAPOs and MAPOs (see Supporting Information). This underpins our previous results revealing that only the use of bisacylphosphane oxides in H_2O or alcohols produces elemental Cu from Cu^{2+}.

The substitution pattern of the BAPO derivatives controls the character of the nanoparticles. We have shown that **1** is more efficient in terms of releasing phosphanoyl radicals (**P**) than **2**. [52] Accordingly, for **1** a higher number of Cu^{2+} ions is reduced to elemental copper than for **2** mirrored by a faster growth of the plasmon band at 570 nm in the case of **1** (Figure 1).

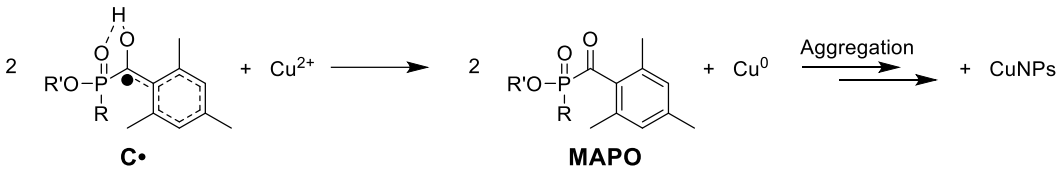

Scheme 2. Reaction pathway for the formation of **C•** upon photolysis of a BAPO in aqueous or alcoholic media and subsequent electron transfer to Cu^{2+}, forming a MAPO and copper nanoparticles (CuNPs)

Consequently, employing **1** as the photo-reducing agent the formation of a high number of small particles is achieved, whereas irradiation of **2** produces of fewer nanoparticles, which then grow by continuous metal deposition during the reduction process. This dependence of the particle size on the rate of the reduction has been previously described and discussed for silver, gold and copper nanomaterials.[27,59,60]

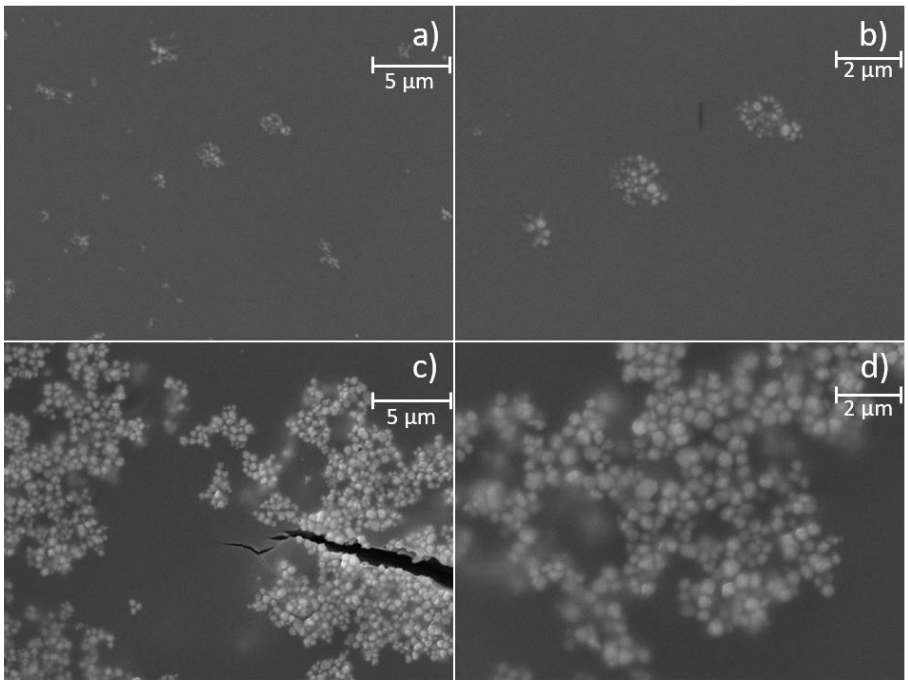

Figure 2. SEM images of nanoscopic copper obtained upon irradiation of a solution of $CuSO_4$ and **1** (a, b) or $CuSO_4$ and **2** (c, d) in presence of the capping agent PVP. Two scales are shown.

This difference in size of the copper nanoparticles is confirmed by dynamic light scattering (DLS). Copper nanoparticles formed from a **1**/$CuSO_4$ solution show an intensity distribution between 75 and 360 nm (Figure 3).

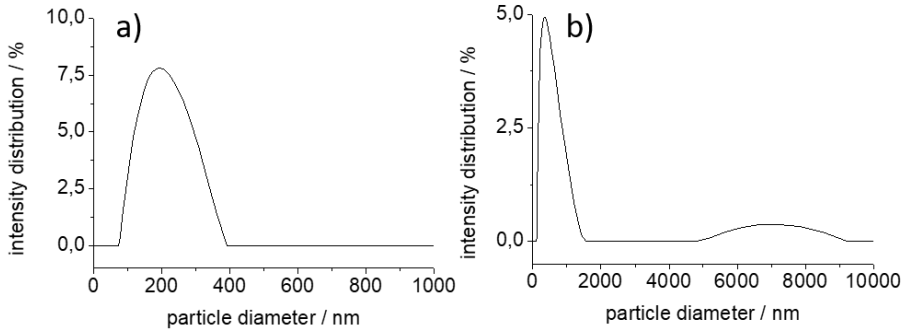

Figure 3. Intensity distribution of copper nanoparticles formed upon irradiating a solution of $CuSO_4$ and **1** (a) and **2** (b) in presence of the capping agent PVP obtained by DLS (The presence of these larger copper nanoparticles leads to interferences in the DLS measurements, and therefore the intensity distribution has to be interpreted with caution).

The solvent-dependent reactivity of BAPOS can be translated into a selective reaction pattern. Irradiation of **1/**$CuSO_4$/styrene in a bi-phasic system consisting of methanol and cyclohexane yields encapsulated Cu nanoparticles: While the **1** is soluble in both solvents, $CuSO_4$ resides in

methanol and styrene in cyclohexane (Figure 5a). Upon irradiation of the methanol-phase, the Cu^{2+} ions are reduced to elemental copper, (Figure 1b, red color). In the cyclohexane-phase, polystyrene is produced, which finally precipitates into the methanol (Figure 5c).

These results show that choosing appropriate solvent/salt/monomer mixtures, the electron-transfer and the initiation functionality of a bisacylphosphane oxide can be selectively addressed.

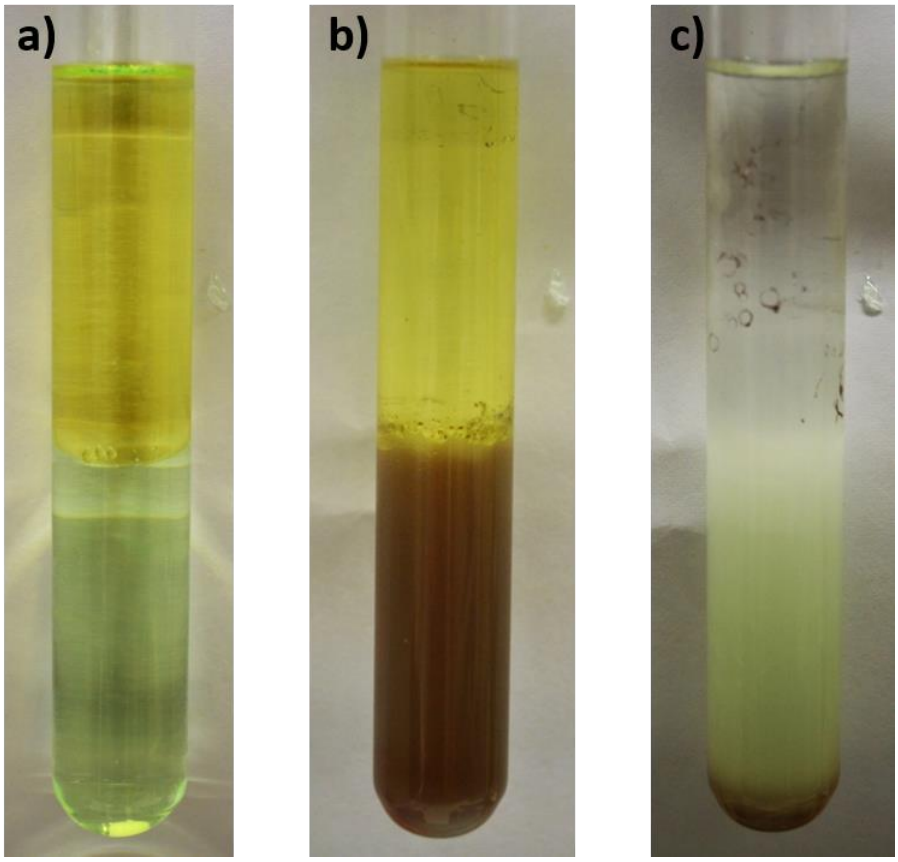

Figure 4. 2-phase system consisting of cyclohexane/methanol containing **1**, $CuSO_4$ and styrene. a) Parent mixture; b) After 120 s of irradiation of the bottom methanol solution c) After subsequent irradiation (120 s) of the upper cyclohexane phase. The milky precipitate is polystyrene.

This bifacial reactivity of BAPOS (ref) offers the unique chance to produce nanoparticles and simultaneously protect them by embedding into a suitable polymer matrix (nanocomposite) in a simple one-pot approach. Irradiating a mixture containing ethylenglycoldimethacrylate (TEGDMA)/methanol (1:1), $CuSO_4$, and photoinitiator **1** with a Hg-Xe lamp produced a Cu/polymer nanocomposite (Figure 6).

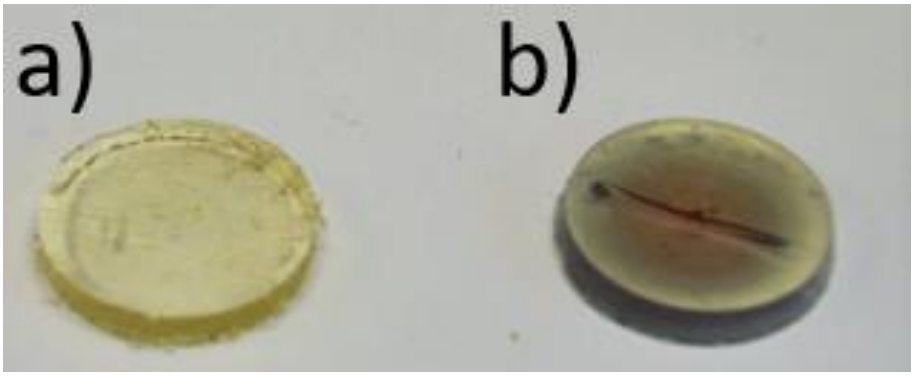

Figure 5. Preparation of polymer/copper nanoparticle nanocomposites: Photo showing nanocomposites after 120 seconds of irradiation of (a) **1**/$CuSO_4$ in TEGDMA/methanol (10:1) and (b) **1**/$CuSO_4$ in TEGDMA/methanol (1:1)

The unprecedented photochemistry of bis(acyl)phosphane oxides in aqueous and alcoholic media leads to the conversion of the primary phosphanoyl radicals **P•** to the persistent radical **C•**. The latter acts as a ground-sate electron donor and is the primary reducing agent converting Cu^{2+} to elemental Cu. Moreover the efficiency for the formation of **C•** can be used to control the size of the nanoparticles, allowing the production of tailor-made nanomaterials for different applications. Moreover, the differing reactivity of BAPOs in protic and aprotic/non-polar solvents can be used for site-selective transformations in multi-phase systems.

3.5.3. References

[1] A. G. Nasibulin, P. P. Ahonen, O. Richard, E. I. Kauppinen, I. S. Altman, **2001**, 385–400.

[2] S. Bhadra, A. Saha, B. C. Ranu, *Green Chem.* **2008**, *10*, 1224–1230.

[3] P. Singh, A. Katyal, R. Kalra, R. Chandra, *Catal. Commun.* **2008**, *9*, 1618–1623.

[4] C.-S. Chen, C.-C. Chen, C.-T. Chen, H.-M. Kao, *Chem. Commun.* **2011**, *47*, 2288–2290.

[5] M. B. Gawande, A. Goswami, F. X. Felpin, T. Asefa, X. Huang, R. Silva, X. Zou, R. Zboril, R. S. Varma, *Chem. Rev.* **2016**, *116*, 3722–3811.

[6] K. Larmier, W. C. Liao, S. Tada, E. Lam, R. Verel, A. Bansode, A. Urakawa, A. Comas-Vives, C. Copéret, *Angew. Chemie - Int. Ed.* **2017**, *56*, 2318–2323.

[7] J. Spivey, F. Tao, *Metal Nanoparticles for Catalysis: Advances and Applications*, The Royal Society Of Chemistry, **2014**.

[8] R. F. Minchin, D. J. Martin, *Endocrinology* **2010**, *151*, 474–481.

[9] Y. Zhang, L. Su, D. Manuzzi, H. V. E. de los Monteros, W. Jia, D. Huo, C. Hou, Y. Lei,

Biosens. Bioelectron. **2012**, *31*, 426–432.

[10] G. Schmid, *Clusters and Colloids: From Theory to Applications*, Wiley, **1994**.

[11] B. C. Gates, *Chem. Rev.* **1995**, *95*, 511–522.

[12] N. A. Dhas, C. P. Raj, A. Gedanken, *Chem. Mater.* **1998**, 1446–1452.

[13] F. E. Kruis, H. Fissan, A. Peled, *J. Aerosol Sci.* **1998**, *29*, 511–535.

[14] H. S. Kim, S. R. Dhage, D. E. Shim, H. T. Hahn, *Appl. Phys. A Mater. Sci. Process.* **2009**, *97*, 791–798.

[15] D. Lai, T. Liu, G. Jiang, W. Chen, *J. Appl. Polym. Sci.* **2013**, *128*, 1443–1449.

[16] D. K. Sarkar, X. J. Zhou, A. Tannous, K. T. Leung, *J. Phys. Chem. B* **2003**, *107*, 2879–2881.

[17] B. L. Cushing, V. L. Kolesnichenko, C. J. O'Connor, *Chem. Rev.* **2004**, *104*, 3893–3946.

[18] J. A. Dahl, B. L. S. Maddux, J. E. Hutchison, *Chem. Rev.* **2007**, *107*, 2228–2269.

[19] A. Roucoux, J. Schulz, H. Patin, *Chem. Rev.* **2002**, *102*, 3757–3778.

[20] R. Mittu, *Int. Adv. Res. J. Sci. Eng. Technol.* **2016**, *3*, 37–40.

[21] M. Sakamoto, M. Fujistuka, T. Majima, *J. Photochem. Photobiol. C Photochem. Rev.* **2009**, *10*, 33–56.

[22] S. Kapoor, T. Mukherjee, *Chem. Phys. Lett.* **2003**, *370*, 83–87.

[23] S. Giuffrida, L. L. Costanzo, G. Ventimiglia, C. Bongiorno, *J. Nanoparticle Res.* **2008**, *10*, 1183–1192.

[24] N. Nishida, A. Miyashita, N. Hashimoto, H. Murayama, H. Tanaka, *Eur. Phys. J. D* **2011**, *63*, 307–310.

[25] M. Schmallegger, G. Gescheidt, *Monatshefte für Chemie - Chem. Mon.* **2018**, *149*, 499–504.

[26] N. L. Pacioni, A. Pardoe, K. L. McGilvray, M. N. Chrétien, J. C. Scaiano, *Photochem. Photobiol. Sci.* **2010**, *9*, 766–774.

[27] A. Beil, G. Müller, D. Käser, B. Hattendorf, Z. Li, F. Krumeich, A. Rosenthal, V. K. Rana, H. Schçnberg, Z. Benko, et al., **2018**, 1–7.

[28] Y. Yagci, M. A. Tasdelen, S. Jockusch, *Polymer (Guildf).* **2014**, *55*, 3468–3474.

[29] S. Dadashi-Silab, S. Doran, Y. Yagci, *Chem. Rev.* **2016**, DOI 10.1021/acs.chemrev.5b00586.

[30] B. J. Adzima, Y. Tao, C. J. Kloxin, C. A. DeForest, K. S. Anseth, C. N. Bowman, *Nat. Chem.* **2011**, *3*, 256–259.

[31] H. B. Song, A. Baranek, C. N. Bowman, *Polym. Chem.* **2016**, *7*, 603–612.

[32] W. Rutsch, K. Dietliker, D. Leppard, M. Köhler, L. Misev, U. Kolczak, G. Rist, *Prog. Org.*

Coatings **1996**, *27*, 227–239.

[33] K. Dietliker, T. Jung, J. Benkhoff, H. Kura, A. Matsumoto, H. Oka, D. Hristova, G. Gescheidt, G. Rist, *Macromol. Symp.* **2004**, *217*, 77–98.

[34] Y. Yagci, S. Jockusch, N. J. Turro, *Macromolecules* **2010**, *43*, 6245–6260.

[35] P. S. P-, U. Kolczak, K. Dietliker, J. Wirz, **1996**, *7863*, 6477–6489.

[36] G. W. Sluggett, P. F. McGarry, I. V Koptyug, N. J. Turro, *J. Am. Chem. Soc.* **1996**, *118*, 7367–7372.

[37] G. W. Sluggett, C. Turro, M. W. George, I. V Koptyug, N. J. Turro, *J. Am. Chem. Soc.* **1995**, *117*, 5148–5153.

[38] S. Jockusch, I. V Koptyug, P. F. McGarry, G. W. Sluggett, N. J. Turro, D. M. Watkins, *J. Am. Chem. Soc.* **1997**, *119*, 11495–11501.

[39] S. Jockusch, N. J. Turro, *J. Am. Chem. Soc.* **1998**, *120*, 11773–11777.

[40] I. Gatlik, P. Rzadek, G. Gescheidt, *J. {…}* **1999**, 8332–8336.

[41] D. Hristova, I. Gatlik, G. Rist, K. Dietliker, J. P. Wolf, J. L. Birbaum, A. Savitsky, K. Möbius, G. Gescheidt, *Macromolecules* **2005**, *38*, 7714–7720.

[42] D. Hristova-Neeley, D. Neshchadin, G. Gescheidt, *J. Phys. Chem. B* **2015**, *119*, 13883–13887.

[43] A. Eibel, M. Schmallegger, M. Zalibera, A. Huber, Y. Bürkl, H. Grützmacher, G. Gescheidt, *Eur. J. Inorg. Chem.* **2017**, DOI 10.1002/ejic.201700140.

[44] H. Grützmacher, J. Geier, D. Stein, T. Ott, H. Schönberg, R. H. Sommerlade, S. Boulmaaz, J.-P. Wolf, P. Murer, T. Ulrich, *Chim. Int. J. Chem.* **2008**, *62*, 18–22.

[45] A. Huber, A. Kuschel, T. Ott, G. Santiso-Quinones, D. Stein, J. Bräuer, R. Kissner, F. Krumeich, H. Schönberg, J. Levalois-Grützmacher, et al., *Angew. Chemie Int. Ed.* **2012**, *51*, 4648–4652.

[46] G. Müller, M. Zalibera, G. Gescheidt, A. Rosenthal, G. Santiso-Quinones, K. Dietliker, H. Grützmacher, *Macromol. Rapid Commun.* **2015**, *36*, 553–557.

[47] S. Benedikt, J. Wang, M. Markovic, N. Moszner, K. Dietliker, A. Ovsianikov, H. Grützmacher, R. Liska, *J. Polym. Sci. Part A Polym. Chem.* **2016**, *54*, 473–479.

[48] J. Wang, G. Siqueira, G. Müller, D. Rentsch, A. Huch, P. Tingaut, J. Levalois-Grützmacher, H. Grützmacher, *Chem. Commun.* **2016**, *52*, 2823–2826.

[49] A. Eibel, D. E. Fast, J. Sattelkow, M. Zalibera, J. Wang, A. Huber, G. Müller, D. Neshchadin, K. Dietliker, H. Plank, et al., *Angew. Chem. Int. Ed. Engl.* **2017**, *56*, 14306–14309.

[50] J. Wang, S. Stanic, A. A. Altun, M. Schwentenwein, K. Dietliker, L. Jin, J. Stampfl, S.

Baudis, R. Liska, H. Grützmacher, *Chem. Commun. (Camb).* **2018**, *54*, 920–923.

[51] J. Wang, A. Chiappone, I. Roppolo, F. Shao, E. Fantino, M. Lorusso, D. Rentsch, K. Dietliker, C. F. Pirri, H. Grützmacher, *Angew. Chem. Int. Ed. Engl.* **2018**, *57*, 2353–2356.

[52] D. E. Fast, M. Zalibera, A. Lauer, A. Eibel, C. Schweigert, A.-M. Kelterer, M. Spichty, D. Neshchadin, D. Voll, H. Ernst, et al., *Chem. Commun.* **2016**, *52*, 9917–9920.

[53] R. Stösser, M. Siegmund, *J. für Prakt. Chemie* **1977**, *319*, 827–834.

[54] S. Kapoor, D. K. Palit, T. Mukherjee, *Chem. Phys. Lett.* **2002**, *355*, 383–387.

[55] J. Hambrock, R. Becker, A. Birkner, J. Wei, R. A. Fischer, *Chem. Commun.* **2002**, *1*, 68–69.

[56] G. H. Chan, J. Zhao, E. M. Hicks, G. C. Schatz, R. P. Van Duyne, *Nanoletters* **2007**, *7*, 1947–1952.

[57] Y. Yu, L. Zhang, J. Wang, Z. Yang, M. Long, N. Hu, Y. Zhang, *Nanoscale Res. Lett.* **2012**, *7*, 1–15.

[58] I. Pastoriza-Santos, L. M. Liz-Marzán, *Adv. Funct. Mater.* **2009**, *19*, 679–688.

[59] K. L. Mcgilvray, M. R. Decan, D. Wang, J. C. Scaiano, *J. Am. Chem. Soc.* **2006**, *128*, 15980–15981.

[60] K. Stamplecoskie, J. Scaiano, *J. Am. Chem. Soc.* **2010**, 8.

4. Additional Publications

4.1. The Antioxidant Activity of Beer: An EPR Experiment for the Undergraduate Physical Chemistry Laboratory

Max Schmallegger[a] and Georg Gescheidt[a]

[a] Institute of Physical and Theoretical Chemistry, Graz University of Technology

Published in: *J. Chem. Educ.* **2018**, *95*, 2013−2016.

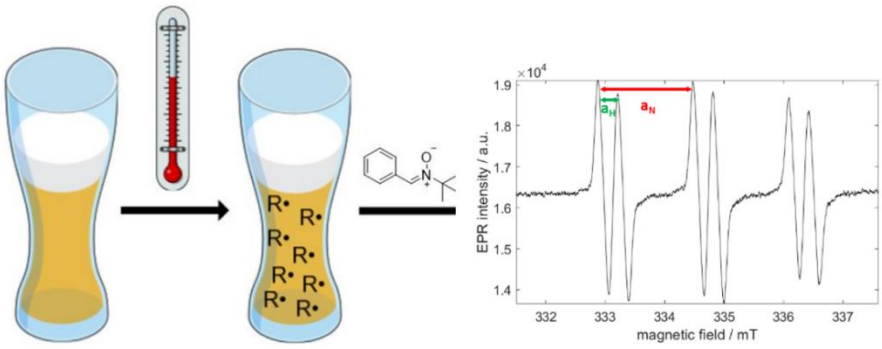

4.1.1. Abstract

This laboratory experiment utilizes exploring the storage stability of beer to introduce basic aspects of electron paramagnetic resonance spectroscopy (EPR). Radicals formed upon aerobic forced aging of beer samples are established by using a spin-trap. The students are introduced to basic principles of EPR spectroscopy, food- and radical chemistry with a simple example taken from everyday life. The methodology reported provides the students with valuable insights into EPR spectroscopy and the role of free radicals in food-chemistry.

4.1.2. Background

Electron paramagnetic resonance (EPR) spectroscopy is a powerful method for studying species that contain unpaired electrons, such as organic free radicals, transition-metal ions and molecules in excited states. The underlying theory and principles are similar to those of nuclear magnetic resonance (NMR) spectroscopy, which probes nuclear spin transitions of molecules. However, EPR spectroscopy is not commonly introduced to undergraduate students, even though some laboratory exercises have been reported.[1–3] One of the reasons for this is the limitation to (often) short-lived paramagnetic species in combination with the high costs of EPR spectrometers. Nevertheless, in the recent years, substantial progress has been made, leading to the development of affordable and easy-to-use benchtop EPR spectrometers.

EPR spectroscopy allows detecting free radicals in degradation processes of food and beverages. The understanding of radical processes in food samples is a highly relevant topic since free radicals and their follow-up products are responsible for undesirable sensorial and biological effects in food.[4–6] However, due to the short life-times of radicals generated in food, a direct observation is feasible only at low temperatures.[7,8] One possibility to overcome this limitation is the use of spin-trapping techniques: Spin-trapping allows the indirect detection of food-derived radicals by forming stable spin adducts in detectable quantities, allowing for both characterization and quantification of the trapped radical. *N-tert*-Butyl-*α*-phenylnitrone (PBN, Scheme 1) is frequently used as a spin trap for this purpose. [5,9,10]

Scheme 1. Spin trapping of a radical •R by PBN

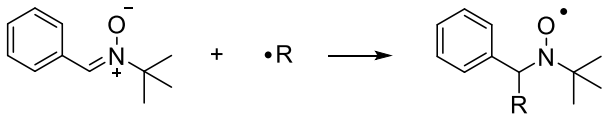

PBN spin adduct

It is well established that free radicals are reaction intermediates in the oxidation processes in beer. Therefore, spin-trapping is used to assess the type and quantity of radicals produced even in industrially validated procedures. [11–13] The importance of radical processes has been linked to the presence of oxygen and metal ions like iron(II) and copper(II).[14,15] Moreover, it was demonstrated that the addition of iron(II) ions and hydrogen peroxide additionally accelerates the formation of radicals. [16] These results suggest that Fenton-type reactions take place in beer and

that oxygen forms hydrogen peroxide, which subsequently reacts with metal ions such as iron(II) to yield hydroxyl radicals (Scheme 2).

Scheme 2. Fenton reaction between iron(II) and hydrogen peroxide yielding iron(III), hydroxyl radicals and hydroxyl anions

However, this Fenton-type reaction is very slow at room temperature. Therefore, the technique of aerobic forced aging, where the beverage is heated to 60 °C, is frequently employed to accelerate the oxidation processes. Still, even under these conditions, naturally occurring antioxidants in beers delay the radical-induced oxidation. These antioxidants are mostly (poly-)phenols protecting the beer by terminating free-radical pathways, thus delaying oxidation. This so-called lag-time, the period it takes until all antioxidants in the beer are consumed and radicals can be detected by EPR, acts as an indicator for the concentration of antioxidants in beer.
The primary 1-hydroxyethyl radical is formed during the aerobic forced aging and subsequently reacts with PBN to give a stable spin adduct. It is formed from ethanol upon reaction with the highly reactive hydroxyl radical. The full reaction scheme leading to the formation of the detectable spin adduct is depicted in Scheme 3.

Scheme 3. Reaction scheme for the production of hydroxyl radicals in a Fenton reaction with subsequent formation of the 1-hydroxyethyl radical and trapping by PBN to form a stable radical adduct.[11]

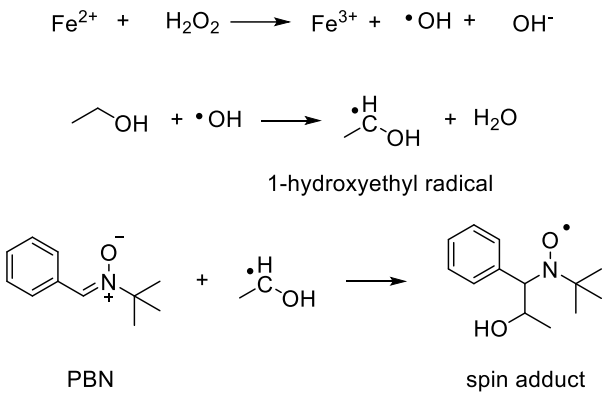

In this laboratory experiment, students determine the antioxidant potential of beer using EPR spectroscopy: The lag-time is evaluated employing the above-described methods of aerobic

forced aging and spin trapping of the radicals produced. This provides valuable insights into EPR phenomena and the generation of free radicals combined with food chemistry and offers an addition to already existing lab experiments dealing with the stability of beer.[17–22]

4.1.3. Hazards

In addition to goggles, the use of nitrile gloves is recommended. *N-tert*-Butyl-*α*-phenylnitrone (PBN) is an irritant. The laboratory experiment should be carried out in a well-ventilated lab space.

4.1.4. Experiment

Learning Objectives. The experiment was designed to be carried out by eight students at a time, working in pairs for 3.5 hours. The laboratory exercise was performed by a total of 112 students. The students accomplished four learning objectives:

- The students evaluated the lag-time of a commercially available beer that underwent oxidation by aerobic forced aging using EPR spectroscopy applying the spin-trapping method.
- The students evaluated the hyperfine coupling constants of the formed stable spin adduct of PBN.
- The students calculated the g-factor of the spin adduct by comparison with the signal of a 2,2-diphenyl-1-picrylhydrazyl (DPPH) solution in beer.
- The students developed a schematic representation of the Zeeman levels and applied selection rules in magnetic resonance, which are sufficient to explain the six-line spectrum of the spin adduct. Moreover, they acquired knowledge on the reactivity of free radicals.

Prior to the experiment, the students had to pass a short written examination. To prepare for this examination, a student handout was provided, including the basic theory of EPR, spin trapping and radical processes in food with references to literature (refer to the Supporting Information for both the student handout and the exam).

Materials and Equipment. *N-tert*-Butyl-α-phenylnitrone (PBN) was purchased from TCI chemicals (> 98 %) and used as received. Iron sulphate heptahydrate was purchased from Carl Roth (> 99.5 %) and used as received. Maerzen beer (Gösser Märzen) was bought at a local supermarket.

The laboratory was equipped with four computers for data analysis (one computer per group), 1 ml and 4 ml pipettes (four sets), 50 ml beakers, ringcap capillary pipettes and capillary tube sealing kits, Eppendorf Safe-Lock tubes and 4 ml glass vials with screw caps for sample preparation. One EPR spectrometer was shared by all participating students (eight). The measurements were carried out on a Magnettech Miniscope MS300 benchtop X-band EPR spectrometer. Data analysis was carried out using the spectrometer's accompanying software "Multiplot" and Microsoft Excel.

Sample Preparation. Carbon dioxide was removed from the beer by placing it in an ultra-sonication bath for 15 minutes and subsequent decanting every day before the experiment by the instructor. The removal of CO_2 is necessary since bubbles in the capillaries could disturb the EPR measurements.

Student Laboratory Work The undergraduate chemistry students were provided with the degassed beer and PBN. The students prepared a 0.05 M solution of PBN in 4 ml of beer, using a volumetric pipette and screw-cap glass vials. The sample underwent aerobic forced aging in a drying oven at 60° C. Every 15 minutes, students prepared a sample for EPR measurements: a ringcap capillary pipette was used to take up 50 µl of the PBN solution and was subsequently sealed using a capillary tube sealing kit. The sealed capillary was placed directly in the EPR spectrometer and measured with a single scan for 60 seconds to reduce measurement time. The recorded spectra were analyzed using the Multiplot-software; the Peak-to-Peak height – which is directly proportional to the radical concentration – is extracted from the spectra and plotted vs. the time (in minutes). In addition, every group prepared a sample of 5 mg DPPH in 4 ml beer to determine the g-factor of the PBN spin adduct according to the formula displayed in Box 1. Furthermore, the students determined the hyperfine coupling constants (*a*) of the spin adduct directly by measuring them in their obtained experimental spectra, also using the Multiplot software. Additionally, the students were given the task to present a theoretical scheme explaining the six-line spectrum recorded during the laboratory experiment.

Box 1. Determination of the g-factor of an unknown using DPPH as a standard with known g-factor

$$g_{PBN} = g_{DPPH}\frac{B_{DPPH}}{B_{PBN}}$$

g_{PBN}…	g-factor of the PBN spin adduct
g_{DPPH}…	g-factor of DPPH (= 2.0036)
B_{PBN}…	Resonance magnetic field of the PBN spin adduct
B_{DPPH}…	Resonance magnetic field of DPPH

Students summarized the results of this laboratory exercise within one week as a written report. This report was based on the following formal criteria:

- An abstract, summarizing the experiment and the main results.
- An introduction, highlighting the scientific question, giving some theoretical background and stating all equations necessary for evaluation of the experimental data.
- An experimental part, stating all chemicals and instruments used during the experiment and a short description of the sample preparation and the measurement.
- The experimental results, including all schemes and figures.
- A discussion of the experimental results and their relevance, as well as a discussion of possible sources of error.

4.1.5. Results

The lag-time of beer under forced aging conditions was determined in a straightforward manner by using spin trapping and EPR detection. An example of the data obtained by students is shown in Figure 1. The obtained curves show the typical behavior of an initial slow increase, followed by a fast linear increase of the EPR signal intensity. The crossing between the slow-increase regime and the fast-increase regime represents the lag time of the beer sample (the time at which all antioxidants in the beer sample are consumed by free radicals). Employing this approach, the majority of students were able to determine the lag-time of their beer sample, which is around 36 minutes in the example displayed in Figure 1.

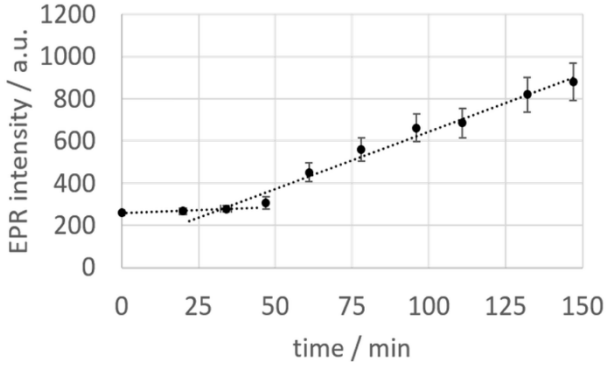

Figure 1. Example of a lag-time measurement of beer obtained by students during the laboratory experiment

In addition, the students managed to extract the hyperfine coupling constants from the experimental spectra. Figure 2 shows an experimental spectrum obtained by students during the laboratory exercise. From the experimental six-line spectrum, it is obvious that two hyperfine coupling constants are detected in the PBN spin-adduct. One stems from the nitrogen right next to the radical center. Nitrogen has a nuclear spin of $I = 1$, leading to a splitting into three different lines. The additional splitting stems from the H-atom located on the carbon neighboring the N-atom with a nuclear spin $I = ½$, resulting in a total of six lines. For these two respective nuclei, the students obtained hyperfine coupling constants a of $a_N = 1.58 \pm 0.02$ mT and $a_H = 0.34 \pm 0.02$ mT, which are in very good agreement with published data. [11,13]

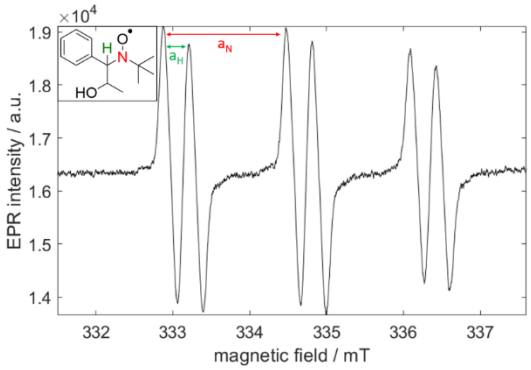

Figure 2. Example of an EPR spectrum of the PBN spin adduct recorded after 150 minutes of aerobic forced aging at 60° C used for the determination of the hyperfine coupling constants obtained by students

Using DPPH (g = 2.0036) as the reference, students determined the g-factor of the PBN spin adduct with the equation displayed in Box 1 (g = 2.0059 ± 0.01, Figure 3).

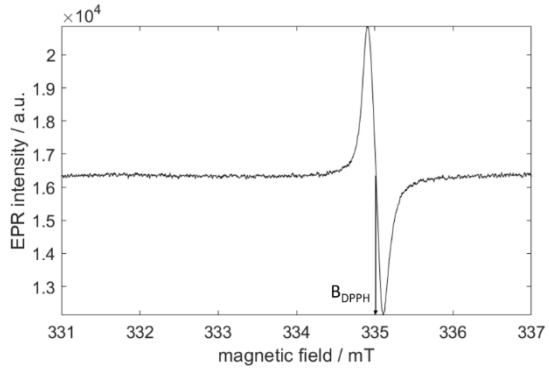

Figure 3. Example of the EPR spectrum of DPPH recorded by students used for the evaluation of the g-factor of the PBN spin adduct

The students also developed a theoretical explanation for the EPR spectrum during the lab exercise. They had to present a schematic representation of the Zeeman and hyperfine splittings and the corresponding energy levels which explains the six lines observed in the EPR spectrum. This was usually done by all 8 students by discussions during the experiment and then was integrated into the lab report by all individual groups. An example for this schematic representation is given in Figure 4.

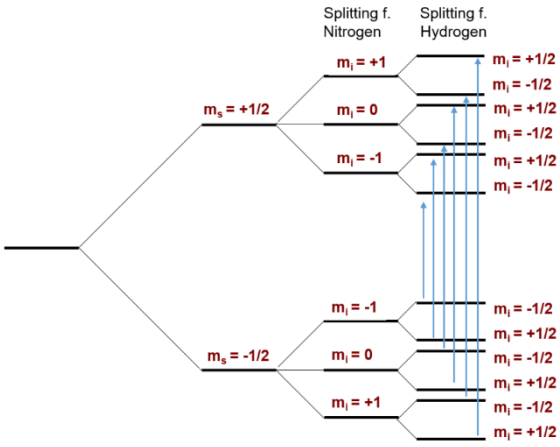

Figure 4. Schematic representation of the Zeeman and hyperfine levels of the spin adduct recorded in the laboratory exercise; the arrows represent the six transitions corresponding to the six lines of the EPR spectrum in Figure 2

4.1.6. Conclusions

We described a laboratory exercise designed to teach EPR spectroscopy and radical formation in food to undergraduate students employing the method of spin trapping. The exercise was designed to ensure completion in a single 3.5 h laboratory period.

Using beer as an everyday thing, students have been introduced to EPR spectroscopy, spin trapping, and the role of free radicals in food chemistry. They determined the lag-time of a beer sample upon forced aerobic aging, extracted hyperfine coupling constants from experimental EPR spectra and calculated the g-factor of the spin-adduct. The theoretical basics of EPR spectroscopy have been presented. The students had to demonstrate their knowledge by fulfilling tasks revealing concepts of EPR spectroscopy and radical chemistry. Special emphasis was directed toward a careful analysis and presentation of data in the written report.

This laboratory exercise was incorporated into an existing lab course on molecular analytics and spectroscopy comprising nuclear magnetic resonance spectroscopy (NMR), infrared spectroscopy (IR), cyclic voltammetry (CV), X-ray spectroscopy, UV-VIS spectroscopy and fluorescence spectroscopy. This exercise proved to be a valuable addition to the lab course, as it familiarizes the students with an additional spectroscopic method, which is of high relevance in basic research and in industrially validated procedures e.g. food control.

4.1.7. References

[1] Butera, R. A.; Waldeck, D. H. An EPR Experiment for the Undergraduate Physical Chemistry Laboratory. *J. Chem. Educ.* **2000**, *77* (11), 1489–1491.

[2] Sojka, Z.; Stopa, G. Analysis of the Isotropic EPR Spectrum of K3[Cr(CN)5NO]: An Inorganic Chemistry Laboratory Experiment. *J. Chem. Educ.* **1993**, *70* (8), 675–678.

[3] Garribba, E.; Micera, G. The Determination of the Geometry of Cu (II) Complexes An EPR Spectroscopy Experiment. *J. Chem. Educ.* **2006**, *83* (8), 1229–1232.

[4] Kanner, J. Dietary Advanced Lipid Oxidation Endproducts Are Risk Factors to Human Health. *Mol. Nutr. Food Res.* **2007**, *51* (9), 1094–1101.

[5] Szterk, A.; Stefaniuk, I.; Waszkiewicz-Robak, B.; Roszko, M. Oxidative Stability of Lipids by Means of EPR Spectroscopy and Chemiluminescence. *JAOCS, J. Am. Oil Chem. Soc.* **2011**, *88* (5), 611–618.

[6] Barriuso, B.; Astiasarán, I.; Ansorena, D. A Review of Analytical Methods Measuring Lipid Oxidation Status in Foods: A Challenging Task. *Eur. Food Res. Technol.* **2013**, *236* (1), 1–15.

[7] Huvaere, K.; Skibsted, L. H. Flavonoids Protecting Food and Beverages against Light. *J. Sci. Food Agric.* **2015**, *95* (1), 20–35.

[8] Geoffroy, M.; Lambelet, P.; Richert, P. Role of Hydroxyl Radicals and Singlet Oxygen in the Formation of Primary Radicals in Unsaturated Lipids: A Solid State Electron Paramagnetic Resonance Study. *J. Agric. Food Chem.* **2000**, *48* (4), 974–978.

[9] Papadimitriou, V.; Sotiroudis, T. G.; Xenakis, A.; Sofikiti, N.; Stavyiannoudaki, V.; Chaniotakis, N. A. Oxidative Stability and Radical Scavenging Activity of Extra Virgin Olive Oils: An Electron Paramagnetic Resonance Spectroscopy Study. *Anal. Chim. Acta* **2006**, *573–574*, 453–458.

[10] Thomsen, M. K.; Kristensen, D.; Skibsted, L. H. Electron Spin Resonance Spectroscopy

for Determination of the Oxidative Stability of Food Lipids. *J. Am. Oil Chem. Soc.* **2000**, *77* (7), 725–730.

[11] Andersen, M. L.; Skibsted, L. H. Electron Spin Resonance Spin Trapping Identification of Radicals Formed during Aerobic Forced Aging of Beer. *J. Agric. Food Chem.* **1998**, *46* (4), 1272–1275.

[12] Andersen, M. L.; Outtrup, H.; Skibsted, L. H. Potential Antioxidants in Beer Assessed by ESR Spin Trapping. *J. Agric. Food Chem.* **2000**, *48* (8), 3106–3111.

[13] Kaneda, H.; Kano, Y.; Osawa, T.; Ramarathnam, N.; Kawakishi, S.; Kamada, K. Detection of Free Radicals in Beer Oxidation. *J. Food Sci.* **1988**, *53* (3), 885–888.

[14] Bamforth, C. W.; Parsons, R. New Procedures to Improve the Flavor Stability of Beer. *J. Am. Soc. Brew. Chem.* **1985**, No. 43, 197–202.

[15] Irwin, A. J.; Barker, R. L.; Pipasts, P.; St, S. The Role of Copper , Oxygen , and Polyphenols in Beer Flavor Instability. *J. Am. Soc. Brew. Chem.* **1991**, *49* (3), 140–149.

[16] Uchida, M.; Ono, M. Improvement for Oxidative Flavor Stability of Beer: Role of OH-Radical in Beer Oxidation. *J. Am. Soc. Brew. Chem.* **1996**, No. 54, 198–204.

[17] Vogler, A.; Kunkely, H. Photochemistry and Beer. *J. Chem. Educ.* **1982**, *59* (1), 25–27.

[18] Korolija, J. N.; Plavsic, J. V.; Marinkovic, D.; Mandic, L. M. Beer as a Teaching Aid in the Classroom and Laboratory. *J. Chem. Educ.* **2012**, *89* (5), 605–609.

[19] Stewart, G. G. The Chemistry of Beer Instability. *J. Chem. Educ.* **2004**, *81* (7), 963–968.

[20] Pelter, M. W.; McQuade, J. Brewing Science in the Chemistry Laboratory: A “Mashing” Investigation of Starch and Carbohydrates. *J. Chem. Educ.* **2005**, *82* (12), 1811–182.

[21] Gillespie, B.; Deutschman, W. A. Brewing Beer in the Laboratory: Grain Amylases and Yeast’s Sweet Tooth. *J. Chem. Educ.* **2010**, *87* (11), 1244–1247.

[22] Khalafi, L.; Doolittle, P.; Wright, J. Speciation and Determination of Low Concentration of Iron in Beer Samples by Cloud Point Extraction. *J. Chem. Educ.* **2018**, *95* (3), 463–467.

4.1.8. Supporting Information

Supporting information for this article is available on the WWW under *http://dx.doi.org/10.1021/acs.jchemed.8b00329*

4.2. A new mechanism for enhanced electrocatalytic nitrogen reduction based on partial anion substitution in titanium oxide-carbon composites

Qing Qin,[a]† Yun Zhao,[b]† Max Schmallegger,[c] Tobias Heil,[a] Johannes Schmidt,[d] Ralf Walczak,[a] Georg Gescheidt,[c] Haijun Jiao,[b] and Martin Oschatz[a]*

[a] Max Planck Institute of Colloids and Interfaces, Department of Colloid Chemistry, Am Mühlenberg 1, 14476, Potsdam, Germany

[b] Leibniz-Institut für Katalyse e.V. an der Universität Rostock, Albert-Einstein-Straße 29a, Rostock, 18059, Germany

[c] Graz University of Technology, Institute of Physical and Theoretical Chemistry, NAWI Graz, Stremayrgasse 9, 8010, Graz, Austria

[d] Technische Universität Berlin, Institute of Chemistry, Division of Functional Materials Hardenbergstraße40, 10623, Berlin, Germany

Submitted to: *Angew. Chemie Int. Ed*

4.2.1. Abstract

The electrochemical conversion of N_2 at ambient conditions using renewably generated electricity is an attractive approach for sustainable ammonia (NH_3) production. Considering the extremely challenging 6 electron transfer process, rational design of efficient catalysts is required. In order to explore a new mode for activation of N_2, we use a Titanium-based metal-organic framework (MOF) as the precursor and pyrolyze at high temperature (800-1100 °C) to obtain noble metal-free C-doped TiO_2/C (C-Ti_xO_y/C) material with porous structure and abundant oxygen vacancies (OVs). At -0.4 V vs. RHE, a high Faradaic efficiency (FE) of 17.8 % can be achieved with remarkable NH_3 yield of 9.2 μg h^{-1} mg^{-1}. No decay in the current and NH_3 yields is observed during the long-time stability test. On the basis of the experimental results and theoretical calculations,

the remarkable properties of the catalysts can be attributed to the doping of carbon atoms into OVs and the formation of Ti-C bonds, which are found to be the active sites for N_2 activation. This work elucidates that electrochemical NRR performance can be largely improved by creating catalytically active centers through rational substitution of anions into metal oxides.

4.2.2. Main Text

As expressed by its annual worldwide production exceeding 145 million tons, NH_3 plays an extremely important role in agricultural fertilizers, fuels, as hydrogen carrier and in many other fields.[1] The industrially applied Haber-Bosch process suffers from the need for high temperature and pressure. Even more important, the production of H_2 as reactant by steam reforming contributes significantly to the world energy consumption and the overall cost of the process.[2] Hence, NRR at ambient conditions by using renewable electricity is emerging as an alternative technology towards a more sustainable NH_3 production[3] but the inertness of the N_2 molecule (resulting from the high binding energy of more than 900 kJ mol^{-1}) makes it difficult to be activated which is the main reason for the so far limited efficiency and space-time yield of NRR as well as the high temperature and pressure required for its hydrogenation in the gas phase.[4] In aqueous solution, the increase of the electric potential to enhance activation of N_2 is an option of limited applicability as NRR is under these conditions largely inhibited by competitive hydrogen evolution reaction (HER).[5]

Because of this, developing efficient NRR catalysts has attracted increasing attention. The ultimate requirement to such types of catalysts is to bind and polarize N_2 molecules in a way that the electron density within the molecule is changed enough that the reaction with protons and/or electrons can occur.[6] Until now, various promising catalysts have been investigated for electrochemical NRR, including metals,[7] metal oxides,[8] metal nitrides,[9] metal carbides,[10] metal complexes[11] and carbon-based materials.[12] Among them, noble metals exhibit good NRR performance due to their ability to strongly bind and activate N_2.[7b] But considering the cost, they are not suitable for large-scale implementation of NRR. Main strategies for solving this problem can be either to construct single atom catalytic sites to decrease the amount of noble metal used or develop non-noble metal based materials.[13] However, the latter are much less investigated as it is considered difficult to strongly polarize the N_2 molecules without noble metals.[3b, 5c] Recently, some non-noble metal oxides, carbides, nitrides, and sulfides are proved to be efficient catalysts for electrochemical NRR.[9b, 10c] However, more detailed mechanistic understanding is still needed

in order to enhance their efficiency. In that way, transformative advances can be achieved by exploring entirely new classes of catalysts or by modifying existing catalysts to obtain deep understanding towards NRR and to rationally design advanced catalysts in the future.

As one of the rather abundant transition metals, Ti-based materials can be potential candidates due to their strong binding towards N-adatoms than H-adatoms leading to better N_2 reducing ability.[3b, 14] Thus, TiO_2 and MXenes have been studied for their application in electrochemical NRR,[10d, 15] but the low FE still pose a big challenge, which means that the synthesis of Ti-based catalysts for NRR with higher efficiency is highly required. Our inspiration for a novel synthesis scheme for Ti-based NRR catalysts is coming from the versatile redox chemistry of oxygen-deficient titanium oxides with a wide distribution of possible electronic band structures as well as many possible anionic substitutions leading to the potential to provide abundant active sites for N_2 activation. Furthermore, previous reports have shown that MOF-derived catalysts have tunable porosity, high surface area, controllable functionalization, as well as good conductivity and thus provide great potential as electrocatalysts.[16] To the best of our knowledge, Ti-MOF-derived materials have not been used in electrochemical NRR yet.

$Ti_8O_8(OH)_4(bdc)_6$ (MIL-125(Ti)) (bdc = benzene-1,4-dicarboxylate) has been chosen as the MOF precursor and a novel NRR electrocatalyst based on a carbon-doped, oxygen deficient titanium oxide/carbon (C-Ti_xO_y/C) nanohybrid was prepared via a one-step thermal conversion. During the pyrolysis process, TiO_2 is formed and the organic linkers are carbonized and partly react with TiO_2 to form C-Ti_xO_y, while unreacted carbon is still present as amorphous and electron conducting binder. Further experiments and density functional theory (DFT) calculations show that C can be doped into oxygen vacancies in Rutile leading to the formation of Ti-C bonds. Such partial anion substitution leads to excellent electrochemical NRR performance. At the potential of -0.4 V vs. RHE, the highest FE of 17.8 % can be achieved with a remarkable NH_3 yield of 9.2 µg h^{-1} mg^{-1} at 1 bar and room temperature. DFT calculations are used to investigate the effect of C doping on the mechanism of electrochemical NRR.

MIL-125(Ti) was synthesized according to the literature (see Supporting Information for more details).[17] The low-magnification transmission electron microscopy (TEM) images, X-ray diffraction (XRD) patterns and N_2 physisorption isotherms all demonstrate the successful synthesis of porous MIL-125(Ti) crystals with a high specific surface area (SSA) of 1567 m^2 g^{-1} (Figure S1). C-Ti_xO_y/C hybrid nanostructures (denoted as M-Ts with T representing the pyrolysis temperature) were synthesized by annealing MIL-125(Ti) at 800 °C, 900 °C, 1000 °C and 1100 °C for 2 h under Ar atmosphere. The TEM (Figure 1a-b) and scanning electron microscopy (SEM) images (Figure S2) of as-obtained M-1000 reveal that the transformed MOF particles become

much looser but remain the polyhedral geometry of the former MIL-125(Ti) crystals and contain some smaller nanoparticles. High-resolution TEM (HRTEM) images show that TiO_2 nanoparticles with sizes between 3 and 20 nm are well-dispersed in an amorphous environment (Figure 1c). TEM images of M-800, M-900 and M-1100 also exhibit a comparable structure (Figure S3).

The XRD patterns of as-obtained samples (Figure 1d) indicate that M-800 are TiO_2-containing nanocomposites consisting of tetragonal Rutile (JCPDS No. 21-1276) and tetragonal Anatase (JCPDS No. 21-1272) nanoparticles with the (110) and (101) diffraction peaks located at 27.4° and 25.3°, respectively.[18] For M-900, the diffraction peak of Anatase becomes much weaker, while only diffraction peaks of Rutile appear in M-1000 and M-1100. Notably, because of the carbothermal reduction of TiO_2, a small new diffraction peak at 43.5° appears in M-1000, which can be attributed to TiC.[19] With further increasing temperature, M-1100 shows more intense diffraction peaks of TiC, as its content increases at higher temperature due to the faster carbothermal reduction. Raman spectra of the as-obtained materials (Figure 2a) all exhibit three main bands centered at approximately 249, 413, and 601 cm^{-1}. By comparison of the Raman spectra of TiC, Anatase, and Rutile with M-1000 (Figure S4), it can also be concluded that Ti-C and Ti-O bonds may coexist in M-Ts due to the small Raman shift.[20] Besides, two small bands at ~1350 and 1590 cm^{-1} are assigned to disordered (D) and graphite (G)-like bands of free carbon.[21] It is worth to note that the latter bands almost disappear in M-1100, as more free carbon reacts with TiO_2 to form TiC at higher temperature.

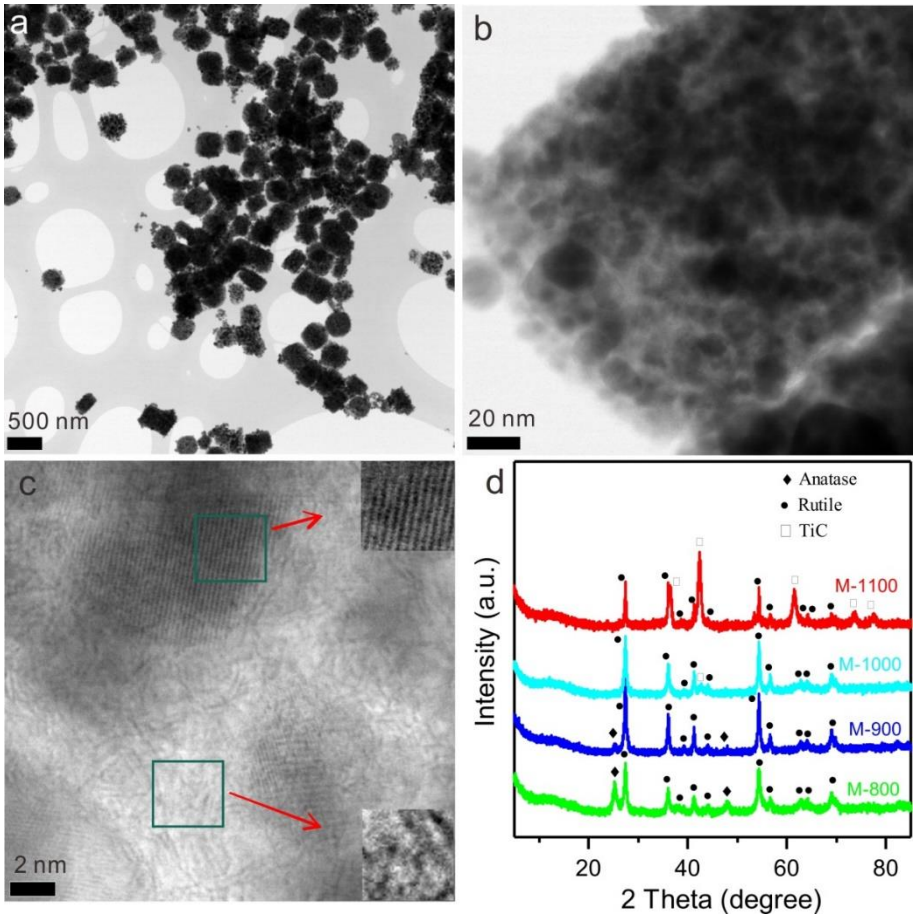

Figure 1. (a-c) Representative TEM images of M-1000. The insets of c are the corresponding HRTEM images of different square area. (d) XRD patterns of M-Ts.

The formation process of M-Ts can also be followed by thermogravimetric analysis (TGA) (Figure S5). The first weight loss step is below 200 °C and can be attributed to the loss of adsorbed water and other volatile adsorbed compounds. The decomposition of organic ligands within the MOF to pristine carbon species appears between 200 and 500 °C. The minor weight loss between 800 and 1000 °C possibly results from carbothermal reduction of TiO_2, that is, carbon insertion into TiO_2 and carbon oxide formation due to oxygen substitution. TGA under air is also used to investigate the structures of M-Ts (Figure 2b). Notably, there is an obvious increase in mass within the temperature range between 164 and 316 °C for M-1000 and M-1100. This can be ascribed to the oxidation and substitution of carbon doped into TiO_2 as well as the carbon in TiC (and thus the following resubstitution of carbon with oxygen) or to the reoxidation of possibly present Ti^{3+}.[22] The higher increase in weight for M-1100 than for M-1000 indicates the higher carbide content in the former which is in line with the XRD results. Notably, the temperature of resubstitution of

carbon is shifted to higher values for M-1100 indicating the higher thermodynamic barrier for reoxidation in TiC than in C-Ti_xO_y. N_2 (-196 °C) physisorption curves (Figure S6) display that M-Ts still have a porous structure with high SSA. In contrast to MIL-125(Ti), the hysteresis loops indicate the presence of additional mesopores which can be beneficial for the accessibility of catalytically active sites and for transport of N_2 and ammonia within the catalysts during NRR. Whereas the sizes of the mesopores seem to remain in the same range with increasing pyrolysis temperature, the SSA and microporosities decrease significantly from M-1000 to M-1100 due to the increasing formation of TiC and the decreasing content of free carbon.

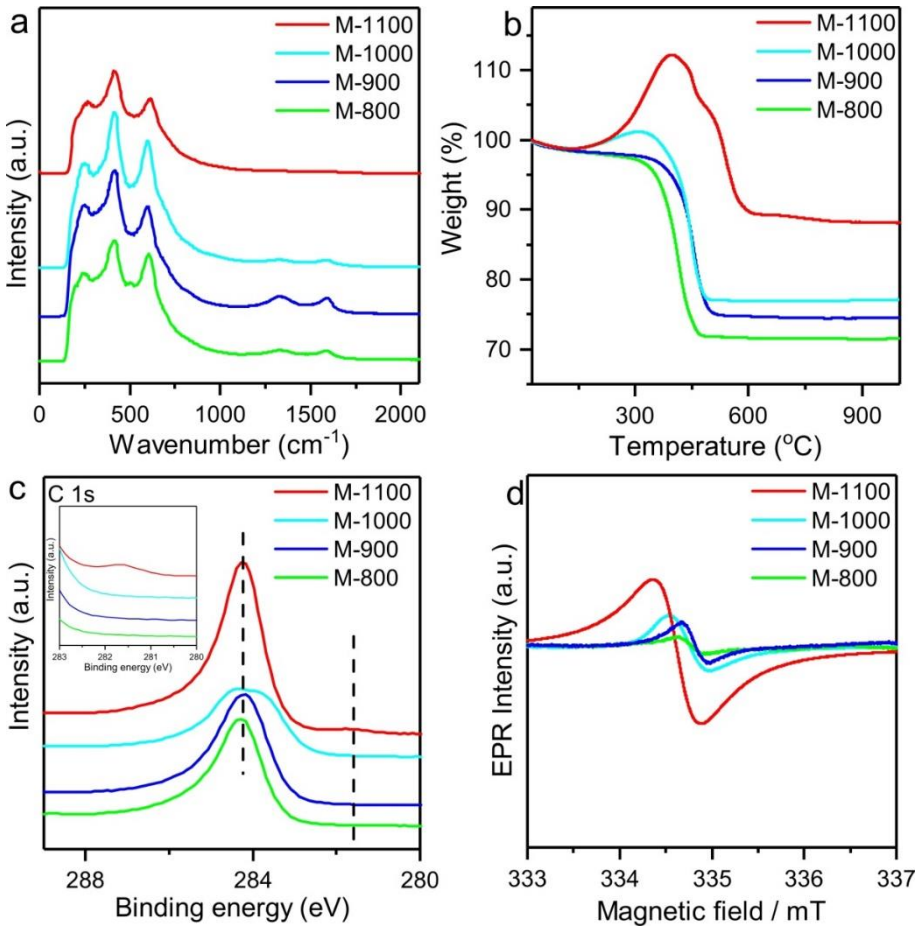

Figure 2. (a) Raman spectra, (b) TGA analysis (under synthetic air with a heating rate of 10 oC min-1), (c) XPS spectra of C 1s and (d) EPR spectra for M-800, M-900, M-1000 and M-1100.

X-ray photoelectron spectroscopy (XPS) measurements are further performed to investigate the binding states of the elements present in the hybrid materials (Figure S7). Although it can be assumed that the majority of carbon atoms in all materials are still bonded in the free carbon phase, the main peak in the C1s spectra exhibits a minor shift towards lower binding energy

(Figure 2c). Apparently, this shift is due to the presence of negatively polarized carbon atoms substituting oxygen in the anionic lattice of Rutile.[23] This binding situation is particularly pronounced in M-1000 where the peak is significantly broadened. This broadening is not observed anymore in M-1100 but instead a new peak centered at 281.7 eV appears in M-1100 due to the existence of carbidic carbon in TiC with rather covalent character.[24] High-resolution C 1s spectra of M-800, M-900 and M-1000 are mainly composed of four characteristic peaks (Figure S8), corresponding to the C-C, C-O, C=O, O-Ti-C structures, respectively.[25] Besides the above four peaks, a new characteristic peak assigned to Ti-C appears in M-1100 (Figure S8).[24] Similarly, XPS spectra of Ti 2p (Figure S9) for M-800, M-900 and M-1000 also show a shift towards lower binding energy in comparison to TiO_2 due to an increasing portion of Ti atoms bonded to carbon instead of the more electronegative oxide anions. Again the peak broadening in M-1000 is seen showing that the content of such “weakly anionic” carbon species is the highest in M-1000. Besides, M-1100 shows a new peak centered at 455.2 eV, which can again be attributed to the presence of oxygen-free TiC.[24] The same binding energy shift is also seen in the XPS spectra of O 1s (Figure S10). Furthermore, the structure and reactivity of paramagnetic species are characterized on atomic level by electron paramagnetic resonance (EPR) (Figure 2d). The similar signal is observed on M-800, M-900, M-1000 and M-1100 with a g factor of 2.0038, 2.004, 2.0043 and 2.005, respectively, which can be attributed to characteristic OVs.[26] Notably, enhanced signal intensity indicates that higher temperature can induce higher concentration of OVs in the M-Ts.

Based on the above analysis, the formation of the M-Ts nanocomposites can thus be understood as follows: Ti in MIL-125(Ti) reacts with the nearby oxygen and aggregates into stable TiO_2 nanoparticles. Meanwhile, the organic ligands also undergo pyrolysis under high temperature to obtain pristine porous carbon. At high temperature, part of this carbon can occupy formed OVs in TiO_2, which means that oxygen in the anion lattice of TiO_2 OVs is replaced. At temperatures above 1000°C not only partial anion substitution takes place but then TiO_2 can be completely converted to TiC according to Equation (1)

$$TiO_2 + 3C \rightarrow TiC + 2CO \quad (1)$$

Besides, as the amount of OVs increases with higher temperature, the amount of C-Ti_xO_y also increases from T-800 to M-1000. Although TiC starts forming at 1000 °C, the amount is quite low as XPS results show. When the temperature is increased to 1100 °C, the free carbon is fully consumed, thus transfer of carbon atoms to OVs is inhibited even though more OVs may form at such high temperature.

For comparison, the gas flow during pyrolysis was changed from Ar to N_2 and the corresponding samples with nearly similar pore structure (Figure S11a) are denoted as M-Ts-N_2. As shown in XRD patterns, the diffraction peaks of TiN appear in M-900-N_2 and M-1000-N_2 (Figure S11b). Furthermore, elemental analysis (Table S1) also indicates a significant content of N in as-obtained M-Ts-N_2, and the amount of N increases with the increase of temperature. As there is no N species existing in the MOF precursor and M-Ts synthesized under argon atmosphere, the N_2 gas obviously participates in the calcination reaction of MOF precursor. In contrast to the M-Ts samples, the OVs formed during the heating of the MOF precursor are not filled with carbon but instead it is thermodynamically favored to filled with more electronegative nitrogen in this case. It is widely known that such oxygen-deficient “Magnelli-Phases” of titanium oxides have versatile redox chemistry with a wide distribution of possible electronic band structures as well as many possible anionic substitutions. [22]

Our idea to use this material for electrochemical NRR is motivated by this versatile chemistry of the anion-substituted titanium oxides and the possible high affinity of the M-Ts materials calcined under Ar towards the binding of N_2. Should that binding be strong enough to polarize N_2 so much that it can be reduced by reacting with protons and electrons and should the binding at the same time be reversible, that is, be weak enough to not lead to substitution of carbon in the anion lattice by nitridic nitrogen, then these noble-metal-free materials would be well suited as NRR catalysts as they in addition come with high porosity, active sites which are embedded into nanocrystalline areas, and a free carbon phase ensuring sufficient electric conductivity. The catalytic performance in the electrochemical NRR is first tested for M-1000 by using a H-cell with three-electrode system. Carbon paper with catalysts deposited is used as the working electrode. As shown in the Linear sweep voltammetry (LSV) curves in Ar and N_2-saturated 0.2 M $LiClO_4$ aqueous solution, current densities in N_2 are obviously larger than in Ar within the applied potential range of -0.3 to -1.0 V vs. RHE, which demonstrates the current response of M-1000 in the presence of N_2 (Figure 3a). With continuous N_2 bubbling and at different given potentials, chronoamperometry tests (Figure S12) were carried out for 10000 s to calculate NH_3 yields and corresponding FEs, based on NH_4^+ calibration curves (Figure S13). The maximum FE of 17.8% with a remarkable yield of 9.2 μg h^{-1} mg^{-1} for NH_3 is achieved at -0.4 V vs. RHE (Figure 3b). Besides, no N_2H_4 is detected as potential product as there is no obvious color change before and after electrolysis at -0.3 V vs. RHE when adding N_2H_4 color reagent (Figure S14a). UV-Vis spectra also confirm that no N_2H_4 is produced independent of the applied potential (Figure S14b). At more negative potentials, FE and NH_3 yield are both cast into shade due to the strong competition with HER.[27] In order to verify that NH_3 in the electrolyte is obtained from electrochemical NRR on M-1000 electrode, the process is

performed under Ar-saturated electrolyte, open-circuit, and by using pure carbon paper as the working electrode. As shown in the UV-Vis spectra (Figure 3c) and optical images (Figure S15), NH_4^+ cannot be detected. Meanwhile, there is no NH_3 produced in Ar-saturated electrolyte at all given potentials (Figure S16). In the recycling test (Figure S17), no obvious fluctuation arises in the FE and NH_3 yield (Figure 3d), demonstrating the good stability of M-1000 during the NRR, which can be also confirmed by the long-time chronoamperometry test (Figure S18a) and the continuous production of NH_3 over reaction time (Figure S18b). TEM images after the chronoamperometry test demonstrate the structural stability as well (Figure S19).

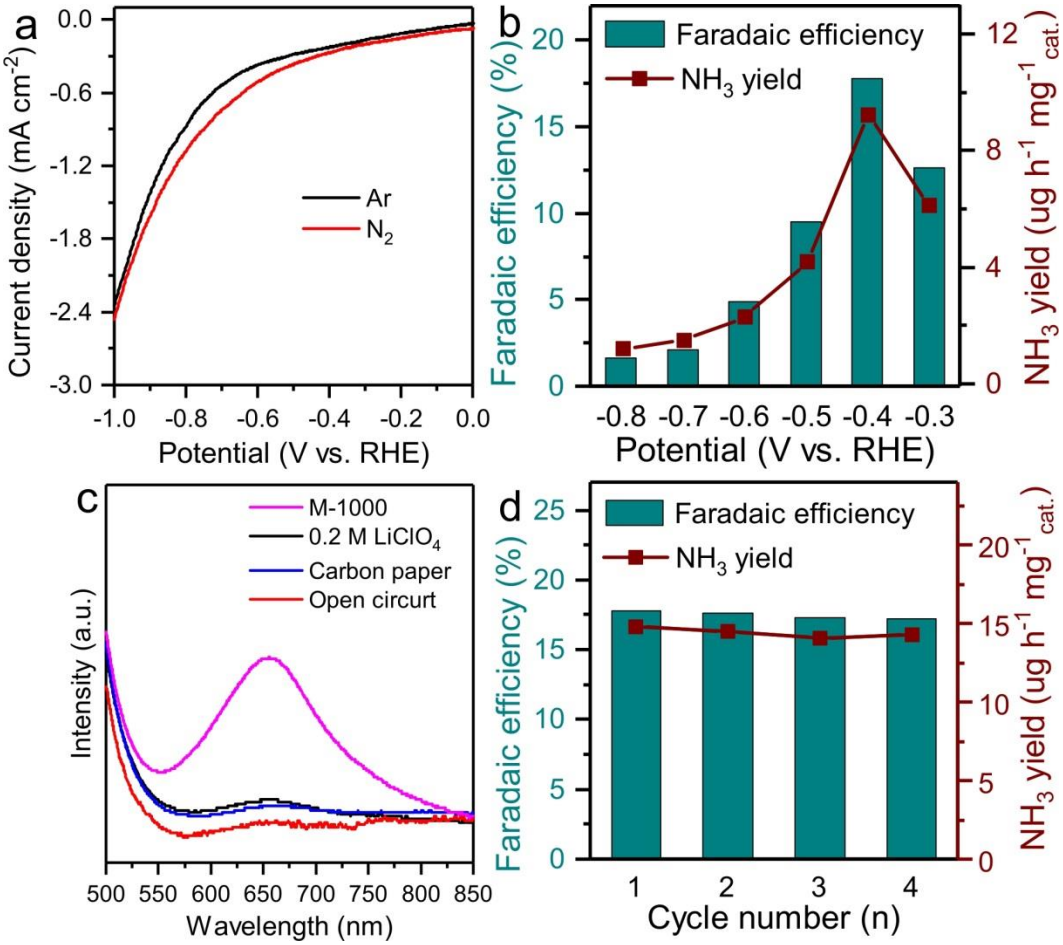

Figure 3. Electrocatalytic NRR performance of M-1000 electrode. (a) LSV curves in N2-and Ar-saturated aqueous solution of 0.2 M LiClO4 under ambient conditions. (b) FE and NH3 yield at each given potential. (c) UV-Vis absorption spectra of the 0.2 M LiClO4 solution with indophenol indicator after charging at -0.4 V vs. RHE for 10000 s under various conditions. (d) FE and NH3 yield during the recycling test under the potential of -0.4 V vs. RHE.

To conclude on the influence of oxygen substitution by carbon in the anion lattice of TiO_2, NRR performance of M-800 and M-900 is also tested. At the potential of -0.4 V vs. RHE, FE and NH_3

yield of M-800 and M-900 lag far behind M-1000 (Figure S20). When the pyrolysis temperature increases to 1100 °C, both FE and NH_3 yield go down again. Considering the structures of M-Ts, there is a higher content of TiC in M-1100, which is apparently inactive for activation of N_2 and leads to predominant occurrence of HER. Further considering different content of doped carbon MT-s, we suspect that the formed Ti-C bonds in Rutile can be the active site for N_2 fixation. NRR is also tested with commercial TiO_2 and TiC electrodes which show bad performance (Figure S20). In addition, the electrochemical active surface area (ECSA) is measured via double-layer capacitance test in 0.2 M $LiClO_4$ solution saturated with N_2 (Figure S21), clearly confirming that the ECSA of M-1000 is larger than those of M-800, M-900 and M-1100 (Figure S22). In contrast to the M-Ts materials, the M-Ts-N_2 materials show significantly lower FEs in NRR tests indicating that TiN is not active for nitrogen activation. Notably, the N species in M-Ts-N_2 are electrochemically unstable, as NH_3 can also be detected without N_2 as feeding gas after the chronoamperometry test (Figure S23).

To gain deep insights into the origin of the enhanced NRR performance of the C-Ti_xO_y/C catalyst and to highlight the role of carbon doping in NRR, DFT calculations were carried out to investigate the mechanism of N_2 fixation on the C-doped TiO_2 (110) surface compared with non-doped OVs enriched TiO_2 (OVs-TiO_2). The typical NRR distal pathway and the corresponding free energy diagram through the distal mechanisms of NRR on C-Ti_xO_y surface are first summarized (Figure 4). After the adsorption of dinitrogen on the carbon site with an energy gain of -0.06 eV (roughly corresponding to a realistic adsorption enthalpy of 6 kJ/mol), the key step of the first hydrogenation of C*N_2 to C*N-NH requires an energy input of 0.64 eV. The subsequent intermediate hydrogenation products are C*N-NH_2, *N (the first NH_3 molecule released), associated with an increase of the N-N bond length from 1.25 Å to 1.36 Å. These two steps are exothermic by 0.49 and 1.56 eV. The subsequent formation of NH*, NH_2*, and the second NH_3 molecule require energy injection of 0.20 0.41, 0.01, and 0.35 eV, respectively. Comparison of the reaction free energies of C-Ti_xO_y and OVs-TiO_2 in the pathways demonstrates that carbon located at the OV site is the most active site for the NRR. Considering the free energy path (Figure 4 and Figure S24), the addition of the first hydrogen atom to the bound N_2 is the rate-determining step in electrochemical NRR. In contrast, the pathway on “a naked” OV site in TiO_2 is energetically less favorable. The hydrogenation of *N_2 forming *N_2H on OV site (1.00 eV) is thermodynamically less favorable than that at a C-doped position (0.64 eV). Therefore, this advantageous low energy barrier on C-Ti_xO_y can significantly enhance the electrocatalytic activity for the NRR, which is in agreement with the experimental results.

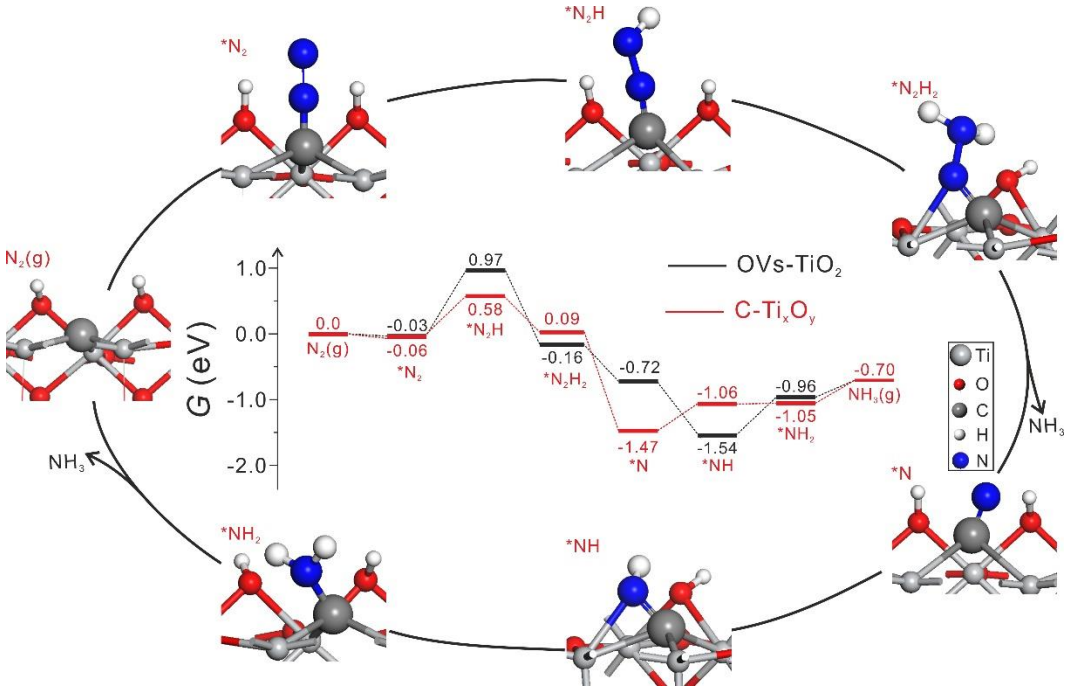

Figure 4. Comparison of free-energy for NRR on C-TixOy- (110) (red) and OVs-TiO2 (110) (black) and the optimized structures of different intermediates on C-TixOy (110).

In conclusion, we presented a novel mode for activation of N_2 by the carbon-doped sites in the anion lattice of Rutile. An efficient NRR catalyst of C-Ti_xO_y/C nanocomposite has been developed via simple pyrolysis of MIL-125(Ti). The density of covalent Ti-C bonds originating from the occupation of OVs by carbon atoms can be regulated by the synthesis temperature. By comparing the NRR performance of M-Ts and studying through DFT calculations, we find that the existence of C-doped TiO_2 is pivotal to activate and reduce N_2. Given by the development of nanotechnology, the strategy to rationally dope heteroatoms into the anion lattice of transition metal oxides to create catalytically active centers may open many new opportunities beyond the use of noble metal-based catalysts for other reactions that require the activation of small molecules as well. In the particular case discussed here it can also be expected that a more controlled nanostructure (i.e., the exposure of more such active sites) could lead to a higher utilization of the active centers and thus even higher ammonia production rate.

4.2.3. Experimental Section

Synthesis of MIL-125(Ti): MIL-125(Ti) was synthesized by a modified method reported in literature. 0.5 g of Terephthalic acid (H_2BDC) and 0.26 mL of tetra-n-butyl titanate $Ti(OC_4H_9)_4$ were added into a mixed solution with dimethylformamide (DMF) (9 mL) and dry MeOH (1 mL). The above mixture was stirred for 1 hour at room temperature, followed by transferring into a 50 mL Teflon-lined autoclave and heating at 150°C for 20 hours. The white products were collected, rinsed several times with acetone and dried under vacuum at 60 °C overnight for further use.

Synthesis of M-Ts: M-Ts were prepared by simple pyrolysis. In a typical procedure, 0.25 g MIL-125(Ti) was transferred to a tubular furnace and heated at different temperatures for 2 h with a heating rate of 4 °C min^{-1} under Ar atmosphere.

Synthesis of M-Ts-N_2: M-Ts-N_2 was prepared by following the procedures of M-Ts, while only changing the protection gas from Ar to N_2.

Material characterization: Scanning electron microscopy (SEM) images were obtained on a LEO 1550-Gemini instrument, operating at 3 kV after sputtering with gold. The crystallinity of as-obtained product was characterized by X-ray powder diffraction (XRD), recorded on a Bruker D_8 advance X-ray diffractometer with Cu Kα radiation. Transmission electron microscopy (TEM), high-resolution TEM (HRTEM), and energy-dispersive X-ray (EDX) studies were carried out on JEOL ARM 200F instrument operating at 200 kV. The samples were first dispersed in ethanol, and coated on a carbon-coated copper TEM grid, followed by drying at room temperature. Elemental analysis was carried out by using a Vario Micro device. N_2 physisorption isotherms measurements were conducted on Quadrasorb apparatus from Quantachrome Instruments at -196 °C. The samples were outgassed at 150 °C for 20 h under vacuum before all the measurements. SSAs were calculated using the multi-point Brunauer-Emmett-Teller (BET) model in the range of $0.05 < p/p_0 < 0.2$. X-ray photoelectron spectroscopy (XPS) measurements were accomplished using Thermo Scientific K-Alpha+ X-ray photoelectron spectrometer with a microfocused, monochromated Al-Kα X-ray source (1486.68 eV; 400 µm spot size). The K-Alpha+ charge compensation system was employed during analysis to prevent any localized charge buildup. The samples were mounted on conductive carbon tape and the resulting spectra analyzed using the Avantage software from Thermo Scientific. Raman spectra were recorded on a Witec (focus innovations) Raman Microscope, carried out with an objective (Nikon, 10x/0.25, ∞/- WD 6.1) and an excitation wavelength of 532 nm and intensity of 3.5 mW. EPR measurements at room temperature (296 K) were carried out on a Magnettech Minscope MS_300 X-band EPR spectrometer. Samples were prepared in 50 µl-ringcaps micropipettes with an inner diameter of

1 mm: approximately 5 mg of each sample were filled into the capillary, resulting in an active volume for the EPR measurement of approximately 1.6 mm^3. Thermogravimetric analysis (TGA) was conducted on a Netzsch TG 209 F_1 device under constant artificial air flow. The sample was put into a platinum pan at a heating rate of 10 °C min-1 to 1000 °C. UV-Vis spectroscopic measurements were conducted with a Cary 50 UV-Vis spectrometer.

Electrochemical measurements: All the electrochemical properties were investigated on a Gamry potentiostat in a H-type cell separated by Nafion membrane. Prior to the test, the Nafion membrane was pretreated by heating in 5% H_2O_2 aqueous solution at 85 °C for 1 h and ultrapure water for another 1 h. Typically, the working electrode, which was prepared by depositing an ethanol dispersion of catalysts ink onto a carbon paper electrode (1*1 cm^2) with 0.60 mg cm^{-2} catalyst loading, and a saturated calomel reference electrode (SCE) were placed in cathodic compartment, while platinum foil (1*1 cm^2) was used as a counter electrode in the anodic compartment. A 0.2 M $LiClO_4$ aqueous solution was prepared with ultrapure water from Millipore system and used as electrolyte. All the potentials in this work were calculated to RHE, E(RHE) = E(SCE) + 0.24 + 0.059 * pH. Linear sweep voltammetry (LSV) tests were conducted in N_2- and Ar-saturated solution with a scan rate of 5 mV s^{-1}. Besides, all LSV curves were steady-state ones after several cycles and directly used without additional iR correction. Before all the potentiostatic tests, which were carried out at different potentials under continuous stirring, pure Ar or N_2 was purged into the cathodic compartment for at least 30 min with a flow rate of 10 mL min^{-1} and kept feeding during the whole test. Electrochemical active surface area (ECSA) was determined by capactive current density which was measured with double-layer (C_{dl}) charging from the scan-rate dependence of cyclic voltammetry (CV) (potential windows was 0 V to -0.2 V vs. SCE). C_{dl} was tested by plotting the current density (△j) at -0.1 V vs. SCE (0.2 M $LiClO_4$ aqueous).

Determination of NH_3: NH_3 quantification was achieved by the modified indophenol blue method. In detail, 2 mL electrolyte solution after electrochemical testing was mixed with 2 mL of a 1 M NaOH solution (contains 5 wt.% sodium citrate and 5 wt.% salicylic acid). Then, 1 mL of 0.05 M NaClO solution was also added into the mixture, followed by addition of 1 wt.% $C_5FeN_6Na_2O$ (sodium nitroferricyanide). As-obtained solution was measured by UV-Vis spectroscopy after staying at room temperature for 1 h, and the adsorption peak of indophenol blue appeared at around 655 nm. In order to accurately quantify NH_3, a calibration curve of concentration-absorbance was plotted by preparing a series of ammonium chloride standard solutions. The linear relation was repeated for three times.

Determination of N_2H_4: N_2H_4 was detected by Watt and Chrisp method with a color reagent containing 5.99 g of para-(dimenthylamino) benzaldehyde, 30 mL of HCl (concentrated) and 300

mL of ethanol. In detail, 5 mL electrolyte was mixed with 5 mL as-prepared color reagent and stirred for 20 min at room temperature.

Calculations of NH_3 yield and FE: FE of NH_3 was calculated according to the following equation:

$$FE = \frac{3 * F * c * V}{Q}$$

NH_3 yield was obtained according to:

$$NH_3\ yield = \frac{c * V * 17}{t * m}$$

where F is Faraday constant; c is the calculated concentration of NH_3; V is total volume of electrolyte in cathodic compartment; Q is the total charge passed through the electrochemical system; t is the total time of chronoamperometry test; and m is the catalysts loading.

Computation details: In this work, all the spin-polarized DFT calculations were performed by using Vienna ab initio Simulation Package (VASP).[28] The generalized gradient approximation was used with the Perdew-Burke-Ernzerh (PBE) of exchange-correlation functional.[29] We used the PBE functional with Grimme's D3 correction to include a dispersion interaction.[30] The valence electronic states were expanded in plane wave basis sets with an energy cutoff of 450 eV and geometry optimizations were performed until the maximum force on each relaxed atom was less than 0.02 eV/Å. Due to the strong correlation effect among the partially filled Ti 3d states, we used the Hubbard parameter, U,[31] for the Ti 3d electrons to take the on-site Coulomb interaction into account. According to previous work, the value of U-J of 4.2 eV was applied.[32]

The Gibbs free energy change (ΔG) of the elementary step was calculated with the equation: $\Delta G = \Delta E_{DFT} + \Delta E_{zpe} + T\Delta S_{vib}$, where ΔE_{DFT} is change of DFT total energy, ΔE_{zpe} and $T\Delta S_{vib}$ is change of zero point energies and the entropy. ΔE_{zpe} and $T\Delta S_{vib}$ are calculated by vibrational frequencies of the surface intermediates within DFT calculation, for the gaseous molecules, the entropy contributions ($T\Delta S$) were obtained from the experimental values.

As XRD analysis proved that the NRR catalysts mainly contain the Rutile phase, we also calculated Rutile TiO_2 model. The calculated lattice parameters of the unit cell are a = 4.69 Å and c = 3.04 Å, in excellent agreement with the experimental values (a = 4.587 Å and c = 2.956 Å).[33] The most stable TiO_2(110) surface is modeled with a p(3x1) periodic slab with 12 layers (Figure S25), and the vacuum between slabs is 15 Å; correspondingly, a 4x5x1 k-point mesh was used.[34] During structural optimization, the lowest three layers were fixed in the bulk positions and the

upper nine layers and the adsorbates were allowed to relax. The stoichiometric Rutile TiO_2 (110) surface exhibits five- and six-fold coordinated Ti atoms as well as two- and three-fold coordinated oxygen atoms (O_{2c} and O_{3c}).

The experiment shows only part of carbon substituting the oxygen on the surface of TiO_2 and form C-Ti_xO_y. The model of C-Ti_xO_y was constructed by replacing an oxygen atom with one C atom (Figure S26). The formation energy was calculated by $E_f = E(CO) + E(TiO_{2-x}C) - E(C) + E(TiO_2)$. The reaction of the substituting of O_{2c} and O_{3c} with carbon is exothermic and the corresponding formation energy is 1.44 and 1.62 eV, respectively. Thus substituting the O_{3c} was the more preferential way (Figure S26a). We also consider three *H hydrogenation at the three O_{2c} sites to simulate the more stable phase under operating potentials (Figure S26a), and the reaction is strongly exothermic by 2.88 eV.

4.2.4. References

[1] a) K. A. Brown, D. F. Harris, M. B. Wilker, A. Rasmussen, N. Khadka, H. Hamby, S. Keable, G. Dukovic, J. W. Peters, L. C. Seefeldt, P. W. King, *Science* **2016**, *352*, 448; b) J. W. Erisman, M. A. Sutton, J. Galloway, Z. Klimont, W. Winiwarter, *Nature Geoscience* **2008**, *1*, 636; c) C. Zamfirescu, I. Dincer, *Journal of Power Sources* **2008**, *185*, 459.

[2] a) C. J. M. van der Ham, M. T. M. Koper, D. G. H. Hetterscheid, *Chemical Society Reviews* **2014**, *43*, 5183; b) P. J. Chirik, *Nature Chemistry* **2009**, *1*, 520; c) Y. Tanabe, Y. Nishibayashi, *Coordination Chemistry Reviews* **2013**, *257*, 2551.

[3] a) D. Bao, Q. Zhang, F.-L. Meng, H.-X. Zhong, M.-M. Shi, Y. Zhang, J.-M. Yan, Q. Jiang, X.-B. Zhang, *Advanced Materials* **2016**, *29*, 1604799; b) C. Guo, J. Ran, A. Vasileff, S.-Z. Qiao, *Energy & Environmental Science* **2018**, *11*, 45; c) S. Chen, S. Perathoner, C. Ampelli, C. Mebrahtu, D. Su, G. Centi, *Angewandte Chemie* **2017**, *129*, 2743.

[4] A. E. Shilov, *Russian Chemical Bulletin* **2003**, *52*, 2555.

[5] a) A. R. Singh, B. A. Rohr, J. A. Schwalbe, M. Cargnello, K. Chan, T. F. Jaramillo, I. Chorkendorff, J. K. Nørskov, *ACS Catalysis* **2017**, *7*, 706; b) J. M. McEnaney, A. R. Singh, J. A. Schwalbe, J. Kibsgaard, J. C. Lin, M. Cargnello, T. F. Jaramillo, J. K. Nørskov, *Energy & Environmental Science* **2017**, *10*, 1621; c) G.-F. Chen, X. Cao, S. Wu, X. Zeng, L.-X. Ding, M. Zhu, H. Wang, *Journal of the American Chemical Society* **2017**, *139*, 9771.

[6] a) A. J. Martín, T. Shinagawa, J. Pérez-Ramírez, *Chem* 2018; b) G.-F. Chen, S. Ren, L. Zhang, H. Cheng, Y. Luo, K. Zhu, L.-X. Ding, H. Wang, *Small Methods* **2018**, *0*, 1800337.

[7] a) D. Bao, Q. Zhang, F.-L. Meng, H.-X. Zhong, M.-M. Shi, Y. Zhang, J.-M. Yan, Q. Jiang, X.-B. Zhang, *Advanced Materials* **2017**, *29*, 1604799; b) M.-M. Shi, D. Bao, B.-R. Wulan, Y.-H. Li, Y.-F. Zhang, J.-M. Yan, Q. Jiang, *Advanced Materials* **2017**, *29*, 1606550.

[8] a) Z. Wang, F. Gong, L. Zhang, R. Wang, L. Ji, Q. Liu, Y. Luo, H. Guo, Y. Li, P. Gao, X. Shi, B. Li, B. Tang, X. Sun, *Advanced Science* **2018**, *0*, 1801182; b) C. Lv, C. Yan, G. Chen, Y. Ding, J. Sun, Y. Zhou, G. Yu, *Angewandte Chemie International Edition*,

[9] a) X. Ren, G. Cui, L. Chen, F. Xie, Q. Wei, Z. Tian, X. Sun, *Chemical Communications* **2018**; b) R. Zhang, Y. Zhang, X. Ren, G. Cui, A. M. Asiri, B. Zheng, X. Sun, *ACS Sustainable Chemistry & Engineering* **2018**, *6*, 9545.

[10] a) H. Cheng, L. X. Ding, G. F. Chen, L. Zhang, J. Xue, H. Wang, *Adv. Mater.* **2018**, e1803694; b) J. Pang, R. G. Mendes, A. Bachmatiuk, L. Zhao, H. Q. Ta, T. Gemming, H. Liu, Z. Liu, M. H. Rummeli, *Chemical Society Reviews* **2018**; c) L. M. Azofra, N. Li, D. R. MacFarlane, C. Sun, *Energy & Environmental Science* **2016**, *9*, 2545; d) Y. Luo, G.-F. Chen, L. Ding, X. Chen, L.-X. Ding, H. Wang, *Joule* **2018**.

[11] E.-Y. Jeong, C.-Y. Yoo, C. H. Jung, J. H. Park, Y. C. Park, J.-N. Kim, S.-G. Oh, Y. Woo, H. C. Yoon, *ACS Sustainable Chemistry & Engineering* **2017**, *5*, 9662.

[12] a) X. Yu, P. Han, Z. Wei, L. Huang, Z. Gu, S. Peng, J. Ma, G. Zheng, *Joule* **2018**; b) S. Mukherjee, D. A. Cullen, S. Karakalos, K. Liu, H. Zhang, S. Zhao, H. Xu, K. L. More, G. Wang, G. Wu, *Nano Energy* **2018**, *48*, 217; c) Y. Song, D. Johnson, R. Peng, D. K. Hensley, P. V. Bonnesen, L. Liang, J. Huang, F. Yang, F. Zhang, R. Qiao, A. P. Baddorf, T. J. Tschaplinski, N. L. Engle, M. C. Hatzell, Z. Wu, D. A. Cullen, H. M. Meyer, B. G. Sumpter, A. J. Rondinone, *Science Advances* **2018**, *4*.

[13] a) F. Bertini, M. Glatz, N. Gorgas, B. Stoger, M. Peruzzini, L. F. Veiros, K. Kirchner, L. Gonsalvi, *Chemical Science* **2017**; b) Q. Qin, T. Heil, M. Antonietti, M. Oschatz, *Small Methods* **2018**, *0*, 1800202.

[14] M. E. Vol'pin, *Journal of Organometallic Chemistry* **1980**, *200*, 319.

[15] R. Zhang, X. Ren, X. Shi, F. Xie, B. Zheng, X. Guo, X. Sun, *ACS Applied Materials & Interfaces* **2018**.

[16] a) H.-L. Jiang, B. Liu, Y.-Q. Lan, K. Kuratani, T. Akita, H. Shioyama, F. Zong, Q. Xu, *Journal of the American Chemical Society* **2011**, *133*, 11854; b) K. Shen, X. Chen, J. Chen, Y. Li, *ACS Catalysis* **2016**, *6*, 5887.

[17] S.-N. Kim, J. Kim, H.-Y. Kim, H.-Y. Cho, W.-S. Ahn, *Catalysis Today* **2013**, *204*, 85.

[18] W.-K. Wang, J.-J. Chen, X. Zhang, Y.-X. Huang, W.-W. Li, H.-Q. Yu, *Scientific Reports* **2016**, *6*, 20491.

[19] C.-H. Huang, D. Gu, D. Zhao, R.-A. Doong, *Chemistry of Materials* **2010**, *22*, 1760.

[20] B. H. Lohse, A. Calka, D. Wexler, *Journal of Alloys and Compounds* **2007**, *434-435*, 405.

[21] S. Mohapatra, D. K. Mishra, S. K. Singh, *Powder Technology* **2013**, *237*, 41.

[22] D. Portehault, V. Maneeratana, C. Candolfi, N. Oeschler, I. Veremchuk, Y. Grin, C. Sanchez, M. Antonietti, *ACS Nano* **2011**, *5*, 9052.

[23] J. Schnadt, J. N. O'Shea, L. Patthey, J. Schiessling, J. Krempaský, M. Shi, N. Mårtensson, P. A. Brühwiler, *Surface Science* **2003**, *544*, 74.

[24] K**.** Krishnamoorthy, P. Pazhamalai, S. Sahoo, S.-J. Kim, *Journal of Materials Chemistry A* 2017, *5*, 5726.

[25] a) F. Dong, S. Guo, H. Wang, X. Li, Z. Wu, *The Journal of Physical Chemistry C* **2011**, *115*, 13285; b) Y. Huang, W. Ho, S. Lee, L. Zhang, G. Li, J. C. Yu, *Langmuir* **2008**, *24*, 3510.

[26] F. Zuo, L. Wang, T. Wu, Z. Zhang, D. Borchardt, P. Feng, *Journal of the American Chemical Society* **2010**, *132*, 11856.

[27] T. Oshikiri, K. Ueno, H. Misawa, *Angewandte Chemie* **2016**, *128*, 4010.

[28] a) G. Kresse, J. Furthmüller, *Comput. Mater. Sci.* **1996**, *6*, 15; b) G. Kresse, J. Furthmüller, *Phys. Rev. B* **1996**, *54*, 11169.

[29] a) G. Kresse, D. Joubert, *Phys. Rev. B* **1999**, *59*, 1758; b) J. P. Perdew, K. Burke, M. Ernzerhof, *Phys. Rev. Lett.* **1996**, *77*, 3865.

[30] S. Grimme, J. Antony, S. Ehrlich, H. Krieg, *J. Chem. Phys.* **2010**, *132*, 154104.

[31] S. L. Dudarev, G. A. Botton, S. Y. Savrasov, C. J. Humphreys, A. P. Sutton, *Phys. Rev. B* **1998**, *57*, 1505.

[32] a) A. Mattsson, S. Hu, K. Hermansson, L. Österlund, *J. Chem. Phys.* **2014**, *140*, 034705; b) S. Chrétien, H. Metiu, *J. Phys. Chem. C* **2011**, *115*, 4696.

[33] J. K. Burdett, T. Hughbanks, G. J. Miller, J. W. Richardson, J. V. Smith, *J. Am. Chem. Soc.* **1987**, *109*, 3639.

[34] H. J. Monkhorst, J. D. Pack, *Phys. Rev. B* **1976**, *13*, 5188.

5. Conclusion and Outlook

This doctoral thesis presents an in-depth investigation toward photo-induced reactivity involving short-lived intermediates. A main part of this work addresses photo-induced ET and PT reactions in model systems for complex biological processes and biomimetic membranes.

Simple phenolic compounds with intramolecularly connected basic moieties were employed to demonstrate a solvent-dependant switch in reaction mechanisms upon photo-induced oxidation. It is shown that in a polar environment, hydrogen bonding between OH-groups and an adjacent base can suppress the otherwise favoured electron–proton transfer (EPT). Oxidation instead proceeds via multisite electron–proton transfer (MS-EPT). This is of particular importance in biological systems such as radical enzymes featuring tyrosyl radicals and in the photolabelling and photografting of peptides, proteins, and oligonucleotides.

Electron transfer reactions in liposomes as biomimetic membranes provide an exclusive insight into long-range ET within an undistorted lipid bilayer. The electron transfer reaction is monitored by the oxidation of a stable nitroxide radical residing in the membrane, with $[Ru(bpy)_3]^{3+}$ serving as the oxidizing agent. These results present crucial information on background ET processes in membranes. This methodology can be applied to systematically study biological and artificial membranes, for example the involvement of π-electrons and/or water bridges in long-range ET in biological samples.

The other major part of this doctoral thesis addresses different aspects of the reactivity of photo-initiators for radical polymerization and the reduction of Cu^{2+} salts for nanomaterial synthesis.

A novel synthetic approach can be used to adjust the hydrophilicity or lipophilicity of bis(acyl)phosphane oxides (BAPO) derivatives. These modifications do not alter the properties of the phosphanoyl radicals formed upon bond cleavage as polymerization initiating species.

Also, the initiation behaviour of these BAPO photo-initiators in water/octane micro-emulsions was investigated. In these systems, phosphanoyl radicals initiate free radical polymerization reacting with both water- and oil-soluble monomers with high reaction rate constants. This opens the

possibility for a tailored design and construction of photo-generated copolymers containing polar and non-polar blocks.

Another aspect is the photochemistry of BAPOs in aqueous and alcoholic media, where unexpected transformations of phosphanoyl radicals into a persistent new radical are observed. This new radical does not participate in polymerization, but is converted to a mono(acyl)phosphane oxide (MAPO) derivative serving as a dormant secondary photo-initiator. This allows the synthesis of complex polymer architectures by performing simple polymerization steps with a single photo-initiator.

Furthermore, the photo-reduction of copper salts by the benzil/amine system is discussed. The benzil radical anion formed upon photolysis in the presence of triethylamine, is highly redox active and can reduce Cu^{2+} to Cu^{0}. This cost-effective and simple approach for the photo-induced reduction of Cu^{2+} to elemental copper can be used for the production of copper nanoparticles by employing different irradiation times to form nanoparticles with defined shape and size.

It is also shown, that the persistent BAPO-derived radical mentioned above can be employed as a reducing agent to convert Cu^{2+} to elemental Cu. This behaviour enables a simultaneous polymerization and metal-reduction. This allows a facile fabrication of copper nanocomposites with possible applications in heterogeneous catalysis.

To sum up, this doctoral thesis covers a wide array of different photo-chemical processes and radical(-induced) transformations. The research comprising this thesis are of importance for fundamental aspects of biological electron- and proton-transfer reactions and can be also used to study complex biological systems. In addition, these investigations may serve as a starting point to build up intricate systems for solar energy conversion based on biomimetic species.

Furthermore, the investigations on the polymerization and reduction behaviour of photo-initiator systems opens the door for the synthesis of metal-polymer nanocomposites. The approaches described in this thesis may allow for simple and straightforward fabrication of conducting polymers, novel systems for heterogeneous catalysis and chemiresistive sensor systems.

6. Appendix

6.1. List of Scientific Publications

9. *Two in One Go: Wavelength- and Site-Selective Generation of Copper Nanoparticles and Polymer Matrices Using Bisacylphosphane Oxides*

   M. Schmallegger, A. Eibel, R. Ricco, A. Chemelli, S. Kovac, F. Mautner, H. Grützmacher, G. Gescheidt, **In Preparation**

8. *Electron transfer across biomimetic membranes: Distance dependence investigated via time-resolved views by photo-induced oxidation of nitroxyls*

   M. Schmallegger, A. Barbon, M. Bortolus, A. Chemelli, I. Bilkis, G. Gescheidt, L. Weiner, **In Preparation**

7. *New modes of N2 fixation by partial anion substitution in titanium oxides for enhanced electrochemical ammonia synthesis*

   Q. Qin, Y. Zhao, M. Schmallegger, T. Heil, J. Schmidt, R. Walczak, G. Gescheidt, H. Jiao, and M. Oschatz, **Submitted to Angew. Chem.**

6. *The Unprecedented Bifunctional Chemistry of Bis(acyl)phosphane Oxides in Aqueous and Alcoholic Media*

   A. Eibel, M. Schmallegger, J. P. Menzel, A.-M. Kelterer, M. Zalibera, C. Barner-Kowollik, H. Grützmacher, G. Gescheidt., ***Chem. Eur. J.*** *– Just Accepted*

5. *Antioxidant Activity of Beer: An EPR Experiment for an Undergraduate Physical-Chemistry Laboratory*

   M. Schmallegger**,** G. Gescheidt, ***J. Chem. Educ. 2018****, 95,* 2013-2016.

4. *Benzil/triethylamine: a photo-reducing system for* Cu^{2+}

   M. Schmallegger**,** G. Gescheidt, ***Monatsh. Chem. 2018****, 149,* 499-504.

3. *Probing the first steps of photoinduced free radical polymerizations at water-oil interfaces*

   D. Darvasiová, Z. Barberiková, A. Eibel, M. Schmallegger**,** G. Gescheidt, M. Zalibera, D. Neshchadin, ***Polym. Chem. 2017****, 8*, 6943-6947.

2. *Extending the Scope of Bis(acyl)phosphane Oxides: Additional Derivatives*

   A. Eibel, M. Schmallegger, M Zalibera, A. Huber, Y. Bürkl, H. Grützmacher, G. Gescheidt, ***European J. Inorg. Chem.* 2017**, 2469–2478.

1. *Proton-Coupled Electron Transfer from Hydrogen Bonded Phenols to Benzophenone Triplets*

   R. Amorati, L. Valgimigli, C. Valglianisi, M. Schmallegger, D. Neshchadin, G. Gescheidt, ***Chem. Eur. J. 2017**, 23,* 5299-5306.

6.2. List of Presentations at Scientific Conferences

07/2018 27th PhotoIUPAC Conference (Dublin, Ireland): poster presentation (Title: *Kinetics of Photoinduced Electron Transfer Across Biomimetic Membranes)*

09/2017 The 8th Conference on Nitroxides (Padua, Italy): oral presentation (Title: *Kinetics of electron transfer across biomimetic membranes investigated by cw-EPR)*

07/2017 2nd International Conference on Hydrogen Atom Transfer (Rome, Italy): oral presentation (Title: *Probing Hydrogen Atom Transfer in Biomimetic Systems*)

04/2017 50th Annual International Meeting of the ESR Group of the Royal Society of Chemistry (Oxford, United Kingdom): poster presentation (Title: *An Approach to Obtain Kinetics of Electron Transfer across Biomimetic Membranes by cw-EPR)*

09/2016 Xth EFEPR Conference (Torino, Italy): poster presentation (Title: *Hydrogen Atom Bonding and Hydrogen Atom Transfer in Phenols: Investigation by CIDNP*)

09/2015 Summer School on Methods in Molecular Energy Research hosted by Max Planck Institute CEC /Gelsenkirchen, Germany)

06/2015 International EPR Seminar, (Graz, Austria): oral presentation (Title: *Reactivity of Phosphanoyl Radicals)*

6.3. Fundings and Awards

10/2018	**Young Scientists Best Paper Award** by Monatshefte für Chemie / Chemical Monthly for the Publication “Benzil/trimethylamine: a photo-reducing system for Cu^{2+}”
09/2016 – 09/2017	**Cooperation project for young scientist**; Aktion Österreich–Slowakei (Project 2016-05-15-003) Title: *“Free radical oxidation of cholesterol and PUFA on liquid-liquid interfaces. First insights”*
05/2016 – 06/2016	**Short Term Scientific Mission** at the National Center for Scientific Research “Demokritos” in Athens, Greece as part of COST ACTION CM 1201 “Biomimetic Radical Chemistry” Title: “*Molecular Insights into Antioxidative Effects in Specific Systems”*
2015	**Annual Merit-based Scholarship** from Graz University of Technology